Multi-Scale Study of Foam Flow Dynamics in Porous Media

Christopher Yeates

Sorbonne Université

Géosciences, Ressources Naturelles et Environnement

École Doctorale 398

IFP Energies Nouvelles – Département Géofluides et Roches

Multi-Scale Study of Foam Flow Dynamics in Porous Media

By Christopher Yeates

Doctoral Thesis in Geoscience

Doctoral Advisor: Dr. Lahcen Nabzar

Doctoral Tutor: Dr. Souhail Youssef

Presented and defended publicly on the 24th of July 2019

To a jury composed of:

Dr. Rossen, William, R., *TU Delft* – Professor – ***Reviewer***

Dr. Bodiguel, Hugues, *Université de Grenoble* – Professor – ***Reviewer***

Dr. Marry, Virginie, *Sorbonne Université* – Professor – ***Examinator***

Dr. Lorenceau, Elise, *Université de Grenoble* – Research Director – ***Examinator***

Dr. Marre, Samuel, *Université de Bordeaux* – Research Fellow – ***Examinator***

Dr. Lopez, Olivier, *Equinor* – Research Engineer – ***Member of the Jury***

Dr. Youssef, Souhail, *IFPEN* – Research Engineer – ***Member of the Jury***

Dr. Nabzar, Lahcen, *IFPEN* – Research Engineer – ***Member of the Jury***

Acknowledgements

This work was enabled by the doctoral program at IFP Énergies Nouvelles which provided financial and overall support, an office and a laboratory, and by the Doctoral School of Geoscience, Natural Resources and Environmental Science at Sorbonne Université which shared scientific oversight and ultimately granted the Diploma.

I would like to offer my sincerest thanks to the people at the Geofluids and Rocks department at IFPEN for giving me the opportunity to carry out this study and being wholly supportive and helpful throughout. I would specifically like to thank my tutor, Souhail Youssef, for his timely and astute guidance on both technical and general levels. I also thank my thesis director Lahcen Nabzar I would like to extend my thanks to Elise Lorenceau for her contributions and significant time spent reviewing papers and helping me shape the way forward in the key periods of the thesis. I must extend my gratitude to the kind members of the jury, that considered my work and travelled to Rueil for the PhD defense in the mid-summer heat. I therefore thank Professor William Rossen, Professor Hugues Bodiguel, Professor Virginie Marry, as well as Doctor Samuel Marre and Doctor Olivier Lopez.

I am deeply grateful for all the enormously competent and kind people I have interacted with during more than 3 years at Rueil Malmaison; notably Joelle Behot, for her patient help with the experimental work and untiring enthusiasm. A great number of smaller interactions also contributed to the final work and are worthy of mention, including Guillaume Batôt and his help to set up the Lattice Boltzmann flow simulations, Matthieu Mascle and Nicolas Gland with whom I had pertinent discussions regarding various aspects of the work. It is also necessary to express my gratitude to the technicians that assisted me, Hervé Deschamps and Herman Ravelojaona. The PhD experience was made infinitely better thanks to the friendships I made at the institute and for this I would like to thank my fellow PhD candidates and friends Hamza, Aurélien, Nicolas, Sebastian, Xavier and all the others. I also wish to thank my previous internship supervisor Sarah Leray, for first taking me on at IFPEN and giving me confidence needed to pursue the PhD.

Finally, I would like to thank my parents and partner, Isa, for their unwavering support and belief in me all the way through.

Thesis abstract

In this work, we use of a high-complexity micromodel of fixed structure on which we perform a series of experiments with varying injection rates, foam qualities, inlet bubble size distributions and injection methods. We perform individual bubble tracking and associate flow properties with bubble size properties and structural characteristics of the medium. We propose new tools describing the local and global flow in different ways. We establish specific behaviors for different bubble sizes, demonstrating that trapped foams are more likely to have smaller than average bubble sizes, while flowing bubbles also tend to segregate in different flow paths according to bubble size. Larger bubbles tend to flow in high-velocity preferential paths that are generally more aligned with pressure gradient, but smaller bubbles tend to access in supplement transversal paths linking the different preferential paths. Furthermore, for our data we establish the pre-eminence of the trapped foam fraction over bubble density within the microscopic explanation of apparent viscosity, although both contribute to some degree. We structurally characterize consistently trapped zones as areas with either low pore coordination, low entrance throat size, unfavorable throat orientation or a combination thereof. High-flow zones however cannot be characterized in terms of local structural parameters and necessitate integration of complete path information from the entire model. In this regard, in order to capture the high-flow zones, we develop a path-proposing model that makes use of a graph representation of the model, from an initial decomposition into pores and throats, that uses only local throat size and throat orientation relative to pressure gradient to characterize paths.

Résumé de thèse

Pour ce travail, nous utilisons un micromodèle à haute complexité et à structure fixe pour faire une série d'expériences en variant la vitesse d'injection, la qualité de la mousse, les distributions de taille de bulles d'injection, et la méthode d'injection. Nous mettons en œuvre un suivi individuel de bulles pour associer les propriétés d'écoulement aux propriétés de taille de bulles ainsi que les caractéristiques structurelles du milieu poreux. Nous proposons de nouveaux outils pour décrire l'écoulement d'un point de vue global et local de différentes manières. Nous établissons des comportements spécifiques à chaque taille de bulle, en montrant que les bulles des mousses piégées sont plus probables d'être de taille inférieure aux tailles de bulles moyennes, alors que les mousses en mouvement accèdent elles-mêmes à différents chemins d'écoulement selon les tailles de bulles. Les bulles plus volumineuses s'écoulent en majorité dans des chemins préférentiels à haute vitesse, généralement parallèles au gradient de pression, mais les petites bulles sont transportées en supplément à l'intérieur de chemins transversaux liant les chemins préférentiels. Ailleurs, pour nos données nous démontrons l'importance supérieure de la fraction de mousse piégée vis-à-vis de la densité de bulles quant à l'explication microscopique de la viscosité apparente, malgré une contribution des deux. Nous caractérisons structurellement les zones piégées à répétition, comme étant soit des zones à faible coordination de pore, de faible taille de seuil d'entrée, d'orientation de seuil désavantageuse, ou une combinaison de ceux-ci. Les zones à fort écoulement échappent à une caractérisation en termes de paramètres de structure locale et nécessitent une considération de l'information des différents chemins traversant la totalité du modèle. À ce but, afin de décrire les zones à fort écoulement, nous développons un modèle générant des chemins, utilisant une représentation en graphe du milieux poreux, basé sur une décomposition initiale en pores et seuils, qui intègre seulement les notions de taille de seuil et d'orientation de seuil relatif au gradient de pression pour caractériser les chemins.

Table of Contents

Introduction

Motivation

With the global energy consumption growing every year, and despite a projected 85% increase in the energy supply from renewables projected for 2040, demand for oil is expected to increase before plateauing sometime in the mid-future, requiring significant levels of investment in new oil to meet oil demand (BP Energy Outlook 2019). With the dwindling of conventional oil reservoir resources and the fluctuation of oil prices, application of new technology to old reservoirs can return significant profits (Muggeridge et al. 2014). Enhanced Oil Recovery (EOR) is the use of various techniques destined to increase oil production with methods such as polymer and surfactant injections, contrasting with traditional primary and secondary recovery methods. Once an oil reservoir has reached peak oil production through established techniques, EOR can be used to prolong its lifetime and recover a supplementary 30 to 60% of oil in place (U.S. Department of Energy 2017). Surfactant-stabilized foams are used as tertiary injection fluids in oil reservoirs to increase sweep and stabilize injection fronts through mobility ratio reduction. In other field applications, foams can be used to plug areas of a reservoir, to block off exploited or uninteresting regions. We can cite the example of using foams in fractured reservoirs to increase oil recovery in the unfractured rock matrix (Conn et al. 2014; Fernø et al. 2016). In this context, foams should display maximal viscosity and stability. Foam reservoir simulators are used to optimize injections for the operation. Incorrect understanding of foam behavior leads to inaccurate predictions which can result in a financial loss.

Elsewhere, foams can be used in the remediation of waste in contaminated soils. As the excavation or ex-situ treatment of polluted subsurface is often expensive and creates subsequent disposal problems, in-situ flushing of soils is preferred. We give the examples of removal of polyaromatic hydrocarbons around disused gas plants (Kilbane et al. 1997), removal of the wood preservative pentachlorophenol in soil from wood plants (Mulligan and Eftekhari 2003) or the flushing of diesel-contaminated sandy soil (Couto et al. 2009). Foam applications in the environmental case present similar advantages to those motivating foam EOR, including increased subsurface sweep and efficient capture of extracted elements at a reduced cost.

We give a brief description of the multi-scale nature of foam and its different uses in subsurface injections. At the field-scale foam use has found trial stage success overcoming three types of gas segregation challenges in gas or water-alternating-gas injections and providing greater conformance control:

- The viscosified gas phase can limit gravity segregation of the gas phase upwards.
- The viscosity difference between the two phases is smaller for foamed gas, inhibiting viscous fingering.
- The channeling of gas is mitigated as the viscosity of foams tends to be higher in more permeable channels, stabilizing injection fronts.

Far from the field-scale, foam research in petroleum engineering is scaled down to the laboratory level using Darcy-scale experiments performed on either truncated cores of real media, synthetic sandpacks or beadpacks. For a given foaming solution, foam film density and the trapped gas fraction are understood to be crucial in describing the effect of foam flow, affecting foam phase viscosity and relative permeability respectively. Also, different flow regimes have been observed in terms of the injected gas to liquid ratio, showing distinct rheological profiles and provide insights into the conformance control mechanisms desired in field use. Foam generation studies also investigate the necessary injection conditions that allow foam to form inside the rock.

At the pore-scale, foams are composed of metastable thin liquid films or “lamellae” and liquid carrying Plateau borders that divide up the discontinuous gas phase. Series of lamellae known as “bubble trains” advance through the medium and may be subject to a number of destruction, creation, trapping, or remobilization mechanisms. Fine understanding of either mechanism is useful for predicting the strength of a foam state deep in the reservoir.

At the foam film scale surfactants made of hydrophobic and hydrophilic elements organize at the interface and stabilize the film at a fixed distance. It is required to overcome the combination of molecular, electrostatic and steric forces to collapse the lamella. Some of the difficulty in finding a simple foam description lies in the interplay of chemical and capillary forces. On one side the chemical forces assure the stability of a foam film and “strength” of foam when injected into rock. On the other side the porous microstructure destabilizes films due to the high capillary pressure environments.

Due to its multi-scale and multi-physics nature, the implementation of foam flow in reservoir simulators is no easy task, keeping in mind the limited computational time available. Many current foam modelling frameworks require *a posteriori* fitting of unintuitive numerical parameters to obtain a predictive model for use on a specific reservoir case. This time-consuming trial-and-error procedure for parameter fits could be greatly alleviated by understanding the influence of structure-based parameters on foam flow, or through a reconsideration of the key phenomena involved in foam flow and their structural origins.

Definition of the Problem

Knowledge of the structure of porous media is essential in understanding how injected fluids will behave as they travel. The structure concerns the physical, geometrical position of the solid medium in relation to the porosity or void that it incorporates. Porous structure can be analyzed on multiple scales, and the extent of the different descriptors used in foam models reflects the complexity and case-dependency of foam flow behavior. This is exposed in the difficulty in achieving general predictive laws. In his general book on fluid transport and pore structure in porous media, Dullien (1992) differentiates between macroscopic and microscopic pore scale parameters, and field scale parameters. Macroscopic pore scale parameters include the parameters that can be averaged over a large sample and measured through macroscopic means, namely porosity, absolute permeability, specific surface area, or electrical resistivity. Macroscopic pore scale heterogeneity concerns for example permeability or porosity differences in subdivisions of the macroscopic measurement blocks. Dullien cites that for all practical purposes, blocks of more than 15x15x15 nodes (or pores) can represent the elementary macroscopic block, and below this limit measures will significantly fluctuate with the size of the sample. On the other hand, microscopic pore scale parameters are obtained by observation of small samples and require a different series of measurement tools. These parameters are explicitly tied to the pores or the characteristics of the pore network itself. We can give examples such as pore shape, network connectivity, distributions of throat and pore sizes and associated statistics such the spatial correlation of pore sizes and other neighborhood properties. Different methods exist to access these properties, either through direct observation and analysis of 2D thin sections of rock or via extraction of pore network characteristics through interpretation of 3D micro-computed tomography images (Youssef et al. 2007).

With application to foams, some attempts have been made to relate phenomena to structure-related parameters in the aim of generalizing the laws to different rock types. Microscopically, most experimental results revolve around 2D micromodels. Huh et al. observed sweep efficiencies of CO_2 foams in terms of the pore size distributions for micromodels of varying heterogeneity. A number of papers look into the role of "aspect ratio" and microscopic parameters involved in the foam generation process (Ransohoff and Radke 1988; Gauteplass et al. 2015). Rossen establishes theoretically a minimum pressure gradient necessary to maintain foam flow through a pore in terms of pore shape, pore asymmetry and the presence of surrounding trapped bubbles (Rossen 1990a, 1990b, 1990d).

Dependencies of phenomena on macroscopic pore scale parameters usually concern the variation with absolute permeability or porosity of the medium. Experimental studies include the work of Pang (2010), showing the dependence of the foam mobility reduction factor to the absolute permeability in sandpacks. The significant results of A. Gauglitz et al. (2002) include a link between the minimum pressure gradient for foam generation and absolute permeability. They find that the minimum pressure gradient scales differently if the medium considered is made of consolidated components (i.e. sandstone rocks) or unconsolidated components (i.e. sandpacks and beadpacks).

While the relationships of macroscopic pore scale phenomena give important insights on generation and flow dynamics of foam in porous media, they sometimes lack generality and remain too case-specific to be useful in an EOR context. Ideally, a predictive model based on pore scale characteristics can be used to predict flow behavior from laboratory analysis of a limited rock sample, and subsequently used in reservoir engineering software to optimize the field-scale solution. This forms the motivation of the current study, in which we believe that a limited number of microscopic pore scale parameters can serve to describe key processes involved in foam flow. Identification of these key parameters then becomes the first step and uncovering them requires visualization, analysis and prospective modelling of flow properties at the pore-scale.

Thesis structure

We provide a summary of the thesis, divided into five chapters. Except from the state-of-the-art section, the thesis uses data exclusively gathered from a series of experiments using a high-

complexity micromodel in which multiple experiments were performed. At the end of the last chapter however, a generalization is shown using data from the literature, characterizing preferential paths in a different model.

In Chapter 1, we expose some of the well-established results across different scales in the study of both foams in bulk and in porous media. This chapter is designed to give the reader an overview of the multi-scale nature of foam flow in porous media and to provide context regarding the complexity and key aspects of foam flow dynamics and their relationship to porous structure. Some examples of foam models will also be given.

In Chapter 2, we give a description of the data acquisition strategy, experimental setup, some data types used and provide initial results from a single experiment. From a methodological point of view, we give details regarding the image processing workflow, the bubble tracking procedure and the creation of quantitative flowmaps. This chapter shows some of the characteristics of foam flow that we observe in the model and makes a comparison of flow distribution and local flow specificity with a 2D simulation of Newtonian flow in a digitized flat version of the model, as well as a supplementary 3D simulation of Newtonian flow in which the model depth is accounted for. In addition, a small section is dedicated to attempting to identify local structural and flow relationships based on naïve approaches linking pore and throat sizes to flow intensity.

In Chapter 3, we present a series of flow experiments and extract data types relating to the flow properties at different scales, bubble size distributions and injection parameters. We then find links between data types of different scales and uncover which injection variables are the most influential and how they affect the downstream flow properties. This chapter deals with observed flow and injection variables without reference to structural properties. We notably establish that the foam trapped fraction is the dominant contributor towards apparent viscosity variation, within the limits of our foam bubble density measurements. We propose a model of apparent viscosity derived from direct observation of flow parameters integrating both elements from the trapped foam fraction and the total sum of bubble interfaces in the medium, which bears resemblance to the bubble density. Furthermore, we demonstrate that trapped foam fractions can have separate sources: in the largest trapped fraction experiments they are closely linked to the injection bubble distributions and local injection foam quality, with drier injection areas creating trapped zones downstream. These zones fluctuate between experiments. The lower trapped fraction experiments

demonstrate however show consistent areas of specific trapped zones, which we hypothesize as having a structural origin.

In a Chapter 4, the local structural links between flow of different intensity are explored. We fine-tune machine learning algorithms to perform an in-depth search to identify (where possible) the key parameters capable of predicting both low- and high-flow zones. We achieve a relatively good predictive capacity for the low-flow zones, with models using uniquely the throat size properties and coordination properties. However, a good prediction of the high-flow zones seems to be unfeasible from a local point of view. Instead, they are a consequence of larger-scale network properties leading to the establishment of preferential paths.

In a fifth and final chapter, we pursue to concept of preferential paths through the introduction of novel graph-based model to characterize and propose paths, based on throat properties derived from the in-depth local structural search of Chapter 4. We then perform a parameter optimization of the model, achieving two fitted models describing two experiments with varying injection properties. We conclude by switching scales again and using network-based characteristics in the local structural models, in a revised attempt to predict high-flow zones locally through the newly established path behavior.

Chapter 1. *State of the Art*

In this section, we lay out the basics for understanding the multi-scale nature of foams, from foam film stability to the complex flow regimes that govern Darcy-scale foam operations, whilst describing the underlying pore-scale mechanisms. We present some key foam flow models and point out the relevance of either model to our research objectives. For the sake of clarity, we distinguish bulk foams, in which many bubbles and foam films exist without significant interaction with the containing medium, to foams in porous media, in which interactions with the constraining medium creates new phenomena.

1.1 Bulk foam generalities

Liquid foams describe a complex state of matter defined as "gas bubbles which are closely packed within a liquid carrier matrix" (Drenckhan, Saint-Jalmes 2015). In this section we give an overview of bulk foam properties, which are also carried through to porous media.

1.1.1 Interfacial considerations

As with all types of dispersed media, it is fundamental to understand the nature of the two-phase interactions that exist at the boundary between the gas and liquid phases.

a) **Interfacial tension**

Within a volume of liquid, attractive intramolecular forces ensure the cohesion of particles with each other. A single molecule is surrounded by an isotropic force of attraction created by its neighbors. In a volume of gas, the situation is analogous albeit for a less dense fluid and hence weaker force. At the interface between the two fluids, the bordering molecules on the liquid experience a higher energy state as on one it sides it no longer shares bonds with water molecules. Because of this state, the molecules will attempt to create the minimum energy surface for the given conditions. For a small volume of gas in a large volume of water, a spherical bubble is created. Each added molecule to the boundary will increase the total Gibbs free energy G of the system by a specific amount at a given temperature T, pressure P and density n. The interfacial tension γ is simply the measure of the added energy per unit area of boundary created. As such:

$$\gamma = \left(\frac{\partial G}{\partial A}\right)_{T,P,n} \quad (1)$$

In other words, interfacial tension results from the cohesive energy of the molecules at the interface, who limit as much as energetically possible interface expansion (Schramm 2005).

b) **Young-Laplace equation**

The curvature of the interface separating the two phases is closely linked to the pressure difference between them. For interfacial curves, including foam bubbles, the mean curvature is related to the pressure difference ΔP across interface by the interfacial tension γ via the Young-Laplace equation. This relationship will hold locally for any smooth section of a bubble and give an expression in terms of principal radii of curvature R_1 and R_2:

$$\Delta P = \gamma \left(\frac{1}{R_1} + \frac{1}{R_2}\right) \quad (2)$$

This equation can be simplified for spherical bubbles of radius R in which $R_1 = R_2 = R$ as:

$$\Delta P = \frac{2\gamma}{R} \quad (3)$$

1.1.2 Bulk foam structure

Foam structure depends on the proportion of water and gas that composes it. Liquid fraction is defined as the fraction of the total liquid volume V_l over the total foam volume V_t such as $\phi = {V_l}/{V_t}$.

For dry foams ($\phi < 0.05$) Plateau's laws become relevant to study of foams, where the lack of aqueous solution forces the bubbles into close contact. Dense packing minimal surface problems arise from the interfacial cost. Plateau made a series of experimental observations for dry foams that dictate the behavior of foams at very low water content. He discovered that dry foam bubbles always meet in threes and that lamella junctions at Plateau borders between bubbles always form 120° angles between each other. Figure 1-1 shows the basic elements of foam structure.

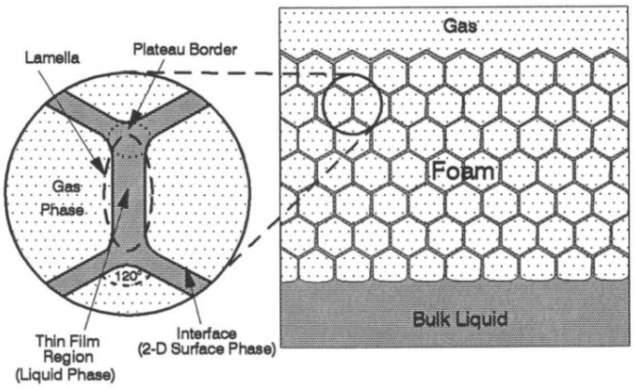

Figure 1-1: Basic foam structure composed of a discontinuous gas phase separated by thin liquid films than intersect at 120° in Plateau borders. Taken from (Schramm and Wassmuth 1994).

In turn, Plateau borders branch out in different directions and cross in fours at vertices at an angle of 109.49°, also known as the tetrahedral angle (Plateau 1873).

For a monodisperse foam restricted to a two-dimensional plane, the lowest energy stable foam structure is the honeycomb pattern, which minimizes the total interface perimeter. The morphology of the discontinuous gas phase depends on the gas fraction in the two-phase state. For lower liquid saturations (high foam quality), the gas bubbles tend to create angular intersections that produce polyhedral volumes as opposed to the spherical "ball type" foam brought about by high liquid saturation (low foam quality). These two extreme cases serve as boundaries for the intermediate shapes situated between polyhedra and spheres, depending on increasing liquid saturation. Figure 1-2 shows these two extreme foam types with an intermediate state.

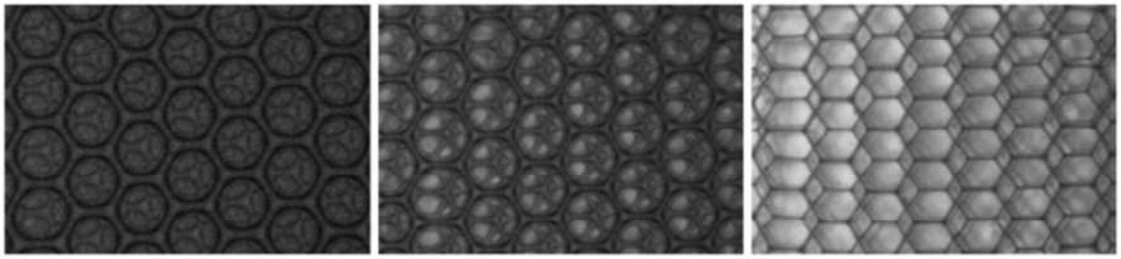

Figure 1-2: Varying foam structure with decreasing water saturation: the monodisperse foam bubbles are almost spherical when a high quantity of interstitial liquid is present but progress towards shapes with sharp hexagonal faces at lower saturation, taken from (Höhler et al. 2008).

1.1.3 Foam Stability

Bulk foam lamellae are thermodynamically metastable. The use of ionic surfactants modifies surface interaction forces. Film stability is ensured by the adsorption of surfactants on the gas-liquid interface, creating a situation in which it is energetically favorable to maintain the given film thickness. Ionic surfactants reduce the surface tension between two phases because of their polar nature. They are most often molecules made up of two separate components, a hydrophilic head and a hydrophobic tail. In the context of foam applications, the lower surface tension can facilitate creation of foam bubbles (although a surface tension too low in fact inhibits foam formation) but they serve primarily the purpose of stabilizing foam lamella. The lifetime of a foam film may be influenced by a number of physical parameters, and multiple phenomena exist that account for the thinning or stabilizing of thin stabilized films in bulk foam. Sheng (2013) gives a list of these.

a) **Stabilizing phenomenon**

In the Marangoni effect, a sudden decrease of surfactant concentration at an interface, due to interface expansion or due to other loss of surfactant effect, causes a net liquid flow towards this same area. A region with higher surface tension (lower surfactant) will “pull” more liquid towards it. This in turn re-equilibrates the surfactant concentration and stabilizes the film. This effect is illustrated in Figure 1-3b.

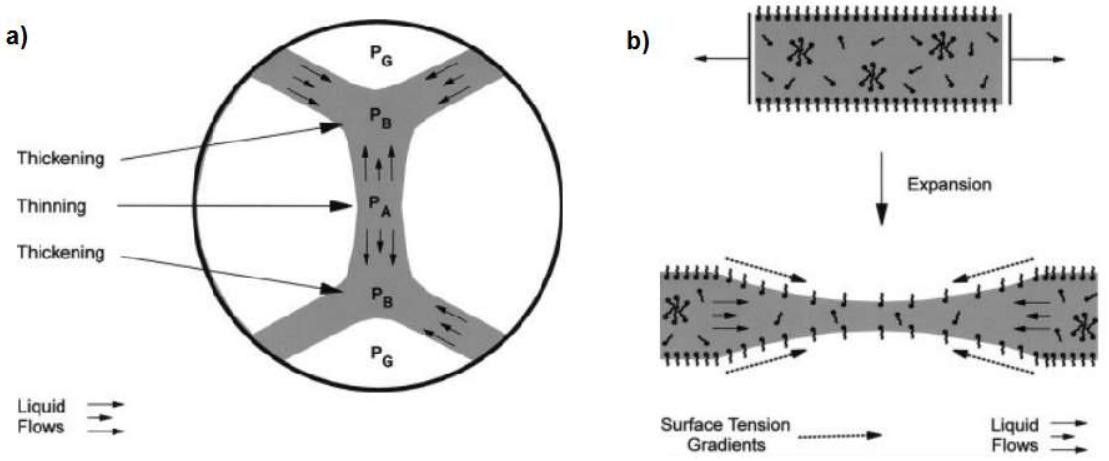

Figure 1-3: Dynamic lamella processes: a) destabilizing Laplace capillary suction: the liquid pressure in the Plateau borders (P_B) is lower as curvature is higher for constant gas pressure P_G; b) stabilizing Marangoni effect in which the lower surfactant concentration causes a migration of fluid that re-establishes thickness. Adapted from (Schramm 2005)

b) **Destabilizing phenomena**

Leading to thin film coalescence:

- Gravity drainage, in which the force of gravity pushes the liquid out of the thin films downwards.
- Laplace capillary suction, in which the difference in curvature between the sharp Plateau borders and the flat thin films creates a difference in pressure, in accordance with the Young-Laplace equation. This pressure gradient phase redirects the fluid into the Plateau borders. This effect is illustrated in Figure 1-3a.

Other foam destabilizing phenomena:

- Coarsening, where a larger Laplace pressure will exist in smaller bubbles, causing gas to diffuse through the thin lamella into the more voluminous neighbors due to the concentration gradient. The pressure difference is additionally increased. This leads to a runaway effect that culminates in the disappearance of the smaller bubble.

1.1.4 Bulk foams – Rheology

Foam macroscopically behaves both as a solid under low stress and as a liquid under high stress. It has a characteristic yield stress, when it transitions from one behavior to another (Dollet and Raufaste 2014). The elastic behavior of bulk foam is explained by the small increases in gas-liquid

interfacial area that arise from small stresses, which corresponds to a higher energetic state, causing the foam structure to relax back to its initial equilibrium state. We can therefore characterize a bulk modulus of the foam in this elastic state. When the applied stress becomes sufficiently high, the foam bubbles spontaneously rearrange to a new topological state (Höhler and Cohen-Addad 2005), which corresponds to a liquid behavior. The foam reorganization is process illustrated by the application of a constant stress on an ideal 2-dimensional dry foam represented Figure 1-4.

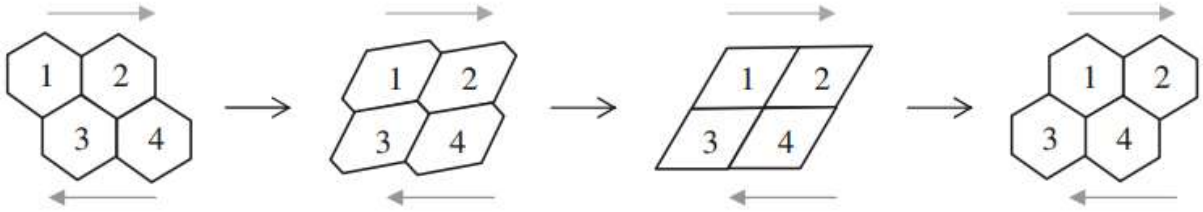

Figure 1-4: Dry foam cell reorganization, a constant stress is applied that initially causes a bubble deformation, before jumping to a new topological state, similar to the initial configuration. Taken from (Höhler and Cohen-Addad 2005).

The yield stress corresponding to cell reorganization is dependent on the foam quality, and it is highest for dry foams (Weaire and Hutzler 2001). Above the yield stress, foams can be considered as shear-thinning fluids and are usually well described by the phenomenological Herschel-Buckley law, seen in equation (4).

$$\begin{aligned} \dot{\gamma} &= 0 \qquad \text{for } \tau \leq \tau_y \\ \tau &= \tau_y + \xi \dot{\gamma}^n \quad \text{for } \tau \geq \tau_y \end{aligned} \tag{4}$$

This relationship shows that for shear stresses τ lower than the yield stress τ_y, the shear rate $\dot{\gamma}$ is zero. Parameters ξ and n are the consistency and flow indexes. For foams, the flow index is found to be somewhere between 0.25 and 1 (Höhler and Cohen-Addad 2005).

1.2 Foams in porous media

Foams in porous media share many of the characteristics of bulk foams. They are also composed of thin films and Plateau borders, whose stability and structure can be partially understood in terms of the phenomena described above. However, they exhibit unique behavior in porous media over a series of scales. Foam lamella creation and destruction at the pore-scale is governed by several *in situ* processes that can affect gas phase viscosity as a function of the lamella

density. Macroscopic foam flow in porous media shows multiple regimes, in which measured pressure differences are strong functions of the fluid injection rates, structural properties of the media and surfactant properties.

1.2.1 Basic petrophysical concepts

Here we present some concepts used in porous media studies that are essential to understanding foam dynamics.

a) **Young's equation and wetting angle**

For two static fluids in contact with a third solid material such a rock surface, the tangent of the two fluid's interface at the intersection with the rock surface is described by a contact angle θ. The wettability, quantified by the contact angle, is a measure of balance of affinity of either fluid to the rock, owing to the energetic preference of interface creation of either fluid with the rock. In Figure 1-5 we give a graphical representation of the contact angle.

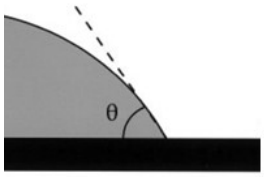

Figure 1-5: Contact angle θ at the intersection of two fluids (white and grey) in contact with a flat solid surface (black).

Young's equation is an application of the force balance created at the intersection of the three components for the specific case of a flat solid surface. For the example of a liquid drop on a flat surface, surrounded by gas, the interfacial tensions at the three interfaces projected onto the direction parallel to the surface, we obtain:

$$\gamma_{W/G} \cos\theta = \gamma_{S/G} - \gamma_{S/W} \quad (5)$$

In which $\gamma_{W/G}$ is the surface tension between the liquid and gas phase, $\gamma_{S/G}$ is the surface tension between the solid and gas phase and $\gamma_{S/W}$ is the interfacial tension between the solid and liquid phase. For an angle of $\theta = 0$ the solid is completely wetted by the liquid, but for $\theta < 90°$ in practice is considered to represent wetting conditions. Inversely, $\theta > 90°$ represents non-wetting conditions (Schramm 2005).

b) **Darcy's law**

Flow in porous media can be understood via Darcy's law, a constitutive equation that enables us to explain the viscous flow of fluids through a permeable medium. If we exclude any external forces acting upon the fluid apart from a pressure difference, for single phase of viscosity μ, transport in a medium with a given permeability k, Darcy velocity v, volumic flow rate q and pressure difference ΔP over the horizontal transporting medium of length L and sectional area A, then Darcy's law relates these parameters as:

$$v = q/A = \frac{k\,\Delta P}{\mu\,L} \tag{6}$$

Darcy's law is only applicable in laminar flow situations, and typical reservoir injections have a Reynold's number small enough to allow its use. Despite being established in a simplified set of experimental conditions (incompressible flow, saturated flow, steady-state-flow, isotropic media, laminar flow), Darcy's law can be applied to a variety of situations outside of its initial scope (Freeze and Cherry 1979). Certain simplifications are made to model foam using Darcy's law. Usually, foams are represented as a high-viscosity gas phase and not considered as a third phase, distinct from foamer solution and gas. For multiphase flow, Darcy's law expresses the flow rate $q_{i,j}$ component for each phase i,j individually:

$$v_{i,j} = q_{i,j}/\mathrm{A} = \frac{k k_{r_{i,j}} \Delta P_{i,j}}{\mu_{i,j}\,L} \tag{7}$$

In which $k_{r_{i,j}}$, $\mu_{i,j}$ and $v_{i,j}$ represent the relative permeability, viscosity and Darcy velocity of each phase, while $\Delta P_{i,j}$ represents the pressure drop over each phase.

c) **Capillary pressure**

In the context of a two-phase interface, the difference between wetting phase pressure p_w and non-wetting phase pressure p_{nw} such as aqueous solution and gas given by $p_c = p_{nw} - p_w$ is called the capillary pressure or p_c. Capillary pressure is established similarly as is Δp in the Young-Laplace equation, by balancing forces across the interface (equation (2)). In porous media, this pressure difference is defined by incorporating the wetting angle of the three phase interaction θ as (Bear 1988):

$$p_c = \frac{2\gamma \cos\theta}{R} \tag{8}$$

1.2.2 Foam effect on flow

Through this section we will look at the effect of injecting a foaming solution and gas or a preformed foam into a porous medium. We proceed initially from the Darcy-scale corefloods, to understanding in detail how the foam comes into existence and is transported in the porous network on a microscopic level. We will follow this decomposition to explain each phenomenon.

a) **Gas mobility reduction**

Foam affects flow in porous media in multiple ways. To overcome the problems inherent to gas or water injections in oil reservoirs such as channeling and gravity segregation, foam is used to create a thicker fluid that will propagate in a more uniform manner through the rock. In this manner, foams can increase sweep efficiency. This enables a significant amount of fluid diversion into low permeability areas in heterogeneous or fractured media (Li et al. 2013). The effect of foam is usually quantified by a mobility reduction factor defined simply as (Schramm 1994):

$$MRF = \frac{\Delta P_{foam}}{\Delta P_{nofoam}} \tag{9}$$

Where ΔP_{foam} is the measured steady state foam pressure drop and ΔP_{nofoam} is the pressure drop for identical injection conditions without foaming agent. In Figure 1-6 we show some typical mobility reduction factors in terms of gas types at 50°C and 30 bars in Berea cores.

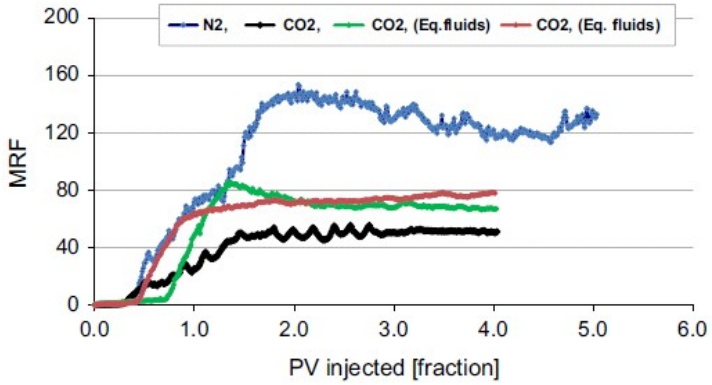

Figure 1-6: Mobility reduction factors in terms of gas type at 50°C and 30 bars. Taken from Aarra et al. (2014). PV signifies the Pore Volume inside the core.

b) **Gas mobility reduction - Microscopic explanation**

For foam transport in water-wet media, the water and gas phases rearrange upon entering the medium. The wetting phase occupies predominantly the smaller pores and channels and can propagate through this network unaffected by the existence of a gas phase, which is situated in larger pores as isolated bubbles. Liquid can also circulate through the continuous network of Plateau Borders. Therefore if we describe the foam by its individual constituents, both the viscosity and relative permeability of the aqueous phase are unchanged by the existence of the foam (Bernard and Jacobs 1965). However it is established that the creation and propagation of a foam phase in porous media can affect the viscosity and permeability of the gas phase (Bernard and Holm 1964). The mobility reduction is therefore explained by two foam effects in parallel. We can see this by looking at the definition of the gas phase mobility:

$$\lambda_g = \frac{k k_{r_g}}{\mu_g} \tag{10}$$

We can make the distinction between continuous and discontinuous gas foams. Falls et al. (1988) summarize foam classification in porous media and provide explanatory diagrams. We display these diagrams in Figure 1-7. They describe two types of discontinuous-gas foams, where bubble trains transport gas across the medium, in opposition to continuous-gas foams, in which at least one percolating passage exists across the medium uninhibited by liquid lamellae. They note that in terms of mobility, the continuous gas foams only affect the relative permeability of the gas by blocking certain channels, and leave the bubbles trapped and immobile. On the contrary, discontinuous gas foams affect both relative permeability of the gas and viscosity of the gas, by forcing lamellae to propagate through the medium.

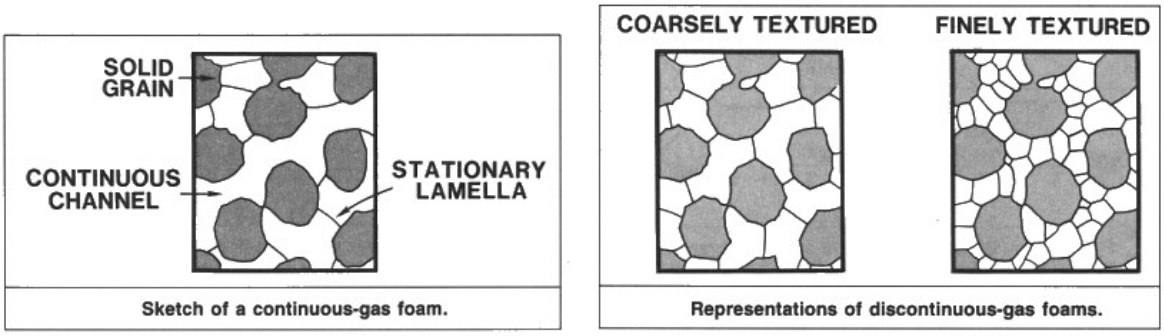

Figure 1-7: The distinction between continuous and discontinuous-gas foams. For the discontinuous-gas foams, the higher density of bubbles in the finely textured example shows a larger increase in viscosity over the coarsely textured foam. Taken from Falls et al. (1988).

Although direct *in situ* observation of a higher lamellae density is difficult at foam generation in corefloods, it has been established that the viscosification of the gas phase is a function of "foam texture", or foam bubble density.

c) **Foam viscosity models**

For foam flows we define an apparent viscosity μ_{app}, used in opposition to the constant viscosity of a Newtonian fluid.

Hirasaki and Lawson (1985) measured viscosities in smooth glass capillaries of uniform diameter, and established a theoretical model describing foam viscosity with experimental fitting of parameters. They describe different types of foam transport of equivalent bubble size r_B in smooth capillaries of radius R, and distinguish cases where $r_B \gg R$ (individual lamella foam) and $r_B \ll R$ (interconnected lamellae or bulk foam).

For individual lamellae foams, the apparent viscosity is derived by evaluating two individual contributions of a series of bubbles. These are given in the following relationship:

$$\frac{\mu_{app}}{\mu} = \left(0.85\frac{n_L}{r_c}[{r_c}^2 + R^2] + n_L \mathrm{R}\sqrt{N_s}\frac{(1-e^{-N_L})}{(1+e^{-N_L})}\right)\left(\frac{3\mu U}{\sigma}\right)^{-\frac{1}{3}} \qquad (11)$$

in which μ_{app} is the apparent foam viscosity, μ is the liquid viscosity, U is the interstitial gas velocity, n_L is the lamellae density per unit length, r_c is the capillary radius of the bubble edge, σ is surface tension between the foamer solution and the gas, and N_L and N_s are respectively the dimensionless length of the thin film portion of bubble and dimensionless surface tension gradient

effect. The first term on the right-hand side accounts for the viscous drag created by the liquid rearrangement from the gas displacement. The second term describes the drag from surface tension gradient created by the expansion and compression of the interface at the front and back of the bubbles. The authors find that the contribution of the first term dominates. As with Bretherton's (1961) work, the foam viscosity is found to scale with $U^{-1/3}$. The lamellae density per unit length also appears in each term. This equation is appropriate for "bubble train" lamellae displacement in series characteristic of porous media, and is simplified and used in a great deal of foam models (see section 1.3.1).

d) **Gas relative permeability reduction via foam trapping**

A key phenomenon in understanding the foam dynamics in porous media is the existence of "foam trapping". Once a foam is formed and as it progresses through a medium, high volumes can become stationary in moderate pore sizes, limiting the flow to the higher permeability zones. The pore space occupied by trapped foam is shown in Figure 1-8:

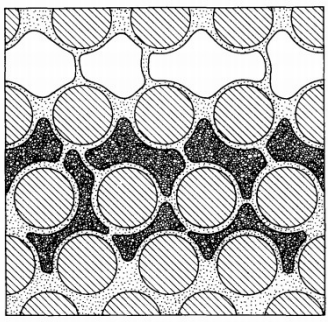

Figure 1-8: The distribution of trapped and flowing foam in a porous medium. Grains are filled with diagonal lines. Flowing gas is white, whereas trapped gas is black, remaining interstitial space is occupied by the wetting phase. Larger flow channels are located sequentially towards the top of the picture. The larger pores allow foam to flow. The intermediate sized pores show trapped foam. The smaller pores only contain wetting phase. Taken from Radke and Gillis (1990).

Trapping has been observed qualitatively at the pore-level in micromodels (Mast 1972; Chambers and Radke 1990; Prieditis 1988) and beadpacks (Falls et al. 1989). Nguyen et al. (2002) use a 28.5 Darcy micromodel to assess the significance of gas tracer diffusion in evaluating trapped gas fractions. They note that flow paths change intermittently, and a steady state of foam patterning was not found, with stable trapped and flowing fractions. To overcome this, pure gas is injected after a certain amount of time, and the trapped fraction is measured from the remaining foam

volume after its passage. The trapped fraction was measured consistently around 65% at different injection speeds.

More recently, Jones et al. (2018b) study the fraction of trapped gas in a relatively complex micromodel of 849 pores. They observe a linear decrease in the trapped fraction with increasing injection rate and a linear relationship between observed "apparent viscosity", including both gas relative permeability and viscosity effects.

Nguyen et al. (2009) use *in situ* computed tomography images of Xenon tracers to provide an estimate of the trapped fraction and evaluate some of the assumptions used in previous publications for trapped fraction measurements. Injection rates were also changed, and they find that trapped fraction decreases with increasing gas-injection rate and may increase weakly with liquid injection rate. They also find no relationship between pressure gradient and trapped fraction. Some CT images of tracer concentration are visible in Figure 1-9.

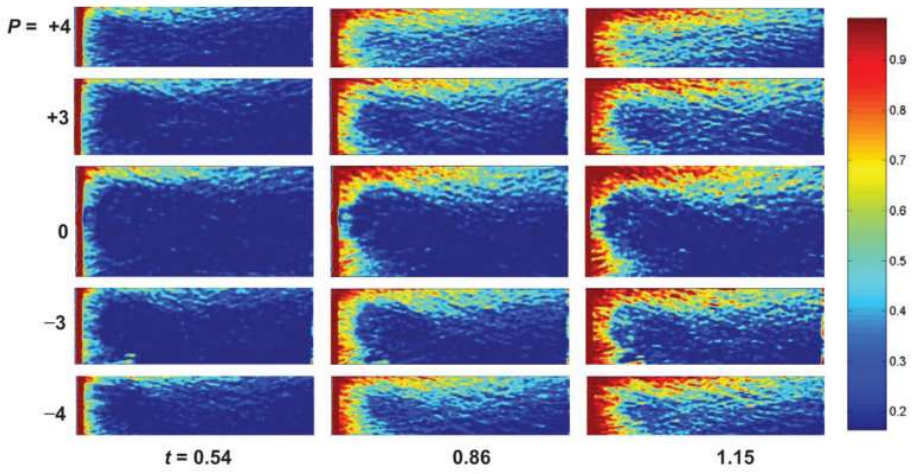

Figure 1-9: Axial CT scans of tracer displacement in steady state "Foam A" in terms of a dimensionless time t, taken from Nguyen et al. (2009). The P value represents the axial slice with respect to the central slice P=0. Warm colors mean high concentrations of tracer. The flowing fraction is visible at the top of the section, with a measurable tracer concentration at the end of the core already by t=0.54. A slower diffusion phenomenon progresses through the middle and lower sections of the core. The authors propose that the low flowing fraction in the central section is due to a higher water saturation in the central part of the entrance area, measured elsewhere (Nguyen et al. 2007) that inhibits foam flow.

To attempt to understand and predict mobilization of trapped foams, Rossen and Wang (1996), describe for certain injection conditions, the pressure gradient over the medium plays a key role. In four substantial papers, Rossen (Rossen 1990a, 1990b, 1990c, 1990d) evaluates the minimum

pressure gradient necessary for maintaining flow of a "bubble train", or a linear sequence of already formed stationary bubbles. Rossen derives expressions for the minimum pressure gradient in terms of pore body and constriction geometry (shape, asymmetry, aspect ratio), gas compressibility, contact angle hysteresis, and with the added possible presence of stationary lamellae in pores adjacent to the direction of flow, with successful comparisons to experimental data from Falls et al. (1989).

e) **Foam generation**

Foam injections in experiments typically consist of injecting at a low flow rate and increasing the overall injection rate or injection pressure until a large sudden increase in pressure difference ΔP is observed across the sample, signaling the creation of a high viscosity phase blocking the flow path, often called "foam generation".

Different experimental techniques can demonstrate the existence of the foam generation phenomenon. Often, a fixed liquid fractional flow is injected at increasing overall flow rate. A minimum injection velocity v_{min} is therefore observed for foam generation. Ransohoff and Radke (1988) interpret this as the attainment of a critical modified dimensionless capillary number. They also find that the critical capillary number increases with increasing liquid fractional flow for their experiments in beadpacks. We show the curved of Ransohoff and Radke (1988) in Figure 1-10:

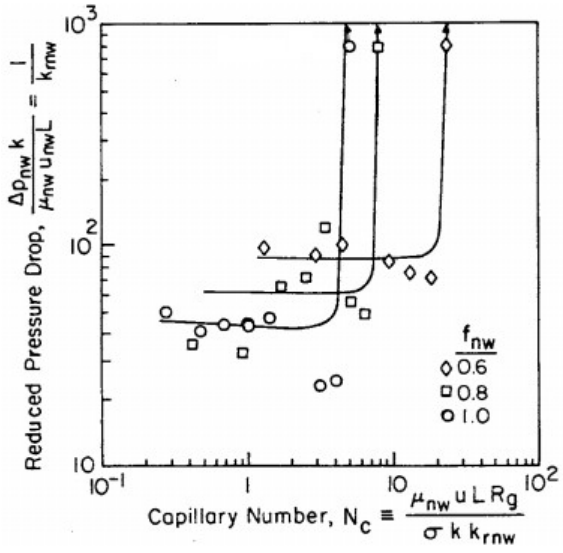

Figure 1-10: The sudden increase in reduced pressure drop across the medium, at a significant capillary number after which foam has generated, for three different liquid fractional flows. Taken from Ransohoff and Radke (1988).

Another experimental procedure, consisting of controlling the pressure drop over core and allowing the injection rates to adapt, yields coherent, but supplementary results to the previous cited cases. Increasing the pressure gradient leads to the critical minimum pressure gradient ∇P_{min} for foam generation and works analogously to the minimum velocity. A. Gauglitz et al. (2002) produce a large amount of data on foam generation through different experimental procedures. Specifically, through experiments at an imposed ∇P (type 1 and 3), an increase in pressure drop at ∇P_{min} creates a decrease in injection rates, at which unstable « intermediate foams » are created. Within this intermediate state the mobility reduction (or resistance factor) is only moderate. The intermediate regime is considered unstable, as maintaining ∇P fixed is difficult as it is measured to be fluctuating. Further increase in pressure drop then leads to an increasing flow rate, as « strong foams » are retrieved such as in the fixed injection rate experiments.

f) **Lamellae creation processes**

Traditionally, foam creation processes at the pore-level have been observed as three distinct phenomena, as described by Sheng (2013). Here we show, for simplicity, diagrams taken from Ransohoff and Radke (1988) in which the processes are observed for drainage only:

- Snap-off: Occurs when gas penetrates through a liquid-filled constriction, and a sudden decrease in local capillary pressure in the constriction refills the constriction with liquid. A discontinuous gas bubble is formed, and a lamella is situated inside the constriction. Snap-off creates a lamella perpendicular to the direction of flow. The exact decrease in capillary pressure necessary depends on the geometry of the constriction, but for straight cylindrical throats, the capillary pressure must fall approximately to half of the entrance capillary pressure.

- Lamella division: Occurs when a pre-existing liquid lamella passes a bifurcation in the medium, and simultaneously invades both passages, dividing into two, and hence resulting in the creation of a net new lamella.

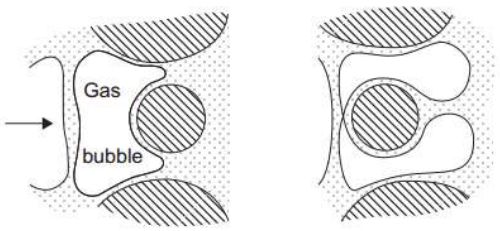

- Leave behind: Occurs when a gas phases invades two adjacent pore bodies leaving a liquid filled constriction intact and isolated as a new lamella. Leave-behind created lamellae are parallel to the direction of flow.

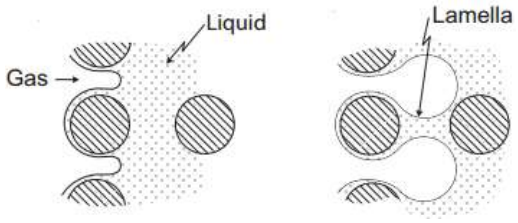

Due to the difficulty of directly observing in-situ pore-scale mechanisms, simplified models are used to assess the relative importance and specific context regarding each of the three types. Two-dimensional micromodels and glass beadpacks have been very often used with varying characteristics.

More recently, observations in a simple one-constriction micromodel by Liontas et al. (2013) revealed the existence of other, neighbor-induced bubble creation mechanisms. They observed foams in which the "bubble train" lamella-by-lamella state was no longer valid and observed bubble-bubble interactions that lead to new bubble creation. As two or more bubbles approach a constriction, with enough velocity they could pinch-off one another and created new bubbles before they had time to reorganize into a bubble train. They found that the new mechanisms become accessible at a minimum capillary number and show dependence on the bubble size and topological organization of the bubbles as they approach the constriction.

A significant debate regarding the predominant formation mechanism, at "foam generation", and occurring within transport of pre-established foam, has been ongoing for multiple decades. Essentially, it is unclear as to whether the snap-off or lamellae division mechanism is the primary one involved in the sudden viscosification and creation of a strong foam in a 3D porous medium.

g) **Foam flow regimes**

Within highly viscous strong foams, flow behavior is shown to be dependent on the ratio of liquid to gas injection rates. Similarly to the liquid static fraction that determines foam structure in bulk foam, for dynamic flow in porous media the gas fraction determines the flow regime that is attained. If the fluid injection rate is given by Q_l and the gas injection rate by Q_g then the volumetric gas fraction is given by $f_g = \frac{Q_g}{Q_g + Q_l}$.

In particular, the flowing foam can be categorized into either a high-quality (high gas fraction) or a low-quality (low gas fraction) regime. Khatib et al. (1988) explored a series of injection ratios through beadpacks and sandpacks while simultaneously directly measuring in situ capillary pressure and observing bubble size. He found that at a sufficiently high gas fraction and capillary pressure, a change in behavior occurs, after which the measured ΔP over the sandpack becomes proportional to the liquid flow rate u_w and independent of the gas velocity u_g, this new regime is the high-quality, or coalescence regime. Inversely, in the low-quality regime the pressure drop only scales with the gas velocity u_g. We show the two regimes observed in Figure 1-11:

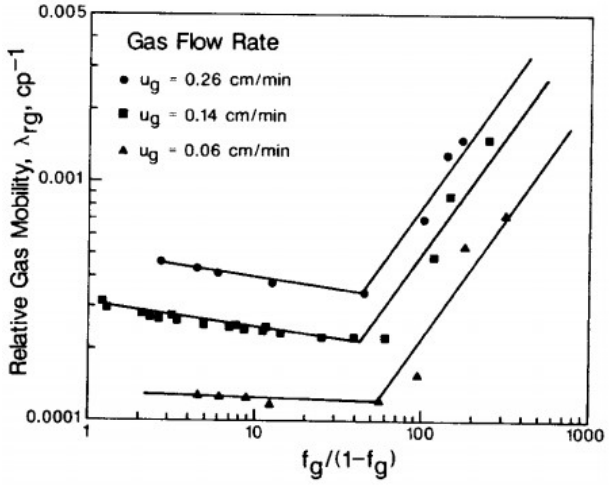

Figure 1-11: Measured gas mobility for a series of gas fraction injections demonstrated by Khatib et al. (1988). A distinct foam transition is visible at approximately the same fraction for all gas injection rates.

Osterloh and Jante (1992) studied foam flow for 49 combinations of u_w and u_g into a sandpack cell. They found that in the high-quality regime, the pressure drop increased with respect to u_w to

the power of 0.31. In the low-quality regime, the pressure drop increased with respect to u_w to the power 0.33. The transition quality f_g^* was found to be 0.94. Their data was presented in a useful manner demonstrating the two different regimes and dependencies on flow rates. However, in contrast with previous results, they found that the liquid saturation was approximately constant, at around 0.06 for either flow regimes.

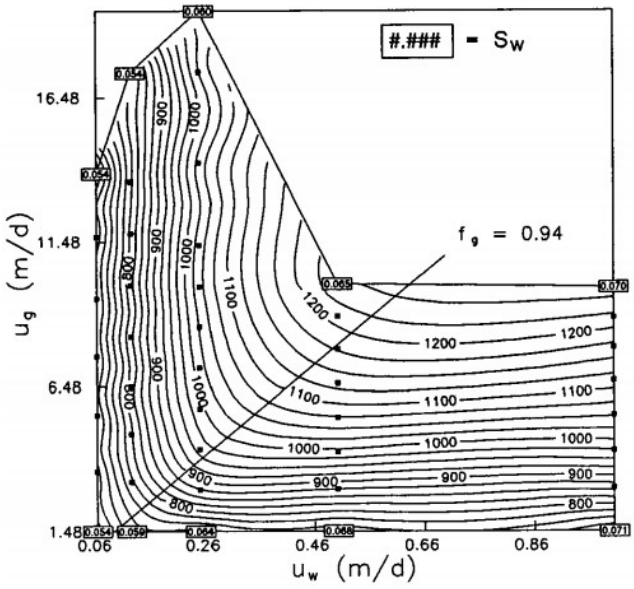

Figure 1-12: An example of the measured pressure differences over a series of injection rates for a two-inch sandpack. The high-quality or coalescence regime is visible in the top left side whereas the low-quality regime is in the bottom right side. The transition occurs at a foam quality of f_g = 0.94.

h) **Foam flow regimes – Microscopic explanation**

Here we give an overview of the different models and observations that have led to an approximate understanding of the dynamics governing foam flow regimes, in which characteristic macroscopic observations can be attributed to pore-scale effects, notably a series of bubble-size regulation mechanisms that we will describe first.

Bubble size regulation mechanisms

To fully understand the specific regime behaviors, we first need to understand how lamellae can be broken, before seeing how these mechanisms come into play in relation to the two flow regimes.

For foams in porous media, size regulation mechanisms are essentially the same as those found in the coarsening of bulk foams. Concepts such as the thin film stability, gas diffusion and capillary

suction coalescence are applicable. As such, not a great deal of detail is given in describing these. Some remarks on the differences with bulk foams will nonetheless be presented. Within a porous medium, two main coarsening phenomena are observed: capillary-suction coalescence and gas diffusion. The small characteristic lengths involved in porous media and the dynamic nature of foam flow ensure that gravity drainage is usually irrelevant.

- Capillary suction coalescence

Direct visual proof of the dynamic capillary suction coalescence phenomenon is given by Jiménez and Radke (1989) who observe coalescence repeatedly at certain sites of rapid increase in capillary thickness. We can observe their photographs in Figure 1-13.

The limiting capillary pressure P_c^* before coalescence in porous media is the counterpart of the characteristic pressure gradient necessary to overcome the stabilizing thin film forces in bulk films. The isolated nature of single films in porous media indicates a higher resistance to capillary pressure than for bulk films. Khristov et al. (1979) measured both for the same solution of Sodium Dodecyl Sulfonate (SDS). Results are presented in Figure 1-14.

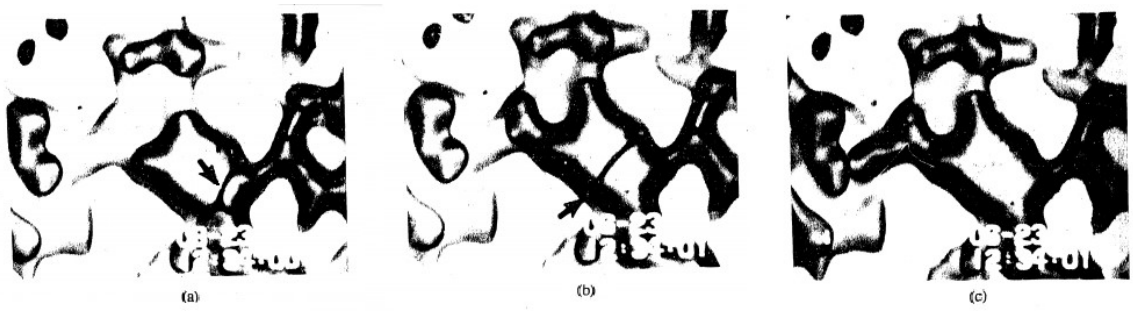

Figure 1-13: Successive micrographs of the lamella evolution and eventual coalescence in the micromodel of Jiménez and Radke (1989). The black arrow indicated the position of the liquid lamella. Progression through the pore body is observed from snapshot (a) to (b) and eventual disappearance in snapshot (c).

NaCl Concentration (mol/L)	Film Type	Critical Capillary Pressure (psi) Single Film	Bulk Foam
0.001	Ordinary thin	≥ 2.9	0.7
0.1	Ordinary black	≥ 15.0	7.0
0.4	Newtonian black	≥ 17.0	15.0

Figure 1-14 : Differences in measured critical capillary pressures before coalescence for single and bulk foams for different salt concentrations and film types for a 0.001 molar solution of SDS. Figure taken from Khatib et al. (1988), data originally from Khristov et al. (1979).

Khristov et al. (1979) interpret the higher capillary resistance of single films by two reasons : the radii of bulk films are larger, and the collective effect of the bulk film's neighbors, in which disturbances propagate and the coalescence of one film can trigger coalescence of the others.

- Diffusion

Diffusion in porous media between adjacent gas bubbles leading to coalescence was observed in Chambers and Radke (1990). Just as in bulk foam diffusion, smaller bubbles transferred mass into their larger neighbors with lower capillary pressure. The smaller bubbles eventually disappeared, and their liquid component was reintegrated into the surrounding liquid network. However, in the visual examples provided, the smaller bubbles were surrounded by other bubbles in a pore body and didn't meet the walls of the micromodel. Due to the long timescales involved in diffusion processes, diffusion-driven coalescence mainly occurs in stationary, trapped volumes of foam (Almajid and Kovscek 2015).

Although not leading to coalescence, another manifestation of gas diffusion can be observed, in which interaction with the medium plays a larger role. As bubble size increases to radii the size of pore bodies, the lamellae separating the bubbles are attached on either size to a solid as Plateau borders. The lamellae must intersect the solid at an angle of 90°, as verified by Prieditis (1988) under various circumstances. At the exit of a constriction the solid medium presents diverging surfaces that impose a convex lamella shape, due to the 90° intersection with the pore wall. For this lamellae curvature, a pressure gradient must be felt across the lamella, driving mass exchange from the rearward bubble to the forward bubble. The convex lamella is then pushed back to a symmetric position inside the constriction. This mechanism is visualized in Figure 1-15.

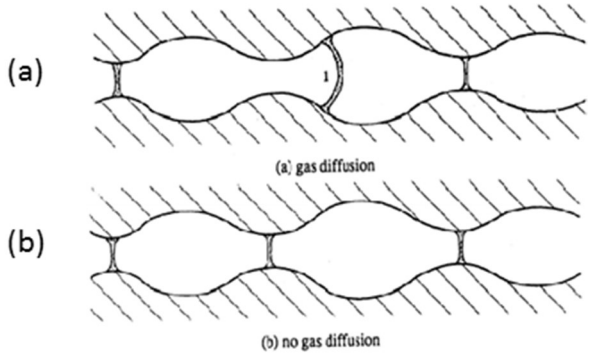

Figure 1-15: Gas diffusion process leading to a one-per-pore size distribution inside the porous media. In diagram (a) mass transfer occurs from left to right at the lamella 1. The system is equilibrated in diagram (b). Taken from Chambers and Radke (1990)

A more in-depth micromodel study has been carried out by Jones et al. (2018a) establishing coarsening dynamics within a model porous medium, they notably establish distinct coarsening regimes as a function of time (and as a consequence, average bubble size). The initial regime, i.e. the self-similar regime is similar to bulk coarsening in which bubble size increases linearly with time and no effect of the porous medium is noted. The second regime displays a deviation from the linear growth demonstrating that wall effects become significant. Finally coarsening is noted to stop as thin films rest in thermodynamically stable positions at pore throats.

Now that we have established the microscopic mechanisms that regulate bubble size, we will see how they can be involved in the macroscopic flow regime differences.

High-quality regime microscopic model

Khatib et al. (1988) observed that the bubble size in the low-quality remained constant and monodispersed throughout, whereas in the high-quality regime the bubble size is a function of the gas fraction. In combination with the capillary pressure measurements, the authors established that bubbles can coalesce at a sufficiently high capillary pressure P_c^* to regulate their capillary pressure environment. As gas fraction is increased, a critical liquid saturation S_w^*, corresponding to a critical capillary pressure P_c^*, is attained at which the bubbles are unable to maintain their smaller size. As gas fraction is increased further, the thin films coalesce, redistributing the liquid trapped in the Plateau borders into the surrounding liquid. The local liquid saturation is therefore increased and maintained at S_w^* and P_c^*. Therefore, this regime is dominated by the effect of the limiting

capillary pressure, known as the limiting capillary regime or sometimes the coalescence regime. The bubble size adaption mechanism via coalescence can be observed in Figure 1-16.

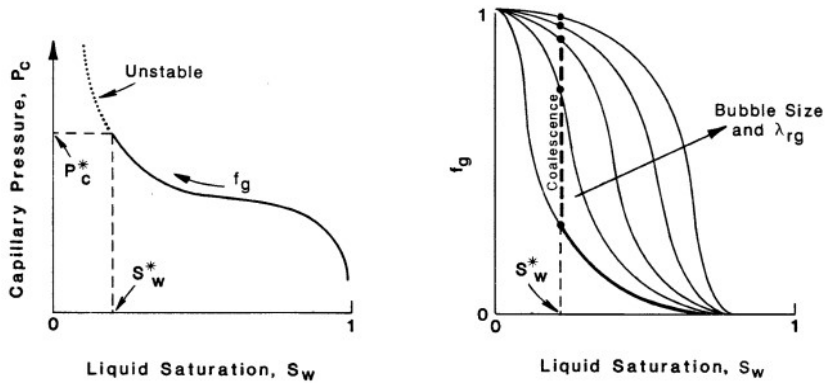

Figure 1-16 : The attainment of the critical capillary pressure P_c^* at the critical saturation S_w^* (left) and the coalescence mechanism maintaining the critical liquid saturation at increasing gas fraction (right). Adapted from Khatib et al. (1988).

Low-quality regime microscopic model

Rossen and Wang (1996) provide a model, and accompanying data, for understanding the low-quality regime. They describe the low-quality regime as dominated by the flow of stable bubbles, where diffusion has ensured that bubble size is approximately the average size of a pore, and bubbles are then mobilized as the pressure gradient is increased. In this regime, lamellae creation is inhibited by the bubble size condition. The higher liquid saturation also creates a lower capillary pressure environment, and coalescence of lamellae does not take place. The foam in this regime behaves as a Bingham plastic: as pressure gradient is increased, previously trapped bubbles reach a fixed yield stress and initiate movement through the medium. Hence, increasing the pressure gradient enables a larger amount of gas to circulate through the pores, and we retrieve the strong dependence upon gas rate characteristic of the low-quality regime. The liquid injection rate, however, shows little effect on the measured pressure. Even if the liquid rate is increased, contrary to the high-quality regime, the bubbles remain in a stable capillary pressure environment. Liquid flow (restricted to the non-occupied smaller pores and Plateau Borders) is only increased, with no effect on the gas bubbles.

Alvarez et al. (2001) provide a definitive overview of the supporting evidence for the two-regime behavior, and generalize these observations towards a unifying model describing behavior in a variety of media, surfactant and flow rate conditions. They notably test the following hypotheses:

- The limiting capillary pressure regime shows a strong dependence to the surfactant used (as P_c^* will increase for stronger lamellae).
- The nature of the porous medium, (or rather the average pore size), plays a key role in the low-quality regime, as the bubble density will adapt to each medium and show a varying rheology.
- That the transition quality f_g^* is a function of both the nature of the porous medium and the ability of the surfactant to stabilize the foam.

Despite some minor issues, the hypotheses tested are generally found to be correct. Furthermore, they measure power-law exponents for the pressure gradient dependencies on flow rates for each regime. In their experiments, they find the high-quality regime consistently shear-thickening, and the low-quality regime as shear-thinning. The exponents on the liquid rate for the high-quality regime (when measurable) span 1.30-2.11 whereas the low-quality regime's gas exponents (bar one value at 1.08) span 0.30-0.46.

1.3 Modelling foam in porous media

Realistic modelling of foam in the reservoir engineering context is an essential step in any successful foam operation. Numerical experiments can be performed to optimize the process at a fraction of the cost of core-scale tests. However, the accuracy of a prediction is only as valid as is the initial foam model used. As described previously, the creation of a foam phase with discontinuous gas pockets in water-wet media is modelled simply as a reduction in mobility of the gas phase, with little effect on the flow of the liquid phase. Modelling techniques generally therefore modify the mobility of the gas phase, either empirically as a single entity, or by increasing the viscosity of the gas (as a function of the foam texture) and reducing the gas relative permeability (due to gas trapping) individually. Foam models can be classified by the method, assumptions made, level of detail or complexity. Ma et al. (2015) propose an exhaustive and clear classification system of foam models. The foam models shown here are all population balance models, due to the emphasis on pore-scale aspects of flow. The models describe foam flow exclusively without oil, which serve as an initial founding block upon which the further complexity of oil interactions can be added afterwards.

Within population balance models, viscosity is a function of the foam texture n_f. Solving a differential equation that sums all bubble creation, destruction and transport processes locally yields a value for n_f. For this reason, these models can describe transient phenomena in which foam texture is yet to reach the equilibrium value. For example, Chen et al. (2010) find that a dynamic-texture model is necessary to describe foam flow at the entry region of a sandstone core. In some population balance models, a supplementary local equilibrium condition is imposed, in which the bubble coalescence and generation rates are set equal. This results in solving a simpler algebraic equation to obtain n_f. Computation time is therefore decreased in comparison to the dynamic texture version (Chen et al. 2010).

1.3.1 Population balance models

Within population balance models, foam texture is calculated *in situ* by solving for the foam texture variable in population balance differential equation comprised of the various creation, destruction, trapping and transport processes, as well as net source or sink terms for lamellae. We give here the general equation used in the population balance formulism for 1D:

$$\frac{\partial(\phi(n_f S_f + n_t S_t))}{\partial t} + \frac{\partial(n_f u_g)}{\partial x} = \phi S_g(r_g - r_c) + Q_b \qquad (12)$$

Where the subscripts f and t denote flowing or trapped foams, meaning that n_t and n_f are the foam textures of trapped and flowing foams. The total gas saturation S_g therefore defined as $S_g = 1 - S_w = S_f + S_t$, meaning the gas phase is exclusively considered as foam, with a variable texture variable. The first term of the time derivative describes the change in texture of flowing foam per unit volume of porous media, whereas the second term is the rate at which lamellae trap. The second left hand term accounts for the convection of flowing foam. The first right hand side term sums the generation and destruction processes r_g and r_c to give a net rate of change in lamellae per unit volume due to internal processes. The final term on the right Q_b accounts for the injection of pre-generated foam into the system and serves as a boundary condition. The debate on the dominating mechanism for foam generation becomes relevant as the expression of the lamellae generation rate will depend on different parameters for each mechanism. Furthermore, model refinements for each mechanism lead to the many different generation rates available in the literature. The destruction rates, while mostly adhering to capillary suction as primary mechanism,

also show some diversity between authors. Population balance models differ in terms of generation and destruction rates, but also in the way the texture variable n_f is integrated into the viscosity or permeability of the gas phase. Models can also approach the trapping of foam in different ways. We shall list some elements of the models in a manner that demonstrates the breadth of possibilities, while noting the assumptions made for each case. We give first some classical examples where local equilibrium conditions are not respected, before providing some examples of the local equilibrium variant.

a) **Classical full population balance models**

Friedmann et al. (1991) give an interesting model, to predict transient foam flow behavior in Berea corefloods. The contribution of the trapped foam fraction x_f is simply given by:

$$k_{rg}^{f} = x_f k_{rg} \tag{13}$$

Also, the authors impose an equilibrium relationship between trapped and flowing foam textures, given by: $n_t = K_f A_f n_f/(1 + K_f n_f)$, where A_f and K_f are bubble trapping parameters. For flowing foams, the authors use the following relationship for viscosity, provided that the calculated foam viscosity is larger than the gas viscosity:

$$\mu_g^f = \mu_g F_g k^{3/2} n_f \left(\frac{v_g}{v_{ref}}\right)^{n-1} \text{ for } \mu_g^f > \mu_g \tag{14}$$

Where F_g is a geometric factor, k is the medium permeability, v_{ref} is a reference velocity (taken by the author as 35 m/d) and n is the power law index, that accounts for the shear-thinning of the foam, found by the authors to be equal to 0.71. The rate equations for lamellae generation and destruction are given as followed:

$$\begin{gathered} r_g = k_1 \left[\frac{10(v_g/v_c - 1)}{1+10(v_g/v_c-1)}\right] \cdot \left[1 + \left(\frac{n_f}{n_c}\right)^5\right]^{-1} \\ r_c = k_2 n_f C_s^{-1.4} \end{gathered} \tag{15}$$

In which k_1 and k_2 are fitting constants, v_c is the critical gas velocity necessary for snap-off (or lamella division) to occur, n_c is the limiting bubble density (approximately one per pore). The first part of the generation rate expression rises smoothly from 0 to 1 as the gas rate passes the critical velocity, fitting with the conditions for generation by snap-off. The generation rate also shows

sensitivity to the limiting bubble density n_c, as lamellae formed at a density higher than one per pore are deemed unstable. The coalescence rate is proportional to the number of bubbles and inversely to surfactant concentration, to account for a higher probability of rupture for a larger lamellae density and for weaker foams. They use this model to fit transient and steady-state foam flow in both SAG and co-injection corefloods.

Kovscek et al. (1995) use a simpler expression for the gas phase viscosity that is preserved in following models, using a power law dependence observed previously for long bubbles in circular tubes (Bretherton 1961; Hirasaki and Lawson 1985) and employ a Corey-type relative permeability model for the gas phase in presence of foam, in which the stationary fraction is included within the Corey exponent, as opposed to models described by Friedmann et al. (1991) or Falls et al. (1988) which include the fraction outside of the exponent. The authors also impose a local equilibrium condition between trapped and flowing foam texture by setting the two equal. Furthermore, the trapped foam volume fraction X_t, is related to the trapped foam texture by the expression $X_t = X_{t,max}\left(\frac{\beta n_t}{1+\beta n_t}\right)$, where $X_{t,max}$ is the maximum fraction of trapped foam and β is a trapping parameter. The relative permeability and viscosity expressions are given as:

$$k_{rg}^f = k_{rg}^0 \left(\frac{x_f S_g}{1 - S_{wi}}\right)^g$$
$$\mu_g^f = \mu_g + \frac{\alpha n_f}{v_g^c} \tag{16}$$

In which g is the Corey exponent determined experimentally for the power-law exponent c is taken as close to 1/3, and the parameter α is said to be dependent on the surfactant system.

The authors also include the liquid interstitial velocity in the lamellae generation rate, and the first mention of an explicit dependence to capillary pressure with the limiting capillary pressure in the destruction rate:

$$r_g = k_1 v_w v_g^{1/3}$$
$$r_c = k_{-1}\left(\frac{P_c}{P_c^* - P_c}\right)^2 v_g n_f \tag{17}$$

Where k_1 and k_{-1} are fitting constants. P_c^* is furthermore made dependent on the surfactant concentration, in accordance to the observations of Aronson et al. (1994), such as: $P_c^* = P_{c\,max}^* \tanh\left(\frac{C_s}{C_s^0}\right)$, in which $P_{c\,max}^*$ is a reference measure of P_c^* for strong foam at a reference molar surfactant concentration of C_s^0. The inclusion of both fluid velocity rates inside the generation rate is based on pore level calculations made by Kovscek to account for the different steps involved in the snap-off process in pore throats (Kovscek and Radke 1996). The coalescence rate includes the notion of lamellae flux by the term $v_g n_f$, as opposed to simple lamellae density found in the model of Friedmann et al. (1991), which could cause coalescence for static foams. The addition of a dependence on capillary pressure is justified by the instability of lamellae as they pass into pore bodies, decreasing their thickness decreases. In a higher capillary pressure environment, the stability reduces significantly, due to the proximity to the limiting capillary pressure. Using this model, the authors fit pressure drops and liquid saturation data to transient and steady-state foam flow experiments in Boise sandstone cores.

Despite their ability to describe diverse foam phenomena, this type of models' practical use is sometimes difficult due to the number of numerical steps required to both solve the differential population balance equation and reuse the foam texture variable in the simulator. To lighten the process, some authors add a supplementary assumption, asserting that generation and destruction rates are equal. Consequently, the differential equation is bypassed, and foam texture is attained by simply rearranging the rate equality. Therefore, dynamic effects are eliminated and the foam texture for a given series of reservoir variables is instantly achieved. This process can be applied to obtain local textures in an injection (i.e. for differing injections in series) or steady state processes.

b) **Local equilibrium variant**

The first use of a local equilibrium expression for foam texture is made by Hatziavramidis et al. (1995) where a simple expression is derived by equaling generation and creation rates described in greater detail by Ettinger and Radke (1992). The relationship for the foam viscosity is taken from the same paper:

$$n_f = \frac{K_g}{K_d} u_g^{a_n}$$
$$\mu_g^f = \mu_g + A n_f D_p^3 \left(\frac{\sigma}{\mu_w u_g}\right)^{a_\mu} \quad (18)$$

where K_g and K_d are constants associated with generation and destruction processes, a_n and a_μ (fixed to -2/3 here) are the exponents associated with the foam texure and the foam viscosity power law, A is a scaling constant, D_p is the pore diameter and σ is the gas-water interfacial tension. The supplementary condition that the pressure gradient be superior to a critical gradient necessary for strong foam production, as described by Ransohoff and Radke (1988) is also imposed. The authors use a constant trapped foam fraction in their relative permeability expression as found in equations. The authors use this model to fit transient foam flow at the field scale, and to predict the future oil production of a South Belridge pilot from 1985 to 1988.

Kam and Rossen (2003) propose a model with some degree of novelty. They use a generation function explicitly dependent on pressure gradient, as opposed to a gas velocity. The authors explain that the pressure gradient is the appropriate variable when considering that new lamella creation results from mobilisation and division of pre-existing lamellae. The destruction also integrates the limiting capillary pressure concept, but instead uses the equivalent limiting liquid saturation S_w^* defined as $S_w(P_c^*)$.

$$r_g = C_g(\nabla P)^m$$
$$r_c = C_c n_f \left(\frac{1}{S_w - S_w^*}\right)^n \quad (19)$$

where C_g, C_c m and n are model parameters. The authors equalize these rates and solve for foam texture such as:

$$n_f = \frac{C_g}{C_c}(\nabla P)^m (S_w - S_w^*)^n \quad (20)$$

Hence the authors give an expression for the steady-state foam texture with only three independent variables: $\frac{C_g}{C_c}$, m and n. They use their foam texture in a viscosity identical to equation (16)**Error! Reference source not found.**, but choose to not make the gas relative permeability perturbed by

the presence of foam, and assert $k_{rg}^{f} = k_{rg}$ throughout. In this sense, the trapped foam fraction is not treated explicitly. By using this relatively simple model, with only four free model-related fitting parameters (three previously mentioned and α from equation (16)), the authors fit data from A. Gauglitz et al. (2002), exhibiting many characteristic features of foam flow in porous media. They reproduce the foam generation at a fixed pressure gradient or gas velocity, show the existence of three multiple foam types upon foam generation: strong, weak and intermediate. They also reveal the experimental data hysteresis and recreate both low- and high-quality strong foams.

A final example is given by the more recent model of Chen et al. (2010), who build on the model proposed by Kovscek et al. (1995), and refine equation (17) by adding the constraint of a maximum lamella density into the generation rate. This constraint has been used before by Friedmann in equation (15). Hence the constant k_1 in the generation rate of equation made into a variable for the Chen model such as:

$$k_1 = k_1^0 \left[1 - \left(\frac{n_f}{n^*}\right)^{\omega}\right] \tag{21}$$

in which k_1^0 and ω are fitting constants and n^* represents the upper limit for bubble concentration or lamellae density, usually set a one-per-pore. This constraint accounts for the difficulty in obtaining bubble densities higher than the one-per-pore maximum, as lamella creation is inhibited when more and more bubble germination sites are occupied by preexisting bubbles. Using this definition for k_1 in the previous Kovscek et al. (1995) model, the authors set $r_g = r_c$ and rearrange for n_f to give a polynomial function:

$$n_f^{\omega} + \frac{n^{*\omega} k_{-1} |v_f|^{2/3}}{k_1^0 |v_w|} n_f - n^{*\omega} = 0 \tag{22}$$

The authors then use $\omega = 3$ and solve the cubic equation for foam texture n_f. Using this added constraint on the generation rate the authors fit transient and steady-state data, predicting in the process the characteristic high- and low-quality strong foam regimes. On top of this, the authors make a valuable comparison of results for the local equilibrium version and full population balance model (by solving the differential equation for n_f), while at the same time measuring *in situ* foam textures experimentally. They find that for their coreflood experiments on Berea sandstone, the

local equilibrium approximation is valid for most of the core, but in the 12 cm entrance region of the 60 cm cores, the intensive net foam generation brings the experiment out of local equilibrium.

Hence, we can see that for population balance models, while displaying continuity through their fidelity to the initial framework, the specific implementation and choice of creation/destruction rates and viscosity/relative-permeability relationships demonstrates great variability. Each microscopic rate relationship is tied to assumptions about the specifics of pore-scale foam flow. Through these model examples, a few elements seem to reappear often:

I. The generation rate is tied to the specific pore level mechanism.

II. The coalescence rate can include the mention of a maximal lamella density, often set as the average density at one-per-pore.

III. Foamed gas viscosity can contain various structure related parameters, such as permeability, pore size, or geometric factors.

IV. The exact effect of trapped fractions on the gas permeability is unclear, but increasing trapped fractions strongly reduce gas permeability.

1.4 Synthesis and proposed research themes

We elaborate here several phenomena that we think may serve as a starting point for analysis of the dependence on microscale pore parameters. Our analysis can be broken down into the following points, which can share some degree of interconnectedness. We will look at foam trapping and foam flow heterogeneity; foam bubble size distributions and their effect on flow; and finally, the appropriate scale for describing foam phenomena.

We will spend some time summarizing each theme and propose a few starting hypotheses.

1.4.1 Foam trapping and flow heterogeneity

Field scale success of foam operations relies on accurate description of foam, including characterization of the stationary gas volume in the reservoir. The sheer breadth of measured trapped fractions, and different ways of including them in modified relative permeability models, provide a reason to investigate the mechanisms. Furthermore, direct observation of trapped foam

is difficult, and many estimates rely on either using indirect tracer experiments or extrapolating data within a specific model framework to provide an estimate.

A link seems to exist between pore-scale structure and the degree of foam trapping through the local heterogeneities that exist in the pore structure. In their low-quality model, Rossen and Wang (1996) describe foam essentially as a series of bubbles fully contained in pores that behave as Bingham plastics with a yield stress related to the upstream throat size as $\propto 1/r$. In this model, when a sufficient pressure gradient allows the bubbles to overcome the throat yield stress, they can flow, otherwise they remained trapped. This suggests local throat size plays a large role in identifying trapped areas. Figure 1-17 shows the tube radius distribution displaying which fraction of foam is flowing or trapped. Hence, in an interconnected porous medium, whole sections could become trapped due to a few tight upstream constrictions, or similarly tight downstream throats could prevent bubble entrance and alternate routes would populate otherwise "closed off" regions, contributing to a trapped gas fraction. In this manner throat distributions and throat neighborhood properties become key in predicting trapped zones and fractions. As previously stated, Rossen (Rossen 1990a, 1990b, 1990c, 1990d) provides a series of theoretical papers detailing the effect of specific pore and throat shapes and relative sizes on the pressure gradient necessary for mobilization of a foam film.

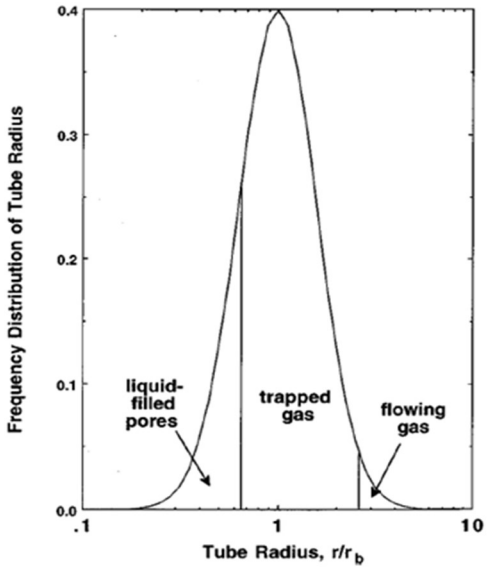

Figure 1-17: Tube radius and gas-liquid occupation in the Rossen and Wang (1996) model. The liquid-wet tubes carry most of the liquid phase in their smaller radii, the trapped gas occupies intermediate radii necessitating large pressure gradients to mobilize, and the flowing gas is found in the larger throats

We supplement this model with the recent observations of Géraud et al. (2016), in which foam is injected through a horizontal transparent Hele-Shaw cell with cylindrical obstacles. The authors observe a series of trapped areas in which grains are closely packed together, coherent with the model described by Rossen. The authors furthermore observe a correlation between bubble size and bubble velocity. While this model is of a larger scale, with characteristic throat radii of 1.75 mm, detailed flow maps show interesting aspects prompting further enquiry.

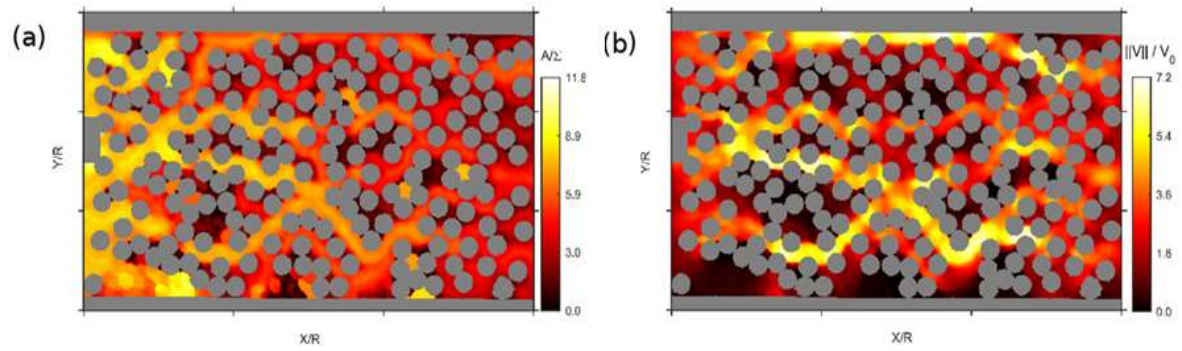

Figure 1-18: Correlation between bubble size (a) and bubble velocity (b) in a 2D model medium, with flow from left to right. Bright yellow passages in both maps show a large overlap of regions between the bubble velocity and bubble size. Taken from Géraud et al. (2016).

Significant regions of the medium contain little flow and the flowing bubbles are seen to transport in a series of preferential paths that locally correlate with higher bubble sizes in the size distribution map. Figure 1-18 displays the velocity and bubble size distribution map. According to foam viscosity models presented previously, such large differences between bubble sizes for flowing and trapped foams would rule out some of the models in which foam textures are set equal for both.

1.4.2 Foam bubble size distributions and their effect on flow

Recent foam models in their entirety adhere to the assumption that foam viscosity depends on an average measure of lamellae density. To support this assumption various experimental proofs are given with experiments on model media, such as Hirasaki and Lawson (1985) and Bretherton's (1961) experiments on smooth capillary tubes, and developments by Falls et al. (1989) to include the effect of constrictions on beadpacks. Further proof is given by experiments on consolidated media, in conjunction with simulations, such as the work Ettinger and Radke (1992) who observed

effluent foam textures and matched pressure profiles using a model, and Chen et al. (2010) who proceeded similarly, but included local sampling of bubble densities.

Moreover, the average bubble size is usually found to be close to average pore size and maintained at this size by: diffusion of gas between bubbles ensures the bubbles remain at a density of one-per-pore; lamella creation mechanisms, such as division of larger bubbles into smaller ones at the passage of a bifurcation, and creation of a new lamella by snap-off, at the passage of an upstream lamella out of a constriction and into another pore body.

However, we believe that a varying bubble size may appear in a significant amount of cases. For example, we may observe larger bubble size distributions in high-quality regimes where high capillary pressure environments force the films to coalesce and adapt to maintain a capillary pressure they can support. This effect is shown in Figure 1-19.

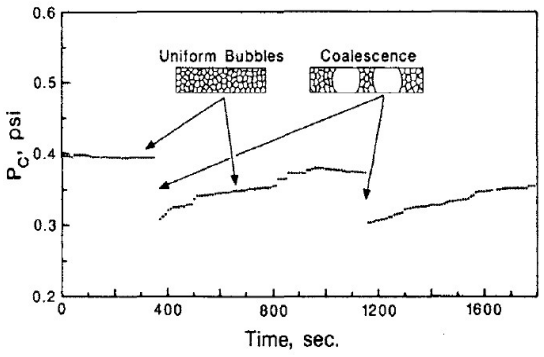

Figure 1-19: Capillary pressure adaptation via bubble coalesce, creating heterogeneity of bubble distribution. Taken from Khatib et al. (1988).

Media with large areas of varying pore size i.e. layered or fractured media, where bubble size will adapt by diffusion to each region, may also contain wide bubble size distributions.

Finally, flow of foam with high injection rates, close to the well for example, may not display monodisperse bubble sizes at one-per-pore due to the larger timescales required for diffusion between bubbles to create such a distribution.

The complex bubble distribution shapes, if studied are often omitted in analyses, as Patzek (1989) describes in his population balance model. The author declares higher moments of the bubble distributions are necessary to correctly model foam. The author explains:

"For example, to model bubble trapping and mobilization, we need some knowledge of the bubble size distribution (usually smaller bubbles get trapped because they offer higher resistance to flow). Diffusional mass transfer between bubbles can be modelled only if we account for bigger bubbles growing at the expense of smaller ones. In addition, any model that relates the flowing fraction of foam to flow conditions and foam texture will have to include bubble trapping and mobilization. In short, any realistic description of foam flow in porous media will make use of at least the second order moments of the population balances. The second order moments are related to variance of the bubble size distribution."

Through our work, we aim to further understand the role of bubble distributions by characterizing inlet bubble distributions and studying bubble size adaptation as well as observing flow properties. With respect to the previous point regarding flow heterogeneity, we can already observe a strong link between the high flow preferential paths and bubble sizes, showing the closeness of these two themes.

1.4.3 The appropriate scale for describing foam phenomena

Classically, most foam studies in porous media focus on either core-scale flow behavior laws, with in some cases observations of fluid saturations and trapped fractions through tracer techniques and imagery, or direct observation of pore-scale mechanisms via direct observation in model media such as micromodels or beadpacks. Intermediate-scale investigation, in which both pore-scale events and larger scale flow properties are observed is burgeoning in the current literature. More intricate micromodel fabrication combined with better image acquisition and processing techniques have given the opportunity to observe more phenomena at different scales using networks of considerable complexity. Observations such as preferential path flow, foam trapping, foam diffusion, and flow in model fractures (Géraud et al. 2016; Géraud et al. 2017; Jones et al. 2018a, 2018b; AlQuaimi and Rossen 2019) have been characterized microscopically. While 2D media have substantial intrinsic weaknesses, notably a lack of full wetting-phase connectedness, generally lower coordination and unrealistic pore-throat aspect ratios, a number of insights can be gained through their use and parallels can be made to 3D media to a certain extent. Following this trend, we believe the use and detailed characterization of a micromodel with simultaneously high-complexity, varying pore and throat geometry and sizes, associated with an image workflow designed to capture both foam bubble sizes and flow properties will shed light into the interplay

of mechanisms of different scale, if and how they can be understood structurally, and their effect on macroscopic flow properties.

Chapter 2. *Foam Flow in a Micromodel: Data Acquisition and Transformation*

Preamble

This chapter will be dedicated to familiarizing the reader to some the different data types and tools used, from the experimental set up with the micromodel characterization, to details regarding the data transformation with created flow maps and bubble size histograms. A single foam experiment will be used for this initial exposé. However, we will use two distinct Newtonian flow simulations for comparison with the measured foam flow velocity map. We will look in detail and the interaction between the bubble size distributions and flow properties before finally looking at relationships between some local structural properties and flow properties.

We will present our results as they appear in a published article, with some minor details added in the text and supplemented by further sections regarding the creation of flowmaps in a supplementary section of the appendix.

Article: New insights of foam flow dynamics in a high-complexity 2D micromodel

Christopher Yeates, Souhail Youssef, Elise Lorenceau

We show a slightly edited version of the article accepted on the 30th April 2019 for publication in *Colloids and Surfaces A: Physicochemical and Engineering Aspects*
Volume 575, 20 August 2019, Pages 184-198

Keywords: Foams; Micromodels; EOR; Pore-scale observation

Abstract:
In this work, we present direct observation of foam flow through a 2D porous microfluidic device. Through a specially designed image processing workflow, we perform individual bubble tracking and establish flow dynamics within the micromodel structure. In addition to our experimental data, we provide 2D and 3D numerical Newtonian flow simulations on equivalent digitized versions of the model, carried out using Lattice Boltzmann simulation codes for comparison. The results show that foam flow in our experimental conditions, low gas fraction and high injection velocity, demonstrate a high degree of similarity to the flow of a Newtonian fluid in both 2D and 3D simulations, in aspects of large-scale flow distribution homogeneity and specific flow passage activation. However, the foam data shows a larger spread of pore-scale flow velocities, spanning from blocked off areas of quasi-zero flow, to zones of high velocity, with velocities well above the Newtonian counterparts. For our model depth and characteristics, the 2D simulation demonstrates slightly more flow heterogeneity and is closer to the foam case. Detailed bubble tracking gives access to other characteristics of the foam flow inside the medium such as the dichotomy between the flow patterns of the smallest bubbles, typically dispersing and accessing most regions available, and the largest bubbles, which travel in long straight preferential paths exclusively. We show that intrinsically tied to these different flow patterns is the relationship between bubble velocity and bubble size, as we demonstrate distinct populations of trapped and flowing bubbles with distinct sizes. Finally, we explore the relationships between microstructural parameters and flow intensity and note a weak correlation to local structural parameters. Our study, which combines high spatial and time resolution, small network dimensions, high network complexity and efficient bubble tracking, therefore sheds new light on the study of foam flow in porous media.

2.1 Introduction

Surfactant-stabilized foams are used as injection fluids in porous rocks in Enhanced Oil Recovery (EOR) as a means of improving recovery and improving reservoir conformance of gas injection due to permeability contrast or gravity segregation (Li et al. 2013). In a confined geometry, where the bubble size is often observed to be of the same order as the pore size, foams exhibit a series of original phenomena unseen in either bulk foams such as distinct flow regimes (Alvarez et al. 2001), trapping (Jones et al. 2018b) or novel properties unknown in other flow situations such as selective mobility control in heterogeneous porous media (Kovscek and Bertin 2003; Tsau and Grigg 2013). Elsewhere in EOR applications, foams can be used to plug areas of a well, to block exploited or uninteresting regions. Lastly, we can mention the example of using foams in fractured reservoirs to increase oil recovery in the rock matrix (Conn et al. 2014; Fernø et al. 2016).

To get a better understanding of foam flow in porous materials, laboratory experiments are often performed either at the core-scale, with observations including apparent viscosity and fluid saturations, or at the pore-scale, through qualitative observation of individual mechanisms or overall oil recovery factors usually using transparent 2D micromodels or transparent beadpacks (Fernø et al. 2016; Ransohoff and Radke 1988; Gauteplass et al. 2015). Although some examples of in-situ flow measurements in porous media are available, various shortcomings may diminish the applicability of these results, such as the unrealistic pore-scale dimensions or low model complexity (low pore-scale heterogeneity or constant coordination number). Despite the lack of direct observation of foam flow in higher complexity networks, many assumptions are made regarding the precise dynamics of flow based on hypothetical models. For example, Radke, Gillis (Radke and Gillis 1990) describe flowing gas occurring in larger pores whereas intermediate sized pores contain trapped immobile bubbles. Since then, advances in imaging, 2D micromodel fabrication and especially data processing provide new tools to address these complex problems statistically. In particular, how the widths of bubble size and pore distributions interplay with the heterogeneity of the flow field remains an open question. Recently, Géraud et al. (2016), provide interesting results by directly observing these correlations in a 2D medium. In polydisperse foams the authors establish a positive correlation between bubble size and bubble velocity, also observing preferential paths for larger bubbles as well as trapped zones. The authors furthermore observe a degree of similarity between the bubble flowmaps and the maps relating to pore sizes and affirms

that preferential paths occur where large pores are connected together. The authors also reference a structural origin for the existence of trapped zones, yet don't systematically explore this relationship and it remains unclear which structural parameter could be the most relevant. Here we exhaust some of the most obvious candidates including the ones referenced by the authors.

Despite this interesting framework, these open questions suggest that there is still some need of detailed quantitative data to obtain better flow descriptors for foam flow in porous geometry. In this work, through an accurate image processing and data analysis procedure that we describe in detail, we gain access to new data types for flow situations at this small scale, notably detailed velocity maps and local bubble size distributions, and combinations of both such as velocity maps for different bubble size categories. We use flow rates that are large but nonetheless realistic in proximity to the borewell. We present and evaluate the created flowmaps in conjunction with the bubble size distributions. We characterize flow with quantitative model-scale markers such as activated passage fractions and global flow distributions. We perform 3D and 2D Lattice Boltzmann simulations on digitized version of the model used. We then compare flow both model-scale and on the pore-scale. Although such comparisons have previously been performed between foam and 3D simulations on models of simpler geometry (Dollet et al. 2014), comparisons between experimental foam flow and simulated Newtonian flow in both 2D and 3D cases, for a network of this complexity are novel. This provides two comparative Newtonian flow results, in order to asses tangibly the pore-scale specificities of foam flow versus a classical Newtonian fluid flow in both 2D and 3D dimensions. We show that for our model depth, foam flow resembles more closely 2D than 3D simulated Newtonian flow.

For the foam data specifically, we witness some significant recurring themes, each representing a key observation in the study of foams in porous media. The structure of our discussion section follows a sequence of increasing complexity and fundamental explanation. We start by showing the interactions between the bubble size distributions and velocity distributions. With only these two parameters, we show that trapped foams are observed at a constant rate throughout the model and show independence to the surrounding flowing bubble size distribution. Secondly, we focus on the flowing foam population, and we show that within the continuum of speeds that contribute to flow, behavior differences are observed between bubble sizes. Here we establish the preferential paths for larger bubbles and demonstrate that the majority of flow in the medium is contained

within these paths. Finally, we look in detail at the porous medium characteristics to attempt to explain some of the variance shown in the bubble flowmaps, in both the trapped zones and preferential path zones. We perform a scan of structural properties demonstrating that local porous structure properties only weakly correlate with the flow properties and higher-complexity network properties are needed.

2.2 Materials and Methods

2.2.1 Micromodel

We use a glass micromodel of inner etched network dimensions of 10 mm wide by 17 mm long. The models are wet-etched with fabrication depth of 40 μm. Each outer longitudinal side of the inner sketching comprises a rectangular entrance zone followed by a flow diverting system of larger canals that serve the purpose of spreading the bubble flow across the model. The flow diverting channels are composed of 3 successive bifurcations of the initial entrance canal to produce 8 channels evenly distributed across the model entrance. Both sides of the model display the same flow spreading configuration inwards/outwards of the inner etching.

The interior model network is based on an image of a 2D slice of Bentheimer rock, obtained from X-Ray tomography. It is modified to include a larger degree of porosity and therefore connectivity, enabling a sufficient 2D percolation to correctly mimic a complex interconnected flow situation. We show a binarized version of the inner model used in Figure 2-1.

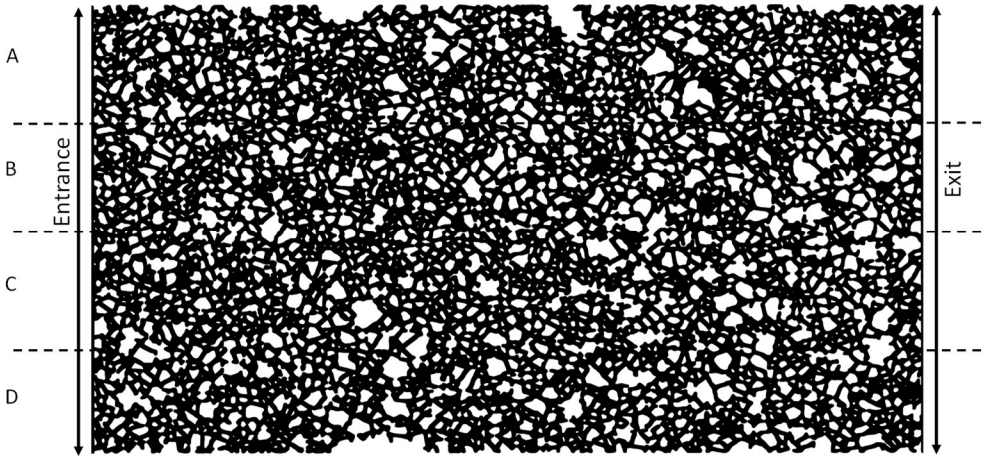

Figure 2-1: Binarized model showing the entrance and exit, as well as the zones used for the longitudinal box intensity analysis described in Appendix 2-C. Obstacles appear in white while porous flow channels are black.

The total amount of full-depth objects impeding flow (assimilated to grains) is 2602. The average porosity of the interior connected network is 69.7%. The permeability of the total model with the flow spreading system is 4.7 Darcy. As the model is made entirely from glass, it is water-wet. Using a modified version of the ImageJ watershed algorithm (Soille and Vincent 1990) on the binarized porous area of the model, local distance minima between obstacles are identified. The watersheds (or basin meeting segments) are created from flooding source points corresponding to the maxima of the distance map of the porous network. The watersheds found are naturally the local minima of the porous space. As the distance of the irregular porous space presents many local maxima to serve as basin sources, the possibility of over-decomposing the medium needs to be avoided. The modified watershed algorithm then only creates watersheds if the radius of the smaller largest inscribed circle of the pores neighboring the watershed is at least two pixels larger than the throat radius itself (or 3.9 µm on the upscaled model image used). A sample of the chosen decomposition and associated statistics is shown in Figure 2-2.

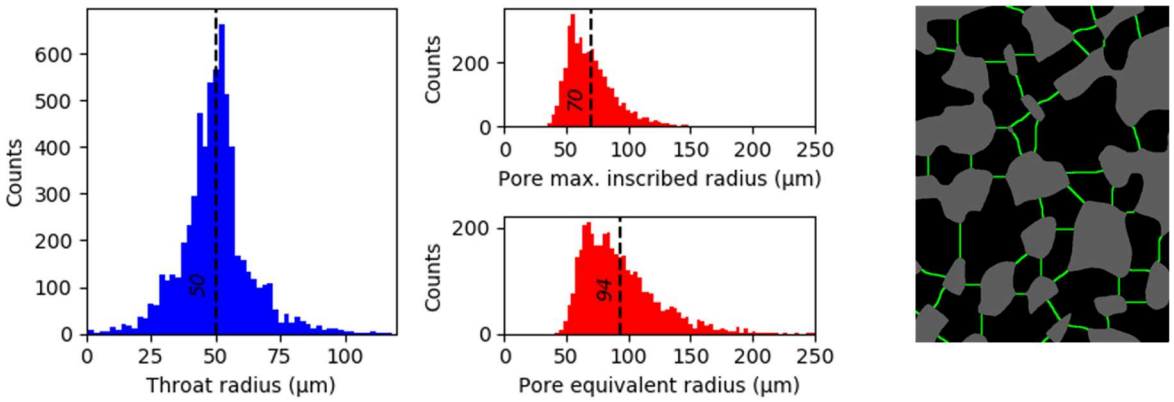

Figure 2-2: Micromodel network characteristics, with mean values shown as dashed lines. A sample of the network decomposition is shown on the right. Throats are shown as light green objects (enlarged for visibility) separating black pores

From the watershedded model, we use an ImageJ network analysis code to extract neighborhood characteristics of the porous area. We obtain, for each pore, sizes of neighboring pores or throat sizes that lead to them.

2.2.2 Fluids

The gas used for the foam is purified N_2. The liquid component is composed of purified water, 30 g/L of NaCl, and an AOS 16-18 anionic surfactant at concentration of ten times the CMC, supplemented by a betaine-based foam booster known to improve the foamability, foam stability

and rheological properties of aqueous foams (Basheva et al. 2000). This solution has a surface tension in contact with air of 28.83 ± 0.01 mN/m at 24°C, measured with a Kruss K100 tensiometer using the Wilhelmy plate method. This foaming solution has been selected for its excellent stability and foamability, for the depth of literature available for AOS foams (Khatib et al. 1988; Chambers and Radke 1990; Ettinger and Radke 1992), and for the proximity of the salinity to that of seawater.

2.2.3 Microfluidic setup

In this section we describe the microfluidic setup that we have developed and tested. This setup includes an injection and monitoring system, with a high-resolution camera for direct observation of foam flow in the micromodel. The camera make is JAI (SP-12000M-CXP4 model) that provides 12-megapixel monochrome resolution (4096 x 3072 pixel) and full-field framerate of 189 frames per second that can be increased if FOV is reduced. The overall experimental setup diagram is shown in Figure 2-3.

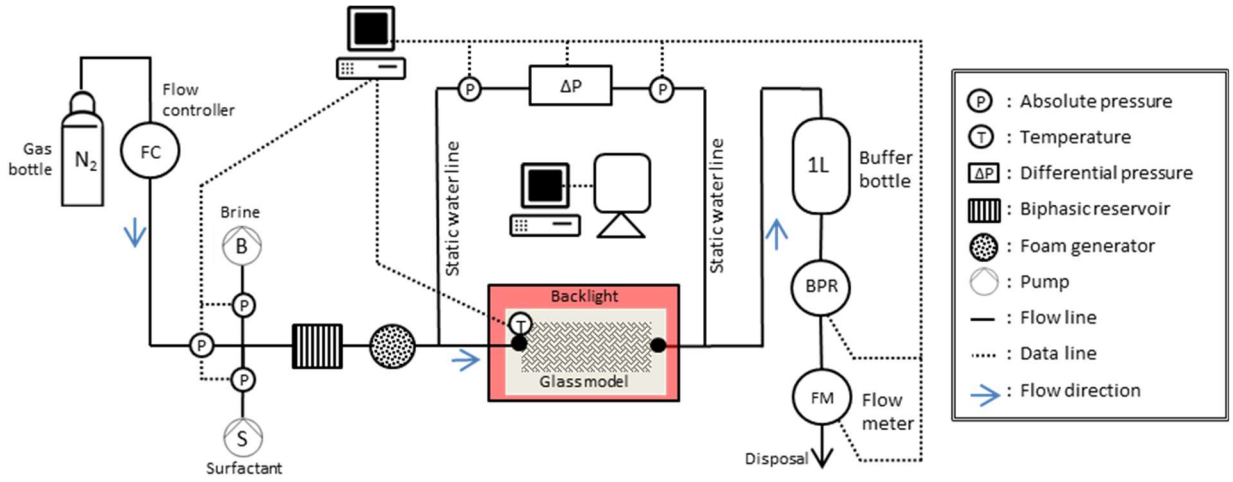

Figure 2-3: Experimental Setup

We use Vinduum liquid pumps, delivering a continuous flow with a minimum volumetric delivery rate of 10^{-4} ml/min. For gas flow, we use a Bronkhorst mass flow controller bounded by a maximum volume flow rate of 0.65 ml/min and a minimal stable flow rate found to be of 10^{-2} ml/min.

The foaming device is a sandpack of SiC grains 80µm in diameter. The sandpack is a cylinder 4 cm long and 1.5 cm in diameter, with a measured permeability of 930 mD. The motivation for using a sandpack is dual, firstly to provide a uniform foam quality before entering the micromodel,

as some supplementary segregation can occur in the tubing, and secondly to break down the gas-liquid biphasic flow into bubbles. Indeed, without creating preliminary coarse foam through the foam generator, we don't observe biphasic flow but rather a succession of distinct liquid and gas phases whose volume can reach a similar order of magnitude as the porous volume of the model. The foam injected into the model is thus both uniform and sufficiently coarse as to necessitate size re-adaptation through the passage in model. Fluids from the micromodel outlet then enter a liquid filled buffer-bottle from the top. The system is held at 3 bars by a backpressure regulator downstream of the buffer bottle. The choice of 3 bars provides a means of minimizing compressibility effects from the pressure gradient over the model. A flow meter measures the liquid output of the buffer bottle (corresponding to the total micromodel output at 3 bars) after the Backpressure regulator. From the total flow output and the liquid injection rate we calculate the gas fraction at the model outlet. The high-frequency, high-resolution camera has a CCD acquisition with integrated RAM for a large image collection capacity, enabling capture of the whole model with part of the outer flow spreading systems, at a frequency of 605 Hz and at a resolution of 2495 by 1496 pixels. The model is secured and levelled horizontally on two flat metallic rods, open to illumination from beneath. The model is backlit with the use of a high-intensity red light. In this configuration, the bubble interfaces are observable with a pixel size of 7.8 µm. Multiple thousand images can also be acquired in succession, all stabilized through the use of an air-suspended breadboard on which the setup is fixed, eliminating any potential laboratory vibration.

2.3 Data acquisition and analysis tools

2.3.1 Experimental procedure

The experimental procedure is designed to create a stable injection condition prior to acquiring steady-state images of flow, representative of a unique gas fraction and injection rate. First, models are saturated with distilled water and an image of the clear model devoid of foam is taken. A biphasic injection is initiated, and surfactant solution and gas proceed first through the foaming device before entering the model. As foam is created in the foaming apparatus, a significant pressure rise occurs at the entrance due to the viscosity of the created foam. In turn, foam propagation and further bubble size evolution across the micromodel creates a pressure drop increase until a plateau is reached. The pressure at the foaming device inlet usually rises for a

longer period of time than the model pressure drop and is also tracked until a plateau is reached. Only at this point is the system considered stable and images are acquired. For the experiment shown here, the injection gas fraction is set at 79%, calculated at the exit of the model from a measure of output liquid flow. At the time of acquisition, the steady pressure drop of 275±4 mBar, when compared to the backpressure of 3 Bars, ensures that the gas fraction is roughly the same throughout the model, varying from 77% at the entrance to 79% at the exit. The overall injection rate is 2.53×10^{-2} cm^3/min, equivalent to a superficial velocity of 84.7 ft/day, as measured at the model output at 3 Bars.

2.3.2 Image acquisition strategy

Two distinct image acquisition strategies are used. Each corresponds to a data type. In the case of the bubble size distributions, we average the individual distributions of images taken every 20 seconds. This low frequency was chosen such that more than 17 pore volumes of fluid could cross the model each time, keeping in mind the need for statistical representativity.

The images serving for dynamic bubble tracking and bubble creation observation were taken at higher frequency. Images sets are composed of 200 of these. Multiple image sets are captured, as one short burst of images may be insufficient to capture the sometimes-fluctuating flow patterns. The number 200 was chosen firstly as the tracking process becomes somewhat computationally demanding after a larger number of frames are used, and secondly as rather than a long single capture, many brief captures were preferred to account for the variability in flow patterns. Here we use 8 different sets acquired with a minute interval in between, corresponding to more than 53 pore volumes. A frequency was fine-tuned through trial and error to ensure we can track suitably all the bubbles (no excessive displacement between frames), while at the same time capturing the maximal amount of flow within 200 frames. The frequency was chosen as 605 Hz

2.3.3 Image processing and exploitation

a) Image processing

Our software analysis tools require binary images of filled bubbles. The grayscale images have to be preprocessed before binarization. Readers are encouraged to refer to appendix 2-A for details regarding the image cleaning and binarization process.

b) **Measured bubble velocity map**

From the high-frequency image series, the bubble tracking procedure was performed and a large data set of individual tracking velocity points was produced. The tracking plugin gives both a value of bubble displacement between two frames and a local bubble area value. From the combined series of tracked bubble values we create a 2D flowmap that gives a quantitative image of the flow over combined data series. The 2D flowmaps show time averages of all local bubble center of mass velocities in 2-by-2 pixel bins of the initial image. When a tracked object passes inside the box its velocity is added to the sum for that box. In this way, we observe a total velocity in a region in a given time, corresponding to a Eulerian description of flow. Each image is then smoothed using a Gaussian filter (implemented by a convolution of the produced 2D array with a Gaussian function with a standard deviation of 3) as the particle-like nature of the bubble tracks can often create small contrasting patches inside a pore.

c) **Numerical flow comparison**

Throughout the study, a detailed flow comparison is consistently made with both a 2D and 3D simulated flow of a Newtonian fluid in a 2D mask and 3D equivalent volume of the network. It is known that 2D and averaged 3D Newtonian simulations of micromodel type geometries can offer greatly different results (Venturoli and Boek 2006). This study provides a comparison of behavior between monophasic Newtonian fluids simulated in 2D and 3D and foam, both on the pore scale and globally within in a complex network. The calculation was performed on the etched network only. The 2D numerical method was a Lattice Boltzmann D2Q9 routine (Talon et al. 2012), whereas the 2D simulation was performed with a D3Q15 scheme (Talon et al. 2012). The 2D model dimensions were 4408 by 2560 pixels. The 3D volume used for the calculated was 4408 by 2560 pixels with a depth of 11 pixels. The calculations were performed until a steady velocity map was achieved and a quasi-constant pressure drop in between each timestep. The resulting velocity field output represents the Stokes flow of an incompressible Newtonian fluid. As the Stokes flow is purely viscous, the flow magnitude is isotropic. We give the velocity maps of both simulations in Figure 2-6.

d) **Flowmap quantitative analysis tools**

In our study of the velocity maps, we make use of some other model-scale quantitative tools that support more firmly observations we can make from inspecting the maps. We define transversal passage activation and longitudinal box flow in detail Appendix 2-B.

2.4 Results

2.4.1 Bubble creation/destruction mechanisms

The injected foams adapt rapidly to the porous network. Bubble creation is observed via the breaking up of large bubbles at bifurcations of the porous network. The division mechanism is described as follows. At a junction between one upstream path and two downstream paths an upstream large bubble enters partially one of the downstream paths, but is it broken up by a following bubble that breaks off the trailing part into a different path. This is a special case of lamella division within porous space previously invaded with bubbles, with a very oblique approach of the bubble to the fragmenting obstacle. This mechanism has elsewhere been described as neighbor-wall pinch-off (Liontas et al. 2013). We observe that if the part of the larger bubble that is committed to the trailing path is not sufficiently large, it will not get broken off, leading to the bubble deforming around the bifurcation and keeping its integrity. An example of both a successful division event and a failed division event is observed in Figure 2-4. We understand that Roof snap-off is unlikely to be observed in a model of this given geometry, due to the required large aspect ratio in a 2-dimensional medium that we observe rarely in our network (Rossen 2008), and due to the smooth surfaces inherent to wet-etched micromodels. For this reason the bubble fragmentation dynamics have not been studied extensively, as is the case in other studies (Géraud et al. 2017). However, other forms of snap-off are theoretically possible in this geometry (Rossen 2003).

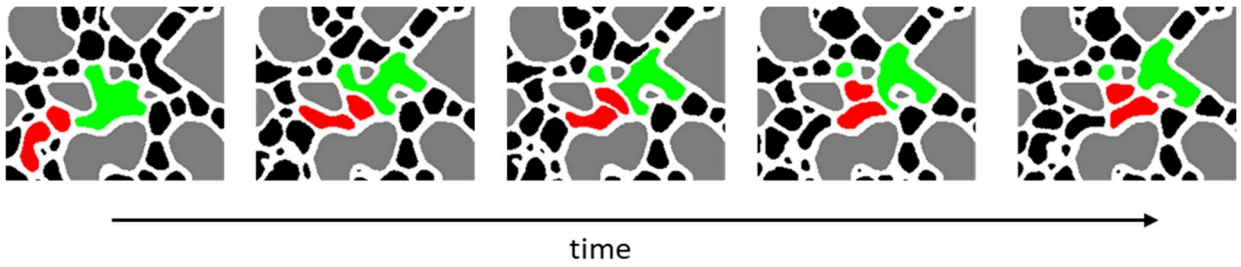

Figure 2-4: Observation of a successful bubble division (green bubble, left pane to center pane), followed by an unsuccessful one (lower red bubble, center pane to right pane). The red bubbles are responsible for pushing the green bubble against a bifurcation. The time between each pane is 3.3 ms

Bubble destruction or destabilization was not observed at these experimental conditions. This could reflect the important liquid fraction of the flow, constantly providing surfactant for film stabilization, or otherwise could be due to the low average aspect ratio of the model. Indeed, a film exiting a throat and expanding into a larger pore will only thin and destabilize if the downstream pore is large enough.

2.4.2 Bubble size distributions

From the low-frequency image series, the images are cut in five sections transversally, from the entrance to the exit of the model corresponding to the first fifth of the model after the entrance, the second fifth etc. up to the final exit box. The goal is to probe the evolution of bubble size throughout the model. The binarized bubble areas are measured. Each area is then associated to an equivalent radius, through circular approximation. The measured bubble radii for 20 different images is then represented in a weighted histogram of 70 equally spaced bins from 0 to a value at which bubble detection becomes negligible. The value in each histogram bin is then multiplied by the center value of the bin, producing a weighted histogram that shows the area occupied by each bubble radius, rather than a simple number count. Through this approach, the histogram then can be associated with a probability density of finding a given bubble size when choosing a location at random in the porous space. We display the produced bubble size distributions in Figure 2-5.

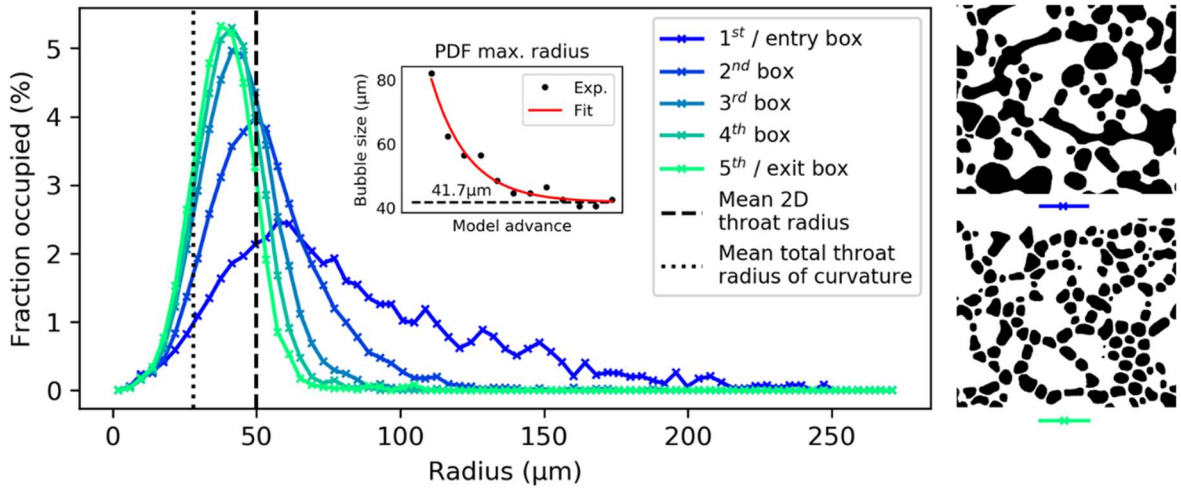

Figure 2-5: Bubble size distributions for different transversal sections of the model. A small example of the processed bubble images is included for the sections closest to the entrance and exit. The maxima of the PDF distribution for 12 section of the model is shown in a nested plot.

The weighted histograms for bubbles contained in each box are shown in a different color on Figure 2-5 ranging from blue (entrance of the model) to green (exit of the model). We display the average 2D throat radius (as shown in Figure 2-2) as well the average total throat radius of curvature, given by $2\left(\frac{1}{r_t}+\frac{1}{r_d}\right)^{-1}$, where r_t is the throat radius and r_d is the radius associated to the model depth, or 20 μm. We observe an evolution in bubble size from large bubbles at the entrance to a smaller, spiked distribution at the end section. The evolution occurs mainly over the first two sections after which the distribution seems to evolve only marginally. Furthermore, the end distribution appears to be symmetrical, with no presence of a right-hand side tail that would account for larger bubbles. We nest a small plot inside Figure 2-5 showing the evolution of the PDF maxima for different transversal sections of the model (12 sections are used for this figure). The PDF maxima were fitted to an exponential decay function tending to a value of 41.7 μm, which is attained by the model distribution in the last third of the model. We therefore expect that a longer model would further increase the monodispersity of the bubbles, due to diffusion processes that occur on a slower timescale than bubble fragmentation observed here, but that the mean bubble size remain around 41.7 μm. Intuitively, the average throat size (as shown in Figure 2-5), or the average total throat radius of curvature, could be seen as the limiting dimensions in the system, expecting the peak of the bubble distributions to be situated on either of them. However, the peak of the final bubble distribution is situated in between both averages. Due to the neighbor-

induced nature of the bubble creation mechanism, the injection rate plays a part in the distance required to reach a stable bubble size distribution. A higher injection rate might leave less time for a trailing part of a bubble to deform around a bifurcation, before a downstream will break it up; therefore, failed divisions, such as observed in Figure 2-4, would become rarer. Elsewhere (Géraud et al. 2017), bubble fragmentation dynamics have been generalized elegantly showing that the for a given model, the normalized bubble size fragmentation dynamic is conserved for different flow rates, injected average bubble sizes and gas fractions. However, the generalized model was established from gathering fragmentation statistics at cylindrical grain sites of the same size and are perhaps not applicable here.

2.4.3 Comparison of velocity maps

We show in Figure 2-6a the overall measured velocity map for the foam experiment, for all the bubble tracks over the 8 datasets of 200 images, as described in Appendix 2-B. While this flowmap may represent average flow in the model, significant flow intermittency and intensity fluctuations were observed but not studied here. The map shows both the velocity field, given in detail by the color-bar of Figure 2-8, and solid elements of the model in dark grey. Looking at the map globally, we note a large number of similarities with the Newtonian flow simulations displayed in Figure 2-6d and Figure 2-6e. We also display the velocity map for the 20% smallest (Figure 2-6b) and 20% largest (Figure 2-6c) bubbles, explored in greater detail in the discussion section. The presence of a velocity intensity gradient is due to the lower number of bubble counts at the entrance of the model, where foam bubbles are larger on average, leading to a lower number of contributions to the flowmap. While the colormap describes the velocity of pores, there is a significant gradient over the model due to the evolving number of bubble counts. Therefore, the signal shown can be thought of as relative velocity intensity. More on the velocity gradient and details on flowmap creation can be found in Appendix 2-E. This difficulty is inherent to flowmap creation from bubble (or any particle) tracks of evolving number density. One notable difference is the flow distribution of smaller bubbles close to the inlet in Figure 2-6b in which we note fewer paths used by the foam. We assimilate this to an area characterized by strong bubble size adaption, and less transport of a stable bubble size. For the overall velocity map (Figure 2-6a) we observe a large number of passages in use. On top of this, the flow seems to be well distributed throughout each section of the model, similarly to the Newtonian simulation. In Figure 2-7a and Figure 2-7b, we observe that

this is also quantitatively true through the use of characterization tools described in Appendix 2-B.

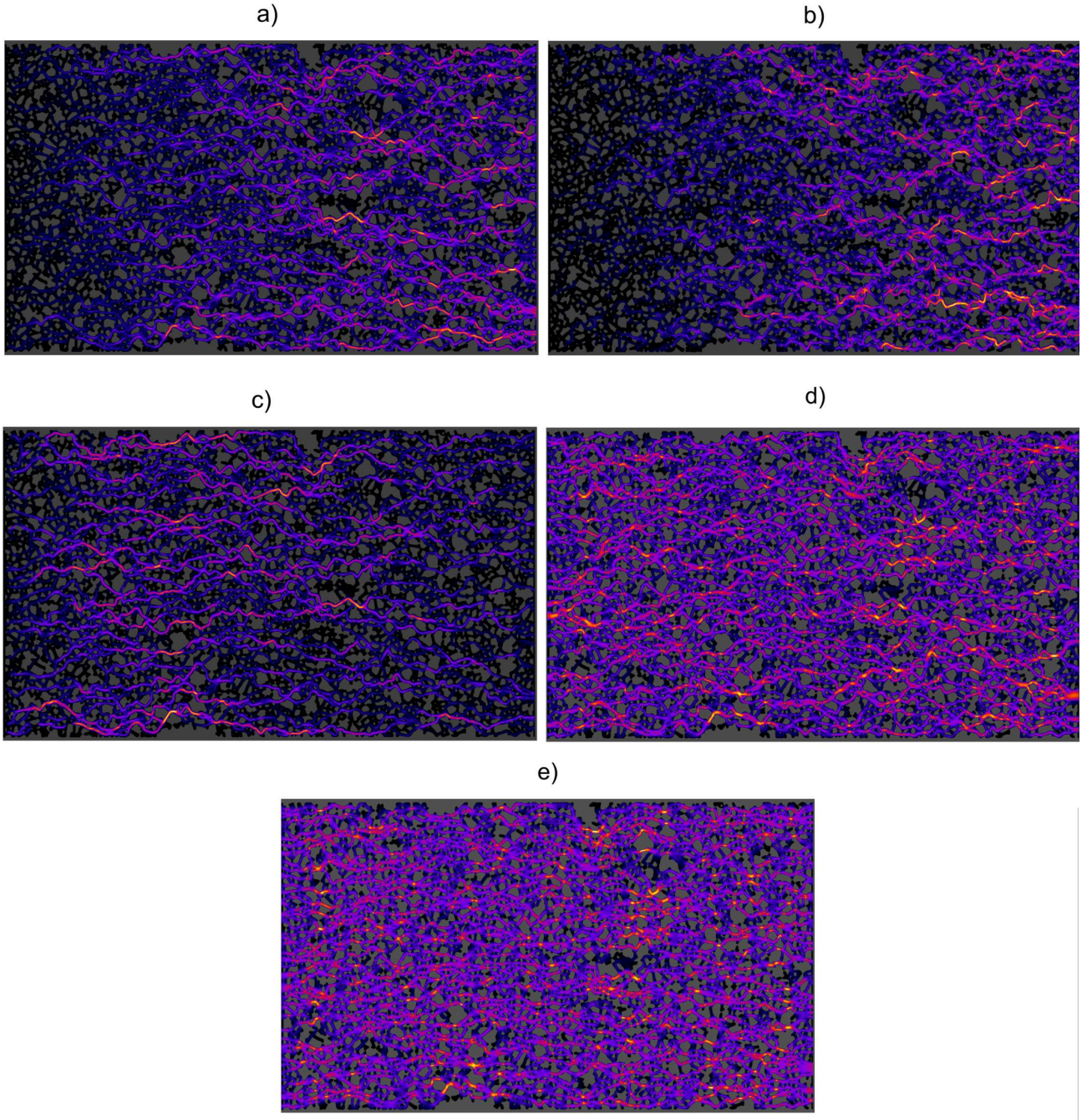

Figure 2-6: Different velocity maps using the same model. Injections are from left to right. a) Foam flow, all bubble sizes. b) Foam flow, smallest 20% of bubbles. c) Foam flow, largest 20% of bubbles. d) 2D Numerical Newtonian flow. e) 3D Numerical Newtonian flow.

This global similarity is confirmed by the breakdown of the flowmaps into the velocity components parallel and perpendicular to pressure gradient. We produce velocity maps for each component in each case (not shown here) and sum the absolute value of the image intensity of the entire image to compare values. The flow decomposition in X (parallel to pressure gradient) and Y (perpendicular to pressure gradient) directions are comparable in all cases, as shown in Figure 2-7c.

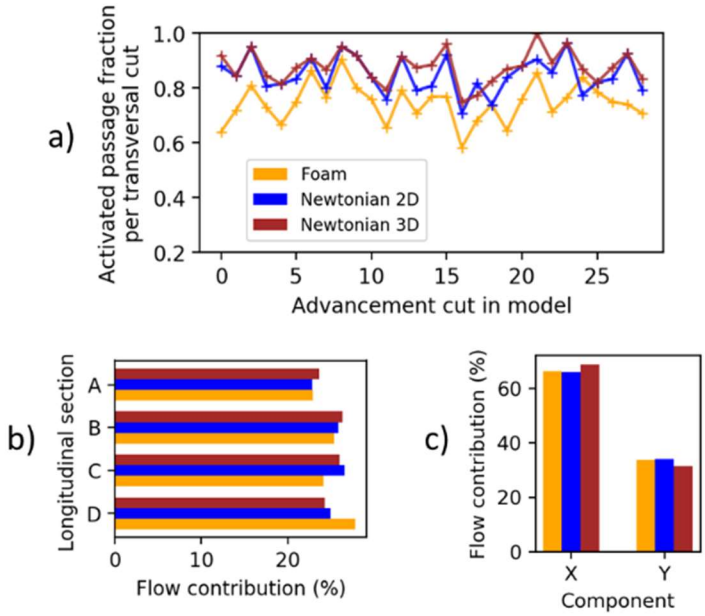

Figure 2-7: Quantitative comparison of numerical Newtonian flow and measured foam flow.

At the pore-scale, further common characteristics are observed. Preferential paths - appearing in bright colors - emerge in both cases. These paths are aligned in the direction of the pressure gradient directed here from left to right. The Figure 2-8 illustrates the three flow situations on a local scale.

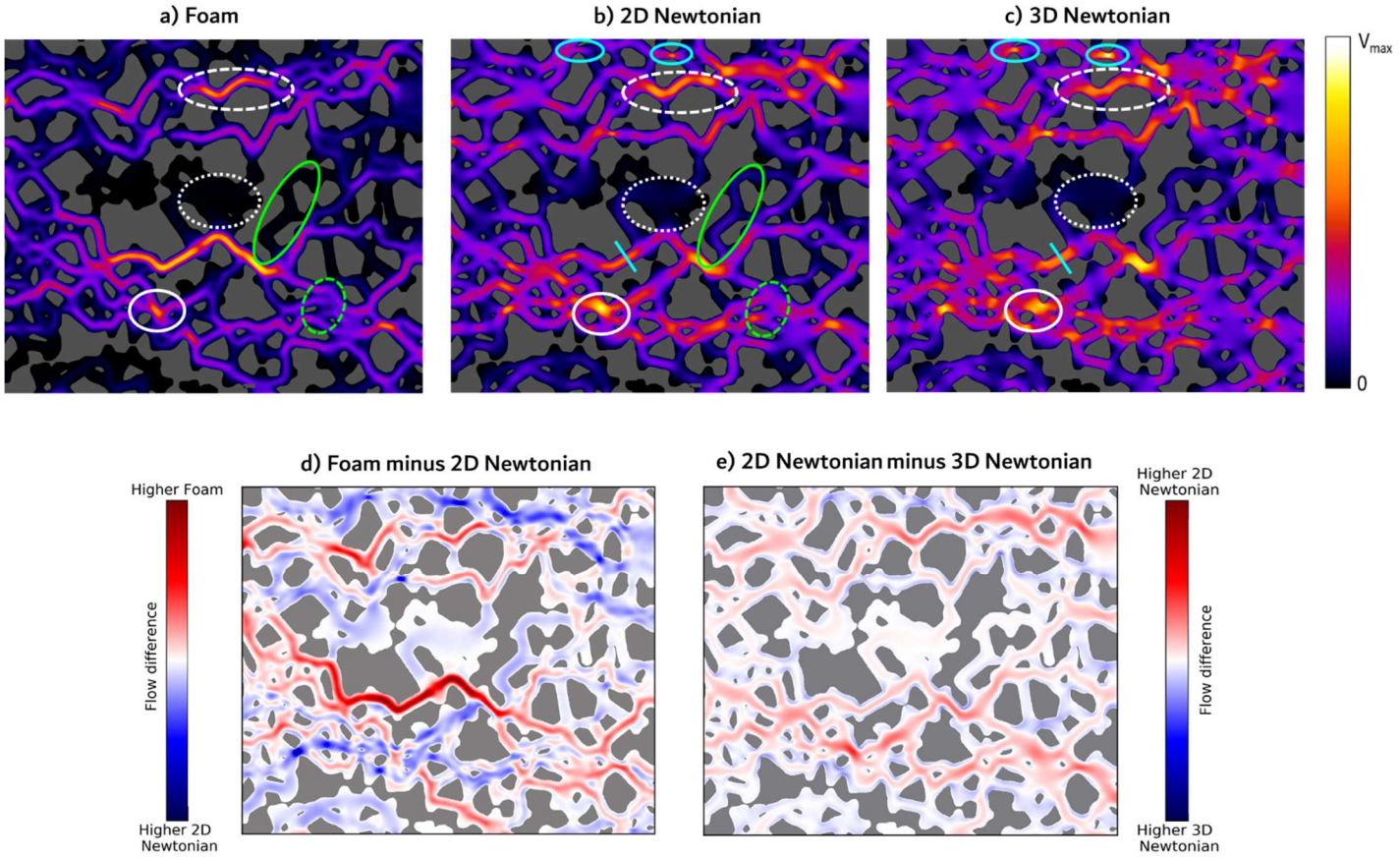

Figure 2-8: The top row shows local foam (a), 2D numerical (b) and 3D numerical (c) flow, denoted with a series of similarities and notable differences described in detail below. White markers show similarity between all images while colored markers denote differences between flow situations (bright green for foam vs. 2D Newtonian, bright blue for 2D vs. 3D Newtonian). The mean bubble speed is 1.26 mm/s. The bottom row shows relative differences between foam and 2D Newtonian flow (d) and between 2D and 3D Newtonian flow (e). Flow is from left to right. The color scale of top row images is normalized individually to cover the full range of values in each image. In the bottom row images, the color scale is set largest range of both images, i.e. image d), to show the smaller difference in flow between the two Newtonian cases (e). The lower row color scale is symmetric around the zero value (white).

We first compare foam versus both 2D and 3D Newtonian flows taken as a whole. The presence of zones devoid or low in flow, visible by the absence of color (thinly dashed white oval), exist in both measured foam flow and both simulated Newtonian Stokes flow. In the foam experiments these zones are filled with trapped bubbles. We similarly observe in all cases path junctions comprising large amounts of flow (solid white oval). Also, longer paths with conserved flow are visible that span multiple network bifurcations (thickly dashed white oval).

However, the microscopic differences in the comparison we give here are not negligible. Overall, a larger degree of flow heterogeneity appears in the experimental image versus the Newtonian cases, shown by the higher contrasting colors. While the flow is non-existent in the dead zones in

the foam experiment, the Newtonian flow cases do show a residual amount of flow in the central marked zone, more clearly visible in image Figure 2-8d. Some passages that turn away from the flow direction (full green ovals) are completely inactive in the foam experiment but show considerable flow in the Newtonian cases. Also, foam flow in larger pores is sometimes represented by more than one trail (dashed green ovals), as opposed to the diffused continuous flow in the Newtonian experiment. This is due to the fact that multiple bubbles flow simultaneously into the larger pores, originating from smaller upstream passages.

Comparison between 2D and 3D Newtonian flow show that the 2D flow is more heterogeneous as flow in higher in certain larger paths shown in red in Figure 2-8e. The 3D flow accesses paths with small throats (bright blue ovals) more consistently. Finally, the distribution of flow within the cross section of a given path that is more evenly distributed in the 3D case (bright blue line), visible by the alternating blue-white-red-white-blue colors in the section seen in Figure 2-8e. The higher flow homogeneity in the 3D Newtonian case is a confirmation of the higher path activation and more balanced flow contribution of the 3D flow as seen in Figure 2-7a and Figure 2-7b.

We explain the larger 3D Newtonian flow homogeneity as an effect of the added non-slip condition imposed on the top and bottom of the model that is non-existent in the 2D case. In the 2D case the Poiseuille flow is only divided at bifurcations relative to 2D throat size of each downstream path, whereas for the 3D simulation, the model depth also contributes the equivalent capillary radius and reduces the flow-impeding property of smaller throats.

In regard to the foam flow, it is important to note that the non-overlapping bubbles travel with interfaces that have one component of radii of curvature fixed by the model depth, given that the vast majority of bubbles have an equivalent diameter larger than model depth. As foam transport through a given throat requires exceeding (for a liquid-filled throat) a pressure gradient of the order of the Laplace entry pressure associated with the throat (Rossen 1990a), it is reasonable to compare foam flow in the micromodel with a 2D Newtonian flow simulation, as shown by the greater similarity of flowmaps obtained in this study.

2.5 Discussion

2.5.1 Bubble velocity and size relationship

It has been previously established (Géraud et al. 2016) that a strong positive correlation exists between bubble size and bubble velocity for foam flow in a 2D analog porous network, specifically for high-gas fraction injections. Our data follows this trend. Figure 2-9 displays density plots of bubble speeds in terms of the bubble sizes, for the full model, entrance box and exit box, as described above.

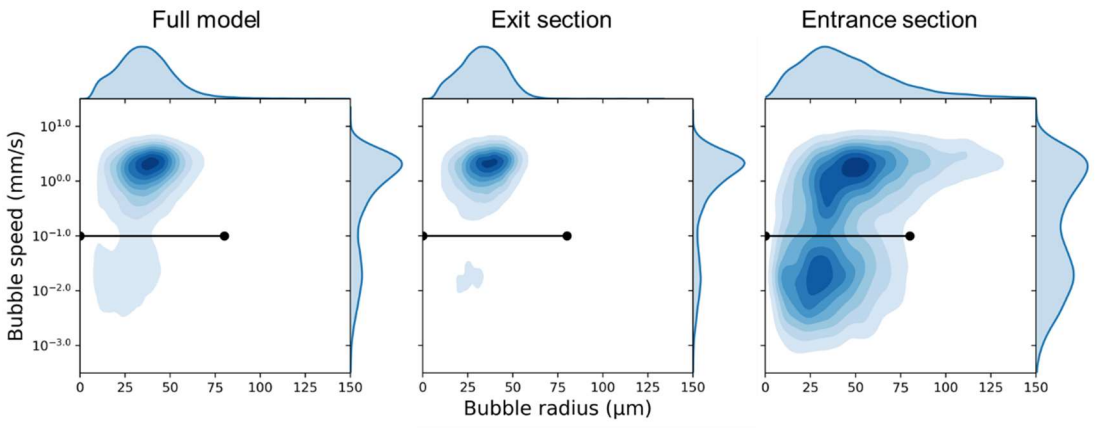

Figure 2-9: Density plots of bubble speeds and bubble radii in different sections of the model. We observe two distinct populations corresponding to trapped bubbles (lower population) and flowing bubbles (higher population). The density map on the left is created with 82623 individual points, each representing a bubble track (50 frames minimum), the central plot is made with 8664 and the plot to the right with 20406 points, demonstrating the unequal number of bubbles in each section. The speed is given by the Euclidean distance of the bubble from the final to initial frame, divided by the bubble track duration. The radius is the average radius over the bubble track.

In the full model density plot (Figure 2-9, left), the main cluster of points shows a weakly positive relationship between bubble size and radius. However, a second, distinct cluster of small, low-speed bubbles exists in the lower left corner of the plot. These points are trapped bubbles. When examining similar plots for each transversal section of the model we observe that the trapped fraction of bubbles are represented more clearly in the entrance of the model (Figure 2-9, right), whereas flowing bubbles appear more clearly at the end. To differentiate between both populations, we divide the plot using a visually chosen line showed in black. As the density plots display the relative distribution of points and not absolute numbers, to complement these observations, we display in Figure 2-10 the number of points contained in each side of the black line, for each transversal box of the model, following the progression of the flow.

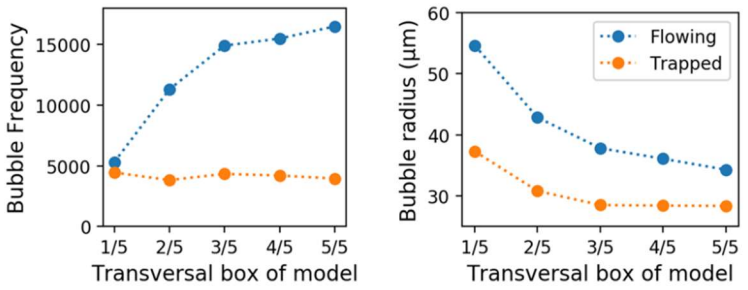

Figure 2-10: Frequency of bubbles and average radius in each bubble population for each transversal box of the model. Note that here the average bubble size is calculated simply over all bubbles. The discrepancy between the peak of Figure 2-5 which displays a weighted histogram, rather than a number frequency histogram) and the average value show here is well understood.

Figure 2-10 shows that while the number of flowing bubbles tends to increase as large bubbles divide up as they pass through the model (18000 at the end vs. 5000 at the beginning), the number of trapped bubbles remains relatively constant in each part of the model Also, we see that the average bubble size in the flowing foam evolves all the way through the model whereas the trapped foam size is relatively constant after the second section. The total trapped fraction (total area of trapped bubbles) is reduced towards the end of the model (not shown here). These opposing behaviors reaffirm the distinctiveness of the two populations. The implications of these observations are significant. The number of trapped bubbles is constant throughout the length of the model, despite the overall bubble fragmentation occurring in the direction of flow. While the observation of inference of a trapped foam is shown elsewhere (Jones et al. 2018b; Nguyen et al. 2002; Nguyen et al. 2009), local evaluation of the trapped foam population and its independence to the surrounding flowing foam size distribution is yet to be observed. We believe the trapped foams seen here will not contribute greatly to the macroscopic steady-state flow properties (small contribution to the apparent viscosity) as they are situated in hard-to-access zones. However, as they can enclose oil in pseudo-emulsion films between the oil-gas interfaces (Bergeron et al. 1993), and deplete surfactant, the small trapped foams should be considered for simulation of foam flow.

We further propose a causal link between the trapped bubble sizes and velocities. We observe multiple mechanisms that contribute to the population of trapped zones by small bubbles. First, we note that the smaller bubbles are more likely to move off the preferential tracks into low-flow areas. The image panels in Figure 2-11 demonstrate our argument, in which we show this mechanism repeating itself twice in the same location in a time frame of 330 ms, or a single dataset of 200 images. In these images, we overlay flow lines on images of bubbles (shown in color),

whilst the solid obstacles are shown in gray. Flow line thickness shows flow intensity. Flow lines were calculated using quantitative data from the combined datasets. We see that two smaller bubbles, shown in red, move into a low-flow zone at the bottom of the image, characterized by an absence of measured flow lines. We observe that larger bubbles, shown in green, feel contained by other bubbles dragging and pushing them to keep to the main flow paths. Indeed, as they cover a larger area, they are more likely to intersect a high flow path, despite part of their interface exploring a low-flow zone. Inversely, once smaller bubbles explore low-flow regions, they can be rapidly locked out. Combined with the fact that their displacement into low-flow zones requires less displacement of static fluids, their chances of successfully entering and staying in the low-flow areas are increased.

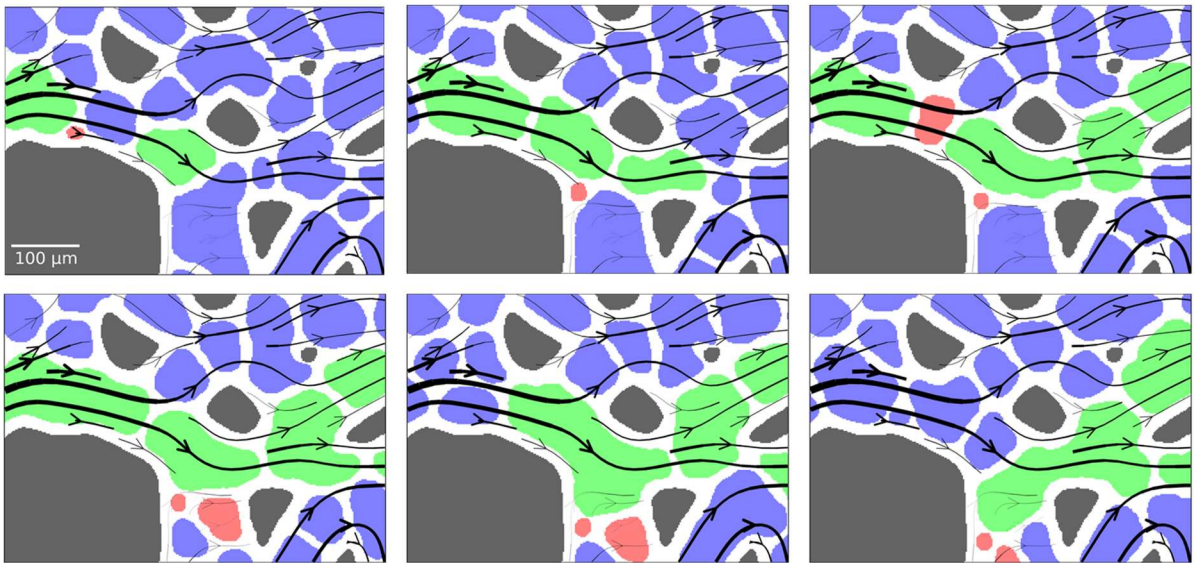

Figure 2-11: Small bubble trapping mechanism. Flow lines are calculated from the combined datasets. Smaller bubbles trapping is shown in red, whilst larger bubbles keeping to the main path are shown in green. Solid obstacles are shown in gray. The time between each panel is 66 ms.

Secondly, we also observe a large amount of trapped bubbles in pore corners and dead-end pores. Examples of both are given in Figure 2-12, in which we show image averages for two locations for a dataset of 200 images. The black isolated bubbles show that they are not displaced during the entirety of the dataset, whilst gray values in the flowing areas show a succession of distinct bubbles.

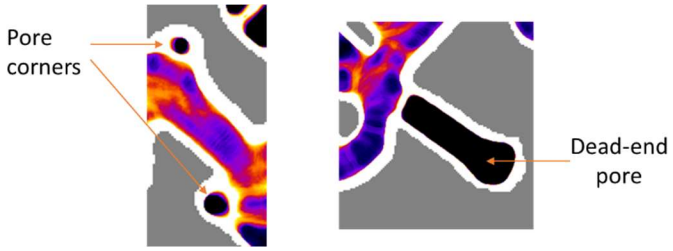

Figure 2-12: Trapped bubbles in pore corners and dead-end pores. An image set of 200 images is averaged to show flowing areas in color, porous void in white and immobile bubble areas in black. The solid obstacles are shown in gray.

Indeed, while low-flow zones, as described above, are structurally connected to the rest of the network in at least two ways: pore corners and dead-end pores have only one outside connection. As bubbles in these areas tend to trap and rarely displace, observation of their specific trapping mechanism is not evident as datasets are acquired in a steady state pressure gradient when flow distribution is well established. However, we argue that for the case of dead-end pores, the trapping mechanism is the creation mechanism described previously, where part of a larger bubble is ripped off *in situ* and occupies the dead end. Indeed, these bubbles fill the dead-end pores entirely and seem to have been tailored for the pores precisely. A few large, trapped bubbles have hence been observed in some larger dead-end pores. Oppositely, trapped corner pore bubbles tend to be a lot smaller and can be created elsewhere in the network that have found a stable position where they are unaffected by flow. In fact, the possibility of creating a pore corner bubble *in situ* seems unlikely as the network does not offer a sufficiently deep bifurcation for larger bubbles to invade and get broken apart by trailing bubbles. The number of smaller, corner pore bubbles greatly outweighs the larger dead-end pore bubbles.

Obviously, it can be difficult to differentiate between qualifying some areas as a pore corner or a dead-end pore, but the distinction is worthy as we believe these areas become populated with trapped bubbles in different ways.

2.5.2 *Preferential path flow for larger bubbles*

Here we take a closer look at Figure 2-6 in which are displayed velocity maps for different bubble size populations. The most striking observation is the differences in velocity intensity gradients appearing over the model in the flow direction. In reality, this simply translates the different amounts of measurement points contributing to the 2D histogram and is another manifestation of the bubble size adaptation. This explains the stronger strength of the intensity gradient for the

smallest 20% image (Figure 2-6b), as this bubble size is inexistent at the entrance of the model, but prevalent near the exit. Inversely, the larger bubbles are seen most at the entrance. The second observation is the difference in flow patterns between the largest (Figure 2-6c) and smallest (Figure 2-6b), bubble sizes. Broadly speaking, the larger bubbles take paths more parallel to the pressure gradient and are present in less paths overall. Also, for larger bubbles, the notion of large-scale path seems to be more significant: in other words, flow intensity is conserved over a single path that can span many pores and throats, and not diffused out into every possible downstream avenue. The smaller bubble flow (Figure 2-6b) is also present in preferential paths as small bubbles are carried along with larger bubbles, but also is visible in many zones unused by the largest bubbles. These paths are often perpendicular to the pressure gradient and are accessed by smaller bubbles through the mechanism displayed in Figure 2-11. The contribution of each component (longitudinal, Vx and transversal, Vy) of the velocity maps for each bubble size category is shown in Figure 2-13.

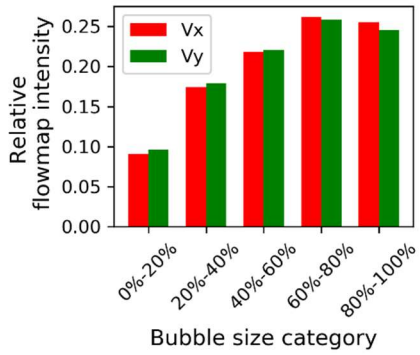

Figure 2-13: Contribution of longitudinal (Vx) and transversal (Vy) velocity components for each bubble size category for the experimental foam data. Note that the overall magnitude of the sum of each component has been normalized for clarity; overall comparison of magnitude of each component is shown in 2-7c.

The flowmap intensities shown here are given by the sum of pixel values for each map, as individual maps were obtained as described for the comparison of Figure 2-7. The values are then normalized for each component. We remark that an increased amount of flow is carried by the larger bubbles (60-80% and 80-100%).

Finally, we note that each velocity component makes a similar relative contribution for each bubble size. This is a surprising result. Indeed, from inspection of the velocity maps of different bubble sizes, the largest bubbles travel in straighter paths aligned with pressure gradient (Figure 2-6c),

while smallest bubbles travel in both preferential and transverse areas (Figure 2-6b). We would therefore expect to see the X-component of largest bubbles contribute more to the overall velocity than of the smallest 20%. This result demonstrates that large-scale preferential paths are not chosen on a basis of immediate local preference for pores in parallel to flow (which would imply a higher relative longitudinal velocity contribution) but instead a more global idea of path shortness or straightness in which flow is not restrained to the longitudinal component. Specifically, we predict that the preferential flow paths are created via a tradeoff of ease-of-flow (through large throats or pores) and shortness of the overall path length. We further explore the idea of global paths in the following section of our discussion.

2.5.3 Local structural relationships

Finally, the relationship between measured velocity and basic structural parameters of the porous medium was explored. Géraud et al. (2016) find a positive correlation between the average velocity and the pore size in the medium. Regarding preferential paths, they suggest "that most preferential paths occur where a series of large pores are connected together". Through this statement they include a notion of both network properties and local pore size. Subsequently, they offer a link between structural elements and trapped foam areas via "bubbles trapped in regions of low flow velocity in-between closely set grains". However due to the cylindrical nature of their grains and the correlation between pore and throat size in their geometrical arrangement, it is unclear whether observed trapped zones are primarily related to a small pore size or small throat entrance.

To investigate these relationships for our data we must first apply some additional steps to our experimental image, as it shows a significant intensity gradient due to bubble size evolution. We refer the reader to Appendix 2-C for further detail regarding overall intensity uniformization procedure. This procedure allows a comparison of structural elements from all transversal sections despite relative measured intensity evolution.

For our structural decomposition in terms of pores and throats we use the same watershedded image as described in Figure 2-2. To achieve a comparable intensity value for each structural element of the medium (pore or throat), we calculate an average intensity value per element.

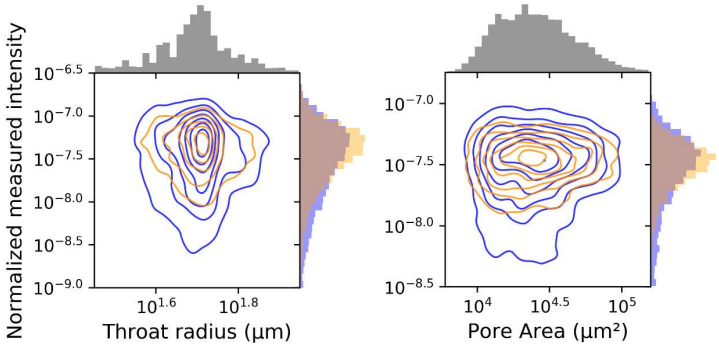

Figure 2-14: Normalized per pixel intensities for throats and pores in the numerical 2D Newtonian flow (orange) and the experimental foam flow (blue) shown as density contours.

We show in Figure 2-14 contour maps comparing the observed average velocity intensities in each pore and throat for both flowmaps (2D Newtonian and experimental foam), along with the histograms on the opposing side of the plot of both the structural parameters and the average measured intensities. For clarity, we show the experimental and only 2D Newtonian case here. The 3D Newtonian case was also explored but contour plots were found to be very similar to the 2D case, if perhaps slightly less dispersed. The pore and throat contour maps were created with around 3500 and 6000 points respectively, as some outliers are excluded for plotting purposes. For each color, 7 distinct contour lines are plotted. In both throat and pore comparisons, we see similar behavior for both flow situations; there does not seem to be any clear correlation between average intensity values and the pore or throat size, showing a symmetrical distribution around the average pore and throat size. However, the foam contours span a larger range of measured intensities for both throats and pores. This indicates a more heterogeneous foam flow, confirming our previous observations; the lower contours of the foam experiment (reaching much smaller values of intensity) can be in part explained by the presence of dead zones in the foam flow (cf. Figure 2-8, areas that display little or no flow).

Pore or throat size, does not, on average, correlate with flow properties. Although some weak trends may appear, the data dispersion is too high to show a solid relationship. Further investigation of more complex local structural parameters, including parameters derived from the previous suggestions (Géraud et al. 2016) regarding the preferential paths and trapped zones, can be found in Appendix 2-D. The conclusions are identical to those above, notably a lack of overarching correlation between local structural properties related to pore and throat sizes and flow properties.

Our explanation for the lack of correlation between local structural properties and foam flow intensity is the higher network complexity of our model, i.e. the larger number of components that make up its length. We show that in networks with a high number of structural elements and possible paths, local relationships are inadequate for foam flow prediction. While this has been shown for simpler geometries and at a larger scale (Géraud et al. 2016), we provide confirmation on a smaller complex model, in which firstly both a larger variety of (potentially discriminating) structural element values may exist, and secondly, in which the balance of forces on the reduced scale resembles more closely real porous media. Indeed, the possibility of flow in a given element is a function of the upstream and downstream elements that surround it. A large pore with a dead-end path downstream will not contain any flow, just as no flow will access a hard to reach pore from upstream. The higher the network length, the higher the probability that flow may be impeded by a structural element some distance away. In this sense, only through a model with a length and complexity as the one shown here does this distinctive path-dependent behavior become evident. In this regard, we explore the dependence on the pore coordination number, which is given by the number of first neighbors each pore possesses. We display the results in the form of a boxplot in Figure 2-15.

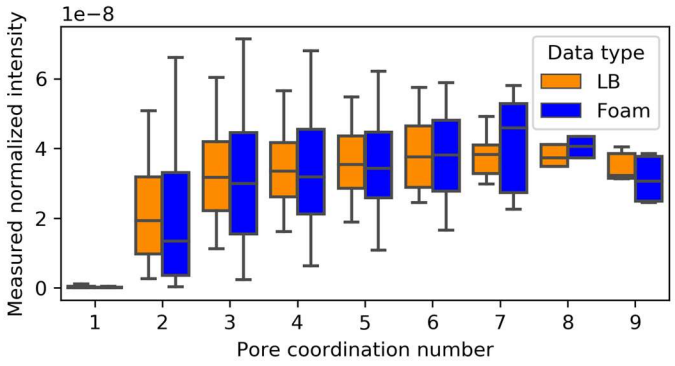

Figure 2-15: Measured per pixel intensity for pores with varying pore coordination numbers, for both numerical 2D Lattice Boltzmann (LB) and foam experiments.

For each box of the plot, the median is shown as a black bar in the middle of the box, separating the data in half; the edges of the box represent the upper and lower quartiles of the data, and the end of the whiskers show the extent of the other data points, excluding the upper and lower outliers, or 5% of the data on each extreme. Again, the experimental data shows a larger distribution of intensity values for each pore coordination value. Both cases show zero flow for pores with a coordination value of 1, or dead-end pores. However, it's worth noting that the median for the

foam experiment rises faster than the Newtonian counterpart, owing to a larger dependence on pore coordination in the case of foam. This implies that for a realistic microscopic prediction of foam flow in a complex porous medium, pore coordination must be considered to a larger degree than in a Newtonian flow situation, and significantly, flow prediction in a complex medium must necessarily integrate network elements such as coordination rather than focusing on local properties of size.

2.6 **Conclusion and perspectives**

Through this study we assess high-velocity, high-liquid fraction foam flow behavior in relation to a Newtonian viscous flow comparison. We gain access and interpret high-resolution unseen data at this scale for foam studies. Overall, we find a large degree of similarities in our global and local comparison of data in both foam and Newtonian situations, including comparable overall passage activation, flow distribution and component-specific velocity distributions. Despite this similarity, the foam flow displays a more heterogeneous array of flow situations. Specifically, elements that were observed and analyzed only in the foam case include trapped foams and long-range preferential paths. While in our model, localized zones of high-intensity flow can be observed in the Newtonian case, the foam preferential paths remain at high intensity and travel in distinct channels for longer distances. An even stronger example is shown in (Géraud et al. 2016), in which the preferential paths sometimes span the entire length of the model and only intersect once or twice with other preferential paths. Notably, we deepen the link between trapped foams and bubble sizes, showing a distinct population of immobile small bubbles exists throughout the model, displaying independence to the surrounding bubble size distribution and to the location in the model. We also observe the existence of high velocity preferential paths, serving as the unique transporting zones for large bubbles, whereas smaller bubbles can either be transported in preferential paths along with the larger bubbles, or in either hard-to-access paths or paths perpendicular to the pressure gradient. Finally, we pursue a naïve attempt of flow prediction in terms of local parameters. From this analysis we conclude that local structure only weakly predicts flow properties and that to fully grasp the notion of preferential paths and trapped areas from a structural point of view, it is essential to integrate notions related to network properties into the prediction process.

However, the results shown here may be somewhat limited to 2D systems in which coordination is lower, leading to larger network-scale behaviors to be more prominent due to the limited diversity of possible flow paths. It is also unclear how these conclusions can be generalized to systems of lower permeability, or 3D networks in which other creation mechanisms can be observed.

Foam transport in porous media has been observed to adopt contrasted situations ranging from trapped immobile bubbles to high-velocity preferential paths. As by definition it is impossible to locally determine the belonging of a pore to a long-range preferential path, we suggest that predicting flow in a given pore necessitates at least some upscaling to the network level to rank possible paths based on ease of flow, and then downscaling back to the pore level to estimate its prevalence within the best paths. Furthermore, we can imagine that a characterization of the preferential paths is a prerequisite for linking porous microstructure to macroscopic properties in foam flow such as apparent viscosity.

Appendix 2-A: Image processing workflow

The following processing procedure is designed to maximize the contrast between the gas bubbles and the liquid-gas interfaces that separates them before binarization. All scripts were written in ImageJ macro language.

The first step is the subtraction of the image of the clear model from the foam image. Subtraction of the initial saturated model therefore creates more uniformity for the gas-liquid interfaces we are interested in. Removal of the solid-liquid interface also ensures that liquid-filled spaces bordering the grains are eliminated. The only remaining contrasting elements are the gas-liquid interfaces. Subtraction of the liquid filled model also serves to erase any illumination heterogeneity that may be created by the backlight system. This step is illustrated in Figure 2-16.

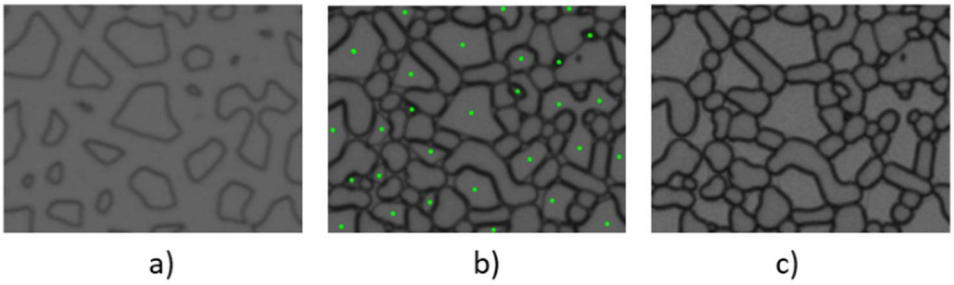

Figure 2-16: Background removal process. a) The initial brine-saturated model. b) The model with foam before the subtraction, grains marked with green dots. c) The result of the subtraction of a) from b), removing all solid interfaces and homogenizing gas-liquid interface gray value.

We then locally increase contrast through the use of the built-in ImageJ function Enhance Local Contrast (CLAHE) (Zuiderveld 1994).After thresholding the contrasted image, the next step of the process is isolating bubbles from the grains. For the solid grain removal, we make use of the liquid-filled image in A-1a on which we apply the default threshold. The resulting binary image of solid-liquid interfaces is then filled. We use the "Ultimate Points" process to return an image with the location of the Ultimate eroded points, representing the centers of particles that would be separated by a local-minima based segmentation. We then filter out the unwanted objects using the Morpholibj plugin (Legland et al. 2016) that allows morphological reconstruction of a binary image from a series of "seeds", given by the Ultimate points. The reconstructed grains and their contours are subsequently removed from the thresholded foam image to leave only the foam bubbles. Figure 2-17 shows this process in detail.

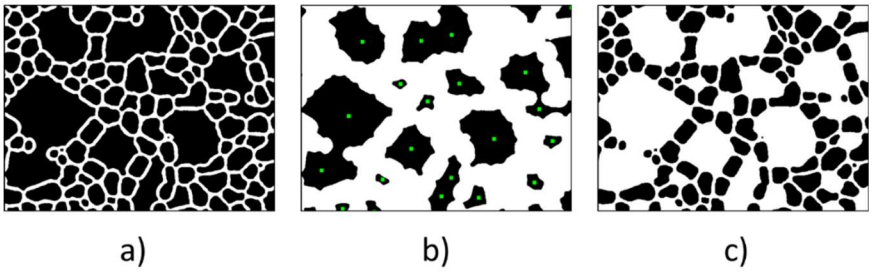

Figure 2-17: Image processing steps showing the removal of unwanted grain objects from an initial binarized image. The initial image is shown left. Grain objects are identified using Ultimate points (shown as green points) from a binarized image of the model and are reconstructed in the original image using morphological reconstruction (center). The unwanted objects are subtracted from the initial image (right).

For the dynamic tracking, we use a plugin originally designed for tracking binarized images of C. elegans nematodes (Nussbaum-Krammer et al. 2015) to track the bubbles through the successive frames, obtaining precise paths and velocities amongst other observations. The bubble tracking

method works in a simple manner, following each object frame-by-frame by evaluating the closest positioned and similarly sized bubble in a successive frame. When multiple candidate objects are equally viable in a successive frame, the algorithm puts a flag on the potential object and works on retrieving other surrounding bubbles first, in hopes of eliminating ambiguity when the flagged object is re-evaluated. Despite its simplicity, the algorithm works surprisingly well and is reasonably fast considering the large amount of densely packed objects in each frame (around 20 minutes for more than 10 000 bubbles). The accuracy of the method owes to the high frequency acquisition. The small bubble displacement between each frame generates low ambiguity in bubble identification. However, the algorithm requires the input of a few parameters. These parameters serve as a means to narrow down potential candidates in the neighbor-evaluating process. The first parameter is the maximum tolerated bubble area change. This value was fixed at 50%, both to allow for bubble compression and bubble subdivision with flow. In the case of a bubble division, the smaller broken off bubble is considered as a new object with its own distinct track and the larger parent is retained in the original track. Multiple subdivisions of an initial bubble in the same dataset are rare. The second parameter is the minimum number of successive frames in which a bubble needs present. This parameter was fixed at 50 frames. The last tunable parameter in the tracking process is the maximal allowed displacement per bubble in between frames. This value was chosen from inspection of the frame-by-frame bubble displacement histogram created by initially letting this parameter take an unphysically large value. When doing this, the algorithm returns a negligible number of bubble displacement measurements all the way up until the unphysical limiting value. Upon examination, displacements at this speed are erroneous and correspond to jumps between bubbles. The choice of the final parameter value is then chosen in accordance with the displacement histogram as approximately the moment when the bubble velocity counts become negligible.

Appendix 2-B: Quantitative flowmap analysis tools

Passage activation is studied via analysis of the measured signal intensity along transversal “cuts” perpendicular to the flow direction. We define a series of equally spaced cuts and look at how the flow is distributed throughout the cuts. We give here the quantitative process of discrimination between active and inactive passages, illustrated with images and results from the Lattice Boltzmann simulation result. The different cuts can be seen in image Figure 2-18. A connected 1D

line intersecting the porous area of the network along this cut is considered as a “passage”. A passage can be considered active or inactive as detailed below.

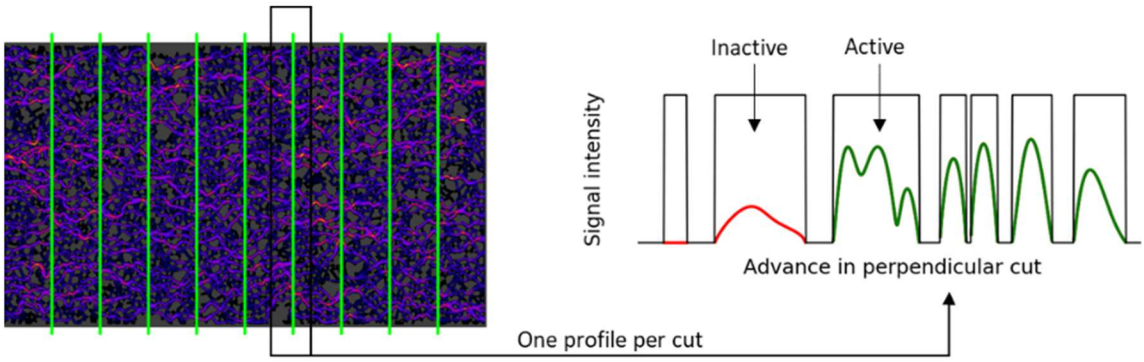

Figure 2-18: Transversal model cuts from the Lattice Boltzmann simulation and measured flow signal

For each cut, the total image velocity profile is normalized to 1, as an intensity gradient occurs across the model. In each passage the velocity intensity can be summed across all the pixels in the passage. The total 1D passage lengths and summed velocities are tallied up for all the passages in all the cuts. A histogram is created giving the average signal for each passage length. The binning on the passage lengths is done by taking 20 points that are equidistant in logarithmic space from the largest to the smallest passage, giving 19 bins. The average velocity sum per length bin serves as reference value. We observe a unimodal intensity distribution with a displacement to the right as the bin size window gets larger. The unimodal distribution indicates that there is no obvious intensity threshold to define an active/inactive passage. The method we choose is to simply take the half of the average value per bin as the cutoff value. As such, if the evaluated passage has a measured summed velocity intensity larger than half of the reference value for its corresponding length bin, it is considered active. After each measured velocity value is compared with the average value for the bin size, we can establish a passage activity ratio by dividing the number of active passages in a cut by the total number of passages in the same cut. We show in Figure 2-18 a sample of the observed velocity signal bounded by the passages and colorize them according to their activity. Through this method we achieve a measurement of overall measurement of passage activation, i.e. how well is the flow distributed transversally. We can also observe the evolution of passage activation in different cuts along the model.

A supplementary global indicator of flow is produced by summing measured image intensities for each longitudinal box of the model (cutting the length of the model into 4 parallel boxes). The

measured velocity signal is then summed over each box. This indicator shows longitudinal flow distribution and homogeneity. This process is shown in Figure 2-19.

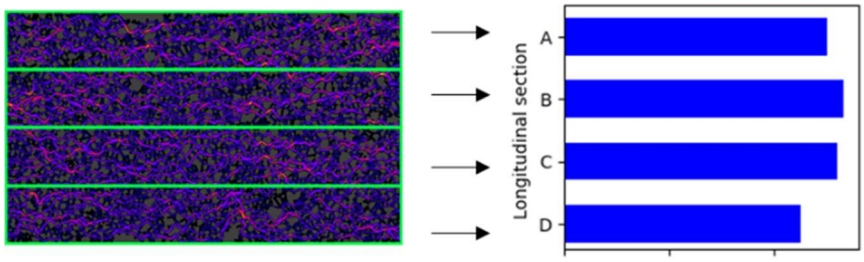

Figure 2-19: Box analysis principle, flow is integrated in each longitudinal box.

Appendix 2-C: Signal intensity uniformization

To overcome the gradient observed over the model due to bubble fragmentation and compare measured intensities of pores from different transversal sections we apply a multiplicative factor at each transversal column i of the $N_i \times N_j$ image that renders the relative intensity uniform. We explain this process here. First, the image is projected longitudinally across all the rows as to obtain a single projected intensity value P_i for each column (a $N_i \times 1$ sized vector). This vector is then smoothed to avoid overcorrecting for each local value rather than correcting for the global intensity trend. The factor F_i is calculated at each column by $F_i = \max(P)/P_i$. Then, each row of the column i is multiplied by the same value F_i such as, in terms of intensity per column: $I_{ifinal} = F_i \times I_{iinitial}$. In Figure 2-20 we show the value of F_i per column. The high number of image columns is due to the use of an upscaled image. This curve shows the difference in measured image intensity from the zone of maximal intensity measurement (the end of the model). Effectively, it gives another visualization of the bubble size evolution through the model, showing that the bubble size is relatively constant in the last third of the model, where a uniform intensity is measured.

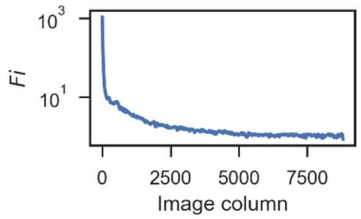

Figure 2-20: Multiplicative factor for each image column in the experimental image to obtain a comparable velocity intensity per local structural element over all transversal sections.

Appendix 2-D: Extended local structural investigation

We investigate parameters derived from the immediate neighborhood of the pores. The top row of Figure 2-21 shows contour plots of measured average intensities for each pore, against various properties of the given pore's neighborhood, such as the average, minimum and maximum pore sizes of the neighbors. In the second row, average pore intensities are shown against mean, minimal and maximal surrounding throat sizes.

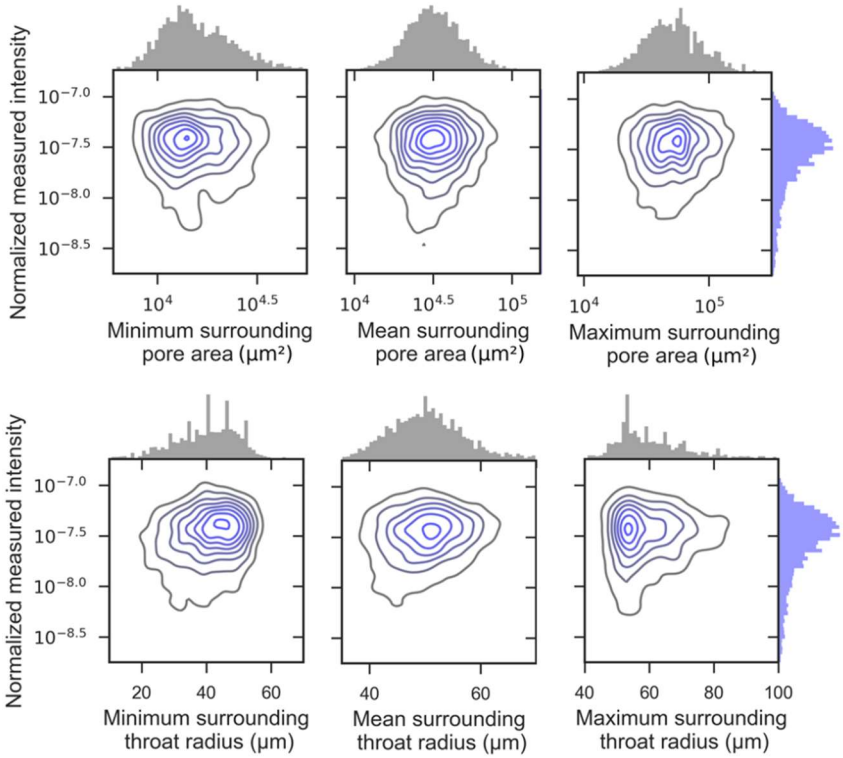

Figure 2-21: Searching for relationships between local structural properties and flow intensity

We explore some local and semi-local structural relationships previously suggested (Géraud et al. 2016) describing preferential paths as zones with "a series of large pores connected together". Using knowledge of the network neighborhood properties, for each pore, we create an algorithm to establish the largest possible average of connected pore sizes, with varying degree of neighbors n, centered on the pore we wish to evaluate. For example, if we take want to take one neighbor on each side of the pore, the algorithm will choose the two neighbors with the largest pore sizes, forming a chain of n = 3 pores. For two neighbors on each side of the pore, the algorithm returns the largest possible pore size mean of a chain of n = 5 connected pores (2 neighbors on each side

plus the central pore we evaluate). We show the results for n= 3,5,7 in Figure 2-22. We show that some although some positive correlation does exist, as demonstrated by the gradient of the linear fits shown as blue lines, no strong relationship was found to be evident.

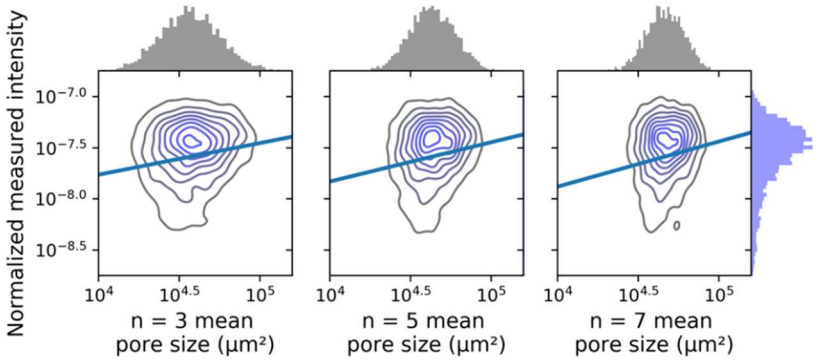

Figure 2-22: Flow intensity against local neighborhood average pore size for each largest chain of n pores centered in the evaluated pore. Despite the large data dispersion, we add a linear fit to the data to show a positive relationship.

Submitted article ends here

Appendix 2-E: Justification and details of flowmap creation

In this section, we provide a more detailed description of the process leading to the flowmap, clarifying the observation of intensity gradients over the model and justifying the choices involved in the map creation. Two aspects we shall describe in more detail are the averaging of the bubble tracks and the smoothing of the created flowmap.

From bubble tracks to local velocity maps

For each pixel represented in the flow map, we add up the velocities of the center of mass of all the bubbles passing the 2-by-2 bin represented in the original tracked data. Passage counts were measured to be from 0 up to 120. The overall measured velocity is then divided by the total time of acquisition. We assimilate this to a Eulerian description of flow. The velocity value of each bin is therefore sensitive to the number of counts as well as the velocity of each count.

For a flow of purely monodisperse bubbles the map produced would be exactly the velocity map. In our case of heterogeneous bubble flow, the interpretation of the map produced is more complicated. Larger bubbles, making up most of the population close to the entrance, are not slower but less counts are measured as their centers of mass are further apart, making the overall sum on the entrance lower relative to the high frequency of passages in the end of the model. For this reason, a large velocity density gradient is observed over the model.

One way to reduce the problem related to polydisperse bubble flow velocity measurement and the shown velocity gradient would be to divide the final velocity sum of each bin by the number of counts on the bin number. We would assimilate this to a Lagrangian description of flow.

To clarify, in the Eulerian description of flow, each final 2-by-2 bin velocity value v, is a sum of the individual bubble passages v_i, for a total acquisition time ΔT is given by $v = \frac{\sum_i^n v_i}{\Delta T}$. For the Lagrangian description of flow, for a total number of passages n in the 2-by-2 bin, the bin velocity value is given as $v = \frac{\sum_i^n v_i}{n}$. We show in Figure 2-23 the velocity intensity gradients over the total flow map.

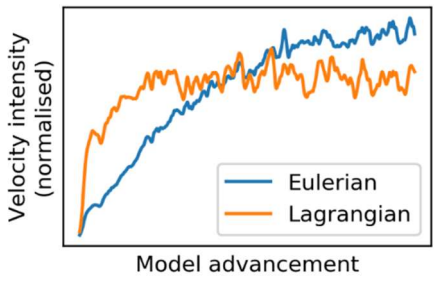

Figure 2-23: Velocity variation over the model for each velocity measurement method

While the Lagrangian technique does allow us to reduce somewhat the visible velocity intensity gradient over the flowmap, the issues created by the Lagrangian technique, that we shall discuss below, seem too important to overcome.

In the Lagrangian description, a single passage in a 2-by-2 bin of a given velocity is equivalent to several passages in a different 2-by-2 bin that have the same average. This obviously doesn't describe the reality of the flow as one-off events are indistinguishable on the flowmap from repeatedly occurring events. Two examples are given. The first is the case of the unique passage of a bubble difficultly squeezed through an otherwise unvisited, small throat, giving a large velocity value for that throat. Secondly, we can consider a large bubble deforming around an obstacle, in which the center of mass displacement would register a measurement on an otherwise unvisited area (or even a non-porous area). In both these cases the 2-by-2 bins in question would show large, unphysical values on the Lagrangian flow map, in locations where no flow occurs, creating a degree of what can be described as noise. We give a comparison of a small region of produced maps in both our Eulerian version (pre-smoothing), and the alternative Lagrangian version of flowmaps. For clarity, in both examples we give two versions of the colormap calibration, in one case to show where the highest velocity pixels are located (colormap calibrated over the entire velocity histogram) and in the second case with the colormap calibrated over most of the values, excluding the outliers.

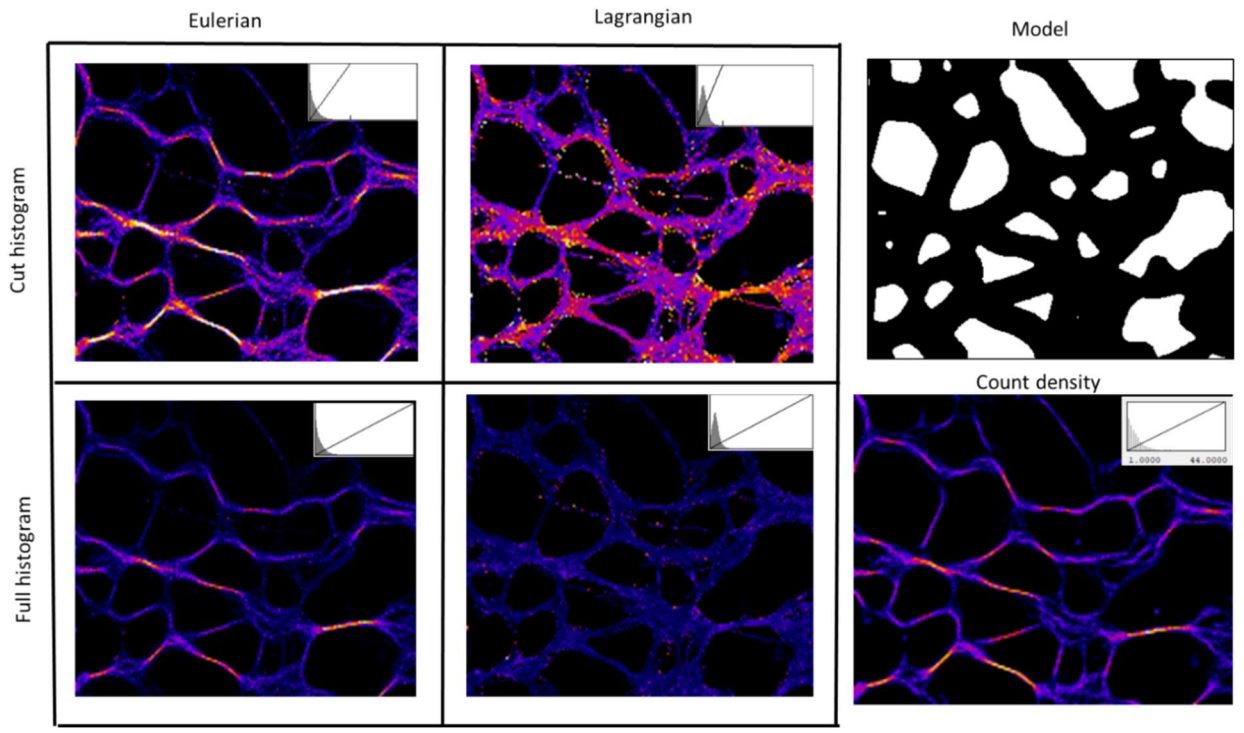

Figure 2-24: Eulerian vs Lagrangian flow map creation methods with different colormap calibrations. The colormap used is the same as the one shown throughout the article. We also show a passage density image which simply adds up the number of counts on each bin.

Figure 2-24 shows the created flow maps for different techniques. The method used in our work, "Eulerian" shows better concentration of high intensity pixels in areas of repeated flow (showed by the count density image). The other technique, "Lagrangian", shows high intensity pixels in areas where little flow occurs corresponding to one-off events that are over-represented in the final flow map.

Figure 2-25 shows smoothed version of the flow maps, such as used in the qualitative and quantitative analysis. We can observe several unphysical aspects such as the presence of flow in the solid grains, discontinuous flow tracks and significant variations of flow intensity inside the same track or flow area without any obvious reason (unlike the joining or branching of channels in the Eulerian case).

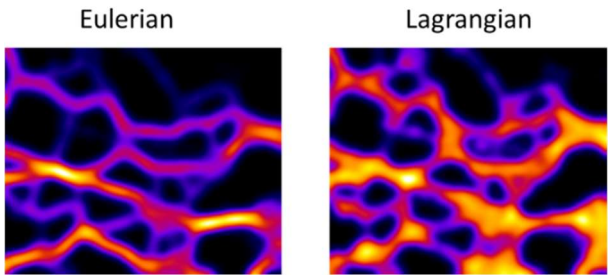

Figure 2-25: Eulerian versus Lagrangian smoothed flow maps

Therefore, we deem that our flow map creation process, while being imperfect due to the presence of a large intensity gradient originating in polydisperse bubble size distribution, translates the reality of flow in the best way.

Ideally, while still tracking the center of mass movement of the bubble, the tracking process would be able to measure all the points on which the bubble was present in each frame and add the center of mass velocity measurement on all the points inside it simultaneously. However, this solution seems technically out of reach for the time being.

Smoothing of flowmaps

The second element addressed here is the smoothing of the produced flowmaps. We believe that the transformation is not only more visually appealing but allows a better visual comparison with the numerical case, whose velocity maps are similar in appearance. Indeed, as the center of mass bubble tracks tend to coincide in the center of the path, a large area of the zone swept by the bubble is not shown as visited, making it hard to qualitatively compare highly localized bubble flow and the diffused Newtonian flow. Furthermore, the smoothing does in fact provide a flow map that better describes the reality by widening the path lines to fill the same area that the bubble sweeps.

One situation in which the smoothed image shows itself useful is that it makes no distinction between cases where all bubble paths within a same canal are overlapping (on a high intensity central track) and when multiple bubble paths are juxtaposed (in neighboring tracks in the same canal). The true velocity profile in the canal should be equivalent in both situations but without smoothing, these cases are different (examples of these cases are shown in a transversal intensity profile comparison below). When comparing a transversal profile of the two flow images, the results will differ. We display this in Figure 2-26.

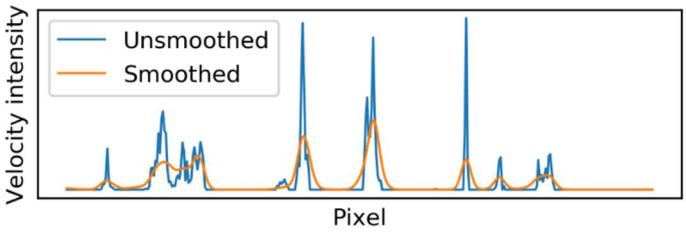

Figure 2-26: Transversal intensity profile section for a non-smoothed and smoothed version of the flow map

Peaks will be wider, and the top of peaks will even be ranked differently. This is to be expected and in fact is desired. Consider the ranking of peaks seen here to be different: two smaller peaks can combine when smoothed to create a larger that better represents overall flow. Oppositely, a large isolated peak, which may correspond to a path line bottle neck that is only present for a couple of pixels is not representative of the flow rate in that region.

As a gaussian filter conserves overall mean, we perform two checks to show that the distribution of flow in each pore and pore flow ranking remain the same in both cases. These are shown in Figure 2-27. We demonstrate that the Gaussian filter has a small enough standard deviation to not effect in any significant way the relative flow distribution. We plot the sum of pixel values for each pore (normalizing them to have a maximum of 1). The pore flow distribution is maintained in almost every case, except for 3 or 4 pores in which they are quite different. This represents 0.1% of the number of pores. We also show that the rank of the total of pixel values for each pore (i.e. the total flow in each pore) is maintained in both flowmaps, with very little dispersion.

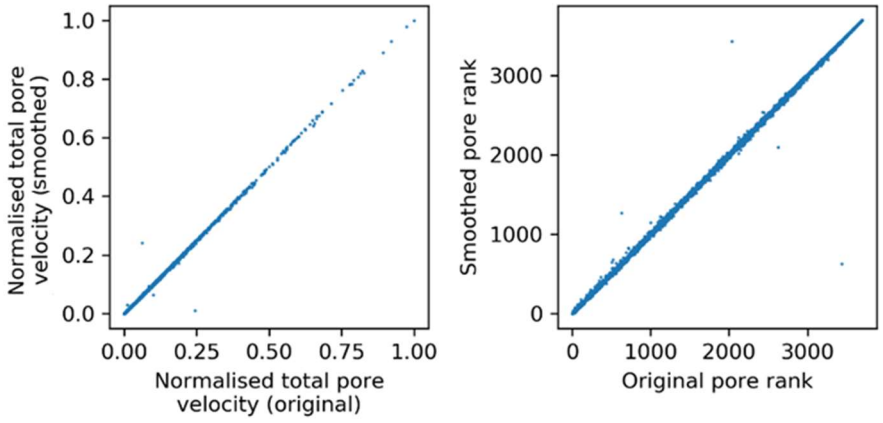

Figure 2-27: Comparison of pore pixel totals and corresponding ranks in smoothed versus unsmoothed images of the flow map. The units of the plot on the left are normalized to 1 for clarity, but by a same factor in both cases (conserved total intensity of Gaussian filter).

Chapter 3. *Micromodel Experiments: Parameter Exploration*

Preamble

Throughout this chapter we present a compilation of micromodel experiments performed on the previously described model. We take care to characterize the experiments in a detailed way, by making use of all the data available to us. We separate injection parameters from induced observables. We describe the experiments with a series of either macroscopic data types directly measured (i.e. pressure gradient, injection rate, or gas fraction), microscopic data types made available through an image processing and data analysis workflow, accessing either bubble-scale parameters that are in some way transformed to characterize the experiment (i.e. bubble deviation angle, trapped fraction, bubble size distribution statistics), parameters at an intermediate scale derived from flow maps (i.e. passage activation or longitudinal section flow distribution), and finally unquantifiable parameters such as the specific micromodel injection method and micromodel orientation. We explore the relationships first between injection parameters with themselves, identifying associations often overlooked in foam experiments, before similarly uncovering correlations between observables, and finally investigating the injection parameter relationships with observables in a systematic manner. The search for correlation in each case will be done neutrally using correlation tables. When appropriate, flow images themselves will be given for illustration or explanation of the stronger data links.

3.1 Injection parameters

In this section we show a series of micromodel experiments whose injection parameters are varied in accordance with previous foam studies in porous media: foam quality f_g, injection rate, foam injection method. As we can observe the bubble distributions in the inlet pool, we can differentiate experiments furthermore by a series of parameters related to the bubble distributions at the inlet of the micromodel. These parameters are mean bubble size, bubble size standard deviation, bubble size coefficient of variation (or normalized polydispersity). The experimental parameters that were

considered fixed during the experiments were: the backpressure at 3 bars, the temperature that varied from 18°-22° Celsius, the foamer liquid and gas composition.

We summarize the different experiments in Table 3-1:

Experiment Name	Inj. Rate (cm^3/min)	f_g	Reversed?	Injection Method	Bubbles $x_0(\mu m)$	Bubbles $\sigma(\mu m)$	Bubbles CV
A1	$2.53 \cdot 10^{-2}$	0.79	No	I1	193.2	55.3	0.29
A2	$8.9 \cdot 10^{-3}$	0.79	No	I1	287.1	112.2	0.39
A3	$2.54 \cdot 10^{-2}$	0.87	No	I1	215.3	75.6	0.35
A4	$5.4 \cdot 10^{-3}$	0.87	No	I1	359.3	172.4	0.48
B1	$1.83 \cdot 10^{-2}$	0.70	No	I2	35.1	10.6	0.30
B2	$7.1 \cdot 10^{-3}$	0.70	No	I2	44.7	22.5	0.50
B3	$9.6 \cdot 10^{-3}$	0.66	No	I2	37.8	8.9	0.23
B5	$1.10 \cdot 10^{-2}$	0.80	No	I2	172.8	79.7	0.46
C1	$2.01 \cdot 10^{-2}$	0.73	Yes	I3	154.0	44.6	0.29
C2	$6.0 \cdot 10^{-3}$	0.73	Yes	I3	234.4	83.2	0.35
C3	$2.09 \cdot 10^{-2}$	0.84	Yes	I3	154.9	58.6	0.38
C4	$6.5 \cdot 10^{-3}$	0.84	Yes	I3	272.8	125.3	0.46
D1	$2.38 \cdot 10^{-2}$	0.77	No	I3	174.8	61.5	0.35
D2	$6.4 \cdot 10^{-3}$	0.77	No	I3	251.1	87.8	0.35
D3	$2.38 \cdot 10^{-2}$	0.86	No	I3	196.0	70.9	0.36

Table 3-1: Experiment parameters explored. Explanation of Injection methods is given in detail below.

We also provide a graphical representation of the spread of the injection rates and gas fractions, as well as the model orientation and injection methods in Figure 3-1:

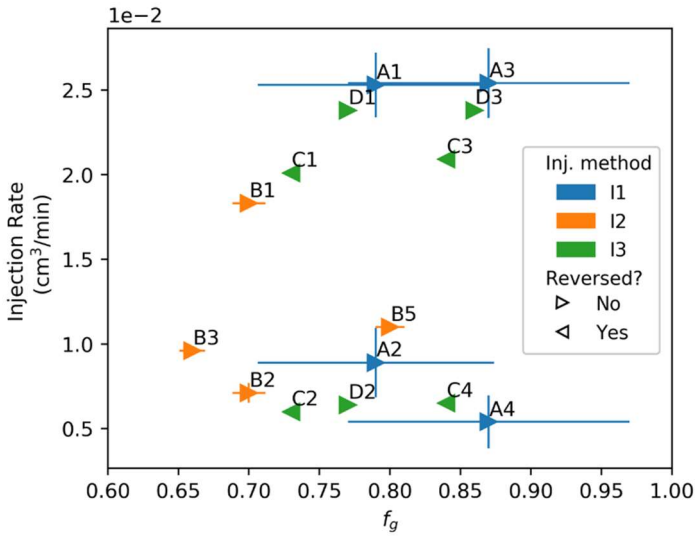

Figure 3-1: Spread of velocities and gas fractions in the experimental study

We provide next descriptions of each varied injection parameter and the measurement method.

3.1.1 Injection rate

We vary the total fluid (gas+liquid) injection rate from a minimum of $5.4 \cdot 10^{-3}$ cm^3/min to a maximum of $2.54 \cdot 10^{-2}$ cm^3/min. A liquid pump was used in combination with a gas flow controller to provide the total injection rate.

The injection rates were set using two different modes depending on the experiment. Note that these modes are not the "Injection method" referred to in the Table 3-1 (the "Injection method" will be described later). In the first mode, two pumps were used in conjunction, the liquid pump delivering surfactant solution, and a gas flow controller delivering a constant gas flow. The biphasic mixture was then pushed through a biphasic reservoir and into the foam generator (see Chapter 2). In the second method, in order to achieve lower injection rates, we make use of the biphasic reservoir, and push the biphasic mixture out of the reservoir only with the liquid pump. Experiments with both pumps used in conjunction are named with odd numbers and will be referred to simply as "odd experiments", whereas experiments in which only the liquid pump was used to push the biphasic mixture are named with even numbers and will be referred to as "even experiments".

While in some experiments, notably the "A" experiments and all the odd experiments, the volume of dead gas in between the gas controller and inlet to the micromodel was large (multiple times the micromodel volume), the pressure drop was finely monitored to ensure a measurement was only performed at steady state pressure drop, ensuring a stable flow rate despite the compressibility of gas at the inlet.

The Vinduum liquid pump was set for constant rate delivery. The gas injection was performed with a Bronkhorst gas mass flow controller. The two injection pipes joined at a T-junction before the foaming device. While the liquid pump was able to deliver low injection rates consistently, the flow controller, which was functioning in the limits of its operating range, often settled on rates that showed significant divergences from the chosen gas rate values. A simple initial grid of 3 injection rates was chosen to provide comparative values between the experiments. However, when the output flow was measured, large deviations from the target flow rates were observed. The solution to this was to calculate the injected rate from the measured output flow rates at steady

state. The output flow rate was measured at a position after the buffer bottle and backpressure regulator, and hence at atmospheric pressure, rather than at the 3 bars minimum of the micromodel. However, as the liquid-filled buffer bottle ensured that liquid only exited to the backpressure regulator, the liquid was deemed incompressible and the flow rate measured was representative of the flow rate exiting the micromodel.

The output flow rate was measured for all experiments, even the odd ones in which only the liquid pump was used. Despite the low uncertainty on the liquid pump rate delivery, decompression of the gas fraction downstream of the foaming device made it necessary to measure flow rates at the outlet of the micromodel.

A calibration of the output flow meter was also done, providing a slight correction to the data provided. The calibration was performed with a reference injection pump used for calibration purposes with low uncertainty. The result of the calibration was to apply a linear function to the data provided by the flow meter to better match the real flow rate as given by the reference flow meter. The linear function applied to the flow meter data is given in the following equation (in cm^3/min):

$$q_{real} = 1.0184 \cdot q_{meter} + 4.016 \cdot 10^{-4} \tag{23}$$

Although the uncertainty on this correction was very large for the lowest injection rates, we still used this correction on all injection rates for lack of a better solution. The final injection rate is the mean of the corrected injection rate, taken over a window of points at system steady state. Errors on the injection rate are shown graphically on Figure 3-1. The error of the injection rate was calculated by taking the standard error on the mean for the points over which the mean flow rate was calculated. The standard error on the mean (SEM) is simply given by:

$$\text{SEM} = \frac{\sigma}{\sqrt{n}} \tag{24}$$

Where σ is the standard deviation of the rate over the sample of n points. The experiments A1, A2, A3, A4 show larger error bars on the injection rate due to the smaller number of points over which the mean was calculated.

3.1.2 Gas fraction

The gas fraction was varied from a minimum of 0.66 to a maximum of 0.87. The gas fraction – often named "foam quality" in the literature concerning foam in porous media - was calculated using the equation:

$$f_g = \frac{q_{gas}}{q_{gas} + q_{liquid}} \tag{25}$$

Again, we observe a large spread of gas fraction values (see Figure 3-1), owing to the uncertainty on the gas flow rates from the gas flow controller. Due to the uncertainty on the gas injection rate from the flow controller and the reliance on the flow rate measurement from the output flow meter, the gas injection rate calculation is not trivial. Two different approaches were used for the gas fraction calculation, depending on the injection mode, as described above.

For the odd experiments, gas flow rate is taken as the total measured injection rate (see above) minus the injected liquid rate. Due to the incompressibility of the liquid phase and the low uncertainty on the liquid pumps, the liquid rate was taken as the target rate chosen on the liquid pumps.

For the even experiments, the biphasic mixture inherited from the preceding odd experiment was pushed by the liquid pump. As the pressure at the micromodel outlet is held at 3 bar in all experiments, and gas fraction is calculated from the micromodel outlet flow rates, the gas fraction in the even experiments was simply inherited from the odd experiment that preceded it, along with the gas fraction uncertainty.

3.1.3 Reversed

The reversed column refers to the fact that for some experiments, the flow was oriented in the other direction, simply by switching the input and output flow tubing, to check for the dependence of the flow distribution on the injection direction. As a large section of the thesis is concerned with the microscopic distribution of flow and preferential paths, an easy way to check for the anisotropy (or lack thereof) in the preferential paths was to flip the model and inject into what was previously the model exit at a similar range of injection rates and gas fractions.

3.1.4 Injection method

Different injection methods were tested to evaluate the effect of the specific injection method on the flow. The injection methods are described here in detail. As previously mentioned, the injection into the micromodel can be done in different ways, as three holes are available on each side of the model, as shown in the micromodel mask in Figure 3-2. The injection can either be done into the two lateral injection canals, with pressure taken in the central inlet hole, which represents injection method I1. The two lateral canals can be closed, and injection done via the central inlet hole only. This setup is shared in injection methods I2 and I3. In this situation, the pressure is taken at a T-junction in the tubing, upstream of the model, before the injection into the micromodel. The downstream pressure tubing placement always mirrors the upstream one, i.e. at the central model outlet hole or at a piece of tubing away from the model, depending on the specific injection method. We show the different injection methods in Figure 3-2:

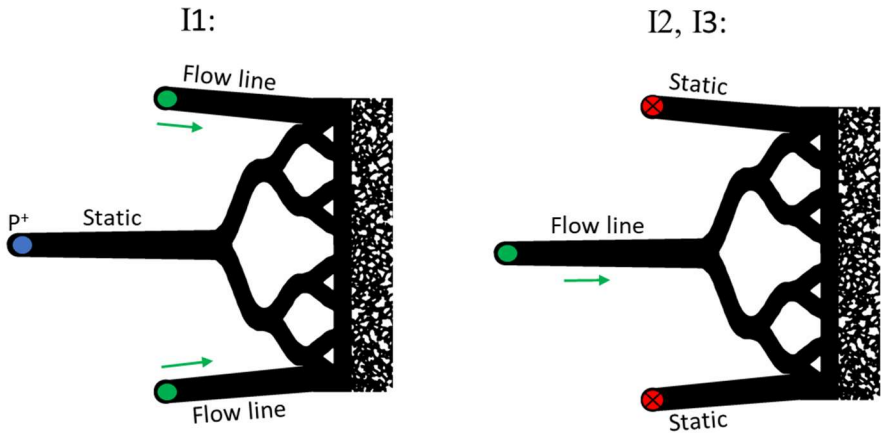

Figure 3-2: Micromodel injection tube and pressure placement for different injection methods.

Injection methods I2 and I3 are distinguished by another aspect of the injection: the distance between the foaming device outlet and the injection inlet. This aspect has a large effect on the inlet bubble size distributions. We note that a significant amount of bubble coalescence and coarsening can occur during the foam transport from the foaming device to the model. This is observed especially for higher gas fraction injections, which present thinner liquid films that are more susceptible to either coalescence or diffuse quicker, both phenomena resulting in an increased mean bubble size. Injection methods are summarized in Table 3-2:

Injection method	Injection zone	Pressure location	Foamer distance
I1	Lateral hole	Central hole	Large
I2	Central hole	Away from model	Small
I3	Central hole	Away from model	Large

Table 3-2: Injection method characteristics

3.1.5 Inlet foam distributions

It is relevant to show foam inlet bubble size distributions as a supplementary injection parameter due to its effect on flow properties. Photos of pre-network bubble distributions are acquired with the low frequency images, in a small injection pool at the entrance of the micromodel. The images are binarized and 2D bubble surface areas are added up over at least 20 distinct images. The equivalent circle radius for each bubble area is then used as characteristic bubble radius which is referred to as bubble size interchangeably in this chapter. We give examples of inlet bubble images with different distributions in Figure 3-3:

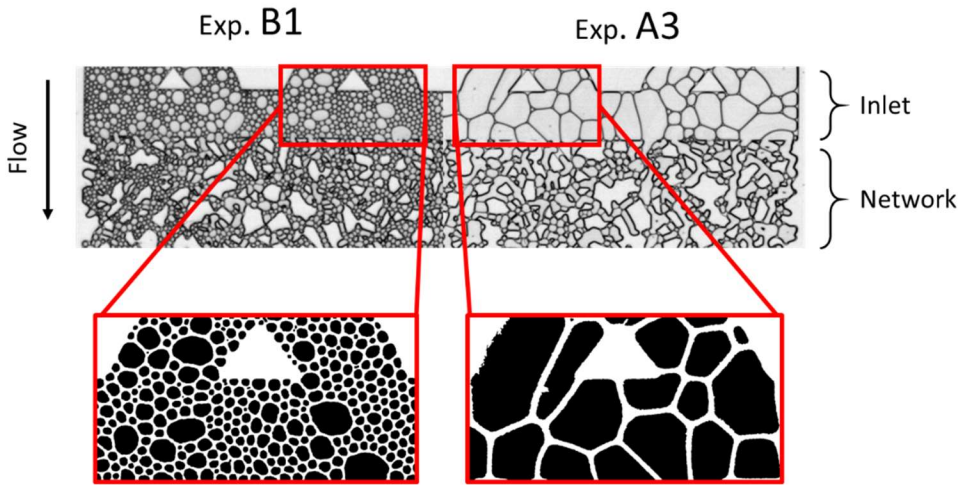

Figure 3-3: Bubble populations accessed from the inlet zone for two experiments with different characteristics. Each half of the image represents a different experiment, and the raw images are stitched together to create an image showing the whole model transversal distance. We show the final binarized versions of the images for two small rectangles shown in red. For calculation of the bubble distribution characteristics, the whole inlet zone was considered. We note that for the distributions with larger bubbles, as in Exp. A3 (right), a considerable number of bubbles are cut from either side of the image, which leads to decreased measured bubble size means and increased size standard deviations.

Inlet bubble size distributions are finally transformed into weighted histograms, as in Chapter 2, with each frequency histogram peak weighted by the mean bubble size of the histogram bin. The

weighted histograms produced are assimilated to a probability of observing a bubble of a given size when choosing a point at random in the entrance zone, i.e. spatial bubble size probability. The inlet spatial probability distributions resemble normal distributions. To characterize them we therefore make use of a Python curve fitting function curve_fit from the Python library SciPy (Jones et al. 2001-) based on Levenberg-Marquardt damped least squares method (Moré et al. 1980). The function to fit is normal distribution, defined as:

$$P(x) = ae^{-\frac{(x-x_0)^2}{2\sigma^2}} \tag{26}$$

$P(x)$ is the probability of observing a bubble of radius x, the equivalent circle radius of the 2D bubble. The parameters that were fitted for each distribution were a the scale, x_0 the mean of the distribution, and σ, the standard deviation.

The parameters of interested here are the mean bubble radius and the standard deviation. We show in Figure 3-4 an example of the normal fits of the four inlet bubble radius distributions for the first four experiments: A1, A2, A3 and A4. The distributions here are normalized to show an equal area under the curve, i.e. a comparable probability.

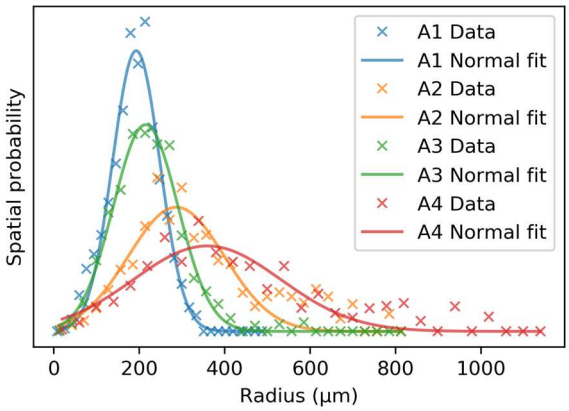

Figure 3-4: Fit of weighted inlet bubble histogram values to a normal function given in equation (26) for the four first experiments.

The final injection variable associated with the bubble size distribution is the coefficient of variation. The coefficient of variation essentially normalizes the standard deviation with respect to the mean bubble size, such as $\mathrm{CV} = \frac{\sigma}{x_0}$, and provides a normalized measure of bubble size polydispersity, similarly to other foam studies (Géraud et al. 2016; Quennouz et al. 2014).

3.2 Correlation of injection parameters

In this section we evaluate the relationships between the different injection parameters. We will approach this task by simply searching for relationships between various parameters pairs. As we have many parameters to explore, many parameter pairs can be investigated. A simple way of scanning through the possible pairs is through correlation coefficients of the data points. Correlation coefficients are simple ways to identify pairs that evolve in a dependent way, expressing some underlying relationship. Values close to 1 show a strong positive relationship between the variables, while values close to -1 show a strong negative relationship between the variables. Values close to 0 demonstrate no relationship. We chose to evaluate parameter pairs by using the Spearman coefficient. The Spearman coefficient (Spearman Rank Correlation Coefficient 2008) simply describes the degree to which the relationship between two variables can take the shape of a monotonic function, and hence makes no assumption on the function shape that relates the variables. A large value (either positive or negative) provides indication that further exploration is necessary. This approach will be used later to compare observables, and then finally to find relationships between parameters and observables. As the correlation matrices are symmetrical, we only show the correlation coefficient half matrix for the injection parameters in Figure 3-5:

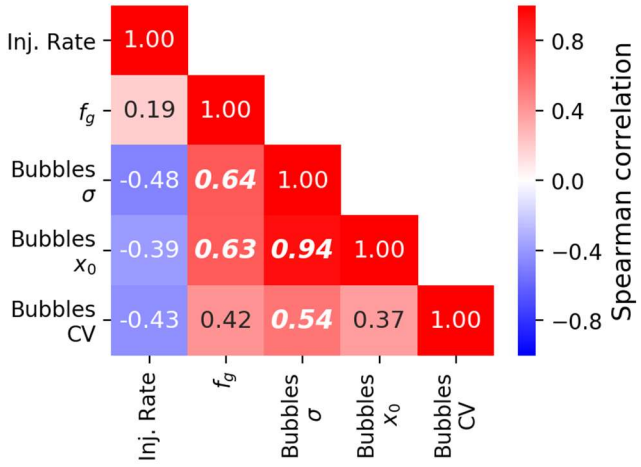

Figure 3-5: Spearman correlation coefficients matrix of injection parameters. Absolute values above 0.5 are emphasized.

3.2.1 Foam distribution correlations

The strongest positive non-trivial coefficient in the coefficient matrix is the relationship between mean bubble size x_0, and the standard deviation of the bubble size distribution σ. We show the corresponding data in Figure 3-6:

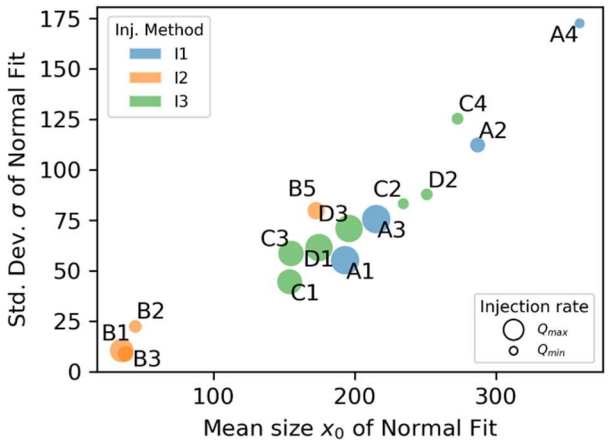

Figure 3-6: Linear relationship between mean bubble size and bubble size distribution standard deviation at the micromodel inlet for each experiment

We observe from the data points that mean bubble size and bubble standard deviation are proportional with a coefficient of $\frac{\sigma}{x_0} \approx 0{,}37$. This effect, that linearly links mean and standard deviation in different distributions, is a well-known phenomenon known as the "proportional effect". It is often seen in distributions of geostatistical measurements (Manchuk et al. 2009). It is unclear why this effect is so strongly visible in our case, for the entire range of injection methods, injection rates and foam qualities.

Such a linear relationship between these two variables of the bubble distributions makes an analysis based on both variables in combination somewhat redundant. This therefore motivates the use of the coefficient of variation $\mathrm{CV} = \frac{\sigma}{x_0}$, as a descriptor showing the deviation from this linear relationship. CV values close to 0,37 will correspond to bubble distributions whose parameters fit within the linear relationship whilst different values show some specificity.

3.2.2 Foam distributions – macroscopic injection parameter correlations

Strong connections between the macroscopic injection parameters (gas fraction and injection rate) and inlet foam distribution parameters can also be observed. Bubble size mean, standard deviation

and coefficient of variation all correlate negatively with injection rate, whereas they show strong positive correlations with gas fraction. We show mean inlet bubble sizes and their relationship with the injection rate and foam quality in Figure 3-7.

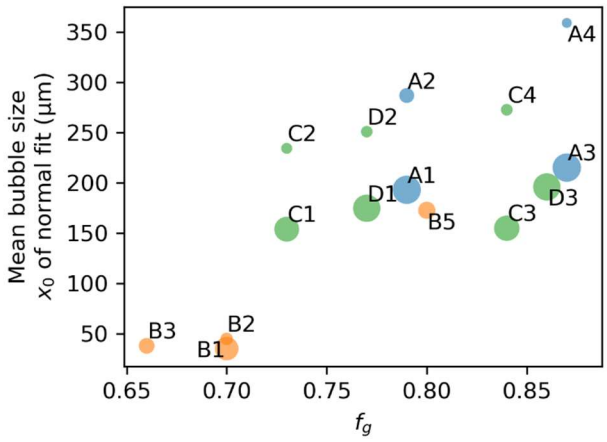

Figure 3-7: Mean inlet bubble sizes in term of injection rates, methods, and foam qualities. Marker size is indicative of the injection rate, as in Figure 3-6.

From this plot we can make a few different observations. First, a negative trend between injection rates (shown by marker size) and mean bubble size is visible. For injections types A, C and D, the lower injection rate (A2, A4, C2, D2) size means are all significantly higher than for their higher rate counterparts (A1, A3, C1, D1). This can simply be explained by the larger time passed in the tube leading from the foaming device to the micromodel inlet, during which time smaller bubbles spend longer diffusing into larger ones before disappearing, increasing the overall bubble size. A second observation is the general positive trend between mean bubble sizes and gas fractions. One possible explanation for this effect is the thinner liquid films separating the bubbles in high gas fraction foams. Thinner films will enable faster gas diffusion from small to large bubbles and are also more susceptible to coalesce during transport in the tube, which has the effect of increasing mean bubble sizes.

While these two observations can be understood in terms of physical processes occurring in the transport to the micromodel inlet, it is also very possible that the bubble distributions directly at the foaming device outlet already carried some of these characteristics. Indeed, it has already been observed that for the same generator, high gas fractions can lead to larger mean bubble size distributions (Gido et al. 1989; Osei-Bonsu et al. 2016) while high injection rates can reduce mean

bubble sizes (Jones et al. 2018b). As the bubble distributions situated directly at the foaming device outlet were not measured, the effect of the foaming device output on the micromodel inlet distributions cannot be excluded.

Fortunately, the I2 method injections help us see more clearly. Injections using this method are characterized by a much shorter tube joining the foaming device to the micromodel. I2 injections (at least B1, B2, B3, B4) produce significantly smaller inlet bubble size distributions than any other type of injection. This high dependence to the tube length demonstrates the strong effect of the foam transport from the foaming device to the micromodel inlet. For similar injection rate and gas fraction combinations (B1 and C1, or B5 and C2) the I2 injections repeatedly average on lower bubble sizes.

Another element to take out of Figure 3-7 is the very small bubble size of the B1, B2, B3, and B4 experiments. These experiments all show entrance mean bubble sizes smaller than the mean throat size of the model. For this reason, we can expect the foam flow in these experiments to be purely transportive, without any significant bubble size adaption through the model.

3.3 Observables

In this section we shall explore the different observables that will serve to characterize the flow experiments. This section either describes observables that are macroscopic in nature (i.e. pressure gradient), observables relating to dynamic aspects of the flow, measured locally but averaged over the entirety of the model (i.e. passage activation, trapped foam fraction, bubble flow deviation from pressure gradient), or finally parameters related to the bubble size distributions or shapes at the outlet.

3.3.1 Pressure drop

The pressure drop was tracked throughout the entirety of each experiment. The pressure drop was measured with an ABB 265 DS differential pressure transmitter with a maximal differential of 2500 mBar. The pressure drop shown here is a mean value taken over the same window of points as the injection rate mean (described above). Two different pressure point measurement locations are used in the series of experiments, as described by Table 3-1.

We discuss here some of the difficulties we met when measuring pressure drops over the micromodel. In the initial setup, with I1 injection method, we observed some rare but significant irregularities (sudden decreases of pressure drop without any corresponding flow change) in the pressure differential signal. The observation of these irregularities led us to stop taking pressure measurements on the micromodel in the first place. Indeed, we discovered that pressure lines that were attached to the micromodel rapidly became populated with gas or bubbles. As the pressure lines are filled with static water and are attached perpendicularly to the flat micromodel, the static water rapidly gets displaced by lower density bubbles (i.e. gas) in movement around the micromodel inlet. The inlet pressure line is particularly affected by this static liquid displacement phenomenon. In turn, this influences the measured pressure drop. Firstly, it is not clear how easily pressure will communicate through a series of bubbles, where the yield stress-plastic foam may even act as a blocking fluid, and the measured pressure will not be representative of the pressure in the measurement point. Secondly, assuming the pressure can communicate through a series of bubbles, the timescale for this process may be much longer than for an incompressible fluid, leading to a lag in the measured pressure signal. We illustrate this issue in Figure 3-8:

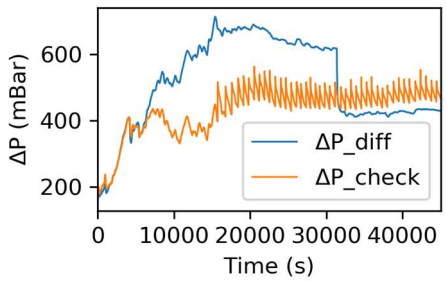

Figure 3-8. Time evolution of pressure drops for experiment A3, which uses the I1 injection method, (i.e. pressure measurement point on the micromodel central hole). The pressure drop value taken was calculated from the points taken after the discontinuity. The discontinuity was attributed to gas or bubbles in the outlet pressure line.

In this figure we see the differential pressure signal in blue, named *ΔP_diff*, suddenly decreases at around 30 000 seconds. We also measure a pressure difference from two points in the system, further out from the micromodel on each side. This verification pressure signal, named *ΔP_check,* reveals a pressure difference signal without discontinuity. As *ΔP_check* measures the pressure drop not only over the micromodel, but also over a certain distance of tubing containing foam, we can expect the pressure difference of *ΔP_check* to be higher. This leads us to believe that the true pressure difference over the micromodel is the second plateau of the *ΔP_diff*, in which the pressure

drop averages around 400 mBar. Indeed, we attribute this discontinuity to the sudden unblocking of the outlet pressure line.

Also, we note that the *ΔP_check* contains a periodic oscillation after 15 000 seconds. This is due to the proximity of the downstream pressure measurement point to the back-pressure regulator, which opens and closes periodically to maintain a constant backpressure of 3 bars.

In the I2 and I3 injections, the pressure measurement point was taken on a T-junction on the tube close to the micromodel. This notably allowed us to orient the pressure lines fully downwards all the way to the pressure transducer, and to limit the entrance of gas or bubbles into the liquid pressure lines. The measured pressure signals are notably different in this case. We show an example in Figure 3-9:

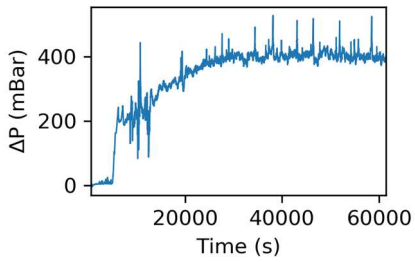

Figure 3-9: Pressure differential signal for experiment D1 (see Figure 3-1), an experiment using the I2 pressure measurement method, with a better placement of pressure points in the system.

We observe that the pressure drop signal is more stable in the long-term when the measurement point is away from the model. In addition, we observe a larger amount of short-term oscillation around a mean value in these measured signals. This is again due to the proximity of the downstream pressure measurement point to the back-pressure regulator.

We understand that any added length of tubing between upstream and downstream measurement points (with the I2 and I3 injections) will necessarily add millibars to the pressure differential signal and reduce the representativity of the measurement to the flow in micromodel. However, this solution was found to minimize the issue of bubbles populating the static pressure lines and represents a tolerable trade-off.

Finally, we note that the pressure gradient shown in this example, calculated to be over 23 bar/m, is considerably larger than the pressure gradient required to mobilize dispersed bubbles inside pores and can be found only in close proximity to the well in an oil recovery context.

3.3.2 Viscosity

A measurement of apparent viscosity was derived from knowledge of pressure drop and injection rate. Apparent viscosity μ_{app} was obtained by applying the single-phase Darcy law, such as:

$$\mu_{app} = \frac{K\Delta PA\phi}{LQ} \tag{27}$$

In which K is the model permeability ΔP is the measured pressure drop, A is the model injection face size, ϕ is the model porosity, L is the model length, and Q is the total injection rate.

Apparent viscosities in our experiments were found to fluctuate between 5-25 centipoise.

3.3.3 Longitudinal section flow distribution

For each experiment's overall averaged flowmap, we performed the box flow analysis described in Chapter 2, Appendix 2-B, in which we simply summed measured intensities for each of 4 equally sized longitudinal sections covering the full model length, to show the flow distribution in the transversal axis only. From the 4 values obtained, we then calculated a mean and a standard deviation. The 4 values are then normalized by dividing by the mean, allowing comparison between experiments. If flow is perfectly well distributed in each section, each section carries a fraction of 0.25 of the total flow, and the standard deviation is 0. We give an example for two different experiments A1 and A2 in Figure 3-10. The higher standard deviation value of experiment A2 translates the higher flow heterogeneity along the transversal axis.

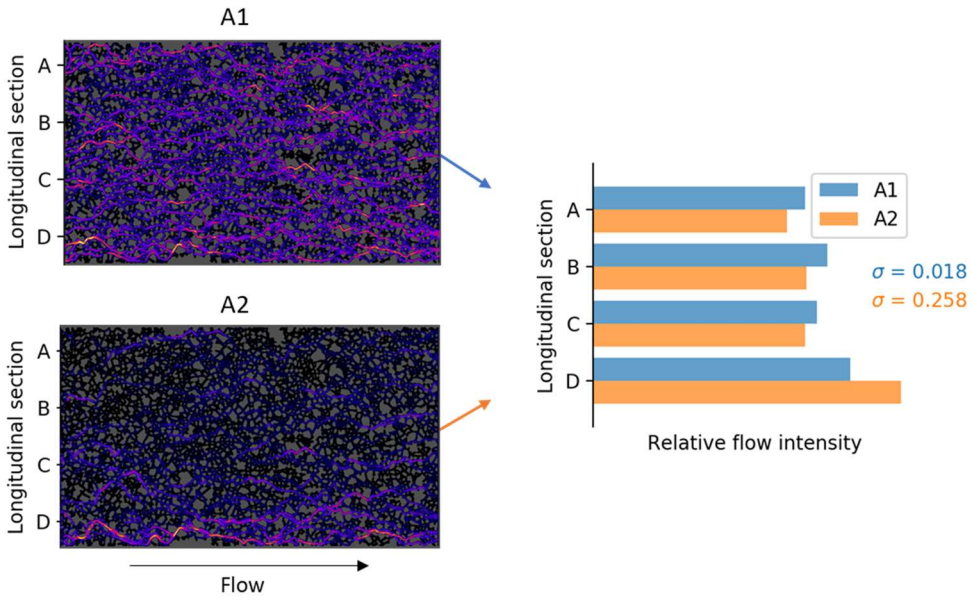

Figure 3-10: Longitudinal flow distribution and associated standard deviation for experiments A1 and A2.

3.3.4 Dataset flow intermittency

One global observable unmentioned previously is the global flow intermittency in between dataset. For each experiment, a series of 8 or more sets of 200 images are averaged to create a flow map. We can also create individual flowmaps for each dataset. The dataset flow intermittency calculation applies a similar principle to the longitudinal section analysis shown above but compares total intensities of flowmaps for individual datasets. Summing the values for all the pixels in the created flowmap then provides a global measure of flow strength in the dataset. A standard deviation of flow strength can then be calculated from the flow strength values of all the datasets. The standard deviation was calculated on normalized intensities of the flowmaps. This was done by dividing each dataset intensity by the mean of all dataset intensities for that experiment. We show an example of the normalized flow strength per dataset for two experiments in Figure 3-11.

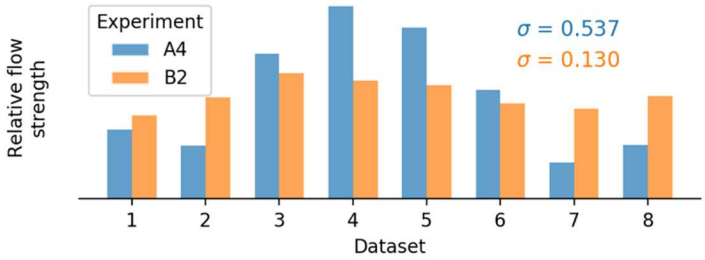

Figure 3-11: Relative flow strength of successive datasets for two different experiments. The A4 experiment notably shows a higher standard deviation than the B2 experiment.

3.3.5 Passage activation

For each experiment, flow heterogeneity also was measured through the previously defined (see Chapter 2, Appendix 2-B) passage activation. In each case, the mean passage activation was calculated, averaged over all 29 equidistant transversal cuts in each overall flow map to give a single value.

3.3.6 Trapped fraction

As bubble tracks are available individually, it was possible to measure the displacement of a single bubble over the entire track taken the Euclidian distance from the start to end point ΔTot. The bubble displacements for each experiment can then be divided into flowing and trapped foams by segmenting a bimodal distribution in the displacement log-space, as shown in Figure 3-12 for two different experiments. Note that the threshold value changes between experiments. The areas of the bubbles in the trapped section are then added together and compared to the sum of areas of all the bubbles, providing an estimation of the trapped area fraction inside the model. We note that the trapped foams can have in fact non-zero total displacements. The non-zero displacements are either negligible (inferior to 1 µm in 200 frames), or can be due to small bubble rearrangement inside pores without transport out of pores, for cases of pores containing multiple bubbles.

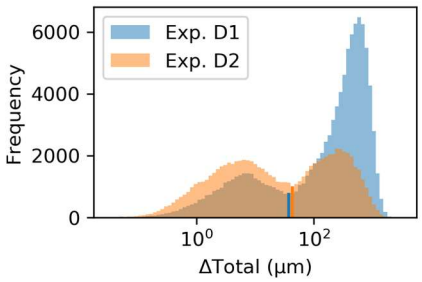

Figure 3-12: Total bubble displacement distribution for the experiments D1 and D2. Each distribution displays a bimodal distribution whose minimum is used for segmenting flowing and trapped bubble populations. Trapped fractions in experiment D1 and D2 are 19% and 46%, respectively.

3.3.7 Bubble flow deviation from pressure gradient

It was also possible to measure the displacement perpendicular to flow, ΔY and compare it to the total displacement of the bubble ΔTot. For this measurement we only use the tracks belonging to the flowing part of the total bubble displacement distribution showed above (right hand side of the distribution). The ratio of these two distances $\frac{\Delta Y}{\Delta Tot}$ gives the sine of the angle that describes the deviation from pressure gradient direction, while the inverse sine of this ratio gives the angle. We show a typical distribution of angles in Figure 3-13 and the associated distribution of deviation angles.

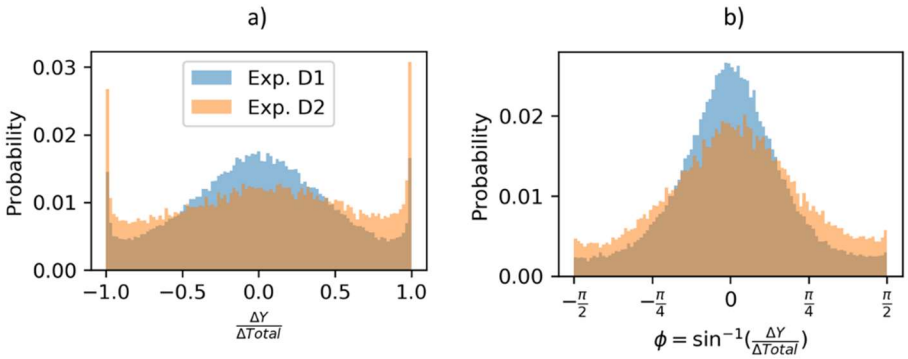

Figure 3-13: Full-track bubble displacement ratio distribution and associated angle of deflection from pressure gradient. The bubble deviation is calculated using the flowing bubble tracks only, as shown in Figure 3-12.

To extract a single numerical value from the angle distribution we take standard deviation. In the cases shown here, the mean standard deviation value for the D1 experiment was 0.57 radians (32 degrees) and the for the D2 experiment it was of 0.70 radians (40 degrees). Higher values indicate distributions less spiked in the center (around 0), i.e. experiments with higher deflection.

3.3.8 Outlet foam distributions

In a similar manner to the inlet bubble distribution, the bubble distributions in the model outlet pool were analyzed. Mirroring the inlet distribution properties, we can associate bubble size means, standard deviations and coefficients of variation to the outlet bubble size distributions.

3.3.9 Inlet/Outlet evolution ratios

A measure of the transformation of bubble size distributions is included in the observables. We simply define ratios of mean bubble size such as: $R_{x_0} = \frac{x_{0\ inlet}}{x_{0\ outlet}}$.

Similarly, we provide ratios for bubble size standard deviations and coefficients of variation.

3.3.10 Total bubble perimeter

From the binarized images of bubbles in the low-frequency image sets, we measure the sum of all bubble perimeters inside the model and take a mean value per image for each experiment. This provides a complementary information to the mean bubble sizes at the inlet or outlet, and instead serves as a global measurement of the total length of gas-liquid interfaces inside the model. Classically, foam lamella density is understood as being proportional to measured foam viscosity (see equation (11)). The total bubble perimeter correlates positively with lamella density and offers a degree of refinement. For monodisperse foam injections (i.e. constant perimeter) these two values correlate perfectly. However, the notion of total perimeter is specifically useful in our case as the micromodel bubble size distributions are polydisperse and undergo size evolution in the model.

3.3.11 Bubble specific surface area (SSA)

Recently (Ouali 2019), a strong relationship has been observed between the *in situ* specific surface area of a foam in a 3D medium, retrieved using small-angle neutron scattering, and the measured pressure gradient over the medium with the specific surface area. A bubble specific surface area was estimated in our case by multiplying the bubble perimeter by the model height and adding twice the bubble 2D area to form a closed bubble in 3D. We used the same images and averaging method for this parameter as for the bubble perimeter.

3.4 Correlation of observables

In this section, the observables described previously are first rapidly scanned for relationships with each other. In this manner, we hope to understand if some flow observations can be understood in terms of other parameters at a different scale. We proceed to use the same method of initially checking for Spearman correlation between parameters before investigating the strongest relationships and looking deeper to explain them. We first present a global Spearman correlation matrix in Figure 3-14. For clarity, we only show one half of the symmetric matrix. We split the parameters into three categories: macroscopic; local dynamic; and observables related to the bubble size distributions or shapes, i.e. outlet distribution parameters or ratios of parameters between inlet and outlet.

Despite the large number of parameters and correlation values, we have bolded some strong relationships (Spearman correlation above 0.5) that we will comment in some detail below.

This section will not try systematically to establish causal links between observables but rather show that some observable parameters can be understood in terms of observations from a different scale.

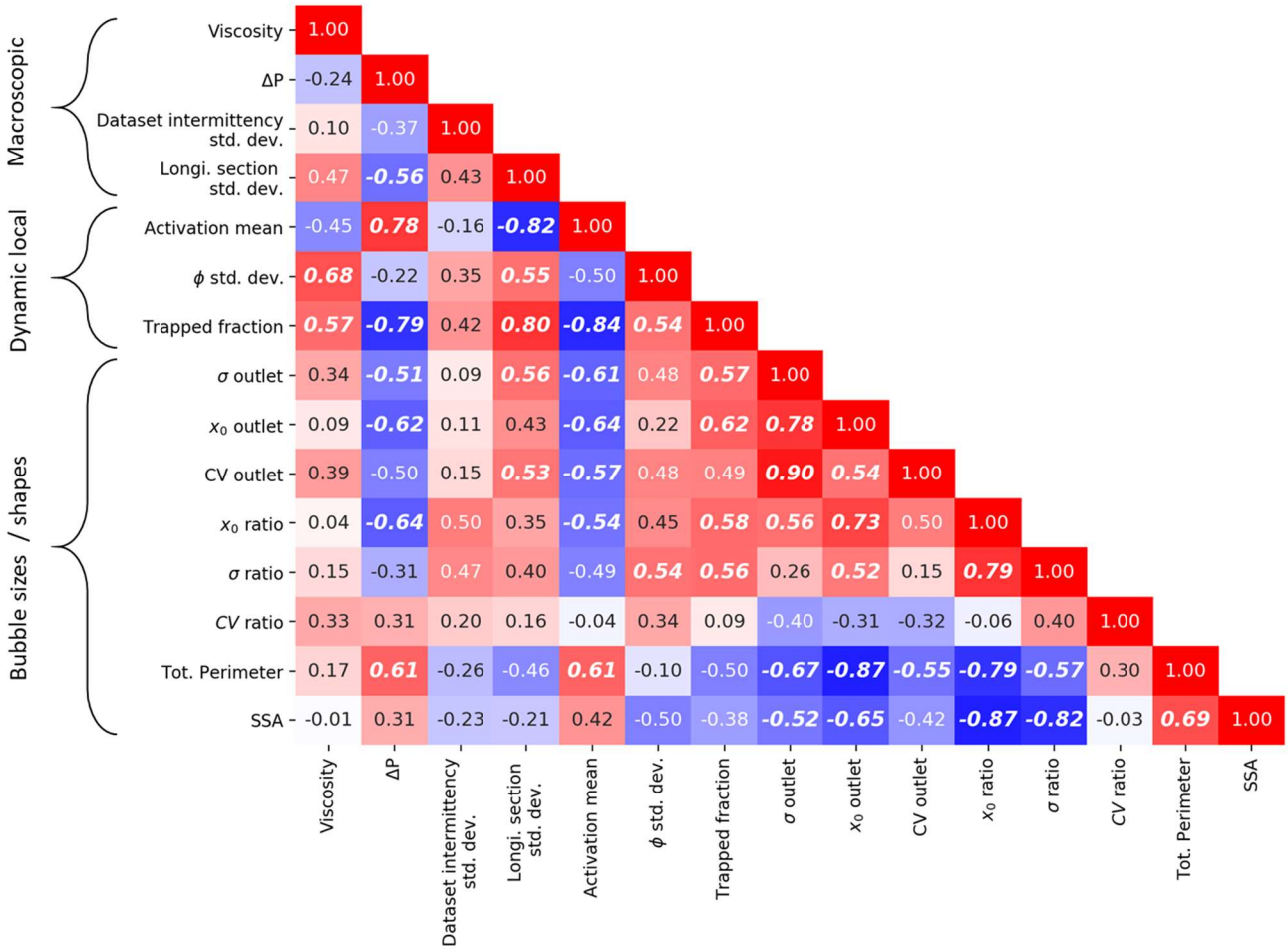

Figure 3-14: Spearman correlation coefficients matrix between observables

3.4.1 Correlation of trapped foam variables

We observe a strong positive relationship between the apparent viscosity and the trapped fraction. It is well established trapped foams can contribute to an overall increase in apparent viscosity by reducing the available sweep inside the medium (Tang and Kovscek 2006; Kovscek and Bertin 2003; Jones et al. 2018b). The measured pressure gradient shows the opposite correlation with the trapped fraction. Stated reciprocally, a low-pressure gradient cannot sufficiently mobilize foams that remain trapped inside certain zones and create large measured trapped gas fractions.

Mean passage activation correlates positively with the measured pressure gradient. This can be understood as demonstrating classical foam mobilization at high pressure gradients (Rossen 1990a), in which a minimal pressure gradient must be achieved to mobilize a trapped foam

lamellae and a higher number of active paths are observed. Therefore, the trapped fraction in turn correlates negatively with the passage activation mean. Also, the trapped fraction correlates positively with the standard deviation of longitudinal flow distribution. Indeed, experiments with high longitudinal flow distribution standard deviation are synonymous with presence of low flow areas containing a high proportion of trapped bubbles in a section of the model. This is often the case for the high gas fraction and low injection rate experiments in which large sections of dry foam are unable to be mobilized. This causal link will be explored in the next section in more detail.

The activation mean is a flow homogeneity marker that is more resolved than the longitudinal section flow distribution standard deviation as it takes all the porous sections over the transversal cuts. It could be possible to have a completely uncorrelated activation and longitudinal standard deviation if say, for example, that one out of every two paths were active in a transversal cut, as opposed to all the paths. The activation mean between the two cases would be halved but the longitudinal standard deviation would remain the same. However, in many cases they seem to describe similar (absence or presence of large trapped zones) and for this reason they are so strongly correlated.

To synthesize, the passage activation, trapped foam fraction, and longitudinal section flow distribution standard deviation form a "triad" of somewhat redundant information describing trapped foam. But they nonetheless have different measurement origins. To illustrate their relationship, we display the three datatypes simultaneously in Figure 3-15.

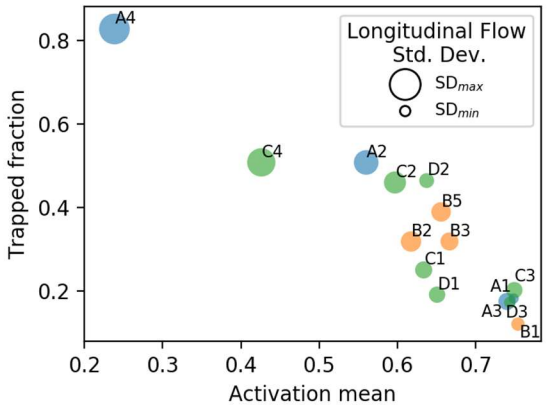

Figure 3-15*: The "triad" of information relating to trapped foams.*

3.4.2 Pressure gradient and bubble size distribution parameters

We note that the pressure gradient correlates positively with the total perimeter, and negatively with the outlet mean bubble size and bubble size evolution ratio. These connections all loosely correspond to saying a higher bubble density will induce a larger pressure gradient due to the increased number of travelling interfaces contributing to the foam viscosity, or reciprocally that a large pressure gradient will be capable of breaking bubbles to a larger degree and creating larger total perimeters. However, as the pressure gradient shows a significantly stronger correlation to the bubble size distribution parameters than the viscosity, we further conjecture that the causal link between the two observable types is oriented from the pressure gradient to the bubble size and not vice-versa. Indeed, the lower correlation of the total perimeter and the outlet bubble size indicate that while these parameters may contribute to a certain extent to the viscosity, they are not the principal contributors. Instead, the trapped fraction seems to correlate much more strongly with the foam viscosity. Therefore, while a larger pressure gradient seems to create smaller average bubble sizes and larger total perimeters, we cannot say this transformation has a major effect on the foam viscosity. We illustrate this point by showing the measured pressure gradient plotted against the total measured perimeter in Figure 3-16. The marker size indicates the apparent viscosity.

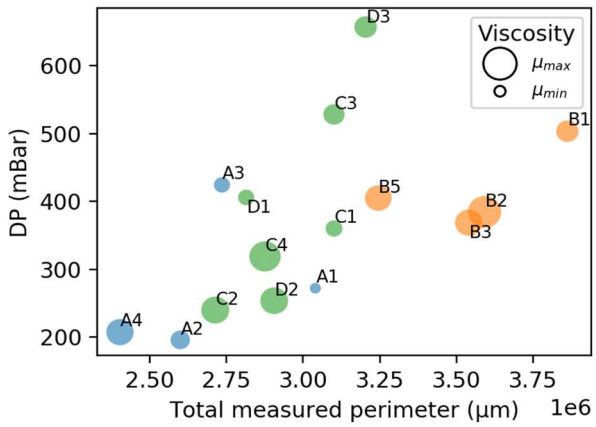

Figure 3-16: Relationship between measured pressure gradient, total bubble perimeter and apparent viscosity

While a positive relationship exists between the pressure gradient and total perimeter, this does not correspond to larger viscosities for larger total perimeters.

3.4.3 Viscosity and bubble deviation angle

One less obvious relationship is the positive correlation between the apparent viscosity and the deviation angle to the pressure gradient. Intuitively, we could expect the effect of trapped foams to be hiding behind this correlation, as a high trapped fraction will force flowing foams into tortuous flow paths to avoid trapped zones, while at the same time contributing to increase the apparent viscosity by decreasing sweep. However, the correlation between the deviation angle and trapped fraction is, while positive, much less strong. This relationship could then be understood not necessarily in terms of a reduced sweep, but in and of itself, as a higher angle that represents a larger amount of movement of interfaces that don't contribute to flow towards the model exit, and requires a larger amount of useful work to transport these bubbles out of the model.

Finally, we look at some of the stronger correlations that we won't explore in detail and provide justifications for not doing so. Strong relationships do exist within the set of bubble distribution parameters themselves, shown in the right section of the table. For example, the mean outlet bubble size $x_{0\ exit}$ and outlet bubble size standard deviation σ_{exit} correlate positively, although to a lesser degree than for the inlet distributions. We believe this correlation is in fact inherited from the strong proportional effect observed for the inlet injections and demonstrates that while evolution of bubble size is observed, the size distribution shape in the model outlet hasn't fully achieved steady state, in which the final distributions are unrelated to the injection distributions.

Another series of strong correlations are observed between some of the evolution ratios and their components (i.e. the bubble size ratio R_{x_0} and the outlet mean bubble size $x_{0\ exit}$). However, these demonstrate the sensitivity of the created evolution ratio to the change in the parameters composing it, rather than any meaningful relationship. These kinds of relationships will therefore not be explored in detail.

Lastly, some pairs of bubble distribution observables translate similar information, such as the total perimeter and the exit mean bubble size. Indeed, a very small outlet bubble size will create a higher number of parameters contributing to the total parameter variable. Similarly, the specific surface area uses the total perimeter in its definition, and therefore shows a strong positive correlation to the total perimeter.

3.5 Injection - Observable relationships

In a similar fashion, we combine injection and observable pairs to establish a primary indication of the most relevant parameters in the foam flow experiments. We will scrutinize some of the strongest relationships while, where applicable, giving examples of the mechanisms at play, proposing causal links by using flow examples.

We display in Figure 3-17 the correlation matrix for observables and injection parameters for all the experiments, with observables on the y-axis and injection parameters on the x-axis.

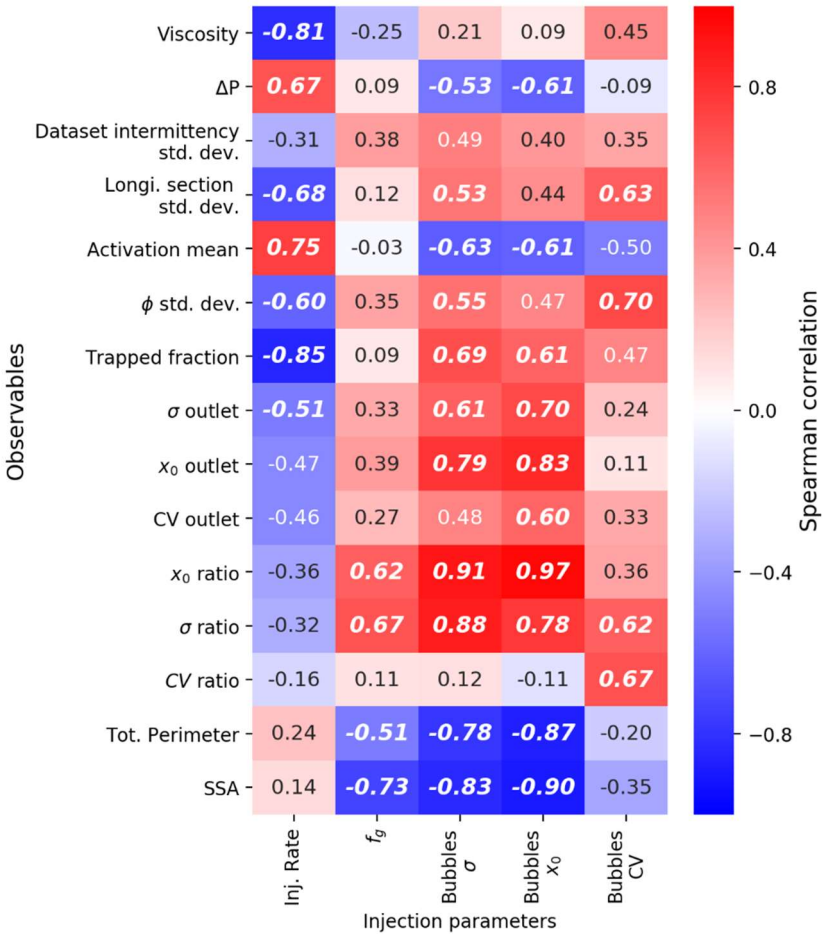

Figure 3-17: Correlation maps of different injection parameter-observable pairs.

Evidently, some observables are highly correlated to input parameters. Some are to be expected, such as the negative correlation between viscosity and injection rate, i.e. the shear-thinning effect. In the next section we explore some high correlation relationships noted from this correlation map.

3.5.1 Viscosity relationships

The relationship between measured apparent viscosity was studied in some detail due to the importance of viscosity in reservoir simulation software.

a) **Shear-thinning effect**

A shear-thinning effect was observed in the micromodel experiments. Apparent viscosity was found to decrease for higher injection rates. We show the observed apparent viscosities in terms of injection rates in Figure 3-18. We also display the same data in a log-log basis on the right of Figure 3-18. We include a best fit trendline in the log-log plot. The trendline was found using the SciPy curve_fit function. A series of weights was also used in the curve fitting process. The weight of each point in the process is equal to the inverse of the standard error of the mean of the injection rate value, displayed by black error bars in the plot on the right of Figure 3-18. Despite the large spread of points around the trendline, the line's slope indicates that a power law links the foam apparent viscosity to the injection rate through the equation $\mu_{app} \propto Q^{-0.58}$. Inclusion of one standard deviation on the slope fit gives $y = -0.58 \pm 0.2$.

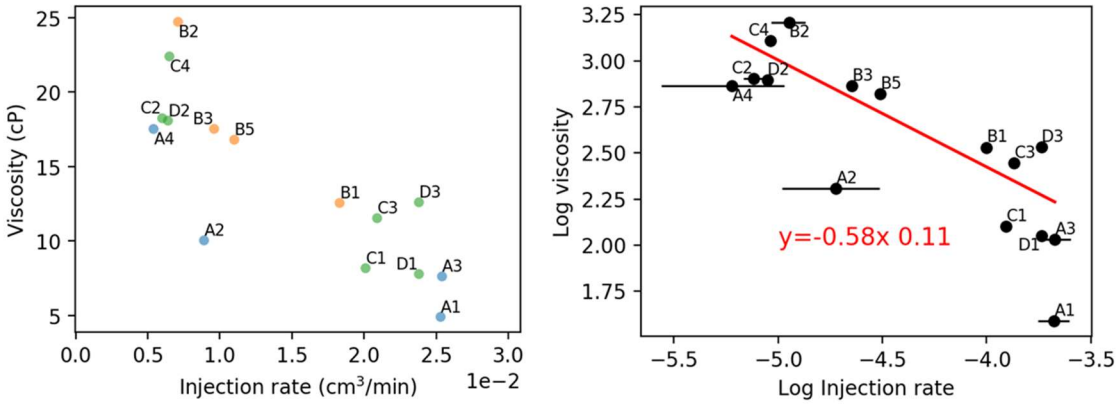

Figure 3-18: Viscosity measurements for all experiments in terms of injection rate. In this plot the marker sizes are all the same.

Various exponents have been found in the literature linking injection rates to apparent viscosities. Our exponent here is different to the value of -1/3 classically given in Bretherton's law (Bretherton 1961). However, Bretherton's law deals with simple geometries of lamellae displacement in tubes, notably without the notion of foam trapping observed here. Observations of an exponent closer to -2/3 have been made in other studies however (Falls et al. 1989; Pedroni 2017).

b) **Modelling viscosity through microscopic observables**

As described in Chapter 1, foam mobility is a function of both foam viscosity and foam relative permeability. Foam viscosity is generally considered to be dependent of the foam lamellae density while foam relative permeability is affected by foam trapping and reduction of sweep. In our case, both are integrated into the measured "apparent viscosity" that we display here. Due to the strong relationship between the trapped fraction and the injection rate, we believe that the primary factor contributing to the apparent viscosity is the trapped fraction, showing a stronger negative correlation with the injection rate to viscosity than with any of the bubble size distribution variables. The relationship between the trapped fraction and the viscosity explains the high correlation to other parameters of the "trapped foam triad" section. We show a graph of the trapped fraction as a function of the injection rate in Figure 3-19.

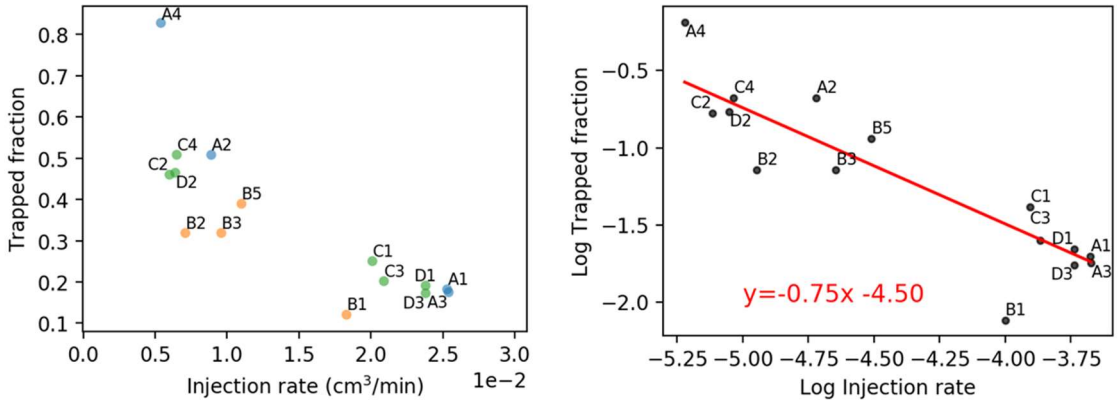

Figure 3-19: Foam trapped fraction as a function of injection rate. A log-log linear fit is provided on the right.

We observe a decaying function spanning high trapped fraction (> 0.8) at low gas rates to low trapped fractions (<0.2) as higher rates are used. We can fit the relationship with a power law shown on the right of Figure 3-19. The relationship in fact shows less dispersion that the viscosity relationship to injection rate.

We believe this general shape, i.e. a power law reduction of trapped fraction with increasing injection rate could be responsible for the shear-thinning effect of the foam. We provide a model for describing foam viscosity in terms of both the trapped fraction and including a notion of bubble sizes into the viscosity. Indeed, it may be that a dependence exists between viscosity and bubble size distributions, but only has been rendered negligible in front of the trapped fraction dependence.

In the previous section we showed that despite being linked to pressure gradient, the bubble density didn't have a major effect on the foam viscosity. However, it's possible that it has a minor contribution that is not obvious to observe in front of the considerable dependence of viscosity on the trapped fraction. We show the sum of bubble perimeters, which is closely linked to the bubble density as a function of injection rate in Figure 3-20:

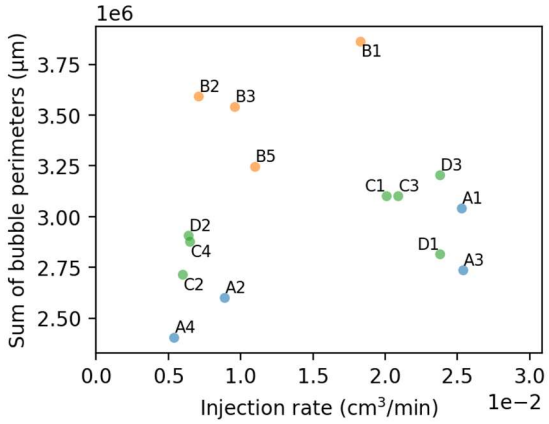

Figure 3-20: Total bubble perimeters in the model for each experiment in terms of injection rate.

We see that three clusters of points appear: the first one is shown by the lowest bubble sizes at all rates (highest sum of perimeters), i.e. the I2 injections. The other group clusters the I1 and I3 injections according to the injection rates, or odd and even experiments, with the lower injection rate group displaying lower observed total perimeters.

Interestingly, we observe that this data is complementary to the trapped fraction when comparing to the apparent viscosity measurements. For example, experiment A4 shows a high gas fraction but only a moderate apparent viscosity. The total bubble perimeter for this experiment is the smallest, however, implying a smaller bubble density and viscosity. Oppositely, the "B" experiments show a moderate trapped fraction, but high viscosities, with the experiment B2 showing the highest viscosity. The experiment B2 however has the largest total perimeter, explaining the higher measured viscosity.

Therefore, we propose to model the viscosity by sharing the rate dependence with the trapped fraction, i.e. using the same exponent as the trapped fraction fit to injection rate: -0.75. The viscosity will then be refined to integrate a fitted dependence to the total bubble perimeter for each experiment.

To integrate this information into the model we first take the exponent obtained from fitting the trapped fraction dependence to injection rate, that is -0.75, and fit the viscosity with this exponent. The residuals, i.e. the difference between the model fit and the data points, will then be fitted to a separate model that accounts for the total perimeter. The residuals from the fit also showed the strongest Spearman correlation (0.69) with the total perimeter, of all the observables and injection parameters described above. We show on the left of Figure 3-21 the model fit using the exponent gathered from the trapped fraction dependence, with the residuals shown on the right themselves fitted to an affine function of the total perimeter.

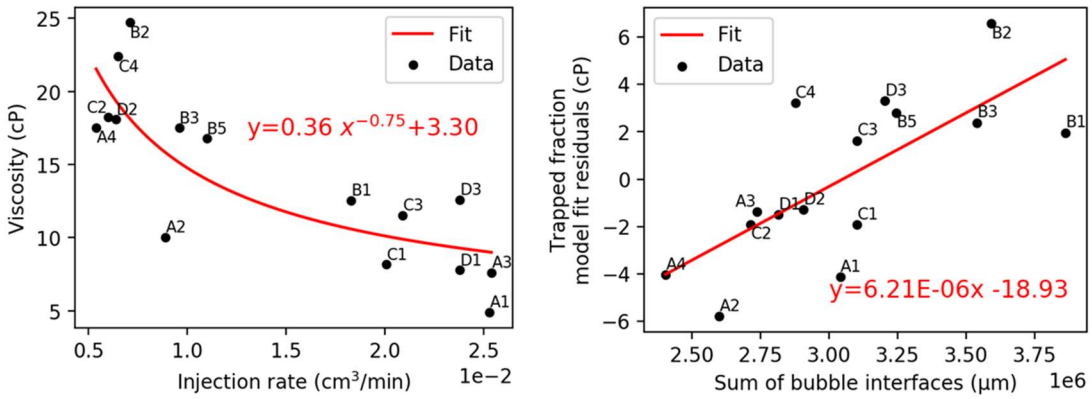

Figure 3-21: Left: Viscosity fit using the exponent from the trapped fraction dependence to injection rate. Right: Fit of residuals to the total perimeter using an affine function.

The fit from the residuals to the total perimeter then provides us with a second physical variable in the model. Finally, both fits shown in Figure 3-21 are added together to provide an estimate of viscosity in terms of both the trapped fraction dependence to injection rate and the total bubble perimeter for each experiment. We display the result in Figure 3-22, left, in which we show the measured data viscosity data points, the fit with the trapped fraction exponent only, and the data points fitted to the 2-variable model, detailing the final model in orange on the graph. On the right, we display a comparison of model prediction to measured values only.

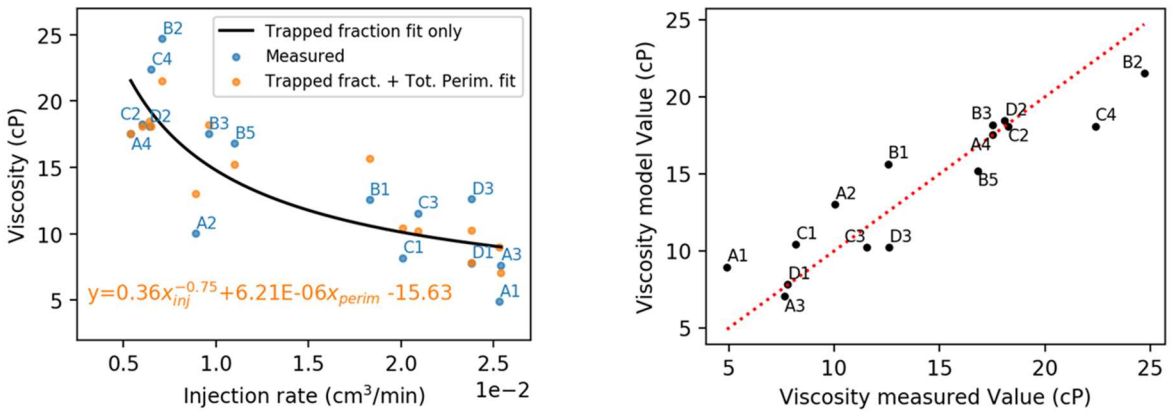

Figure 3-22: Final viscosity model using two parameters: the injection rate, with an exponent derived from fitting the trapped fraction, and the total perimeter, with parameters fitted from the residuals of the trapped fraction model.

The final fitted model points are shown in orange. As the model includes two parameters, we cannot show the model prediction as a continuous line such as for the trapped fraction model, but instead as isolated points just as the experimental data points. We observe that the final model points seem to achieve a closer prediction to the measured points that the simple trapped fraction fit. While the fitted and measured points are far from overlapping, they almost all move "in the right direction" when compared to the trapped fraction model. For clarity, only the labels of the measured data points are shown. The labels of the model points can be deduced easily as these points are on the same position on the x-axis as the experimental points. The 2-variable model also achieves a higher R^2 score than the simple fraction fit model at 0.83 versus 0.65 for the trapped fraction only model. The R^2 score is an established statistical measure of model goodness of fit. It is given by the amount of explained variance captured by the model divided by the total variance shown in the data. It is situation between 0 and 1, and for perfect models is equal to 1.

This model shows that trapped foams play a large role in determining the effective viscosity of a foam during an injection into a porous medium. The role of bubble density, approached here through the total bubble parameter in the model, also plays minor role in the model and serves to refine measured viscosities on top of the trapped fraction contribution.

3.5.2 Trapped fraction sources

As observed in the correlation table between injection parameters and observables, a non-negligible relationship exists between the trapped fraction and the inlet bubble distributions, with

the strongest being the relationship to the inlet bubble size standard deviation. We show this relationship in detail in Figure 3-23:

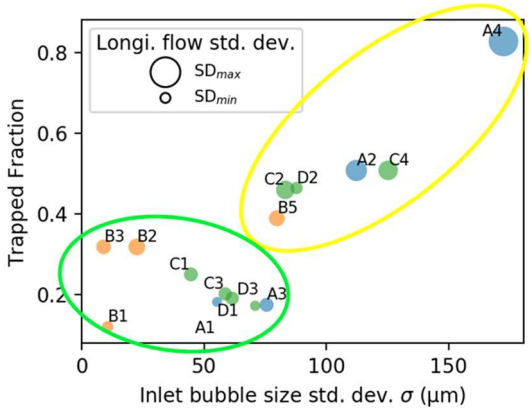

Figure 3-23: Trapped fraction dependence to inlet bubble size standard deviation. Two different groups are shown in colored circles.

We observe two groups of points within this plot. The first group, highlighted by a yellow oval in Figure 3-23, displays a positive relationship between the trapped fraction and the bubble size standard deviation. They also show a larger trapped fraction than all the other experiments. This group also includes the experiments with the largest degree of longitudinal flow distribution standard deviation, expressed by the marker size. The second group, highlighted by a bright green oval, displays low trapped fractions with a lower (and even seemingly inverse) relationship to the inlet bubble size standard deviation. Combined with the knowledge of mean bubble sizes (Figure 3-6), we note that the B1, B2 and B3 experiments furthermore have bubble sizes lower than the mean throat size. This gives some reason to believe that the trapped fractions observed in both experiments have different origins. While the trapped fraction for experiments shown in the yellow oval show a strong dependence to the inlet bubble size standard deviation, the trapped fraction for the second group must have a local origin, perhaps of a structural origin, rather than being a direct consequence of inlet flow distribution parameters. To explore this hypothesis, we look at some flowmaps for each experiment.

When observing the flow maps for experiments in the yellow group, we observe that foam is only flowing in certain zones of the model with other entire sections devoid or containing less flow. Figure 3-24 shows four examples of flowmaps for experiments in the yellow group.

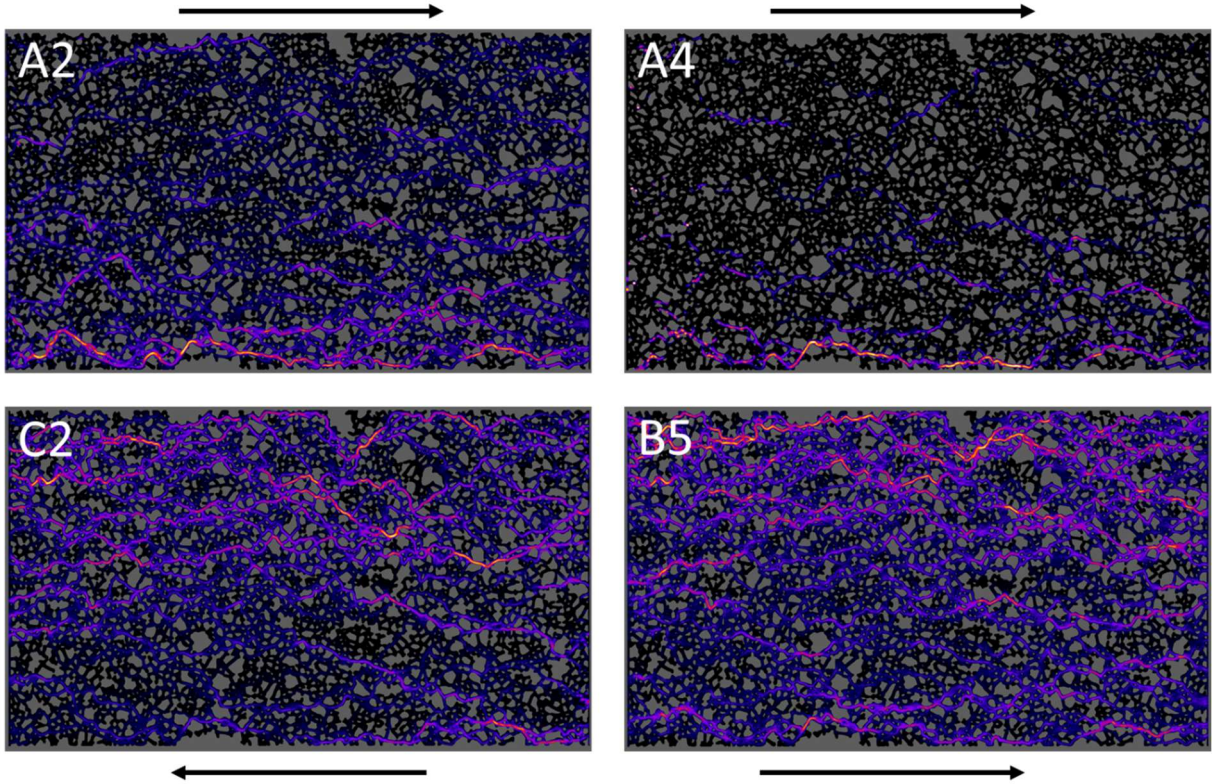

Figure 3-24: Overall flowmaps for four experiments belonging to the high trapped fraction group shown in yellow in Figure 3-23. The images have had their intensity equalized over the longitudinal direction according to process described in Chapter 2, Appendix 2-C. The black arrows indicate the flow direction.

We first note that in all these experiments a significant longitudinal portion of the flowmap contains less flow. From the extreme case of the A4 experiment in which only a few flow lines in fact visible, to the more moderate case of the B5 experiment in which the lower half contains less flow, while still showing some flow at both extremities. This fits well with the theory that the trapped fraction corresponds to a global trapped area of the model, representing a large portion of the model, rather than small isolated pockets. As we observe that the areas containing flow can change between the different experiments, (i.e. upper half for A2, A4, lower half for C2, B5), this indicates that inlet bubble properties determine to a great degree the downstream flow distribution in the model and the trapped foam fraction visible here.

Looking at images of the inlet distributions themselves, we see that locally drier foams at either side of the inlet tend to inhibit flow in the corresponding section of the model. We illustrate this by showing in Figure 3-25 an inlet distribution of experiment A4, where a visible foam dryness gradient is observed over the model inlet. The drier foams on the right-hand side of the image are

noticeable by the thinner lamellae that appear less dark, and the angular junction points between the lamellae and the solid medium.

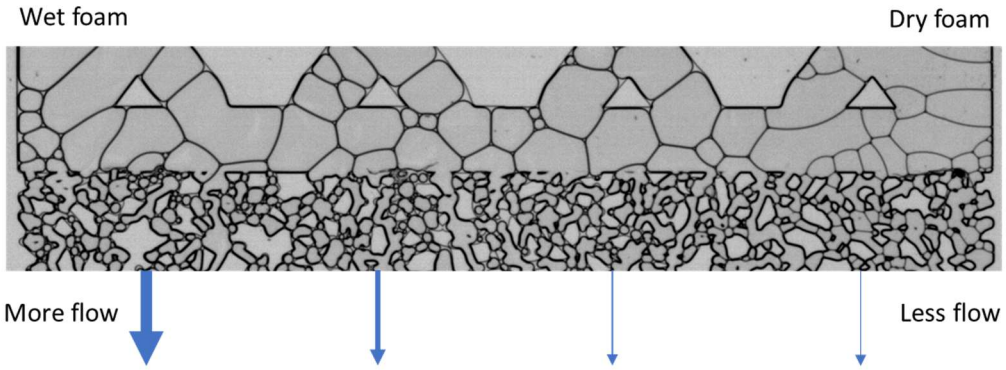

Figure 3-25: Foam dryness gradient over the model inlet for experiment A4, and the effects on the flow distribution that this causes.

The drier foam inlet areas create a lower flow in the same downstream sections of the model. The existence of foam dryness gradients is a consequence of the lower injection rates and the larger time of travel in the tubing leading to the model from the foaming device for injection types I1 and I3. Slower injection rates do not necessarily lead to foam dryness gradients, as observed by the I2 type experiments (in which case the tubing is much shorter). In the case of the I1 and I3 experiments, the larger time spent travelling as bulk foam in the tubing leading up to the model allows diffusion and coalescence processes to coarsen the foam and create variations in dryness and bubble size at the same time. Therefore, a strong correlation is observed between the trapped fraction and the bubble size distribution standard deviation. Hiding behind this correlation is in fact the local foam dryness variance that is responsible for blocking off certain zones of the model.

While the large dryness variance is a product of the lower injection rates and large travel time in the tubing, its effect is compounded by the fact that lower injection rate experiments will show higher sensitivity to local variations in foam dryness, as the pressure gradient becomes insufficient to displace certain areas of the inlet foam.

In comparison to these examples, we show in Figure 3-26 the flowmaps for experiments situated in the lower group, i.e. the group circled in green showing lower trapped fractions and lower longitudinal flow standard deviation.

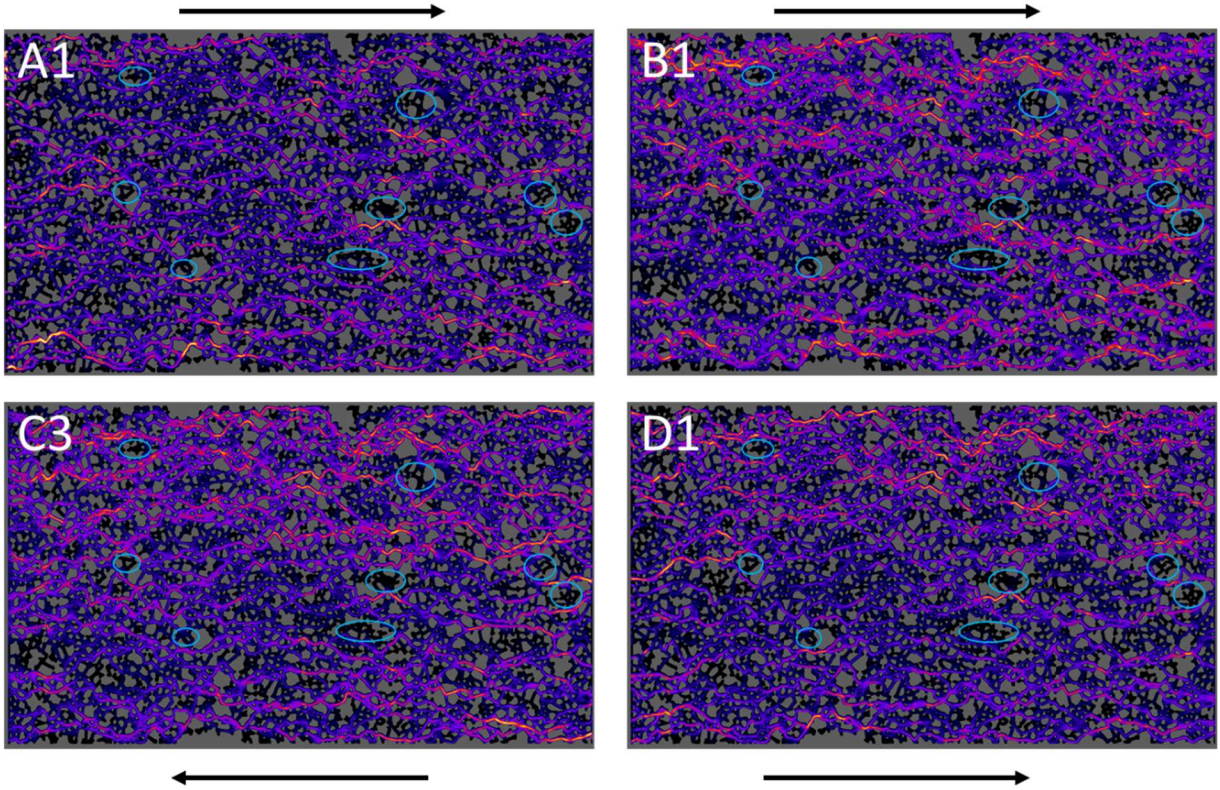

Figure 3-26 Overall flowmaps for four experiments belonging to the low trapped fraction group shown in green in Figure 3-23. The images have had their intensity equalized over the longitudinal direction according to the process described in Chapter 2. The black arrows indicate the flow direction.

These images have the common characteristic of displaying well distributed flow in all sections. The trapped fractions in these experiments are dark patches in the model, rather than entire sections, that correspond to areas that are locally disadvantageous to flow. Also, we can note that the darker areas are consistent in all experiments, even in the C3 injection which was performed in the opposite way. Some dark areas that are common in every flow map have been highlighted in light blue. This is a strong indication that the trapped foam fractions in these experiments are of a structural nature and are common to all the experiments with high injection rates and low inlet size distribution.

Therefore, we can identify two separate sources for the trapped foams. First, for some low flowrate experiments that travel a large distance from the foaming device, the variance of foam dryness as well as bubble sizes in the injected foam can account for a large degree of the trapped fractions observed in the model. Furthermore, we observe that the sections of the model that are trapped can change between experiments. For these reasons, we believe this phenomenon naturally doesn't

have a structural origin. The second type of trapped foams can be observed in certain isolated areas of the model, and are much smaller in size, spanning perhaps a few pores and throats. These areas seem to be consistent throughout all the experiments, displaying almost no flow in every case. We suspect these zones can be characterized structurally.

3.6 Conclusion

Throughout this chapter we show a series of experiments on a single micromodel. We spend time to characterize the injections and observed flow in an extensive way. For the injection characterization, we identify parameters relating to the bubble size distributions as well as the injection rates and foam qualities. The specific injection method was also noted. Flow observables can be divided into different categories. They can be either macroscopic, such as pressure gradient and flow variance between datasets; microscopic, but taken over the complete model, such as the trapped fraction and the passage activation mean, or finally relating to the bubble size distributions in the model or at the outlet, such as the mean bubble size ratio or the total measured perimeter.

We observe that several injection parameters evolve together in the experiments (such as injection rate and the mean bubble size) creating difficulty establishing causal links between the different correlations found with the observables. For the model observables themselves, we note that many describe similar information in different ways and show significant correlation, such as the trapped fraction, the longitudinal section flow distribution and the activation mean.

We observe that the trapped fraction is a key observation in linking macroscopic to microscopic parameters as it correlates strongly with pressure gradient and viscosity. We then propose to fit the viscosity evolution with injection rate using the same exponent as the evolution of trapped fraction (-0.75), and further refine the model with the addition of a dependence to the total sum of bubble perimeters in the model.

Finally, we show that in fact the trapped fraction can have different origins. For low flow rates, a high trapped fraction can be a consequence of inlet bubble properties, creating blocked off areas downstream. Separately, some smaller, specific trapped zones are repeatedly observed in every experiment leading to the assumption that they have a structural origin and necessitate a deeper structural investigation.

Chapter 4. *Predicting Local Flow from Structural Parameters: A Machine Learning Approach*

Preamble

Within Chapter 3, an initial parameter search was performed to attempt to link local flow properties with local structural properties of steady state foam flow in a 2D micromodel based on the measured intensity in the averaged flow map for the experiment A1. We attempted to link local pore area and throat radius to local flow intensity, and with reference to recently published work, attempted a semi-local approach, in which chains of large connected pores and throats of varying length, as well as large connected pores and throats aligned with pressure gradient were checked for positive relationships with flow. No overarching relationship was observed indicating that either a more complex approach is needed, i.e. a large-scale modelling effort, or that the structural parameters used were not the most relevant parameters to describe flow.

In this section we perform a more in-depth local structural approach, both in terms of the diversity of structural parameters used, and in terms of the methods employed to integrate these parameters into a complex prediction framework of local flow.

For this section we shall employ some terminology specific to data science, in which a model will use a series of features (in our case structural local parameters) to predict a target (data pertaining to flow intensity).

4.1 Modelling framework and goals

In this chapter, we will make comparisons between various modelling approaches. We will use algorithms available in the scikit-learn machine learning (Pedregosa et al 2011) Python package to generate different local models to predict flow properties. The algorithms train classifiers that will attempt to discriminate between elements labelled either active or inactive, that are labelled using different average velocity intensity thresholds as previously described. Thus, our classification attempts will always only use two distinct classes – active or inactive - in each case, otherwise known as binary classification. We strictly use supervised learning algorithms, which

will divide the available (already classified) data into two sets, by randomly selecting a fraction of data samples and setting it aside as a test set. The machine learning algorithms will then be trained on the remaining training set, i.e. the algorithm will attempt to establish why each sample was attributed to either class, to produce a trained model. The model will then be used on the test data that has been kept aside and not seen by the model, to check for model generality, using a given evaluation metric.

Comparing the different model results represents a small challenge. Indeed, some classes are unbalanced (i.e. only a few pores exceed the highest intensity thresholds) and determining the accuracy of predictions in this case requires more complex evaluation metrics than simply the percentage of correct predictions. We shall give more information on the metrics used as we progress through the analysis.

Initially we label the samples as we have a continuum of average velocity values. In other words, we establish which are to be considered active or inactive before any models are used. The same labelling procedure is used for both throats and pores, although performed separately. The elements (3698 pores or 6284 throats) are split up into 19 distinct size categories (according the pore area or throat radius) with the same number of samples in each (see later in Structural parameter space). In Chapter 2, we classified active and inactive pores by setting a threshold average intensity value within each size category. The threshold chosen was half of the average pore intensity for each size category, with samples in the size category above this value were considered active. Supplementary classifications will be done by setting thresholds that are equal to the mean intensity value itself and one and a half times the mean intensity value. In this way, modelling a series of different classification thresholds will make it possible to understand what characterizes the elements with the least flow as well as those with the most flow separately.

The choice of successive binary labelling with different thresholds was done for clarity and interpretability. Indeed, as we use four labels in total (inactive in all classifications, active, highly active, very highly active), separated by three thresholds, the problem could be assimilated to a multi-class problem in which the algorithm's role was to attribute each element to one of the four classes. However, we believe this style of classification would lead to less interpretable results. For example, while it can be possible to extract the general importance of each feature in multi-class classifiers, it is more difficult to extract the specific features responsible for classifying one

class versus another, whereas in a series of binary classifiers the feature importances are rendered explicit in each case. This is also the reasoning for not performing a regression-type analysis in which predicted values are not discrete class labels but continuous numerical values, which could have typically been average element intensity here. A regression framework was avoided to account for the potentially different structural sources between low flow zones or very high flow zones. Creating one large function to predict, let's say, the whole spectrum of pore intensities seems inapplicable when the flow state of each pore can have distinct structural origins. Certain mechanisms are responsible for creating trapped foams while on the other end of the spectrum, the high flow pores could be explained structurally by other parameters than those involved in trapping. Such global models would then either lack predictive power or would be hard to interpret and convey less information on the specificities of belonging to each intensity category.

We will perform our analysis on a series of flow maps from different experiments and different bubble size categories to check for differences in key local structural elements for each case. An analysis will also be done comparatively to the numerical experiments.

4.2 Classification types

In this section, we shall give some examples as of how the measured velocity intensity data for pores and throats can be labelled based on their relative intensity.

We use the data from experiment A1 and show three types of classification. In each case a different threshold is used for diving up the elements of a size category.

As described in Chapter 2, we demonstrate that categorizing each element based on size, and then performing a classification relative to the mean values within that size category removes any assumptions relating to the way velocity intensity is spread out over the different pore sizes. We perform this classification individually in every size category despite the evident lack of correlation between average intensities and sizes, as evidenced in Chapter 2 during the initial structural search. While no global effects can be seen, some larger pores or throats may be prejudiced as they only contain one or two flow tracks within their whole area. We show examples of splits for data of pores on the total flowmap of Experiment A1, in Figure 4-1.

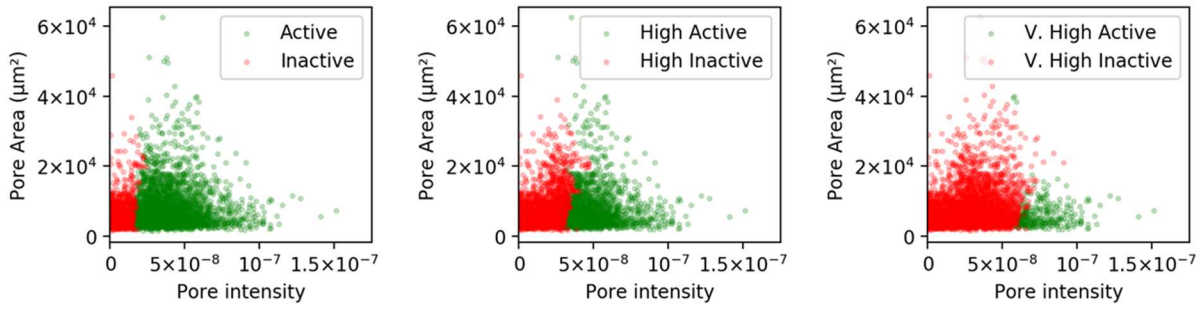

Figure 4-1: Different binary classification splits used for model classifiers. The leftmost plot splits pores based on a threshold of half the average measured velocity intensity for their size category. The central plot simply takes the mean as threshold for each size category. The plot on the right takes 3/2 the mean as a threshold value for each size category.

In any case, the classifications of the data show that the different types of classification in fact show little sensitivity to pore area, splitting active and inactive elements mainly based on average pore velocity intensity. For some types of flow maps, the average pore intensities are much closer together than shown here, typically the numerical experiments which show higher flow homogeneity.

4.3 **Machine learning algorithms**

Here we shall describe in limited detail the different model types used and the motivation for them. The aim of a binary classifier is to establish a border to separate the feature (parameter) space into two different zones based on a classification rule. This border is called the decision boundary. In our case the feature space is the available structural parameters and the zones represent active or inactive elements. Obviously, only the structural parameters are used by the models to predict activity and the element velocity intensity is not accessible by any of the algorithms.

The decision boundary between the two classes can take many forms, just as the models that lead to its definition. For a simple, 2-dimensional space, a decision boundary is the curve that splits the two classes in the best way (according to the evaluation metric chosen). For higher dimensional problems of n dimensions, the decision boundary is therefore a hypersurface of dimension n-1.

The border can be either expressed analytically or defined by a limited number of in-model parameters which limit the model degree of freedom. This is what is known as a parametric model. On the other hand, non-parametric algorithms create decision boundaries that become increasingly complex when adding training data. For example, adding a series of “if” statements regarding

feature values such as for a decision tree, or averages of feature values themselves creating "nearest neighbor zones" which can be used to decide to which class a new data point should belong.

We give some examples here to show that different algorithms were tested, before focusing on the classifiers that worked best on our data, and finally documenting the features used to construct the decision boundary and how they affect its definition.

While we don't provide mathematical details of model functioning or justification here, we shall still briefly summarize the classification algorithms used. All the following classifiers have in common that they require some tuning of "hyper-parameters", or algorithm parameters, that necessitate user intervention, in order to creating models that are neither too general (under-fitting) nor too specific (over-fitting) to the data provided in the training data set.

The different algorithms we will describe here are K-nearest neighbors, Logistic Regression, Decision Tree and Random Forest. To grasp some of the behavior of the algorithms, we initially show fitted models that attempt to classify three types of input data sets, each represented by a different row in Figure 4-2. The classes both have a same number of samples in each case. The locations of the data points were generated showing a small amount of random noise but according to some rules that create data either clustered in a linearly separable way (top row), clustered according to interleaving moon-like shapes (central row) and not clustered at all (bottom row). The training set points are shown as semi-transparent color whilst the test sets are shown in full color. The vertical and horizontal axes represent two arbitrary dimensions and have no physical meaning. The model accuracy (fraction of correct test data predictions) is shown as a white number in the bottom right hand corner.

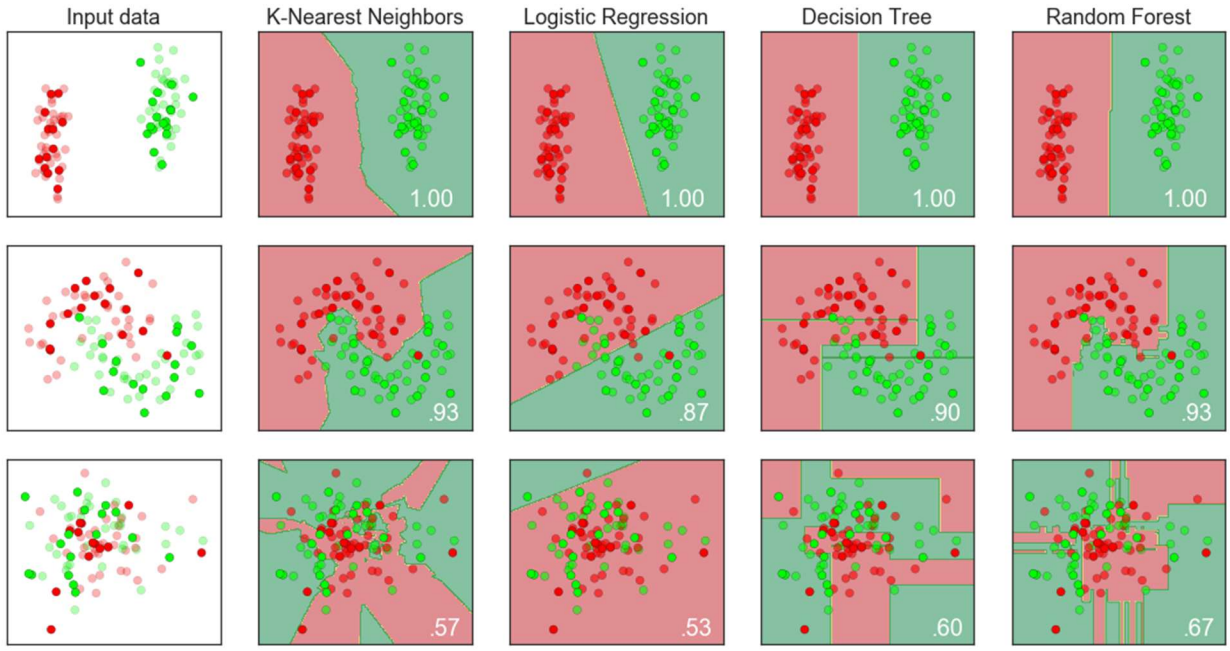

Figure 4-2: Different input datasets and models with shown accuracy on a 60/40 train/test data split.

In these plots, the initial data is given on the left column, and the successive model attempts at classifying the data is shown in the following columns. A contour plot showing the model prediction and decision boundary is shown as a contour plot in the background. Python code for creating visualizations of this type is available online[1].

The top row is well classified by all the models, all achieving an accuracy score of 1. The middle row boundaries are required to be of a more complex shape to correctly predict the data, and the linear logistic regression model achieves a lower score. The bottom row shows data that demonstrates too much mixing to be separable in a meaningful way, and we see the models struggle to classify a situation in which no generalizable classification can be done.

We see some of the main features that distinguish these models from the figure instantly.

We observe that the decision boundaries for the K-nearest neighbors, Decision tree and Random Forest are clearly non-parametric, while it is linear for the Logistic Regression. We shall give some

[1] https://scikit-learn.org/stable/auto_examples/classification/plot_classifier_comparison.html

more detail regarding these models in the next section. Note that parametric models are not necessarily linear and such decision boundaries can take polynomial or other shapes.

4.3.1 K-nearest neighbors

When considering a new data point, this model straightforwardly takes the majority class of the K-nearest already classified neighbors and attributes it to the point under evaluation (Altman 1992). The distance used to establish the first K neighbors is usually the Euclidian distance from the point. Each point of the feature space can be attributed to a class this way and a decision boundary is formed. The number of neighbors represents a hyperparameter chosen by the user. In the case above it is chosen as 3. A higher number of neighbors tends to smooth the decision boundary and generalize the model. Consequently, this model is highly sensitive to the different scaling of features. This means that features that vary between large numbers (for example pore area which can be arbitrarily large) will contribute to the Euclidean distance in the feature space to a much larger degree than features with smaller ranges (such as cosines that vary between 0 and 1). In this form, K-nearest neighbors only defines neighbors based on the most highly varying features. One simple solution is to scale them all to a common range (say 0-1), but even when scaled, features of different importance (i.e. different usefulness is achieving correct predictions) are given equal value in deciding the closest neighbor. This simple version of the K-nearest neighbors algorithm is not robust to irrelevant features and perhaps isn't the best choice for our task which requires filtering out the less relevant features.

4.3.2 Logistic regression

Logistic regression is a historical algorithm (Walker and Duncan 1967) still finding a lot of use today. Despite its name, logistic regression can be used for classification problems. In linear regression, the input variables X_1, X_2, ..., X_n are combined in a linear equation, each with an associated weight β_1, β_2, …, β_n such as $y = \beta_0 + \beta_1 X_1 + \beta_2 X_2 + \cdots + \beta_n X_n$

The sigmoid $p = 1/(1 + e^{-y})$ is then applied to the linear function, which is constrained between 0 and 1. Choosing a cutoff value between 0 and 1 then serves to determine the data points as either class. The logistic regression algorithm then finds the correct set of features and model weights that best classify the training set on either side of the cutoff value.

4.3.3 Decision tree

This algorithm learns a series of rules that best split the data according to the classes. Decision trees have been historically present in many contexts but are studied in detail by Breiman et al. (1984). Successive rules can be applied on each side of an initial decision, creating the "branching out" of a tree. The created models are both simple to visualize and interpret. One large benefit of this algorithm is that it combines different types of data (in our case, continuous data such as angles or sizes, with integer values such as coordination), and is non-sensitive to the scaling of features. We can see the shape of the boundary created by a decision tree model, i.e. a series of cuts in the feature space. We believe this type of model may be well fitted to our problem. Indeed, certain flow situations may have multiple, non-interacting origins. For example, a low flow zone may either be impossible to access due to a very small entrance throat, but not only. Some low flow zones are simply in poorly connected areas, turn away from flow direction, or are next to flow zones that are highly advantageous and contain all the flow. As these multiple conditions are not necessarily linked and integrate different data types, they cannot be easily modelled by a continuous function, and require a series of conditional statements to be best expressed.

4.3.4 Random Forest

Random forests (Breiman 2001) are combination of decision trees that are all trained independently on different subsets of the available training data, which are then averaged to provide a more general prediction. Random forests are what is known as an ensemble machine learning method, combining multiple weaker predictors that by themselves do not achieve significantly greater predictions than random. When combined, using either a majority vote system or a more complex rule, these weaker predictors can achieve much higher accuracy.

4.4 Structural feature space

Here we list the features used in the prediction process. All the features used here are local or are related to local features in the close neighborhood of either the pore or throat.

4.4.1 Throat structural features:

We measure some geometrical features associated with each throat. However due to the simplified geometrical properties of the throats extracted from the images (i.e. 1D lines), strictly geometrical

features related to the throats are only radius and the orientation angle ν, describing the angle of the normal of the throat in relation to the positive pressure gradient direction.

We define some other features related to the positioning and orientation of the throat in relation to the two pores that are connected by the throat. Specifically, we give the angle μ, defined by the alignment of the centers of mass of the pores in relation to the pressure gradient, and distances between the centers of mass of the pores ΔPP, as well as the total distance between both pores passing through the throat center ΔPtP. We also define distance between pore centers in the Y-direction Δ_yPP. A visual description of these features is given in Figure 4-3:

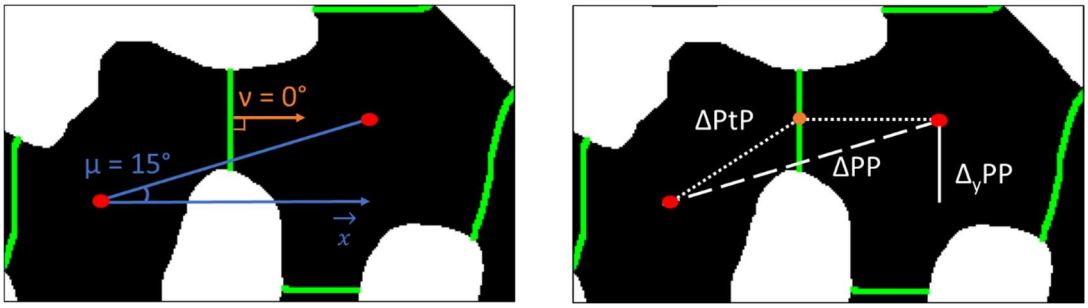

Figure 4-3: Visual description of some throat features. Pores are shown in black separated by throats in bright green. Pore centers of mass are shown as red circles. The throat orientation angle ν is given by the angle between the normal to the throat (shown in orange) and the positive pressure gradient, in this case ν is equal to 0. The orientation the neighboring pores centers of mass in relation to pressure gradient is given by the angle μ. The distance from neighboring pores centers of mass is given by ΔPP (shown in thickly dashed white). The total distance between the centers of mass passing by the throat center is given by ΔPtP (shown in thinly dashed white).

One final feature that necessitates some description is the equivalent hydraulic length of the throat. We can extract a characteristic hydraulic length from each throat with the knowledge of the surrounding pore shapes that it separates.

In classical Pore Network Modelling, throats are defined by constant length. However, in real media, such as the network shown here, the throat opens progressively to the pore and as such, a simple distance measure such as the ΔPtP to associated pores may be a poor descriptor of the length associated with each throat. We therefore propose to integrate the hydraulic length l_{eq} for 2D media. The hydraulic length is described in more detail in Youssef et al. (2007). While this derivation may apply specifically to circular canal cross-sections, we still include it in our

analysis due to the added information it provides, and due to the relatively smooth flow corners we can expect from the acid etched glass micromodel.

It is defined by analogy to the equivalent conductance g_{eq}, as the sum of n elements (pixels) in series, each of length l_i, radius r_i and conductance g_i. The fluid conductance of a fluid of viscosity μ in an elementary cylinder i is defined by $g_i = \frac{\pi r_i^4}{8 \mu l_i}$. The conductance g_{eq} of the equivalent cylindrical tube of radius r_{min} is defined by:

$$\frac{1}{g_{eq}} = \sum_{i=1}^{n} \frac{1}{g_i} = \sum_{i=1}^{n} \frac{8 l_i}{\pi r_i^3} = \frac{8 l_{eq}}{\pi r_{min}^3} \tag{28}$$

The equivalent hydraulic length is then given by:

$$l_{eq} = \sum_{i=1}^{n} l_i \left(\frac{r_{min}}{r_i} \right)^3 \tag{29}$$

The process for accessing the hydraulic length is described visually in Figure 4-4:

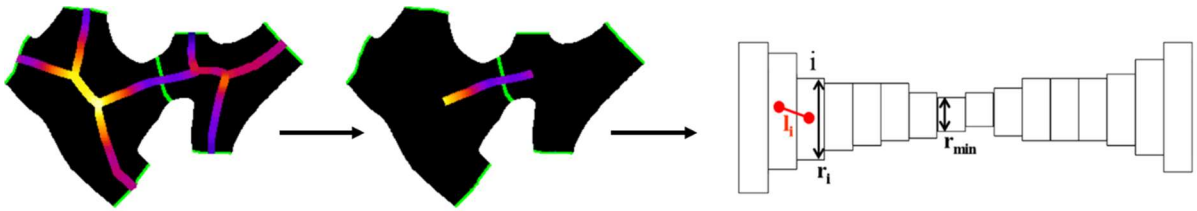

Figure 4-4: Process for access the hydraulic length l_{eq}. The diagram on the right was taken from Youssef et al. (2007).

Using a distance map of the porous medium, we can gain access to the distance of each pixel from the nearest grain. When skeletonizing the porous area, and selecting this area on the distance map, we can access the distance from the solid grains at every point along the skeleton of the porous medium. This is shown in the left image of Figure 4-4 as a colored vein superimposed on two black pores with a central throat in bright green. Warmer colors represent higher distances from solid grains. The skeleton is enlarged here for clarity. We use the central branch of the skeletonized distance map only, intersecting the throat of interest. It is accessed with the Strahler Analysis ImageJ plugin (Tiago Ferreira 2016), and shown in the central image. As the image is pixelated, in our analogy l_i is constant throughout. The hydraulic length is then accessed by summing the

ratios $\left(\frac{r_{min}}{r_i}\right)^3$ along the central branch, as shown in the image on the right. We now list the features available to the machine learning algorithms for the throats.

a) **Geometrical features used:**

The following two features are purely geometrical properties of the throat

- **Radius (r):** As some throats are not straight lines, in fact we take the Minimal Feret diameter for each throat as a measurement of throat radius for extra precision.
- **Throat angle ($\cos \nu$):** We take the cosine of the angle of the throat orientation in relation to pressure gradient as described above

b) **Neighborhood features used:**

The following features consider properties and positioning of the throat relative to the 2 pores associated with the throat.

- **Pore-to-pore angle ($\cos \mu$):** We take the cosine of the angle of the pores in relation to the pressure gradient as described above
- **Pore-to-pore center distance (ΔPP):** Distance between neighboring pore centers
- **Pore-to-pore center Y distance ($\Delta_Y PP$):** Y distance between neighboring pore centers
- **Pore-to-throat-to-pore center distance (ΔPtP):** Distance between pore centers passing through the throat center.
- **Hydraulic length (l_{eq}):** Equivalent hydraulic radius as described above.
- **Areas average:** Average areas of the two surrounding pores
- **Areas max.:** Maximal area of the two surrounding pores
- **Areas min.:** Minimal area of the two surrounding pores
- **Coord average**: Average coordination of the two surrounding pores
- **Coord max.:** Maximal coordination of the two surrounding pores.
- **Coord min.:** Minimal coordination of the two surrounding pores.

c) **PCA analysis**

Finally, as we have many highly correlated features representing sometimes small refinements or combinations of other features, we perform a simple PCA (Principal Component Analysis) to visualize some of the features that evolve together. Principal component analysis is orthogonal

transformation that creates a series of linearly uncorrelated components from an initial input of possibly corelated variables. It is an example of dimensionality reduction creating a new coordinate system that best explains the variance of the data. In our case we shall use the first 5 principal components, given in order of decreasing encapsulation of data variance. In Figure 4-5 we show both the magnitude of the contribution to each principal component and the direction of the contribution, i.e. whether the initial variable correlate positively or negatively to the created component. The relative contribution of each component to explaining the total data variance is also given.

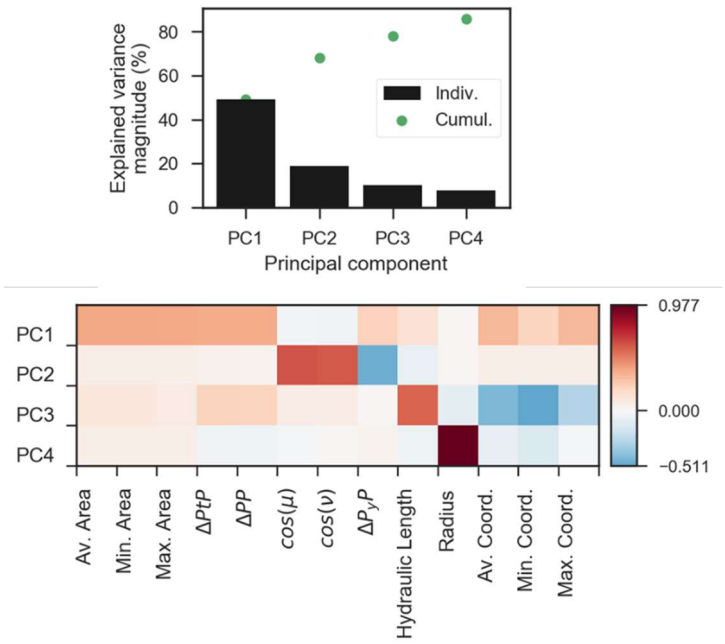

Figure 4-5: Principal component analysis of throat structural features. The amount of data variance explained by each component is shown at the top. The bottom plot shows the specific composition of each component. The colorbar indicates the degree of either negative or positive correlation of the input variable to the created component, and color is unrelated to principal component explained variance magnitude.

We note that the first component captures most of the total data variance, likely due to the large number of features that correlate in the same way. PC1 relates mainly to the surrounding pore properties. The second component describes the alignment of the throat with respect to pressure gradient, as described by both angles (also correlating negatively with the Y-displacement between the neighboring pores). A third component mostly describes the variance due to the hydraulic length of the throat and coordination, while in the fourth describes uniquely the variance of throat

radius. The purity of the PC4 component shows the throat radius values are independent of other features shown here.

4.4.2 Pore structural features

A larger number of features are available for the pores than for the throats. Indeed, the pores are represented by 2D areas and can have more geometrical properties than the 1D lines representing the throats. The purely geometrical features were obtained from applying the ImageJ plugin Shape Filter on the pores (Wagner, T and Lipinski, H 2013). Several features were also extracted from the immediate neighborhood properties of each element. For example, for each pore, the average area of the surrounding pores, or the average radius of the throats leading to the neighboring pores was calculated. We will now list the features we included for pore prediction process.

a) **Geometrical features**

The following geometrical feature descriptions were taken from the Shape Filter Plugin description website[2]:

- **Area ($\boldsymbol{A}$):** measured as the entirety of the area making up the pore as given by the watershedding process
- **Area of convex hull ($\boldsymbol{C}$):** can be visualized as the area a rubber band would take if surrounding the pore
- **Max. inscribed circle diameter:** the diameter of the maximal circle that can be inscribed inside the pore
- **Perimeter ($\boldsymbol{P}$):** The perimeter of the pore
- **Perimeter of convex hull ($\boldsymbol{H}$):** The perimeter of the previously described convex hull
- **Feret diameter:** The largest possible distance between two parallel tangents to the pore outline not intersecting the pore
- **Min. Feret diameter:** The smallest possible distance between two parallel tangents to the pore outline not intersecting the pore
- **Long side Minimum Bounding Rectangle ($\boldsymbol{L}$):** The larger side of the minimum bounding rectangle
- **Short side Minimum Bounding Rectangle ($\boldsymbol{S}$):** The smaller side of the minimum bounding rectangle
- **Aspect ratio:** Defined as $\frac{L}{S}$

[2] https://imagej.net/Shape_Filter

- **Area/Perimeter**: $\frac{A}{P}$
- **Convexity:** Defined by $\frac{H}{P}$
- **Solidity:** Defined as $\frac{A}{C}$
- **Orientation:** The angle of the major axis of the pore from the direction of pressure gradient.

b) **Neighborhood geometrical properties**

The following features were taken from the knowledge of the network properties:

In the following, many of the features have the same definition but are applied to the 1st neighbors, 2nd neighbors etc... We will denote the dependence to the neighbors by using the general notation n as referring to the nth neighbor only.

- $\boldsymbol{n}$ **- Coordination:** The number of n^{th} neighbor pores
- $\boldsymbol{n}$ **- Areas Average:** The average areas of the n^{th} neighbors
- $\boldsymbol{n}$ **- Areas Max.:** The maximal area of the n^{th} neighbors
- $\boldsymbol{n}$ **- Areas Min.:** The minimal area of the n^{th} neighbors
- **Up to** $\boldsymbol{n}$ **- Areas Average:** The average areas of all the pores up to the n^{th} neighbors
- **Up to** $\boldsymbol{n}$ **- Areas Max.:** The maximal area of all the pores up to the n^{th} neighbors
- **Up to** $\boldsymbol{n}$ **- Areas Min.:** The minimal area of all the pores up to the n^{th} neighbors
- $\boldsymbol{n}$ **- Throats Size Average:** The average size of throats leading to the n^{th} neighbors specifically
- $\boldsymbol{n}$ **- Throats Size Max.**: The max. radius of throats leading to the n^{th} neighbors specifically
- $\boldsymbol{n}$ **- Throats Size Min:** The min. radius of throats leading to the n^{th} neighbors specifically
- **Up to** $\boldsymbol{n}$ **- Throats Size Average:** The average radii of all the throats leading up to the n^{th} neighbors
- **Up to** $\boldsymbol{n}$ **- Throats Size Max.:** The max. radius of all the throats leading up to the n^{th} neighbors
- **Up to** $\boldsymbol{n}$ **- Throats Size Min.:** The min. radius of all the throats leading up to the n^{th} neighbors
- $\boldsymbol{n}$ **- Throats** $(\boldsymbol{\cos\nu})$ **Average:** The average cosine of the angle between the normal vector to the throat and the pressure gradient direction, of the throats leading to the n^{th} neighbors
- $\boldsymbol{n}$ **- Throats** $(\boldsymbol{\cos\nu})$ **Max.:** The max throat angle cosine leading to the n^{th} neighbors
- $\boldsymbol{n}$ **- Throats** $(\boldsymbol{\cos\nu})$ **Min.:** The min. throat angle cosine leading to the n^{th} neighbors
- $\boldsymbol{n}$ **– Throats Hydraulic Length Average:** The average hydraulic length as defined above

The number of neighbors n can be chosen as desired. We shall use a value of $n = 3$ when using these features in the machine learning algorithms.

c) **PCA analysis**

As done for the throat features, we shall perform a PCA analysis on the pore structural features. For clarity, here we only show the PCA analysis of the components up to the 2nd neighbors (i.e. $n = 2$). As PCA is sensitive to the scaling of features, prior to this analysis a standard feature scaling is applied to each feature individually. The standard scaling removes the mean of the feature from each instance and scales to a unit variance. It is a standardization method that essentially sets all features on an equal footing for scale-dependent methods. We show the top 5 PCA components in Figure 4-6.

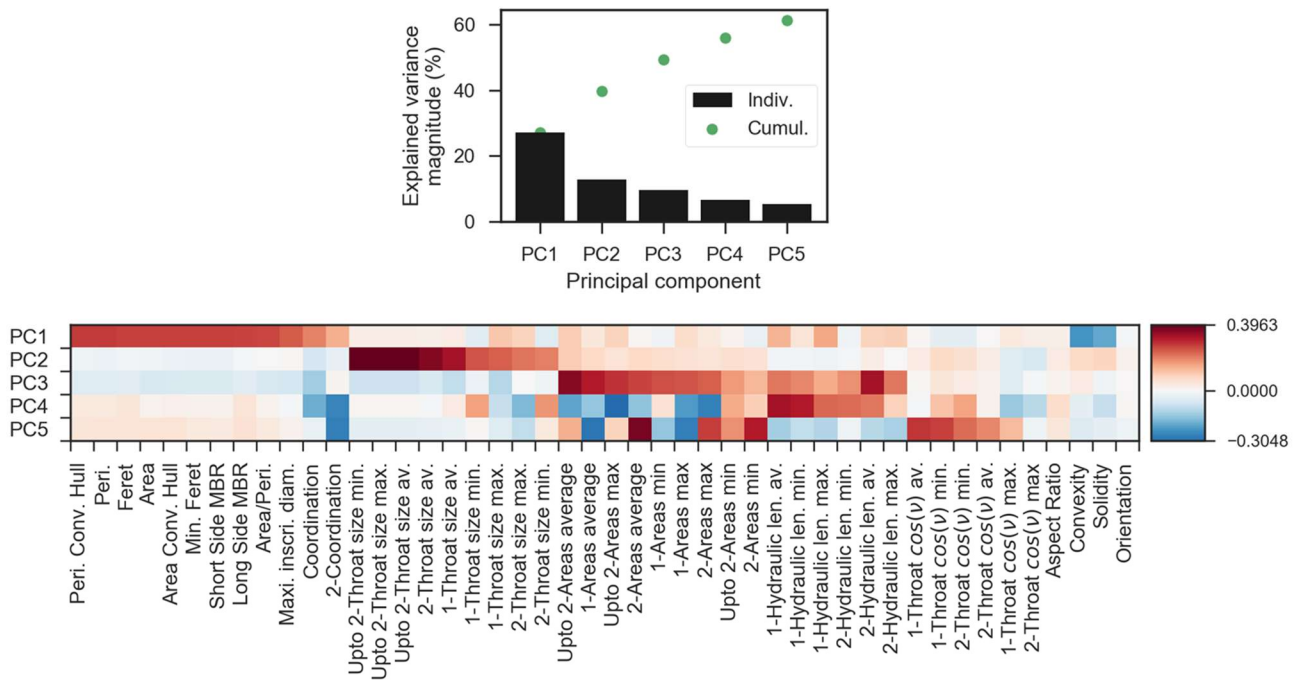

Figure 4-6: Principal component analysis: First 5 principal components of the pore structural features.

We note that the first 5 principal components only represent 67% of explained data variance, shown by the cumulative sum. In the bottom plot, the successive components have been organized into classes according to their origin and ordered showing the most important features in each component clearly.

We observe that variance follows coherent structural patterns. The most variance is explained by a component that follows the evolution of the pore areas and correlated features (i.e. perimeter and other size statistics). Secondly, surrounding throat properties relating to throat size (i.e. throat length) showing their own distinct variance are found to correlate together within PC2. A third component (PC3) is created from the correlated variance of the pore size neighborhood properties and to a certain degree hydraulic length. The fourth component captures in great part the correlated variance of the hydraulic length properties, but also non-negligible variances of other features. The final component uses the common variance of the throat angle properties but also shows significant common variance with other features. The grouping of the features according to these structural groups is done statistically by the principal component analysis and is in no part due to user intervention. It is also to be noted that this analysis does not show which features are the most useful for predicting flow, as they could be irrelevant. Instead this shows the relationships between input data and the distribution of variance to which machine learning algorithms can be highly sensitive, depending on the exact algorithm used.

4.5 Algorithm selection

In this section we shall make a preliminary comparison of the different algorithms to then focus on the ones that predict best the different velocity intensity classes.

4.5.1 Metric used

To compare different models, we use the scoring metric of balanced accuracy, given the sometimes-unbalanced numbers of each class we have. When quantifying the result of a binary classification prediction, we create what is known as a confusion matrix.

The model will predict that some samples are in the first, or positive class, while others are predicted as being in the second, or negative class. If the positive class is predicted correctly, it is a True Positive (TP), if it is predicted positive but is in fact negative, it is a False Positive (FP). Oppositely a correctly predicted negative class is a True Negative (TN), while a positive class falsely predicted as a positive is a False Negative (FN). We display the confusion matrix in Figure 4-7:

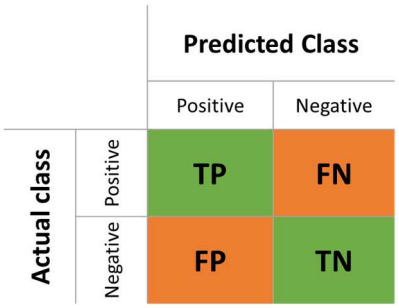

Figure 4-7: General binary confusion matrix

Usually, for datasets with balanced classes, the metric of choice is simply the accuracy, the most intuitive way of accessing the correctness of the prediction. It is given by equation (30):

$$\text{Accuracy} = \frac{TP + TN}{TP + TN + FP + FN} \tag{30}$$

The metric we use to evaluate the model predictions in each case is the 'balanced accuracy' (Brodersen et al. 2010), which is defined in equation (31):

$$\text{Balanced Accuracy} = \frac{\left(\frac{TP}{TP + FN} + \frac{TN}{TN + FP}\right)}{2} \tag{31}$$

Both balanced accuracy and accuracy vary from 0, the worst-case prediction with no true positive or negatives, to 1, for all the predictions true cases. This metric will provide a notion of how accurate the class-specific predictions are for unbalanced class sets. For example, if 99% of the samples are positive, and a model predicts all samples are positive, it's accuracy will be of 0.99, despite missing out on the negative samples. For the balanced accuracy, this model will only score 0.50, getting only half of the classes correctly predicted.

4.5.2 Preliminary algorithm comparison

We must precede any evaluation of algorithms by tuning of hyper-parameters, to make a fair comparison between optimized models. We randomly choose and set aside 30% of the samples as a test set, with the rest of the data samples serving as training data. The intention of tuning hyper-parameters is to find the correct balance between model refinement with the trained set data, that integrates the most detailed trends in the data, without overfitting to the training data (i.e. adapting to each data point individually), which would create a loss of generality in the predictions, i.e. a

low test set balanced accuracy score. For the hyper-parameter tuning we only use the classification of experiment A1 into active and inactive pores (i.e. lowest threshold value).

The training set accuracy should naturally evolve monotonically in the direction of an increasing hyper-parameter as it moves towards overfitting or underfitting to the training set, depending on the specific hyper-parameter used. The test set accuracy however should reach a peak at the optimal value of the hyper-parameter, which represents the sweet spot between overfitting and underfitting. The hyper-parameters are then chosen at values in which the test set accuracy is highest. In our hyper-parameter optimization, we will show training and test set accuracy values for comprehension.

As an example of the importance of hyper-parameter tuning and its relation to under- and overfitting, we show a small case of randomly generated data that is grouped around the shape of two interleaving moons. The data has been classified using a K-nearest neighbors' classifier with the number of neighbors hyper-parameter, n_neighbors, set to 1, 10 and 20. Training set accuracy is shown in black in the bottom left corner, while test set accuracy is shown in white in the bottom right corner for each result. We observe that the highest test set accuracy is achieved for an intermediate value of the n_neighbors parameter of 10. Taking 20 neighbors creates a boundary that is too smooth and doesn't capture data trends, while taking 1 neighbor creates a model that is too specific to the training data (hence a training data accuracy maximum of 1.00) and creates a noisy boundary that is not sufficiently general.

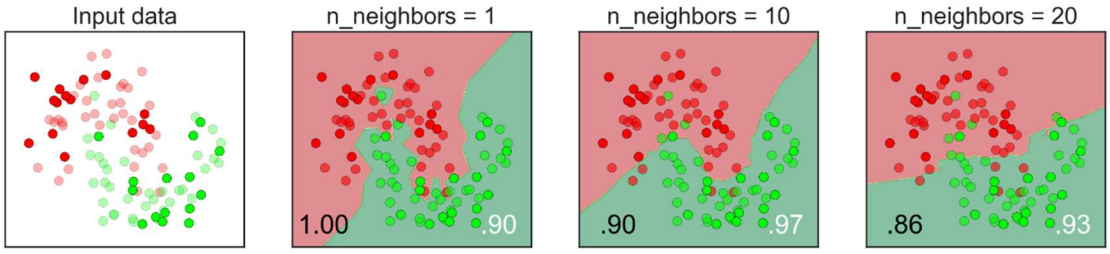

Figure 4-8: The importance of hyper-parameter tuning to avoid over- and under-fitting.

a) **Hyper-parameter tuning**

We show the hyper-parameter tuning process for each algorithm before applying the tuned models to all the different data sets. Note that a standard scaling is applied to the input features to achieve a slightly better prediction for the K-nearest neighbors' models, as they show a strong sensitivity

to feature scaling. Also, for the logistic regression algorithm we use the first 5 components of the PCA analysis performed on scaled data. This was not repeated for other algorithms as they show less dependence on feature scaling or dimensionality reduction. For the hyper-parameter tuning we use 40% of the available samples as the test set.

K-nearest neighbors

For application of the K-nearest neighbors algorithm to our data, the only hyper-parameter we tune is the number of nearest neighbors, with all others set as default out of the box from the sci-kit learn library, version 0.20. We show the achieved balanced accuracy "B-Acc" on the training and test sets while varying the number of neighbors in Figure 4-9.

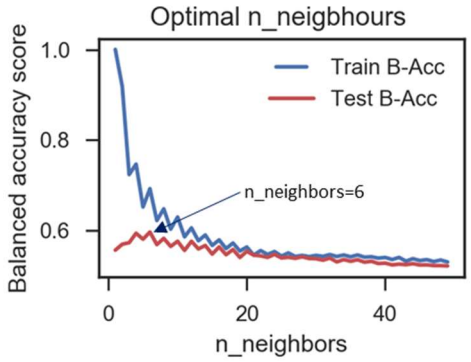

Figure 4-9: Tuning of the optimal number of neighbors in the K-nearest neighbors. The trained balanced accuracy score decreases with larger numbers of neighbors as we lose closeness of fit to the training data and attempt to create a more general model. The chosen value is 6, corresponding to the maximal test set balanced accuracy.

The training set balanced accuracy decreases from 1 in which only the closest neighbor is chosen. When applying this trained model to the test data, where the decision boundary is fixed from the training data, the data points on which the model was trained are no longer necessarily in proximity of the test points, which explains the lower test accuracy at low values of n_neighbors. The small increase of the test accuracy with increasing n_neighbors shows that a more general is created with increasing n_neighbors, peaking at value of 6 neighbors. As the number of neighbors increases further, we don't capture any data specificity and the model represents an averaging too large, decreasing the test accuracy.

Logistic regression

For the logistic regression algorithm, we don't tune any hyper-parameters and use out-of-the-box algorithm values, as they mostly relate to solver specificities. We won't go into such details here, as opposed to the easily interpretable hyper-parameters of the other models shown here. We only set the class_weights parameter to 'balanced' to account for class imbalance in datasets.

Decision Tree

For the decision tree, we tune successively: the maximal depth of the tree, i.e. the number of splits in the tree; the minimal number of samples in either branch per split. As they are tuned in series, when tuning the maximal depth, the minimal number of samples is set the scikit-learn default of 2.

We show the maximal tree depth tuning followed by the minimal number of samples per split tuning in Figure 4-10:

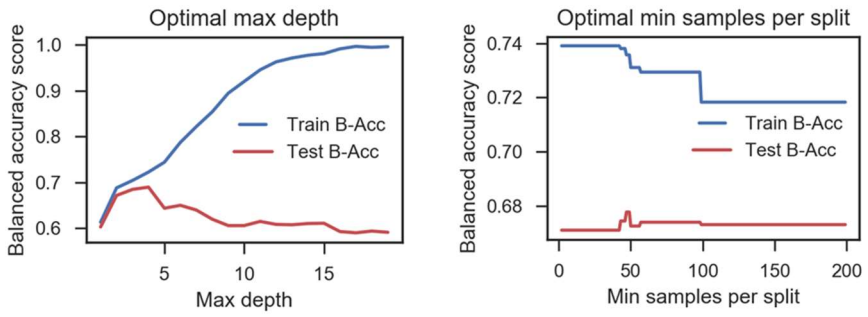

Figure 4-10: Max depth and Min samples per split tuning for the decision tree. The chosen values are 4 for the maximal depth and 75 for the min samples per split.

The best accuracy on the test data set is found for a maximal depth of 4. We then set the maximal depth to 4 and train the number of samples per split. For this parameter we can't see a clear optimal, we therefore choose a value of 75 for the rest of the analysis.

Random Forest

The hyper-parameters for this algorithm are mostly the same as the decision tree, as it represents and averaging of decisions trees. In addition, we tune the number of estimators, i.e. the number of decision trees contributing the final averaged model. We show the successive steps of the hyper-parameter tuning in the Figure 4-11.

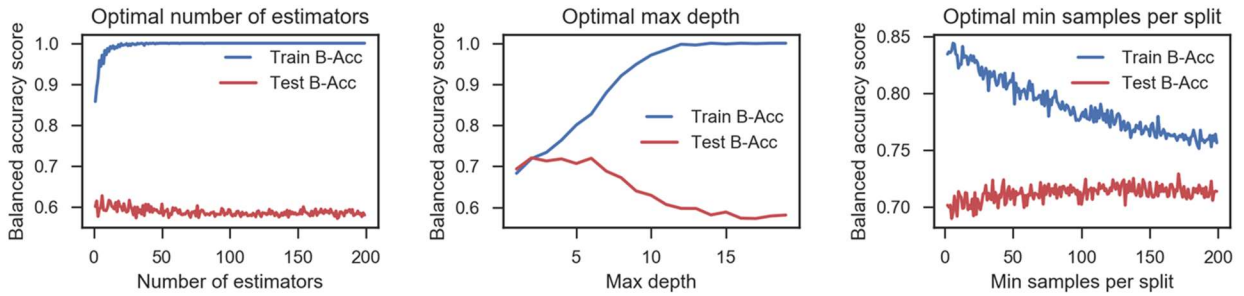

Figure 4-11: Tuning of hyper-parameters for the Random Forest algorithm. The chosen values are 50 for the number of estimators, 6 for the max depth, and 150 for the min samples per split.

As we don't observe a specific optimal number of estimators (left), we take a nonetheless large number of 50 estimators for the rest of the analysis. We show the maximal tree depth per decision tree of the random forest tuning (center), with the number of estimators fixed at 50. We set the maximal depth value as 6. The minimal number of samples per split is shown on the right. This value is set at 150 for the rest of the analysis.

b) **Algorithm comparison**

We start by making a very general comparison of different algorithms trying to predict 2 different intensity classes: we attempt to predict active pores (half average intensity threshold) and highly active pores (more than average intensity threshold). This is repeated on flowmaps created from: the foam experiment flow map with all bubble sizes; the largest 20%, i.e. 80-100% of bubble sizes; the 2D LB Stokes simulation; the 3D LB Stokes flow simulation. Note that for the foam flowmaps, before classifying the pores, an additional step of longitudinal intensity equalization was applied (described in Chapter 2, Appendix 2-C) to account for the measurement gradient seen in the created flow maps due to bubble size evolution.

We perform what is known as 3-fold validation, which makes three different splits within all the samples, such as that all the samples are included in a test set once. The test set size is therefore 33% of all the available samples each time. Therefore, we perform 3 iterations of the model training and testing on different combinations of samples, obtaining 3 different values of balanced accuracy for each classification task. The three values are shown in the Figure 4-12 as the whisker extremities and the central green bar.

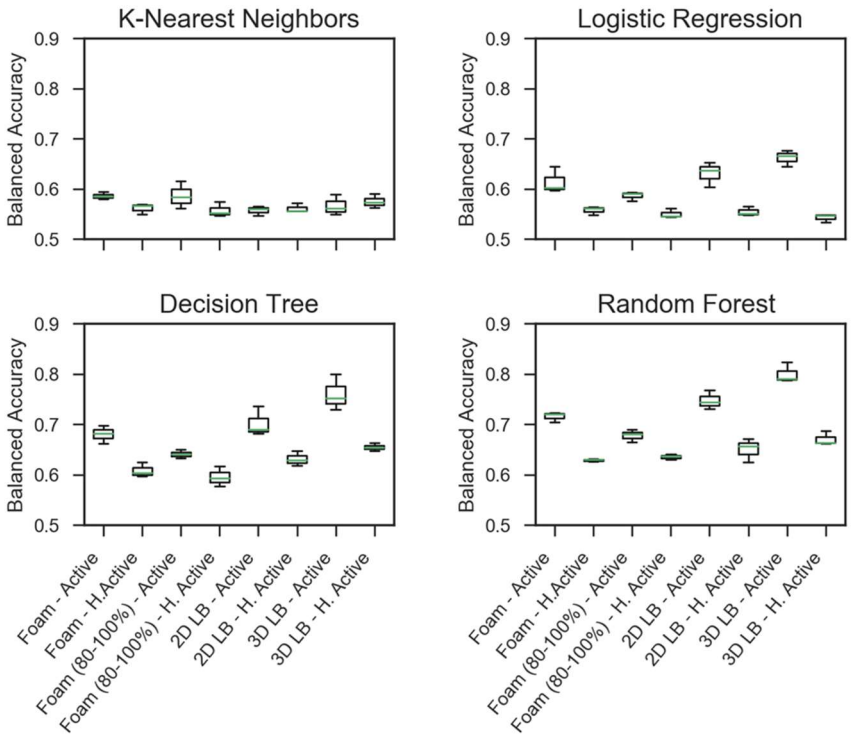

Figure 4-12: Comparison of tuned algorithms on 8 different classification tasks.

The worst performing classifier is the K-Nearest Neighbors, which achieves a barely better prediction than a classifier that chooses the same class every time (i.e. a dummy classifier which would obtain a balanced accuracy score of 0.5). The best classifier is the Random Forest Classifier, achieving consistently higher values than other classifiers for each classification task. Luckily, this classifier is highly interpretable, as it is possible to extract the most important features that do the classification and rank them in terms of importance. This algorithm will be used to classify both the pores and the throats with the same hyper-parameters.

4.6 **Random Forest feature importance**

Now that the algorithm is chosen, we focus on classifying the different activity classes for both pores and throats with the Random Forest algorithm. The feature importances are readily available as an attribute of the scikit-learn trained Random Forest model. The feature importance calculation implemented in this library is based on the method described in Breiman et al. (1984). To increase model interpretability, for some cases we shall give more specific detail regarding the way each feature impacts the model prediction using the open-source SHAP (SHapley Additive

exPlanations) library. SHAP is a new approach to explain the output of any machine learning model. SHAP connects game theory with local explanations, uniting several previous methods (Ribeiro et al. 2016; Lundberg and Lee 2017) to describe how each feature affects the model output, and for our case towards which class every local feature tends to push the algorithm.

We shall examine one by one the features that are most important in the classification process and attempt to interpret these results physically with help of the summary plots gathered from SHAP with source code available on Github[3].

4.6.1 Pore activity classification

We first look at the classification made from the A1 experiment, for the three types of classification displayed at the top, dividing the pores into different flow intensity categories. In Figure 4-13, left, we show the balanced prediction accuracy for the best models in each case. We only show the first 7 features for comparison.

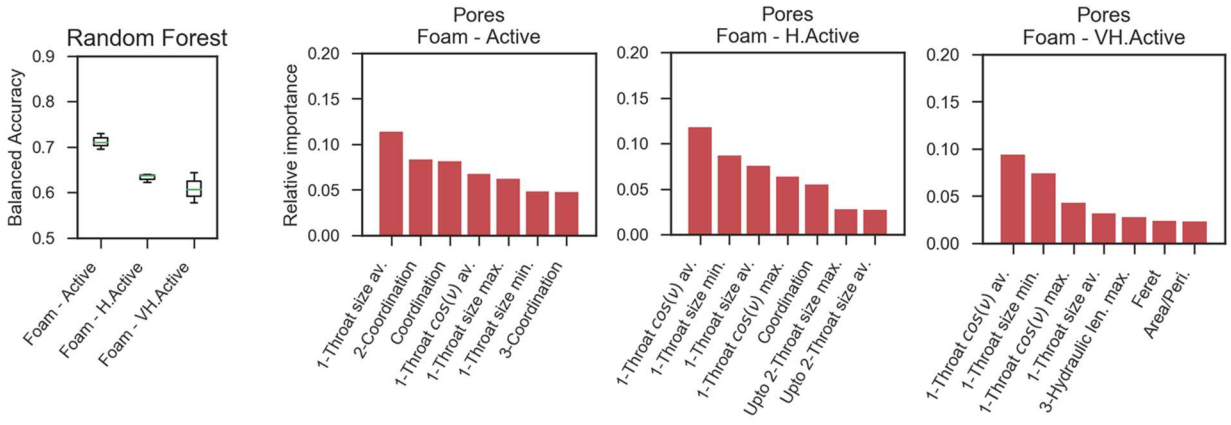

Figure 4-13: Feature importance for the classification of pore activities for all bubble sizes for experiment A1.

We can instantly note that almost all the most important features are related to the surrounding throats or to the coordination of the pores. We observe that not only the throat sizes leading to the neighboring pores are important but also the throat orientation relative to flow. The importance of throat orientation also increases with respect to higher activity classifications. This expresses the

[3] https://github.com/slundberg/shap

fact that the highest flow channels are in the straighter preferential paths also used by the largest bubbles.

Coordination is also less important for higher activity classes but ranks highly for the low activity class. This shows that low coordination pores (i.e. dead-end pores) will not even access the first activity category and contain no flow. However, when distinguishing the high flow pores from the very high flow pores, coordination is of much less importance, and path straightness expressed by surrounding throat orientation becomes more consequential.

We note in the leftmost plot that all the predictions are relatively weak, with perhaps the pore activity showing more accurate predictions at a balanced accuracy of above 0.7. This signifies that only the lowest flowing pores can be distinguished reasonably well from the rest of the pores. When looking at higher pore intensity classifications, we observe that the accuracy decreases.

To confirm these structural dependencies, we look deeper using the SHAP model explanations. We display the explanations for the models fitted to the Active and High Active (center left and center right of Figure 4-13) models. SHAP values interpret the impact of having a certain value for a given input feature in comparison to the prediction we would make if that feature took a reference value. A SHAP value is calculated for each point feature of each sample of the test data set. The Figure 4-14 shows the distribution of SHAP values explaining the trained model making the classification for the lowest pore activity threshold. A negative SHAP value pushes the model towards the 0 class, where the pore activity threshold is not passed, while a positive SHAP value pushes the model towards the 1 class, i.e. the pore activity threshold is passed. We show the SHAP value distribution as a dot plot, in which values with the same x-axis value are stacked vertically. We first show the SHAP dot plot for the lower pore activity classification model.

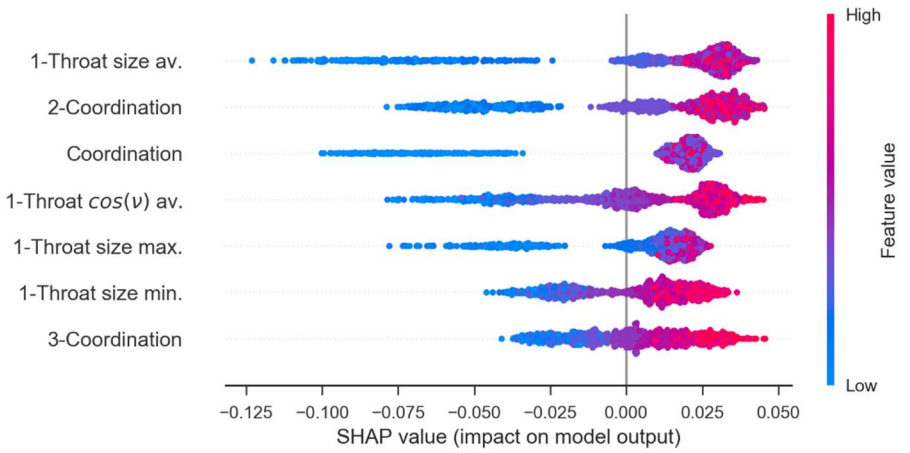

Figure 4-14: SHAP values obtained for each feature and sample in the test set. The relative feature values are shown by the color (higher numerical values are closer to red while lower values are closer to blue). The magnitude of the SHAP value gives an indication of the importance of the associated feature for the given sample, while its sign shows towards which class the model is being pushed. Summing the SHAP magnitudes for all SHAP values for a feature can also give an estimate of overall feature importance, and we see that the rank of feature importances shown here by the vertical position of the feature is coherent with the feature importance calculation performed by the scikit-learn library shown in Figure 4-13.

We observe that the features behave in the way we expected, i.e. low throat size and low coordination push the model to predict the sample as inactive. However, the positive SHAP values show a mix of high and low feature values. Furthermore, the values are not distributed symmetrically, with a large amount of the positive values clustering close to the 0 SHAP value (i.e. low impact) whereas the negative SHAP values reach much lower extremes. This means that whereas it may be possible to easily predict the classes that are certainly not active (i.e. trapped foam areas) if they display very small coordination or throat size average, it is harder to say when a class is without doubt going to be positive or contain flow.

To investigate this last point further, we can look at some threshold values on the average pore intensity histogram (i.e. abandoning the size category reference for now). We take two threshold values in the average pore intensity histogram at notable points. We show these as vertical lines along the intensity histogram in Figure 4-15.

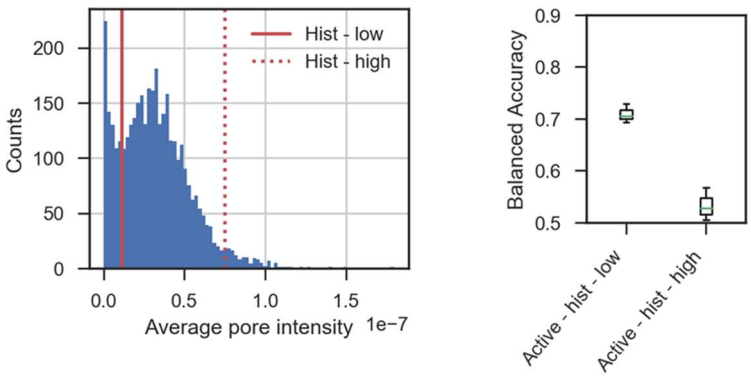

Figure 4-15: Left: Pore average intensity histogram showing two more pore classifications. The local minimum on the intensity histogram shows the first threshold (full red line) and the change of gradient in curve drawn by the histogram peaks gives a second threshold (dotted red line). Samples below the 'Hist – low' threshold are numbered at 721 while samples above the 'Hist-high' threshold are numbered at 135. Right: Prediction accuracy for trained random forest models.

The much lower prediction accuracy for the high intensity pores (around 0.5, the value of a random classifier) shows that it is not feasible to locally predict the high intensity areas, on the contrary of the low histogram classification which still maintains a relatively high value of 0.7. In this sense, flow prediction can only be partially modelled locally. While it is possible to predict (at least some) of the lowest flowing pores based on local structural model, the highest flowing pores cannot be accessed locally. This could indicate a different type of model is required. We can refer to colored images of each type of pore in Figure 4-16:

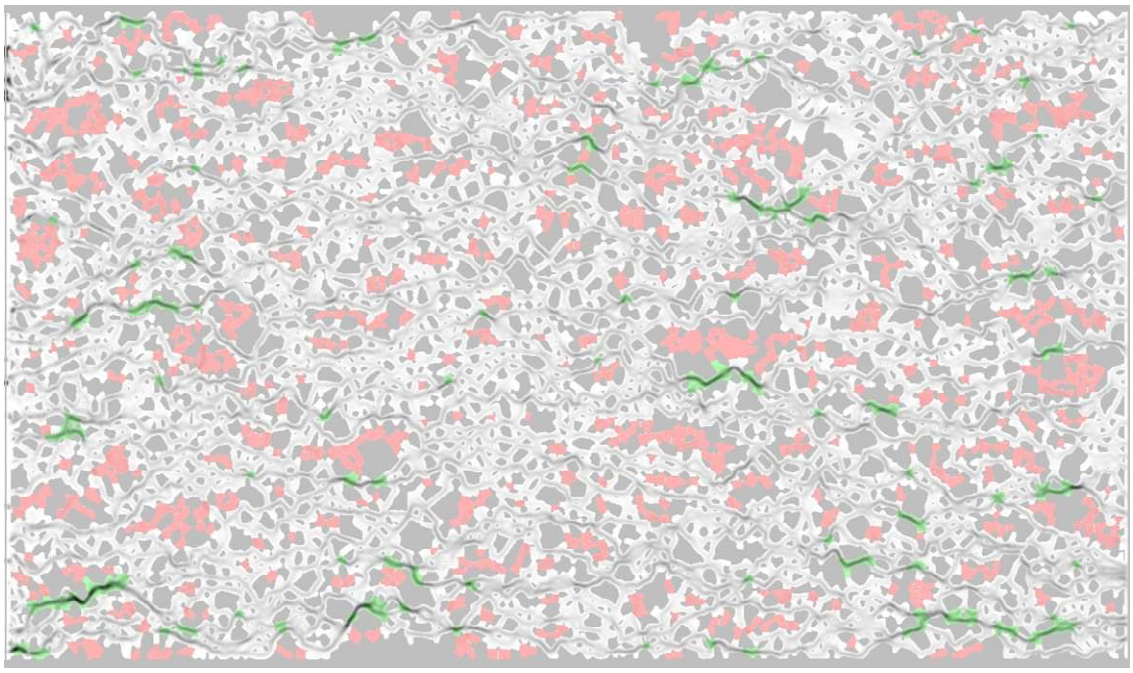

Figure 4-16: Red pores have average intensities lower than the solid line on the intensity histogram of Figure 4-15. The green pores have average intensities higher than the dotted line in the intensity histogram of Figure 4-12. The red pores are observed to be in areas that can be described by a series of local conditions: pores situated in paths transversal to the pressure gradient; pores with small entry or exit throats; dead end pores with low coordination. The green pores however correspond to bottleneck situations where high flow paths join. As the presence of preferential paths and where they join up is non-local, the machine learning algorithms were not able to predict such zones on a local basis. Flow is from left to right.

While this demonstration is shown for flow maps created using all bubble sizes, we could imagine that a different behavior could be seen for other bubble size partitions, which will be studied next.

We now look at the successive classifications for the flow of largest bubbles. We apply the analysis to the flowmap created using bubbles whose average bubble size is in the top 20% of the bubble size frequency histogram. The top 20% of bubbles logically correspond to a larger fraction of the total porous space than 20%. In Figure 4-17, we show the spatial bubble size probability distribution (i.e. frequency histogram weighted by average bubble size) of bubbles in experiment A1, showing the largest 20% of bubbles counts used for this classification.

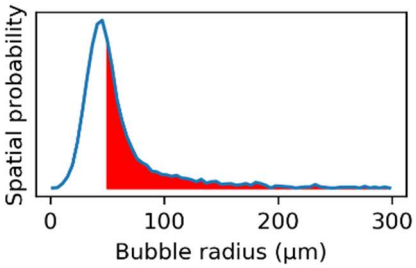

Figure 4-17: Spatial probability of bubble size in Experiment A1. The bubbles used for the largest bubbles flowmap are shown in red.

For this classification, the pores were divided up in the same way as previously described, by showing a measured intensity greater than half of the size category mean (active), greater than the mean (highly active), or greater than 3/2 of the mean (very highly active). For comparison, we show the difference between pore activity (low threshold only) for all the bubbles and for the top 20% largest bubbles in Figure 4-18:

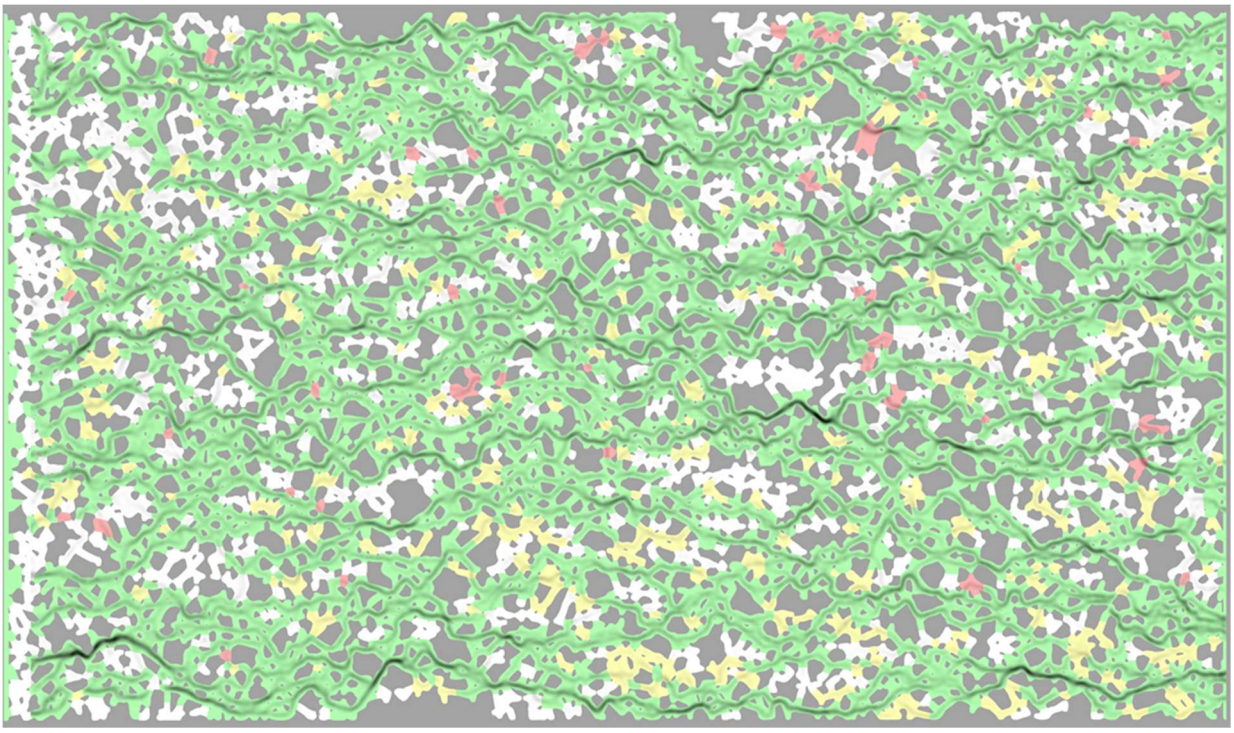

Figure 4-18: Comparison of local pore activity (lower threshold) for different bubble sizes. The flowmap for the largest bubbles is shown in grayscale. The color code is the following: Green indicates the pore activity threshold is passed in both the total histogram flowmap and the flowmap from the top 20%. Red indicates the pore activity threshold is passed only in the top 20%, whereas yellow indicates the pore activity threshold is passed only for flowmap with all bubble sizes. Pores in white are not active in any classification.

The colored maps show that the lower activity threshold is passed in more cases for the total histogram flowmap (more yellow than red pores), which translates the larger homogeneity of flow for the total flowmap. The yellow areas often seem to be in transversal areas in between preferential paths, sometimes oriented away from flow direction but not necessarily. This is coherent with observation of Chapter 2 in which we observed qualitatively a larger number of transversal paths used by smaller bubbles. We also note that the pores in white overlap the pores in red in Figure 4-16, which contain the lowest amount of flow based on the mean pore intensity histogram only (Figure 4-15).

The Random Forest algorithm then creates models to classify different activity thresholds for the largest 20% of bubble flowmap. We show these results in Figure 4-19.

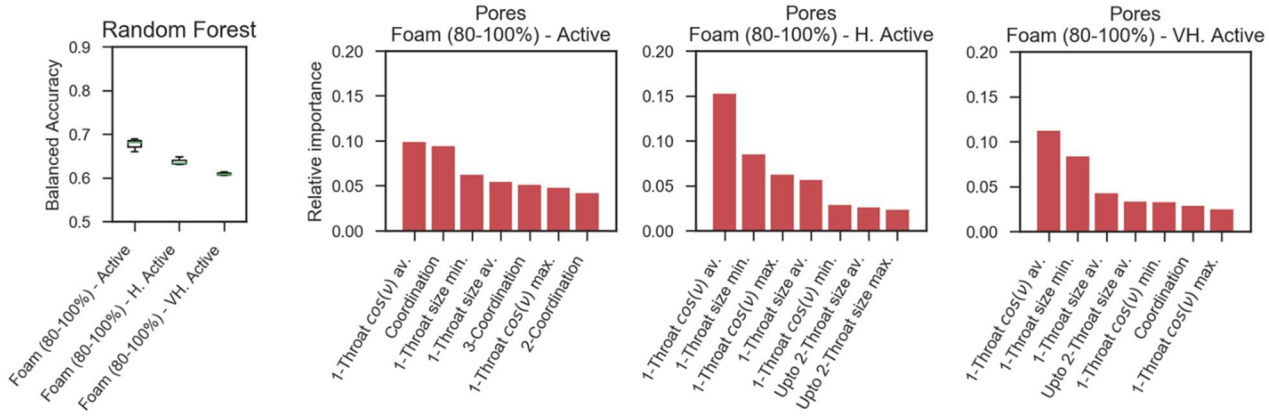

Figure 4-19: Achieved balanced accuracy and feature importance of pore activities for the top 20% bubble size flowmap of experiment A1.

Similar conclusions can be applied here than to the initial series of classifications. The throat features are dominant in every classification scenario, however with a reinforced presence of throat orientation angle **ν**, even for the lowest activity classification. The SHAP analysis, not shown here, also reveals the same direction of the dependences for the larger bubbles, i.e. pores with low coordination and with smaller, less straight neighboring throats contain less flow

This confirms the previous comments on straighter paths being more desirable to flow, and pores that turn away from flow, with throat orientations away from pressure gradient, less likely to be active. For comparison, we perform the same analysis for the 2D and 3D simulations. These results are shown in Figure 4-20. We observe in both cases a much weaker importance of throat sizes in

the LB simulations relative to the foam cases, notably for the lowest threshold classification, with the most important features being coordination and features relating to the neighboring throat orientation in all cases. This demonstrates the absence of capillary entrance effects in Newtonian fluids against the foam case. While inactive foam pores can be determined by low entrance or exit throat size, the Newtonian fluid does not need to overcome a Laplace entry pressure and can access all flow regions.

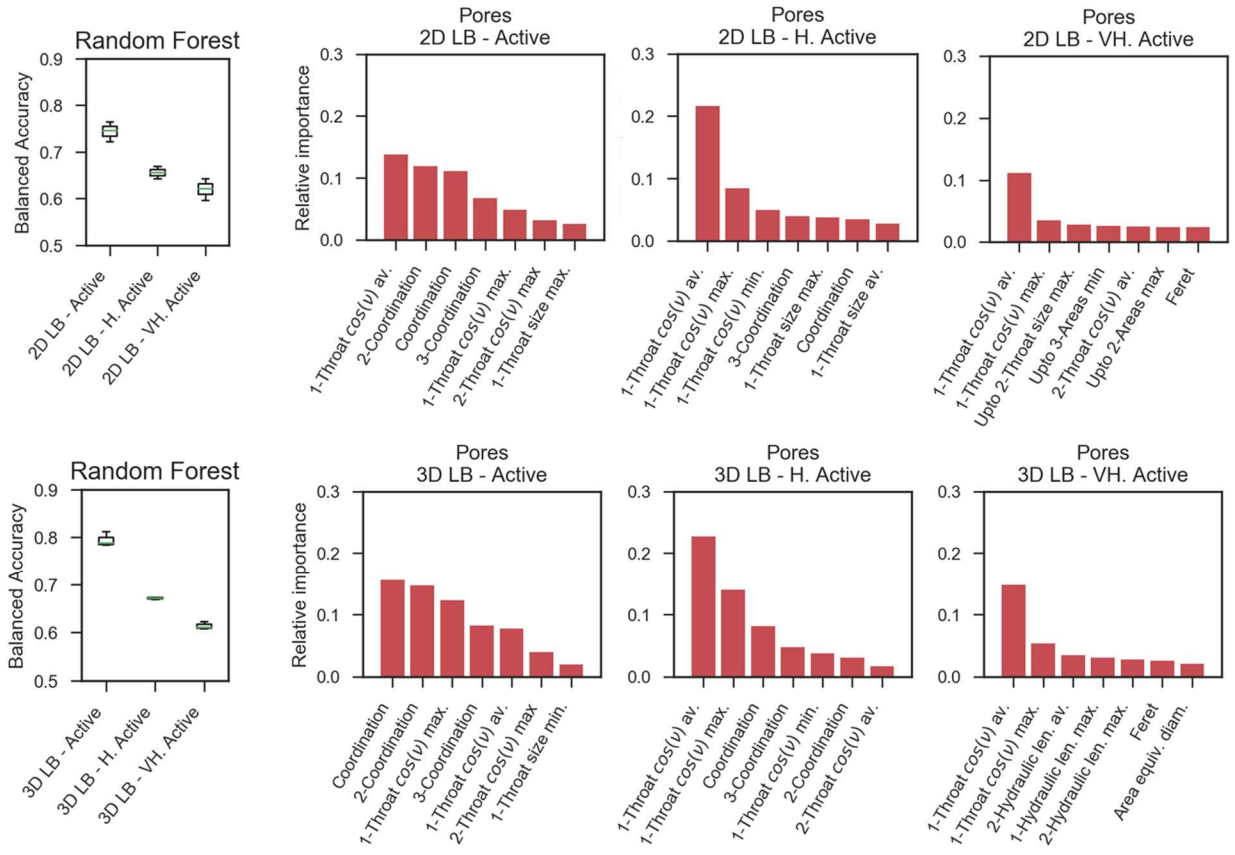

Figure 4-20: Achieved balanced accuracy and feature importance for the pore classification predictions of the two numerical flow maps. Top row: 2D numerical flow map results. Bottom: 3D numerical flow map results.

Intended as a final validation step, we can run the Random Forest algorithm using only the top features, consistently ranked at high importance. Since many highly correlated features are used (especially relating to pore area), it could be argued that their individual relative importance is mitigated in the final models, as they can be used interchangeably because they describe the same variance. To verify that the feature importances shown are in fact indicative of the most influent features we simply select the 4 features that appear the most. These features are: 1-Throat size

average; 1-Throat cos(ν) average; Coordination; 2-Coordination. We then perform the same classification tasks as shown in Figure 4-12. The results for this limited number of features are shown in Figure 4-21. We observe that the prediction accuracies are equivalent to the ones shown in Figure 4-12, demonstrating that these features are positively the most influent. However, this does not mean other features could not somewhat replace the ones shown here due to high correlation, but still indicates that most of the relevant information of the system variance is contained within these 4 features.

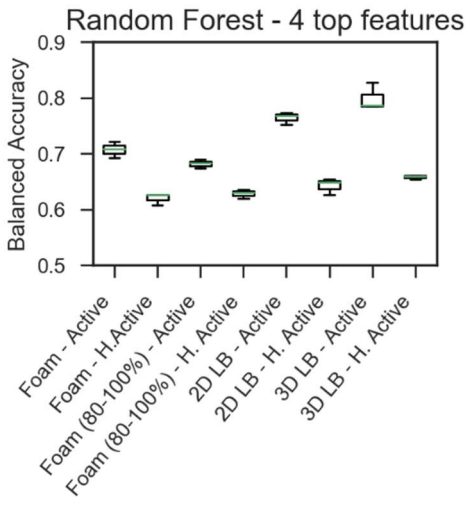

Figure 4-21: Balanced accuracies for classification of the same tasks as shown in Figure 4-12. The classification here is performed using only the best 4 features given above.

4.6.2 Throat activity classification

In the pore activity classification, it has become clear throat properties that surround the pores are the most important features predicting local pore activity. We shall now focus on the activity of the throats themselves in the same style of classification based on taking multiples of the mean intensity for each throat size category (again, taken as 19 successive size categories with same number of elements in each).

The results for the throat analysis are less successful in general than for the pores. We display the results for the foam flow map for the A1 experiment for all bubble sizes in Figure 4-22.

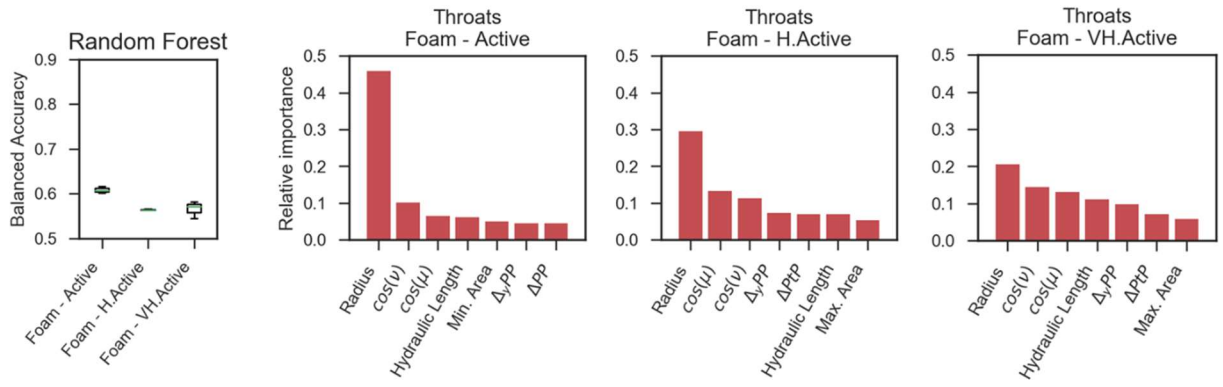

Figure 4-22: Achieved balanced accuracy and feature importance for the throat classification predictions for foam flow map with all bubble sizes.

We interpret the generally lower accuracy score by noting the fewer number of structural features available to the classifying algorithms. Indeed, for the throats, having only two immediate pore neighbors, more complex structural properties become less obvious to list. As the accuracy of the created models is somewhat lower than for the pores, we shall not comment in detail as to the most important features. Nevertheless, we note that throat radius and some notion of orientation (either in the throat itself, or through the alignment of neighboring pores, two features which are in fact strongly correlated) seem to be the most important features. Again, neighboring pore area is not a relevant feature in the flow prediction. We show the SHAP dot plot for the lower threshold classification (left bar plot of Figure 4-22), showing more explicitly the relationship between the features and model prediction.

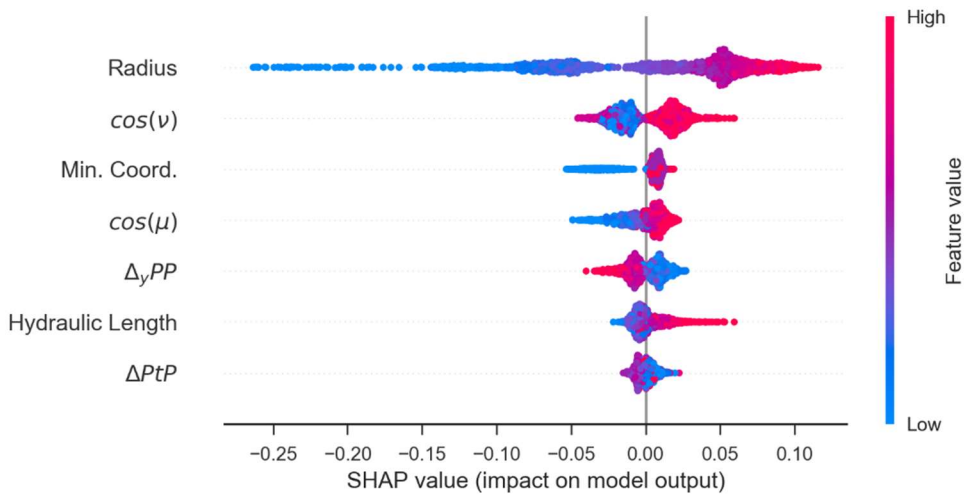

Figure 4-23 : SHAP values obtained for each feature and sample in the test set for the lower activity throat classification. We note that the most important features shown here exhibit small differences with the features shown on the left bar plot of Figure 4-22, owing to the differences in total feature importance calculation.

We observe the strongest relationships of the model describe smaller, less straight throats as less probable to carry flow. Again, the SHAP value distribution for the throat radius is not symmetric, with a much larger tail towards the negative SHAP values, showing that smaller throats are by themselves stronger predictors of absence of flow than large throats are for the presence of flow. We note that the SHAP value and feature value dependence for the $\Delta P_Y P$ feature is reversed, i.e. throats that have adjoining pores closer in the Y-direction are more likely to contain flow.

For completeness, we show the feature importances for the throat classification tasks of the largest bubbles flowmap in 4-24, and for the 2D and 3D Newtonian Stokes flow in Figure 4-25. These classifiers generally show similar features as most important: throat radius, throat orientation (cos(ν)) and alignment of neighboring pores to pressure gradient (cos(μ)).

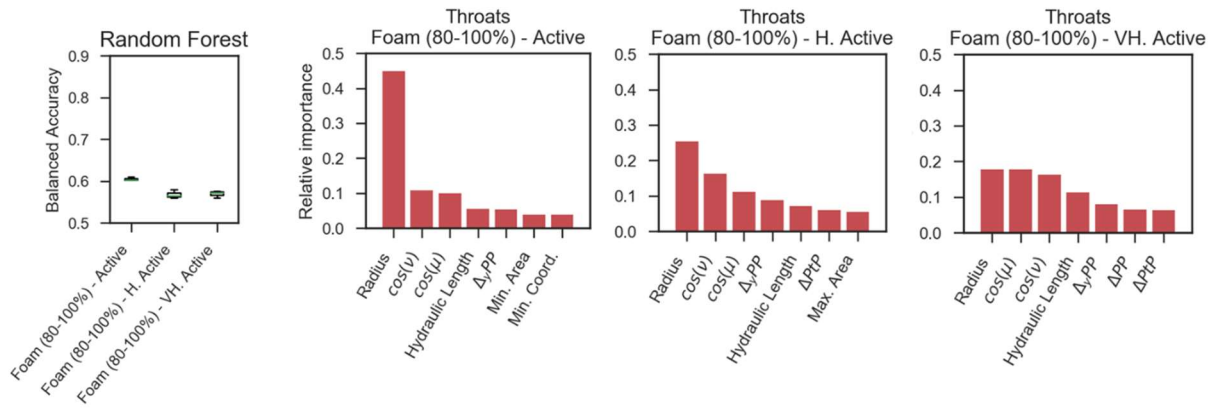

4-24: Achieved balanced accuracy and feature importance for the throat classification predictions for the foam flow map for the 20% largest bubbles

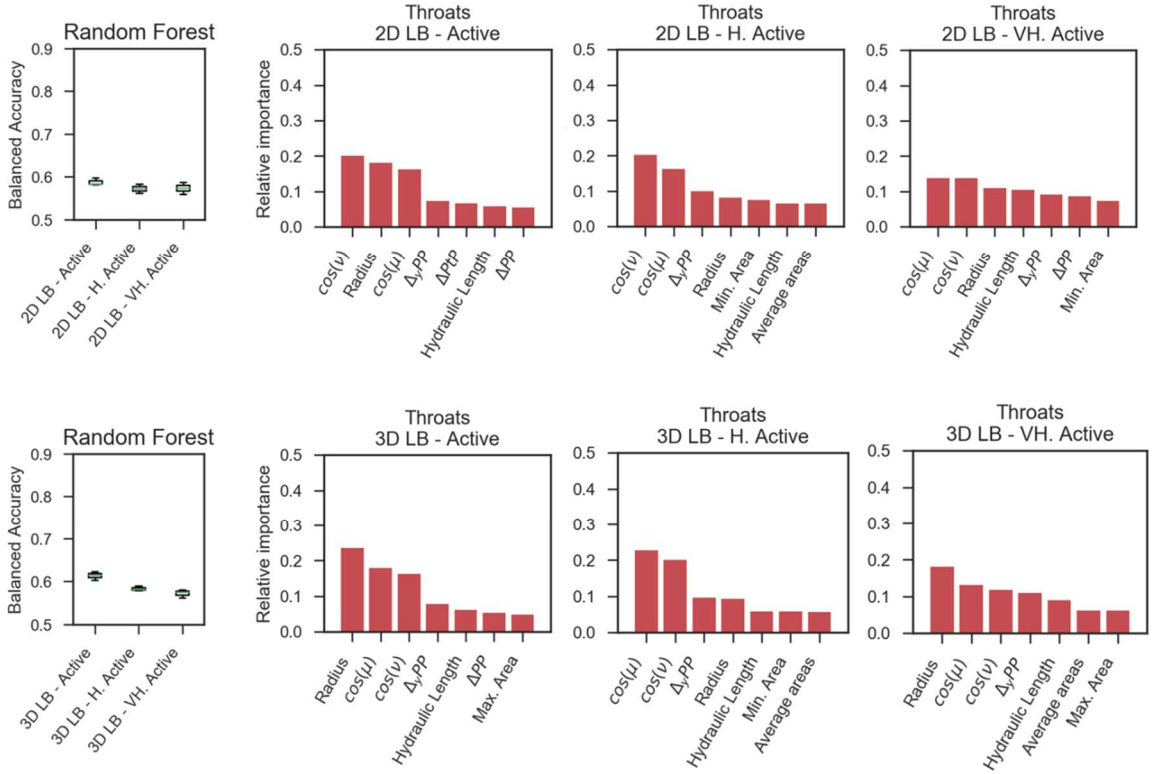

Figure 4-25: Achieved balanced accuracy and feature importance for the throat classification predictions of the two numerical flow maps. Top row: 2D numerical flow map results. Bottom: 3D numerical flow map results.

4.6.3 Generalization

In order to generalize these results to other experiments, we choose an experiment that shows largely different injection parameters. We choose experiment B3, which has a lower gas fraction, injection rate, and lower mean bubble size and bubble size standard deviation. The same classification was performed using the same algorithms and chosen hyper-parameters as described previously.

We show in Figure 4-26 the results for the balanced accuracy of the trained models and the feature importance, showing the same type of key features for the experiment B3.

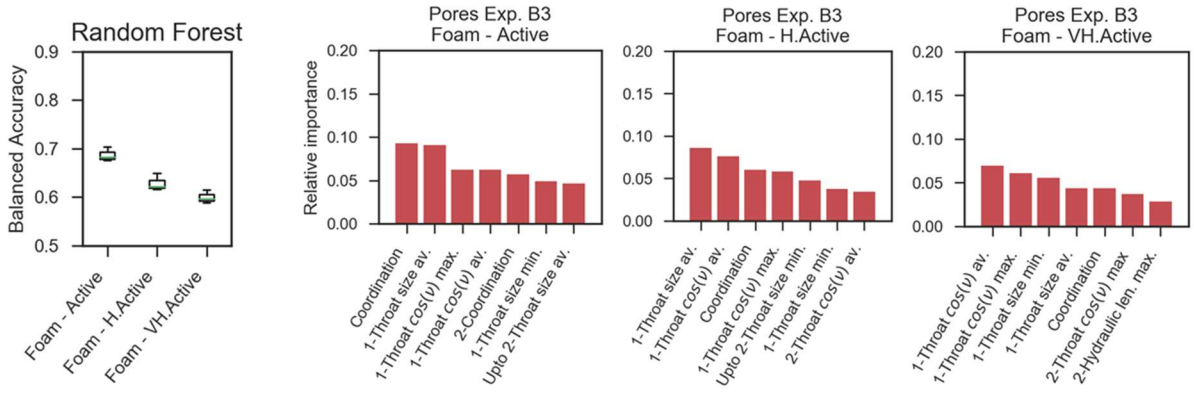

Figure 4-26: Achieved balanced accuracy and feature importance for the throat classification predictions for the flow created from all bubble sizes of experiment B3.

Our observation from the A1 experiment are maintained in this experiment despite the changes in all the injection parameters.

4.7 Conclusion

From this chapter we can gather a series of observations. First, we note a low prediction accuracy for a local structural prediction of flow. Such accuracy rates could mean one of many things. They could indicate a failure in choosing the right algorithm with the best features, despite our efforts to optimize accuracy. Otherwise, it could indicate that insufficient features are given despite our large number of distinct features provided. Lastly, it could express the strong lack of adequacy in describing flow in terms of local structural parameters, and the necessity to implement a larger-scale modelling solution.

We observe furthermore that a description of low flow zones is more adequate through a local parameter description than the high flow zones (lower accuracy of high intensity classifications). While the low flow areas can be locally understood (pores situated in paths transversal to the pressure gradient; pores with small entry or exit throats; dead end pores with low coordination), the high-flow zones seem to represent bottleneck situations and correspond to the overlapping of already used paths. This theme reinforces the notion that a larger-scale type of model is required to characterize high flow areas by integrating network-level descriptions. The inclusion of coordination, i.e. an initial step into network properties, in some of the most important features for many classifications displays this. This type of model will be described in the following section, in which the notion of model-spanning path will be established, and various paths evaluated.

Also, one of main points to take away from this analysis, despite the overall low prediction accuracy, is the dependence of flow properties on local throat characteristics and network properties exclusively. Most flow predictions were based on a combination of throat radius statistics, throat orientation statistics (or neighboring pore alignment with pressure gradient statistics) and pore coordination.

Chapter 5. *Describing High-Velocity Flow Areas Using a Network-Spanning Graph Model*

Preamble

Within this chapter, we shall give results achieved using a new model that was motivated by the necessity to describe high-flow zones in a complex medium from a structural point of view. Within Chapter 4, we establish that while it may be possible to describe low-flow or trapped areas based on combinations of local parameters, high-flow areas require a different type of model altogether as they arise from network-level behaviors such as the overlapping of flow paths in bottleneck type situations, that cannot be accessed locally. Such behavior requires therefore a network-level model. While network level flow simulations such as the lattice Boltzmann simulations show where high-flow zones are located in the foam flow through similarities to Newtonian flow, these are computationally demanding, and furthermore may not be fully applicable to all foam experiments, in which only a restricted number of flowing paths may appear. To simplify the modelling task, the porous medium is reduced to a graph, in which pores represent the network nodes and throats are embodied by the graph edges, or links between nodes. The use of a graph network analog facilitates the characterization of the large-scale connectivity of the network. Motivated by the observation of a limited number of preferential paths, overlapping only for a small portion of the model, we develop a graph model that makes use of a simplified version of the model structure and outputs a series of paths that share the same characteristics as the observed foam flow preferential paths. In this chapter we first describe the model and fit the model to 2 micromodel experiments, giving 2 distinct model fits, before applying the model to flow data obtained an experiment in which the injection direction is reversed. A generalization is shown to an example of foam flow in a 2D network from the literature (Géraud et al. 2016) to test for validity within a distinct, albeit simpler 2D porous medium.

As the following work was written as a standalone article, the experiments 1 and 2 described within it are in fact experiments A1 and A2 as described elsewhere in the manuscript. Experiment A1 is also the experiment studied in Chapter 2.

Article: Accessing preferential foam flow paths in 2D micromodel using a graph-based 2-parameter model

Christopher Yeates, Souhail Youssef, Elise Lorenceau

Under review in *Transport in Porous Media*

Keywords: Foams, Micromodels, Preferential paths, Network analysis

Abstract:

This study uses experimental data of pore-scale foam flow inside a high-complexity network to fit a graph-based model describing preferential flow paths based on characteristics of the porous medium. Two experiments, with equal gas fractions but varying injection rates, are modelled in parallel. Proposed paths are solution paths to the k-Shortest Paths with Limited Overlap (k-SPwLO) problem, applied to a graph representation of the porous medium with edge weights representing throat properties. A 1-parameter model, based on throat radius only is tested before integrating a second parameter, describing the alignment of the pores surrounding the throat with respect to injection pressure gradient. The preferential paths in both experiments vary in quantity and in the specific zones described. As such, fitted models characterizing preferential paths for either experiment show separate dependencies to structural parameters. Overall, the graph-based framework was able to capture many high-flow zones in various model parameter combinations, perhaps as consequence of the relatively spiked throat size distribution of the model. The optimized model for the high injection rate experiment markedly shows a non-zero dependence to the pore alignment to pressure gradient as well as throat size, whereas the lower injection rate experiment was best fitted to a model that made sole use of the throat radius.

5.1 Introduction

Foams constitute an attractive method to enhance oil recovery due to their high viscosity, high potential for conformance control, low cost and low environmental impact.

To implement a large-scale foam operation, prior validation and injection optimization must be performed using a reservoir modelling software. While some attempts have been made to integrate microstructural parameters such as average pore size into upscaled foam models (Ettinger and Radke 1992; Gassara et al. 2017) a great deal of foam behavior laws are derived from Darcy-scale

laboratory experiments, and require significant a posteriori parameter fitting to match observations. The numerical load would be greatly alleviated by the use, or at least constraint of, fitting parameters with a value obtained through a purely structural characterization of the porous medium.

Recent works on 2D micromodels (Géraud et al. 2016; Yeates et al. 2019) have shown that a range of foam behaviors exist that are highly likely to contribute to Darcy-scale flow properties. Indeed, trapped foams and high-velocity preferential paths have been repeatedly observed, displaying ranges of velocity much lower and higher, respectively, than those seen in Newtonian flow Furthermore, it has been shown that high-velocity zones are accessed primarily by larger bubbles in a heterogeneous bubble distribution flow, containing the majority of flow in the model. The interest of characterizing the specific paths that these bubbles will take, as well as the number and rank of equivalent or alternative paths, becomes obvious.

A purely local description of flow has shown to be insufficient to difficultly access larger scale phenomena such as preferential paths and trapped zones For this reason, here we attempt a novel characterization approach, by integrating the notion of overall path (spanning inlet to outlet of the model) and ranking paths according to a numerical value derived from the components that make up it.

Modelling porous media with graph models has been recently given new life. Graph-based models have been used to find least resistance paths and predict breakthrough points successfully in heterogeneous porous media (Rizzo and Barros 2017). Graph models have also found use in discrete fracture modelling to rapidly characterize, query, and interrogate fracture network connectivity (Viswanathan et al. 2018)

The path-proposing is done via an algorithm that makes use of a graph representation of the porous network. Nodes of the graph represent the pores, while the graph edge weights represent throats. This gives a labelled graph of connected objects, with edge weights given by a throat property of our choosing. The sum of edge weights of a given path between the source node and the target node $p(s \to t)$, otherwise known as the path length, is then given by $\sum_{i,j \in p(s \to t)} w(i,j)$. The shortest path is then path that minimizes this sum. Many algorithmic solutions exist for this problem including Dijkstra's shortest path algorithm (Dijkstra 1959) An extension of this problem is interested with the first K paths, ranked by increasing value of path length (K-shortest paths),

and can be solved with Yen's algorithm for example (Yen 1970).When applied to our porous network graph, solutions to the K-shortest paths problem often are small variants of the best path, with one or two elements of the paths changed, even for large values of K (>5000). When combined with our observations of preferential path flow in the micromodels, in which a multitude of somewhat distinct paths serve as preferential paths at the same time, we are motivated to assimilate our problem to an extension of the K-shortest paths problem, finding the K-Shortest Paths with Limited Overlap (k-SPwLO). The path solutions to this problem are the K-shortest paths respecting a condition of maximal path overlap between one another. We make use of the recently published OnePass algorithm, a solution algorithm that efficiently proposes candidate paths with user-chosen maximal path overlap (Chondrogiannis et al. 2017). Experimentally observed flow maps serve as the basis for comparison of proposed paths. Experimental images showing long preferential paths of flow in a fully characterized micromodel are analyzed according to a well-defined statistical workflow to quantify active and dead zones in the network. Paths are then proposed using a graph representation of the porous model. The path fit to experimental data is evaluated by counting the proportion of elements in the proposed paths that are active in experimental flow map, corresponding to a match value.

5.2 Materials and methods

5.2.1 Foam data acquisition procedure and injection conditions

Our experimental data acquisition setup and procedure is described in detail in Yeates et al. (2019). We create velocity heatmaps by averaging local tracked bubble velocities over multiple sets of 200 high-frequency images. Fixed injection rates and gas fraction are injected into a foaming device upstream of the micromodel, then connected in series to the model. Pressure gradient is measured, and images are acquired at steady state (constant pressure gradient over the model). The image processing procedure leading to bubble segmentation as well as the tracking procedure is also described in Yeates et al. (2019).

Injections were done with purified N2 gas. The surfactant solution was composed of purified water with 30 g/l of salt and an AOS surfactant at 10 times the CMC, supplemented with betaine-based foam booster.

Two experiments are described in this study. We compare injections of same gas fraction but different injection rates. The two injections were performed in succession. Experiment 1 was at a gas fraction of 79% at an injection rate of 2.53×10^{-2} cm^3/min. For Experiment 2, as lower injection rates were not obtainable with the gas flow controller, a biphasic reservoir, essentially a long coiled up tube, was used to enclose the gas and surfactant solution at the chosen gas fraction. The mixture was then pushed using the liquid pump, reaching much lower injection rates, into the foaming device. The injection rate for Experiment 2 was 8.9×10^{-3} cm^3/min. Despite a reduction in injection rate of 65%, the measured pressure drop over the model decreased from 275 ± 4 mBar for the high rate experiment to 189 ± 2 mBar for the low rate experiment, corresponding to a 32% decrease in pressure gradient, showing a highly shear-thinning apparent viscosity profile coherent with other foam studies (Alvarez et al. 2001).

As previously shown (Géraud et al. 2016; Yeates et al. 2019), the majority of flow in a polydisperse foam injection into a heterogeneous medium is carried by the largest bubbles, in a series of preferential paths. Furthermore these paths show higher relative flow intensity than for Newtonian fluids (Yeates et al. 2019). Correct characterization and modelling of the flow within these preferential paths will constitute a significant part of macroscopic foam flow modelling due to the large contribution of flow solely in these paths. For the experimental comparison, we therefore only use the flow maps of only the right-hand side of the bubble size distributions.

We show in Figure 5-1 the bubble size spatial probability distributions for each experiment, and highlight the bubbles used contributing to the flow maps used in this study. The spatial probabaility distributions are weighted histograms of bubble frequency histograms, with each histogram frequency peak weighted by the average bin bubble size (taken as bin center value). Such distributions give a more accurate depiction of the bubble size distribution inside the medium. The bubble size distributions are established by counting bubbles measured in the entire model. The bubble sizes contributing to the flow maps in this study are highlighted in red.

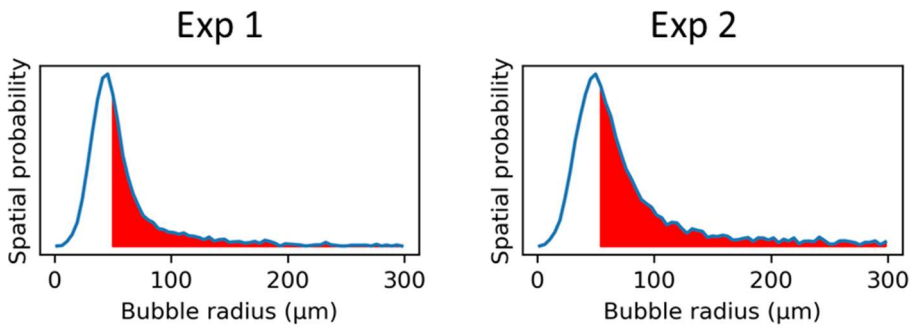

Figure 5-1: Bubble frequency histograms and bubble sizes contributing to flowmaps in each case highlighted in red. We observe that the lower minimum of bubble sizes is approximately equivalent in each experiment, but the experiment 2 distribution shows a larger right-hand tail. It is to be noted that although the higher bound shown here was cut for visibility, larger bubbles were observed (especially in experiment 2) and took up non-negligible areas of the porous volume.

5.2.2 Micromodel structure and decomposition

The 2D micromodel used has previously been studied elsewhere (Yeates et al. 2019). It is a 69.7% porosity glass micromodel with a wet-etched depth of 40 µm. The permeability of the total model with the flow spreading system before and after the model is 4.7 Darcy. A binarized version of the model was decomposed into pores and throats using an adjustable watershed algorithm (Soille and Vincent 1990) with the tunable sensitivity parameter set to 2. The model decomposition gives a total of 3700 pores and 6284 throats. The throat radii show a unimodal distribution with sharp peak at 51 µm. A network extraction algorithm was developed and applied to the 2D decomposed porous medium to find neighborhood properties of each pore and a graph was created. We show the different steps of the graph extraction process in Figure 5-2:

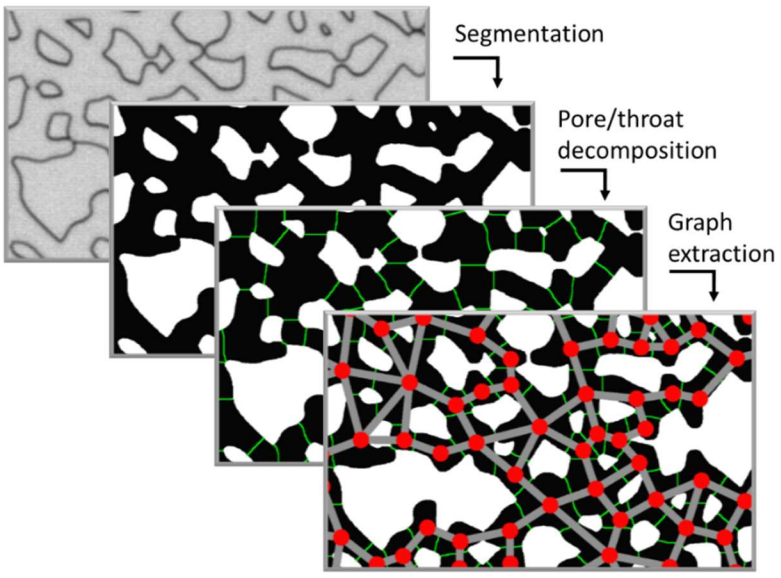

Figure 5-2: Image and network analysis process. Porous area is shown in black. Throats are shown in light green. Extracted graph nodes are shown as red circles with edges represented as grey rectangles joining them. The displayed graph is superimposed on the initial network for clarity.

Note here that this graph simply displays graph topology by positioning nodes on the centers of mass of the pores and edge lengths or widths are not representative of edge weights.

Due to the quantized pixel nature of the model image, and the design of the watershed algorithm, some of the throats were found to not be perfectly straight and resemble S-shapes. As we make substantial use of the throat size in our study, use of the throat length as given by the watershed was inadequate. Instead, we use the maximal Feret diameter of the watersheds, as measured with ImageJ analyze particles tool, to access the exact size of the throats. Half of the measured Feret diameter was then approximated to represent the throat radius, referred to in the rest of the article simply as throat size. We show the model and associated graph in their entirety in Appendix 5-A, with the added artificial inlet and outlet pores (described below) visible at each extremity.

5.2.3 Path-proposing algorithm

We make us of the recently published One-Pass graph algorithm (Chondrogiannis et al. 2017), solution to the K-shortest paths with limited overlap problem (K-sPwLO), to provide a series of paths that resemble the preferential paths visible in our experiments.

In our context, to capture the specificity of the flow in the porous network, edge weights are represented by a function of the throat properties, initially the throat radii, located at the distance

map minima, that will contribute the most to variations in hydraulic conductivity. In this sense, we try to minimize overall sum of contributions of throat radii, rather than distance. Note, that this problem is distinct from the shortest bottleneck, or widest path problem, which yields the shortest source-to-target path with the largest minimum throat size possible.

Naturally, as we desire to find a path that spans the entirety of the model, we construct an artificial source node and target node representing the model inlet and outlet, sharing connections with all the nodes at each extremity of the model, as to not restrict the path-proposing procedure to a specific point in either side of the model.

As we want the largest throats to contribute the less to the overall sum, and hence be chosen in the paths, we use functions of the inverse of the throat size for edge weights. However, it is unclear which (positive) exponent α should be used to integrate this throat size as an edge weight. The shortest path will then minimize the function $\sum_{i,j\in p(s\to t)}\left(\frac{1}{r(i,j)}\right)^{\alpha}$ in which $r(i,j)$ is the radius of the throat connecting pores i to j, and s and t represent the source or target nodes, or vice-versa, as the graph is undirected.

While individual throats radii will preserve their rank if they are raised to a power $\alpha = 1$ or $\alpha = 2$, the rank of a sum of throat radii forming a path will not be conserved for each exponent. The larger the value of α, the more a small, difficult to pass throat will contribute towards the sum. The proposed paths will then avoid smaller throats, at the price of increasing the overall path length and tortuosity. Inversely, a lower value of α will render the algorithm less sensitive to the actual value of throat size, as the virtual length of the path (or number of throats that compose it) becomes more significant. At the extreme of $\alpha = 0$, all weights are the same and we retrieve the shortest path based on number of elements alone. We give an example of different proposed paths for different values of α in Figure 5-3. We see that different throat radii exponents produce different shortest paths when integrated as edge weights.

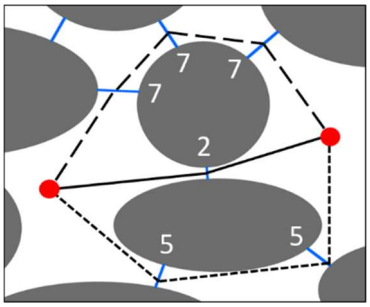

Figure 5-3: Motivational example. Optimal paths for different values of α in a schematic example. Porous space is shown in white between gray solid obstacles. Throats are shown in blue. Multiple paths link the sources and destination pores, shown in red. Throat size values are given in white, next to the relevant throats. For $\alpha = 0$ the path shown by full black line is optimal, for $\alpha = 1$ the path shown by the thinly dashed path is optimal, for $\alpha = 2$ the path shown by thickly dashed line is optimal.

The shortest paths connecting the two nodes marked by red dots are shown for values of $\alpha = 0,1,2$. For $\alpha = 0$, all the weights are equal to 1 and the optimal path is simply the one with the less throats, shown as a full black line passing a throat of size 2. For $\alpha = 1$ the thinly dashed path is chosen with two throats of size value 5. Indeed, the sum edge of weights given by $\sum_{i,j \in p(s \to t)} \left(\frac{1}{r(i,j)}\right)$ is the smallest for the thinly dashed path, such as $\frac{1}{5} + \frac{1}{5} < \frac{1}{7} + \frac{1}{7} + \frac{1}{7} < \frac{1}{2}$ or $0.2 < 0.428 < 0.5$. For $\alpha = 2$, the thickly dashed path is chosen, composed of three throats of size 7. Indeed, the sum edge of weights given by $\sum_{i,j \in p(s \to t)} \left(\frac{1}{r(i,j)}\right)^2$ is smallest for the thickly dashed path, such as $\frac{3}{7^2} < \frac{2}{5^2} < \frac{1}{2^2}$ or $0.061 < 0.08 < 0.25$, despite being the path with the most throats.

5.2.4 Experimental path match

To evaluate a candidate path, we make use of a system of classification of active/inactive pores of the experimental data, as previously described in Yeates et al. (2019), Appendix B. Average pore velocity intensity values are compared to values for pores of similar sizes (split between 20 equidistant intervals of area). If a threshold is passed, then the pore is considered active. The threshold values are chosen as fractions of the average pore intensities for each of the pore sizes categories. In this way we extract ourselves from making any hypotheses on the way velocity intensity is spread out over the different pore sizes and simply recalculate a threshold value for each size category. We chose 19 size categories. We define two classification thresholds: half of average (low threshold) and the average intensity (high threshold). The pores contained the proposed paths can then be tallied up and the proportion of active pores within the proposed path

(situated between 0-1, i.e. the fraction of active pores within the candidate path) assesses quantitatively the match of the candidate path to the preferential path in the experimental image. This binary classification (i.e. active or inactive) method is preferred over a more direct method of taking average pixel intensity values of the whole path for two reasons. Firstly, a direct comparison of average intensity values for pores of different sizes seems prejudicial to larger pores, in which flow is more spread out, creating lower average intensity values. Secondly, due to the high spread of average pore intensities, taking the average pixel value over the path may create the illusion of a satisfactory fit when only a restricted number of high-intensity pores are contributing, and the rest of the candidate path is incorrect.

In Figure 5-4 we show the active/inactive pores for two different threshold values overlaid on the velocity map for both experiments studied. The active pores are shown in green and the inactive pores in red. We notice the path-like nature of the active pores and the low-flow inactive pores, in red, situated in between these paths. In these experimental conditions, we observe an important number of active paths and flow distributed equally throughout all sections of the model.

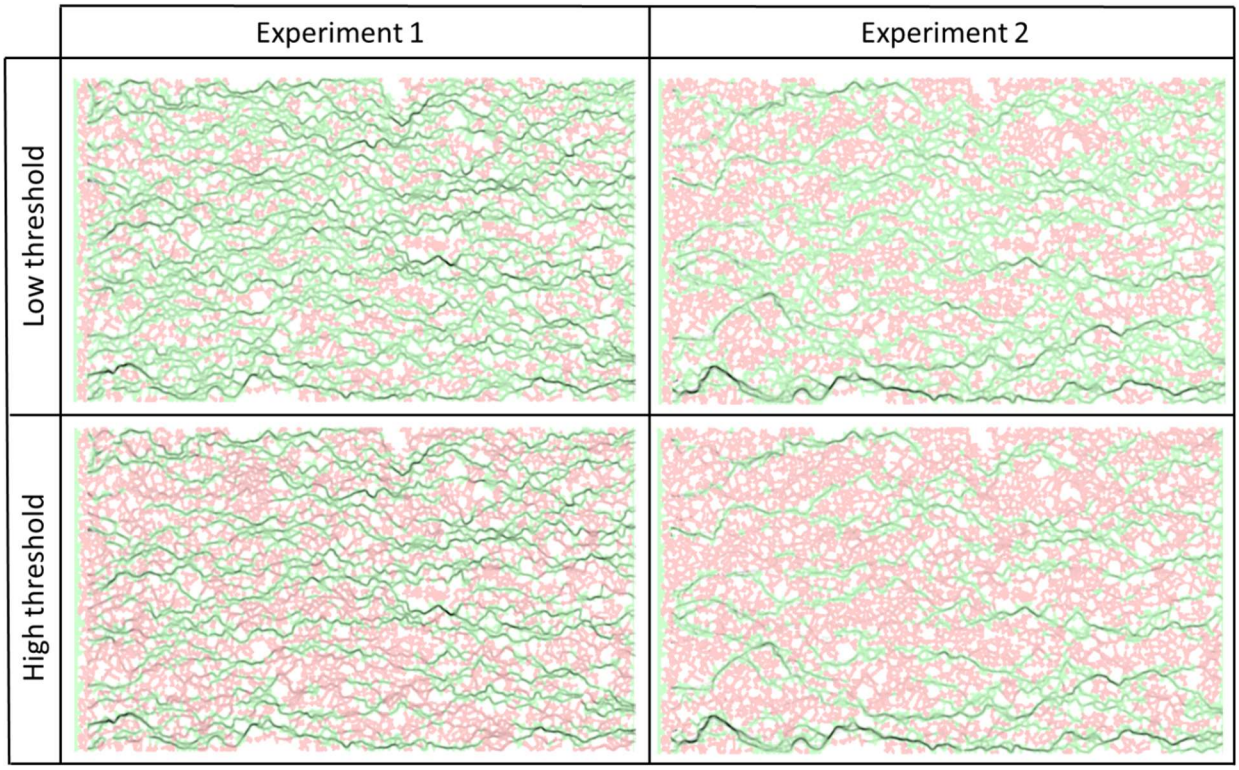

Figure 5-4: Velocity maps with overlaid active/inactive pore classification. Measured velocity in the pores is shown as dark shade in the model. Each pore is colored and overlaid according to its activity. Active pores are shown in green while inactive pores are red. White areas of the image correspond to solid grains. Flow is from left to right.

In Figure 5-1 we display the proportion of active pores for each experiment and threshold value, that serve as baseline values for assessment of the match of proposed paths to the experimental data. We note that the ratio of low to high threshold pores is equal for both experiments, demonstrating the equivalence between the two thresholds for both experiments.

Table 5-1: Proportion of active pores for each experiment and threshold value

Experiment	Low Threshold	High Threshold
Exp. 1	65.6%	41.1%
Exp. 2	50.5%	31.8%

5.3 **Results**

In the results section we proceed by first describing the model used and give associated statistics of the proposed paths in terms of geometrical and network properties only. Secondly, we show the

match with experimental data of the proposed paths. This sequence is repeated twice: for the 1-parameter model, and for the 2-parameter model.

5.3.1 1-parameter model – description and path properties

To propose a series of realistic paths, the parameters we can input into the proposing algorithm are: the graph, that includes a function of throat sizes as edge weights; the number of desired paths, K; and finally the maximal allowed overlap value θ, given between 0, for no overlap, and 1, if one path is fully contained in the other. We share here some statistics for different functions of throat sizes, with varying maximal path overlap value. The number of output paths, K, is maintained at a fixed value of 7. The throat size exponent spans 31 values, varying from 0 to a large value of 6, even if physically unrealistic, for the sake of assessing limiting behavior. The maximal overlap is restricted to 3 values for comparison: 0, 0.1, 0.5. The $\theta = 0$ case describes a situation in which no pore can be shared between any of the proposed paths, effectively slicing the model in two separate parts for each new path found. The $\theta = 0.1$ case allows limited overlap, in which some short passages that could be structurally attractive for flow, can be proposed in all the paths output by the algorithm. The $\theta = 0.5$ case represents a higher boundary, in which the number of shared pores between proposed paths can be up to half of the pores in either of the paths. See Chondrogiannis et al. (2017) for a detailed description of θ calculation.

It is to be noted that for some cases, when calculation time was too long for 7 paths, the algorithm was restarted, aiming for 6 paths, and so on, until it reached a solution in a practical amount of time (here 2 000 seconds). Figure 5-5 shows some characteristics of the proposed paths for each overlap value and throat size exponent. Statistics for each point are calculated over the average for all the 7 paths output by the algorithm for each throat size exponent α and overlap value θ.

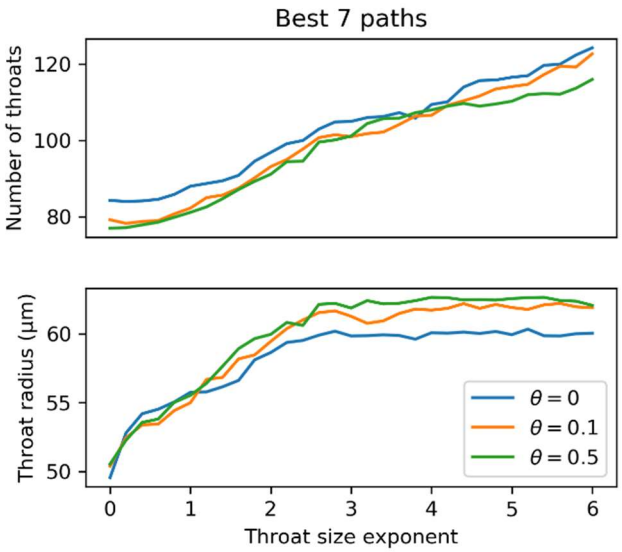

Figure 5-5: Characteristics of proposed paths for different throat size exponent values.

We observe that as the throat size exponent increases, the output path lengths increase, as described previously. We observe that for $\alpha = 0$, the average throat size for the paths is close to the average model, throat size, providing confirmation that these paths are independent of throat size. However, the average throat size seems to reach a plateau around a value of approximately $\alpha = 2.5$. This is understood as follows: for higher exponent values, the algorithm outputs paths that will avoid smaller and smaller throats at the expense of creating longer paths. However there exists a point in which the smaller, avoided throat contributes a negligible amount to the average, as the number of throats contributing to the average is ever increasing.

Another observation is the difference between the characteristics of the $\theta = 0$ paths on one side, and the $\theta = 0.1$ and $\theta = 0.5$ paths on the other side. The number of throats for the $\theta = 0$ paths at the lowest throat size exponent value is smaller and the value of the plateau of the throat size average is smaller. This translates the fact that each proposed path for the $\theta = 0$ output effectively separates the model into two parts and makes it harder to find short paths with small throat sizes in the created sections of the model.

5.3.2 Experimental match: 1-parameter model

We now perform a scan over the proposed paths for each setting and attempt to retrieve the highest fit to the experimental data. We display in Figure 5-6 the active pore match values for both threshold values, for different values of θ and the 31 throat size exponents for both experiments.

Each exponent and θ pair form an algorithm input setting, from which all the pores in all the proposed paths are noted and compared against a dictionary of active pores for both thresholds and both experiments. One input setting is then evaluated in four different ways, as shown by the four distinct plots in Figure 5-6. The match value is the ratio of active pores to all pores in the proposed paths for the given threshold value and is referred to interchangeably as a match percentage.

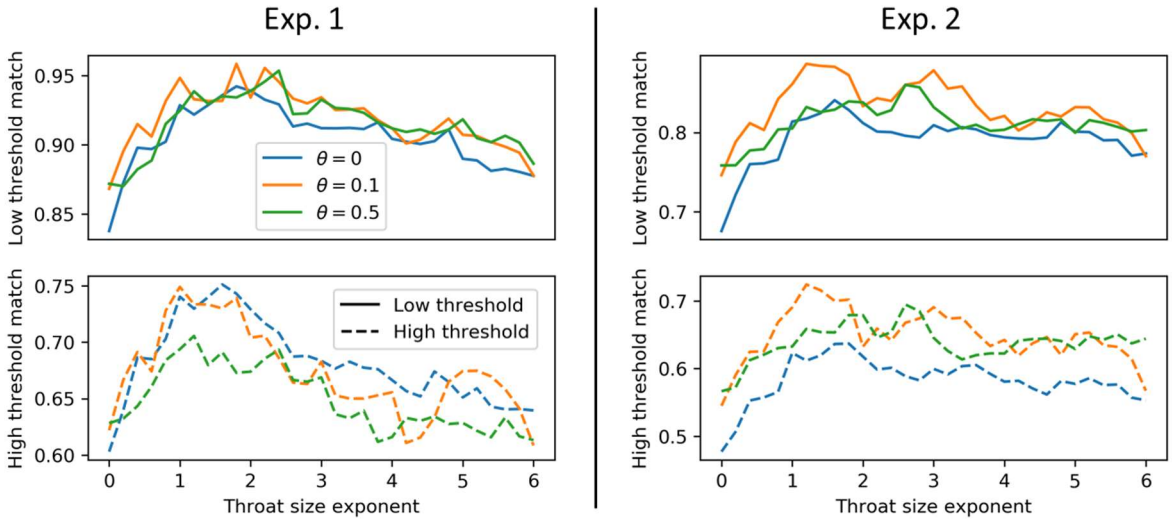

Figure 5-6: Path matches for high and low threshold values of both experiments for different overlap and throat size exponent settings

The observed match is globally very high. For Exp. 1, most input settings propose paths in which 90% of pores are active as defined by the low threshold and 65% as defined by the high threshold. In either threshold such ratios are more than 25% above the model average (see Table 1). For Exp. 2, in most input settings 80% of the proposed pores are active as defined by the low threshold and 60% as defined by the high threshold. The best fits occur for throat size exponents between 1-3 for the low threshold pores and 1-2 for the high threshold pores. This still gives a large degree of uncertainty as to how to best describe foam preferential paths in a characterized porous medium. The match values for $\theta = 0.1, 0.5$ are not significantly larger than the values obtained for $\theta = 0$. The match values for the high threshold for $\theta = 0.5$ however are significantly lower than the other values. For this reason, and for the reasons we previously mentioned issues occurring with the $\theta = 0$ value, we shall use the value of $\theta = 0.1$ for the rest of the analysis.

We first give some examples of relatively satisfying results. In Figure 5-7 we give three images of an overlay of the proposed paths calculated using $\alpha = 2$, $\theta = 0.1$ and displayed on the flow data

of Experiment 2. The active pores represented are from the high threshold activity classification. This is the image with the lowest number of active pores, so statistically hardest to match.

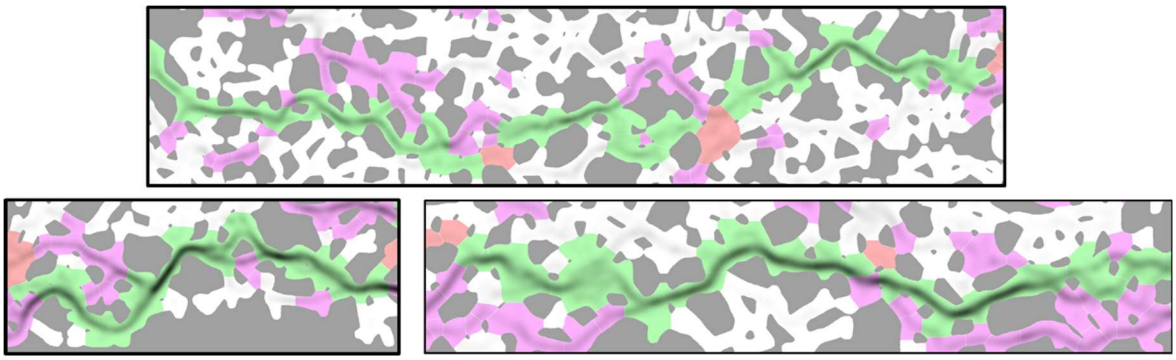

Figure 5-7: Examples of successful matches between model and experiment, flow is from left to right. Experimental velocity fields are shown in greyscale inside the pores (darker is higher velocity). The grains are in solid gray. The color code is the following: green pores are active in both experimental and proposed cases, red pores are proposed active but experimentally are inactive, purple pores are not proposed active but are experimentally active

We observe long sections high intensity flow are identified by the proposed paths (green overlay). The top image of Figure 5-7 shows a chain of 30 pores in which 28 are correctly identified by a proposed path. The bottom right image of Figure 5-7 shows a chain of pores in which 20 out of 21 are colored in green.

While these results are encouraging, we still note some parts of the proposed paths that don't adhere well to the flow reality. One telling example is shown in the bottom right image of Figure 5-7 in which the proposed path takes makes a sharp curve around an obstacle while the flow takes a straighter alternative path. Here we can start to see the limitations of using a simplified model of the network that only takes the throat size into account and disregards any notion of path distance or tortuosity. In Figure 5-8 we give three more examples of proposed path failures occurring for the paths calculated using a throat size exponent of 2, $\theta = 0.1$ and displayed on the flow data of Experiment 1. The active pores represented are from the low threshold activity classification. This is the image showing the largest number of active pores, in which a failed path match should statistically happen the less often.

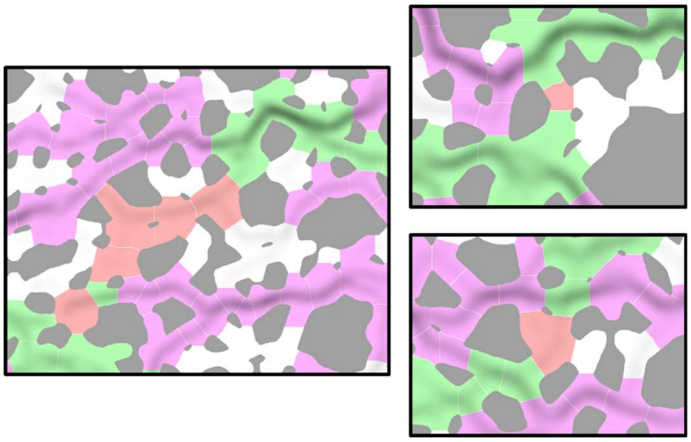

Figure 5-8: Examples of path match failure. Flow is from left to right. See Figure 5-7 for color code

It's worth noting that although many purple pores are visible, these do not describe a model failure as only a limited number of paths were calculated, and it is possible that a larger number of output paths could have included these. In the three cases shown here we identify a common error: proposed paths go off the experimental track by moving into pores that are perpendicular to the flow direction and aren't visited by the foam, despite not showing significantly small throat entrances.

5.3.3 2-parameter model - description and path properties

We make an addition to the 1-parameter model to offset the proposed path failures occurring for pores branching outwards to the flow direction. We introduce a second local parameter in the description of the flow, the angle of the pore centers neighboring a throat in relation to the flow direction: noted μ. The angle is formed by the vector the connecting the two pores (oriented in the flow direction) and direction of pressure gradient. An example of the angle definition is shown in Figure 5-9. We refer the reader to the Appendix 5-B for some statistics relating to this parameter and the independence of the 2 parameters.

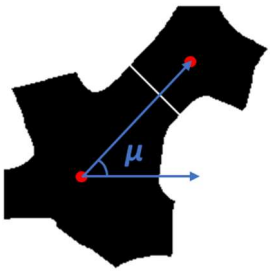

Figure 5-9: Simple example of μ. Two pores in black are connected by their centers (red dots) and projected onto the axis of flow, here shown as left to right.

The value of μ has therefore a maximal value of 90° when two neighboring pores are perpendicular with respect to flow direction, and a minimal value of 0° for pores aligned in parallel to flow. Inclusion of the μ parameter in the edge weight of the throat connecting pores i to j in the graph, as noted by $w(i,j)$, is done by taking a function the cosine of μ and multiplying it by the throat size term. A similar function to the throat size term is used, with a simple exponent β that is left free to vary. We then write the edge weight function, with both throat size and μ angle terms as:

$$w(i,j) = \left(\frac{1}{r(i,j)}\right)^{\alpha} \left(\frac{1}{\cos(\mu(i,j))}\right)^{\beta}$$

For simplicity, the allowed values of the β parameter vary in the same way as the α parameter, in 31 equally spaced values from 0 to 6. We show statistics associated to the proposed paths in the 2D parameter space in Figure 5-10.

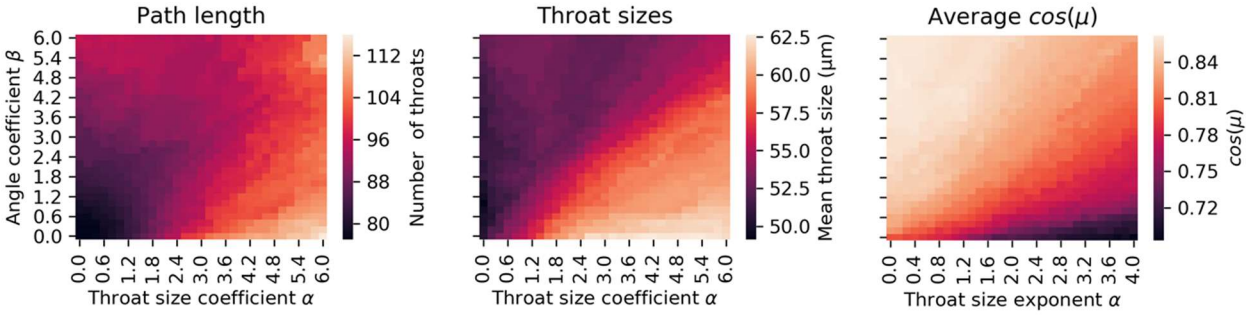

Figure 5-10: Statistics of paths proposed in a 2D parameter space

Interesting 2-dimensional patterns appear. We note that the path lengths (Figure 5-10, left) are of the same order as for the 1-parameter model. While the path lengths heatmap seems to have a

global minimum in the bottom left corner for $(\alpha, \beta) = (0,0)$ it has two local maxima in the bottom right and top right corners for values of $(\alpha, \beta) = (6,0)$ and $(\alpha, \beta) = (6,6)$ respectively. In accordance with the explanation of the 1-parameter model results, path length increases as the algorithm is fed more and more widely spread edge weight values in the graph (i.e. some throat weights become so large that it chooses to take a series of smaller values with a lesser contribution to the overall path sum). The $(\alpha, \beta) = (6,0)$ path length maximum is then understood as occurring because of a widely spread throat size term only, with no contribution from the angle term, explaining the average throat size rise in this zone. The $(\alpha, \beta) = (0,6)$ path length maximum is then understood as the equivalent phenomenon, in which a longer path is chosen purely on the basis on avoiding unfavorable pore-to-pore angles. The average throat sizes in $(\alpha, \beta) = (0,6)$ (Figure 5-10, center) and angle cosine in $(\alpha, \beta) = (6,0)$ (Figure 5-10, right) confirm this observation. For these parameter values, they respectively take the model average throat size and the model average cosine value (for the full model: $\bar{r} = 51\ \mu m$; $\overline{\cos(\mu)} = 0.63$). What is not easily understood is the decrease in path length across the $\alpha = 6$ parameter series, before the rise to the $(\alpha, \beta) = (6,6)$ maximum. Increasing β with a fixed α should create a larger weight spread and lead to longer paths. We refer the reader to Appendix 5-C for this analysis.

5.3.4 Experimental match: 2-parameter model

We show in Figure 5-11 colormaps of experiment match values for each edge weight parameter combination for both experiments and both thresholds.

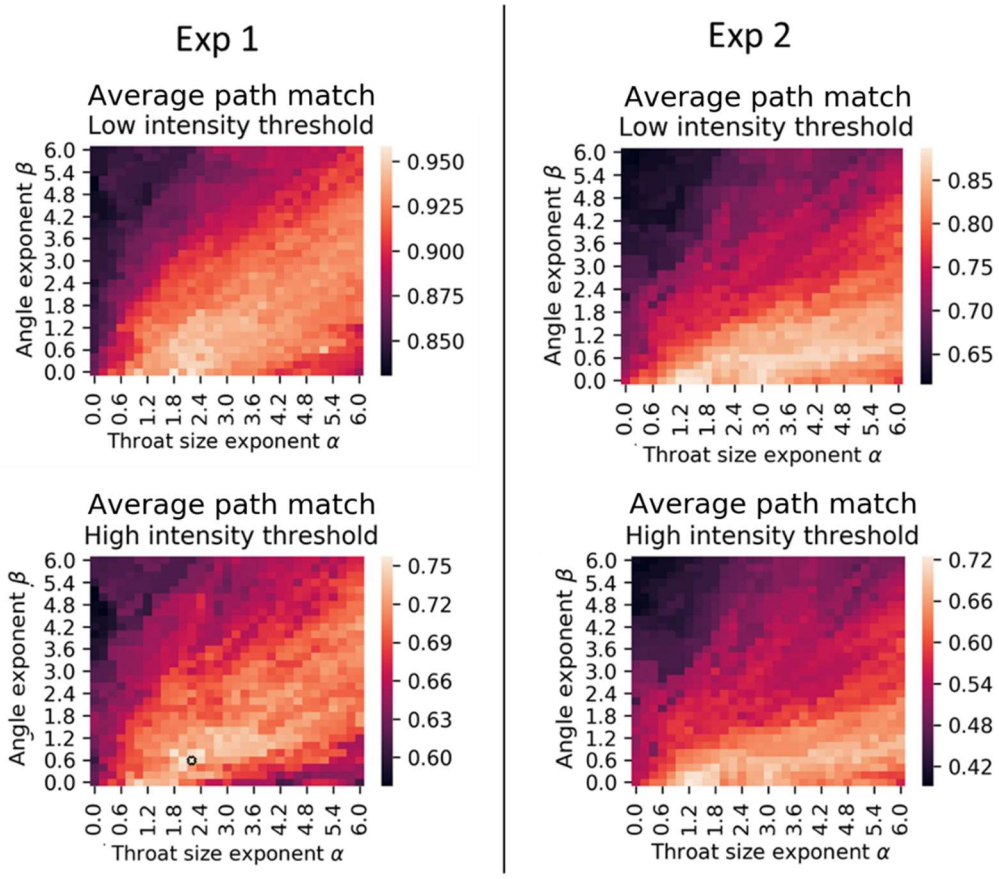

Figure 5-11: Path matches for 2-parameter model combinations for both experiments and thresholds.

We observe that many parameter combinations match well the experimental paths. Low values of β give the best matches. In fact, for experiment 2, the best matches are observed for $\beta = 0$, i.e. the one-parameter model. For experiment 1, while a large zone of good experimental matches is observed for the low intensity threshold for values of $\alpha < 3$ and values of $\beta < 1.6$, the best values for the high intensity threshold are observed for $(\alpha, \beta) = (1.8 - 2.4\,,\, 0.3 - 0.9)$, i.e. for a non-zero β, with the angle parameter adding capacity to match the data more closely. The best fit for experiment 1, high threshold (Figure 5-11, bottom left) using a 1-parameter model is obtained at $(\alpha, \beta) = (1\,,\, 0)$ obtaining a match score of 0.749, while the best fit using a 2-parameter model: $(\alpha, \beta) = (2.2\,,\, 0.6)$, achieves 0.7573, a small but non-negligible 1.1% increase.

To interpret this result, we consider the varying flow rates in both experiments. The lower flow rate of experiment 1 could shows no angle dependence. Indeed, at lower flow rates, we observe that preferential paths are less chosen on the basis of immediate path straightness or pore-to-pore alignment with flow, as described by the angle parameter, and instead are mainly chosen as

tradeoffs between path shortness and throat size, as described by the one-parameter model. With faster flow rates, while the paths seen in the lower velocity experiment are also accessed, we observe more paths are accessed, which in turn creates a more parallel flow. In this way we observe less paths don't branch off perpendicularly to the flow direction.

The colored imaged showing the results from the combination displaying the experiment 1, high threshold best fit, $(\alpha, \beta) = (2.2\,, 0.6)$, shown by a small marker in Figure 5-11, is shown in its entirety in Appendix 5-D. We observe large sections of the flow-carrying paths are correctly matched by the algorithm. While many incorrectly proposed pores, colored in red, do appear, upon inspection they seem to still carry flow and aren't entirely incorrect such as in the examples given in Figure 5-8. Furthermore, as active/inactive pores are determined on a local basis and not included in a path, it is not even guaranteed that a model-spanning path of active pores will truly exist. Rather, the path should be evaluated in its capacity to capture the largest number of active pores in the model.

5.4 Discussion

5.4.1 Path-based flow characterization viability

Here we stress the effectiveness of the path-based formalism by showing the results for the best model fit for experiment 1, $(\alpha, \beta) = (2.2\,, 0.6)$. In Figure 5-12 we display how different models successfully capture high-flow pores, even with the simplest model explored $(\alpha, \beta) = (0\,, 0)$, in which no structural parameters are included into the edge weights, and the paths are simply the shortest (in graph representation). However, the $(\alpha, \beta) = (0\,, 0)$ model does implicitly take the porous structure into account as the decomposition into pores and throats itself was performed using a distance-map based watershed. A comparison is also made to a model proposing paths that minimize physical path distance. The paths minimizing the physical distance were obtained by taking throat weight the sum of the distance between the pore center and throat center for both pores associated with the throat, ΔPtP. The sum of the weights for all throats in the path then was used as physical path distance. In Figure 5-12, left we show for varying values of N, the percentage of N-highest average velocity pores in the entire model that are captured in the paths. For emphasis, the model-proposed paths are also compared to a random choice of pores (right). The success

probability for the random choice of pores was simply the number of chosen pores (same number as in the proposed paths) over the total number of pores.

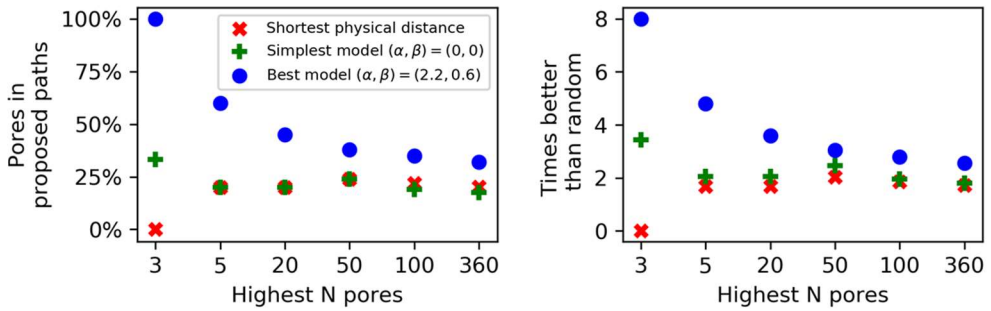

Figure 5-12: Comparison of path prediction performance for experiment 1 for the best fit model, the shortest number of pores model, and the shortest distance model.

We observe that the path-based models perform better than a random choice of pores (Figure 5-12, right). Even the simplest model, based purely on minimizing the number of pores, successfully predicts a large degree of high flow pores, achieving similar results to the physically shortest paths. The similarity between the results of the shortest distance model and the smallest number of pores model seems to indicate that both descriptions are similar and could originate from a spiked distribution of distances between first neighbors. However, upon inspection of the proposed paths, this appears to be untrue and the proposed paths are quite distinct. The paths are shown in the Appendix 5-E. Finally, the best model fully predicts the 3 highest flow-carrying pores and almost 50% of the top 20. This demonstrates the viability of a path-based graph model for characterizing high flow zones for foam injections in a heterogeneous porous medium.

5.4.2 Difference between experiments

We note that the best models for each experiment take different parameter values. The active pores in Experiment 1, the high rate experiment, are best predicted by the 2-parameter model with $(\alpha, \beta) = (2.2\,, 0.6)$. However, Experiment 2, the low rate experiment, is best predicted by the 1-parameter model with $(\alpha, \beta) = (1.2, 0)$. The problem this study attempts to solve, i.e. predicting preferential paths of a polydisperse foam in a heterogeneous porous medium, is akin to finding the paths of least resistance for foam, evaluated for combinations of local structural parameters taken as hydraulic resistance. The path of least resistance then minimizes the sum of resistances between both ends of the model. For a rectangular channel, of width W and of height H, length L and of

fluid viscosity μ, the hydraulic resistance R_h for a monophasic fluid can be approximated by equation (32) as (Tanyeri et al. 2011), for $H/W < 1$:

$$R_h = \frac{12\mu L}{WH^3(1 - 0.63\,H/W)} \tag{32}$$

The path of least resistance then minimizes the sum $R_{tot} = \sum R_h$ for all the channels in the model. The validity of this equation depends on the exact ratio H/W. For values of H/W close to 0.5, the error is approximately 0.15% and for H/W = 0.1 the error drops to 0.003%. For values of H/W > We show a histogram of H/W values in Figure 5-13 showing that most of the throats in our model respect this condition. We note that some smaller throats (as shown by the non-zero number of H/W > 1) are clearly out of the domain of applicability of the above equation and the hydraulic resistance diverges for such widths. For $H/W>1$ the calculation should invert H and W in the equation, retrieving a dependence on the width of W^{-3}. However, we note these smaller throats are very limited in number and therefore shouldn't be considered for the analysis as they have little chance of being used by the foam flow both statistically, and due to high pressure required for capillary entry.

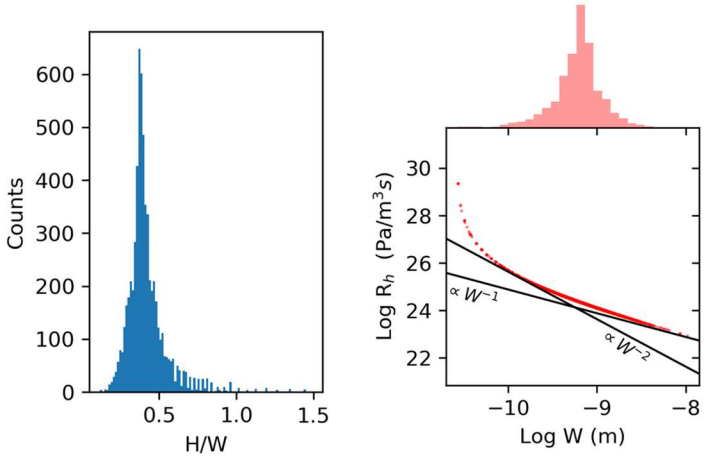

Figure 5-13: Aspect ratio H/W distribution (left) and distribution of hydraulic resistance (right).

The calculated hydraulic resistance from the equation above is also shown in a Log-Log plot making the throat width dependencies apparent (right). For simplicity, the throat length is taken a constant value here, given by half the mean ΔPtP value for all first neighbors, and water viscosity is used. The R_h values are shown as red dots. To guide the reader, we give two lines displaying on

one side the asymptotic dependency of R_h as W^{-1} at large throat widths and provide a W^{-2} line tangent to R_h values at lower widths. We supplement the plot with a histogram showing the distribution of widths in logarithmic space on top of the Figure 5-13. This plot shows that most throats are situated in an intermediate zone of mixed dependence between W^{-1} and W^{-2}, demonstrating that a series of models with values of α between 1 and 2 may in fact be physically appropriate. For this reason, and with the understanding that the average throat size in both models does not change significantly, (see Figure 5-10, center), we will not justify the higher α exponent in the best fit for experiment 1 as its physical justification is not obvious.

The best model fit for Experiment 1 however, includes a non-zero contribution from the angle parameter, with $(\alpha, \beta) = (2.2\,, 0.6)$. This is a demonstration of difference in behavior for higher velocity foams, in which, while showing a strong dependence to throat size, preferential paths are also chosen based on pore-to-pore alignment with pressure gradient, despite their capillary ease of entry.

In supplement, Figure 5-14 displays the average velocity in the pores, rather than the number of active pores, to reinforce the validity of the model as best fit in both experimental matching frameworks. We observe a maximum located in the same parameter pair as found using the active/inactive pore classification.

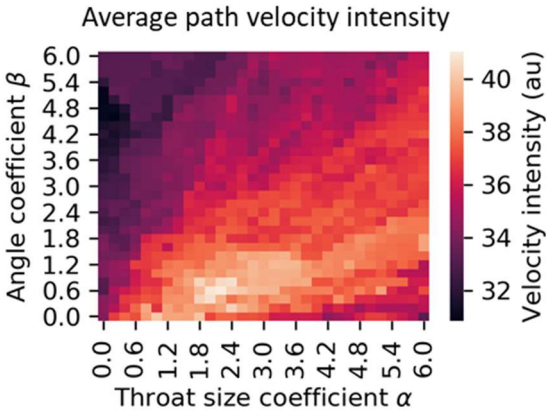

Figure 5-14: Average velocity intensity for all paths in each setting. The best model is the same as shown in the active/inactive high threshold pore framework.

The presence of a non-zero β parameter in the best fit is conformed microscopically by looking at the bubble displacement distributions. Access to individual bubble tracks can provide a

displacement term in the Y-direction (perpendicular to pressure gradient) compared to total displacement in all directions. Y-displacement and total displacement were taken simply as Euclidean distances between start and end point of the bubble tracks. Taking the inverse sine of the ratio of Y to total displacement yields the angle of deviation of the bubble from the pressure gradient direction, named ϕ. We take care here to distinguish the displacement of flowing bubbles from the quasi-zero displacement of static bubbles, which adds noise to the final probability distribution by filling it with the displacement ratios of static bubbles. We show in Figure 5-15 the different bubble displacement distributions that are bimodal in log-space, allowing us to segment the flowing bubbles with ease as the right side of the bimodal local minimum for each distribution.

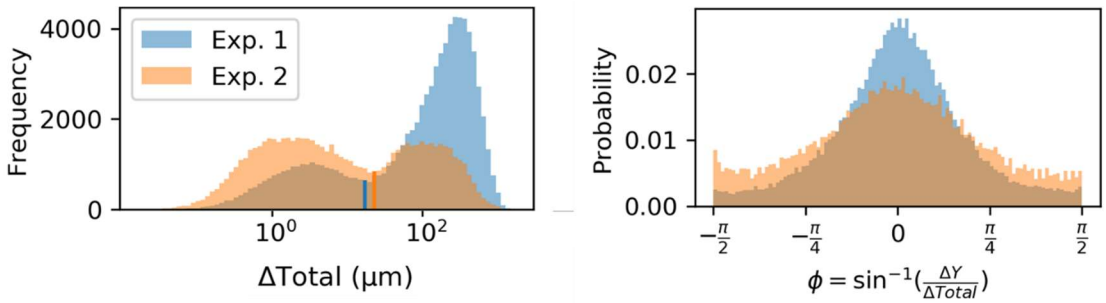

Figure 5-15: Bubble displacement distribution (top) and bubble track deviation angle from pressure gradient (bottom) for both experiments.

The deviation angle distribution confirms microscopically the different model fits for each experiment. While both angle probability distributions are symmetric and centered on zero, the faster flowing foam (Experiment 2) is more spiked in zero, showing a larger tendency for the bubbles to remain in parallel tracks to flow.

We offer the explanation that the higher flow rate and pressure gradient enable a larger number of paths to be accessed by the foam and remain aligned with pressure gradient to minimize the number of flow path intersections in which a large amount of energy is dissipated through viscous shearing. Inactive paths are observed more frequently in the lower velocity case. They can originate from either capillary difficulty of entry or insufficient pressure gradient required to dislodge trapped foams. The larger pressure gradient of Experiment 2 facilitates foam mobilization creating a larger number of active paths. In turn, a flow path to crossing the medium in the Y-direction would imply numerous intersections with other active flow paths in which crossroads situations arise. Flow paths then can't freely traverse the medium in the Y-direction due to pre-existing flow paths,

staying aligned with pressure gradient. In this sense, the initial motivation of overlapping preferential flow paths requires some refining. While we observe that some flow paths join and create higher velocity sections for a given distance, or otherwise split into two branching downstream paths, we rarely observe point-like intersections between two continuously flowing paths from different directions. More precisely, these kinds of intersections create either flow paths that deflect off each other, if the geometry permits, or otherwise creates intermittent traffic-like flow. We give two examples of flow paths that show large vertical displacement in lower velocity experiment, while being contained by surrounding active paths in the high-velocity experiment.

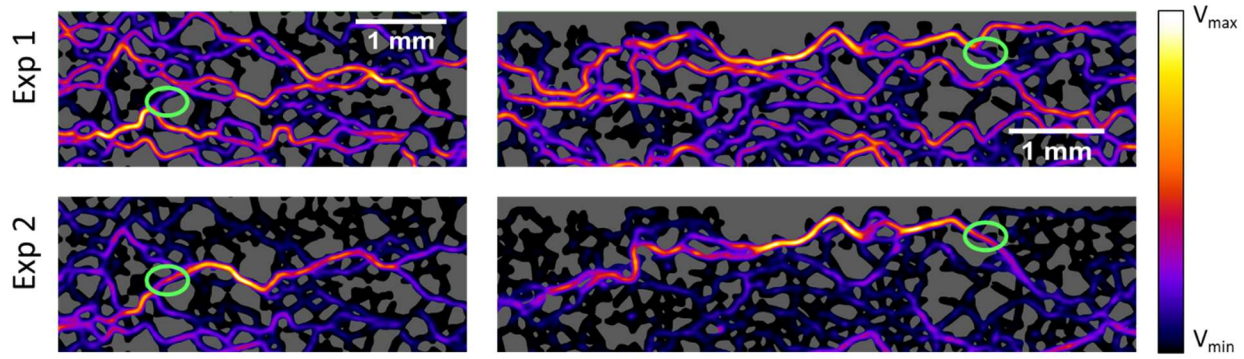

Figure 5-16: Comparison of flow maps for two areas of interest for each experiment. We observe flow path deviation perpendicular to pressure gradient in experiment 2, while access to these zones is denied by the presence of other flow paths in Experiment 1. We circle in green the exact access links that are crucial in keeping the flow in the straighter paths for the high-velocity experiment. Flow is from left to right in both examples. Note: colormap contrast has been forced in each example for clarity.

In Figure 5-16 we can observe two distinct cases in which pre-existing flow paths in the higher velocity experiment inhibits the foam access to these zones. Following the flow from left to right, we see high intensity paths describing significant movement in in the Y-direction only in experiment 2 in two key areas circled in green.

As well as the different injection rates, the experiments also show variable bubble size distributions within the model. Larger bubbles contribute to the flow map in Experiment 2 as shown in Figure 5-1. This could also be a source of dissimilarity in the fitted models. Indeed, while the lower bound of bubble sizes is roughly equivalent, larger bubbles could in fact guide the flow within the Experiment 2. For a lower injection rate and lower induced pressure gradient, the necessary Laplace pressure gradient needed to enter certain smaller throats may not be achieved, and large

bubbles will in fact test multiple downstream throats before entering the widest. The smaller bubbles shown in Experiment 1 will mostly be of the order of the throat size, therefore not probing multiple throats for the widest possible entrance. Instead, in this situation, straighter paths therefore used.

The presence of the higher throat size exponent $\alpha = 2.2$ in the Experiment 1 best fit is more intriguing. This exponent could either reflect a physical phenomenon for faster flowing foams or could be a consequence of the intermediate dependence (between $\alpha = 1$ and $\alpha = 2$) of the hydraulic resistance for our model throats, as shown in Figure 5-13, right. Finally, this effect could be a product of the interaction between the two parameters within the model. Indeed, we can remark that the good model fit zone, shown in bright colors in Figure 5-11, has a shape that evolves diagonally in the positive direction of both α and β. This behavior could show that the two components of the graph weight function interact non-trivially, and is confirmed by the lower skew in edge weight distribution in this area, as shown in Appendix 5-C. In this sense, the higher exponent of the best fit for Exp. 1 could simply be a consequence of the best model necessitating a non-zero value of β.

5.5 Conclusion

In this study we show how a simple graph-based model can successfully capture zones of high-flow in experimental foam data in a porous medium. Structural understanding of high-flow areas or paths could help in predicting larger scale flow properties such as apparent viscosity of foam in the medium. Furthermore, the highest flow zones could be also be indicative of the highest shear stress locations in the medium and pinpoint the exact areas where foam film coalescence and foam destabilization may occur. From experimentally established flow maps for different experiments, we attempt to characterize the paths chosen by the largest bubbles, that have previously been shown to contain a significant portion of the flow in a series of distinct paths. The two experiments investigated here are performed with varying injection rates and display slightly different bubble size distributions. A graph representation of the porous network is used in which edge weights are chosen as functions of two separate throat properties. A model parameter optimization is done to establish the best model fits for each experiment individually. We show how a simple 1-parameter model based on throat size retrieves a large amount of the high flow areas in a complex medium.

Furthermore, we include a 2nd local structural parameter that describes the alignment of pores with respect to pressure gradient. We observe that a larger sensitivity to the pore alignment parameter exists for the experiment with a higher injection rate, with smaller sized bubble sizes, whereas the 1-parameter model best describes slower injections with the presence of large bubbles. While this path-based approach shows promise by identifying high-flow zones in a complex medium using a simple model, further investigation into the effect of varying model structure and injection conditions in necessary to generalize the behavior seen here.

Appendix 5-A: Porous network and extracted graph

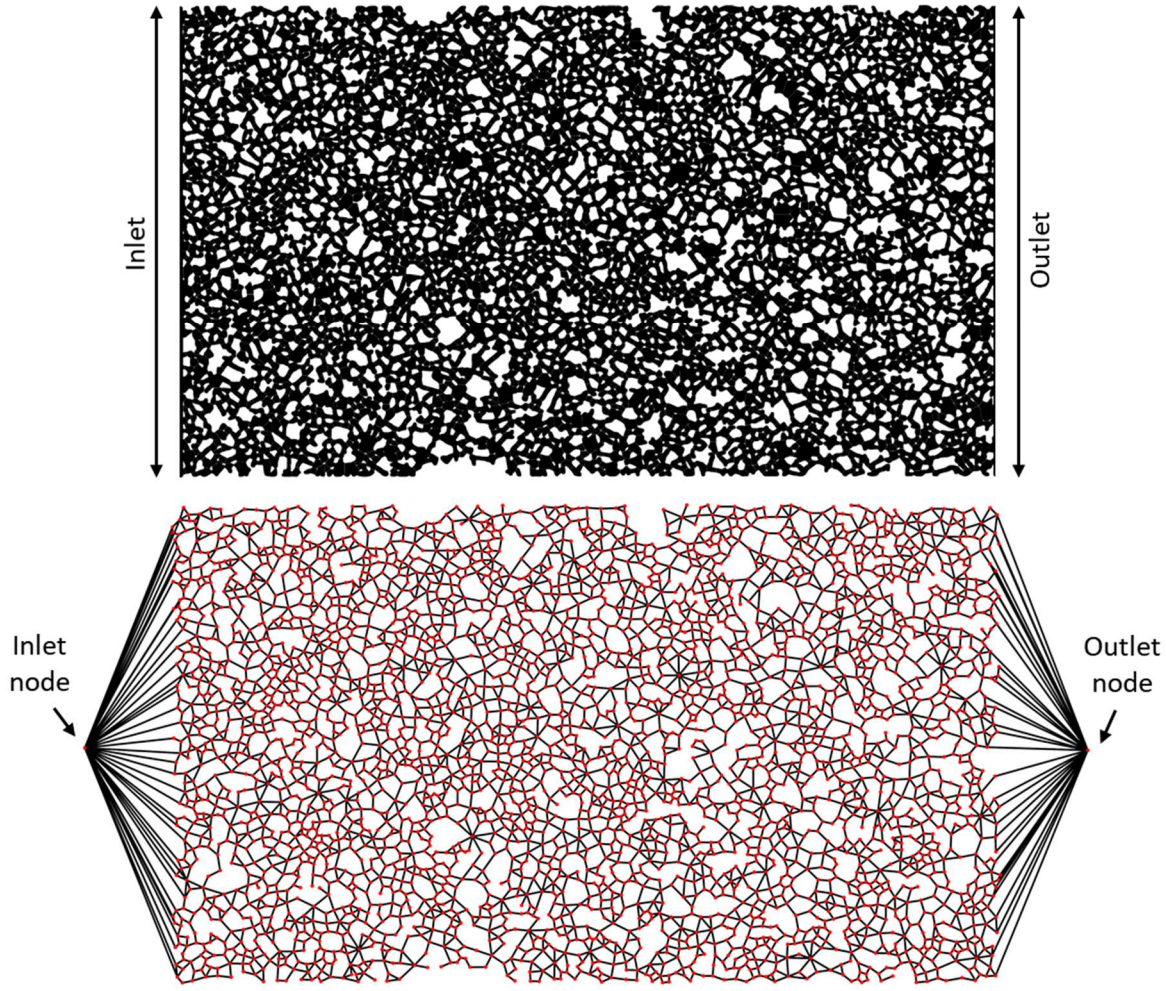

Figure 5-17: Top: Micromodel structure with porous area seen in black and obstacles in white. Fluid injection can be performed on the full width of the model. Bottom: Extracted complete graph with added inlet and outlet node that share edges with all the adjacent nodes to the inlet or outlet of the model.

Regarding the structural parameters used for the weights of the edges connecting the inlet/outlet nodes to the rest of the network the throat size for each edge was trivially the throat that connected the network to the inlet/outlet zone. However, the angle μ that shows the pore-to-pore alignment with pressure gradient was set equal to 0 (perfect alignment with gradient) for all nodes connected to either to inlet or outlet nodes. Indeed, as the center of mass of the inlet and outlet nodes are positioned in the central axis, taking the alignment angle with this position would create erroneous bias against pores outwards from the central axis.

Appendix 5-B: cos(μ) properties and parameter independence

As the parameters are more and more spread out with the increasing exponents α or β, the path lengths along the $\alpha = 6$ parameter series should therefore monotonically rise to the $(\alpha, \beta) = (6,6)$ maximum. This discrepancy reveals either a hidden relationship between the two supposed independent parameters r and cos(μ), or otherwise an oversight on the authors behalf in the way the weight spread is interpreted to contribute to path length.

We first explore the parameter independence. We display in Figure 5-18 a histogram showing the distribution of values of cos(μ), and a boxplot displaying the spread of values of size for each cosine category, dividing the values into 10 quantiles with an equal number of points from 0 to 1.

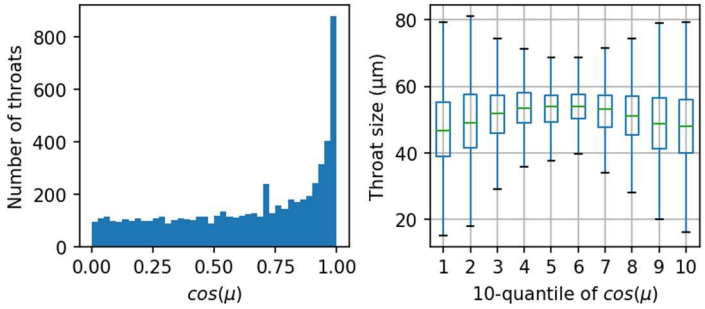

Figure 5-18: Histogram of cos(μ) and boxplot of parameter independence in the 2-parameter model

The histogram shows one-sided distribution for the cos(μ) values. This is a natural consequence of the cosine function, and a similar distribution occurs when plotting the cosine of a random sequence of angles from 0-90°. However, a noticeable unexpected spike occurs around the 0.7 value. The boxplot shows a median throat value that raises slightly in the central quartile and shows a smaller data spread towards the central values of cos(μ). We believe this behavior, as well the spike occurring around 0.7 for the cosine histogram are consequences of the way in which the watershed algorithm establishes throats and pores from the binarized model but does not represent a significant dependence between the two structural parameters used.

Appendix 5-C: Edge weight characterization with respect to parameter combinations in the 2-parameter model

Different combinations of parameters produce different edge weight distributions for the graph input to the path-proposing algorithm. Properties of this distribution are believed to be linked to the path length, we explore here the edge weight distributions and how they affect the proposed paths. Values of the throat size term, r, take values all above 1, displaying a roughly gaussian distribution (Yeates 2019). The values of $\left(\frac{1}{r}\right)^{\alpha}$, therefore lie between 0-1. Similarly, values of the throat size term, $\cos(\mu)$, are between 0-1, while $\left(\frac{1}{\cos(\mu)}\right)^{\beta}$ is bounded as [1-∞[. We show in Figure 5-19 different edge weight histograms for different parameter combinations.

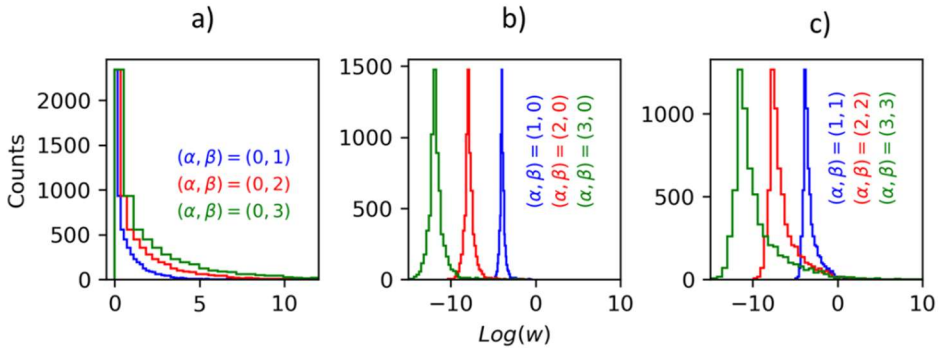

Figure 5-19: Edge weight distributions in terms of different parameter combinations.

We observe in Figure 5-19a that increasing the β parameter spreads the distribution in the positive direction, while maintaining many values at $w = 1$. Raising the α parameter as shown in Figure 5-19b spreads the distribution in both direction and shifts it towards smaller values of w. As the parameters are independent, increasing both in combination therefore combines both effects without any further interaction; it spreads the distribution both ways and shifts it to the left, but creates a more significant spread on the right-hand tail due to the raised β parameter. As we can see, both the variance σ^2 and mean μ of edge weight distributions change with each parameter combination. We show the parameter distribution skew in Figure 5-20. We suspect that the non-monotony of the path lengths function visible on the $\alpha = 6$ parameter series is related to the skewness of the distribution. Indeed, a decrease in the calculated skew of the edge weight distribution occurs where the path lengths dips along the $\alpha = 6$ series. This indicates an interaction

between the parameters in the model that explains why the proposed paths match experimental data relatively well in a large zone diagonally situated in the positive α and β directions. The edge weight distribution is significantly less skewed in this region, which leads the path proposing algorithm to output shorter paths that closer matches to the preferential paths observed in the foam experiments.

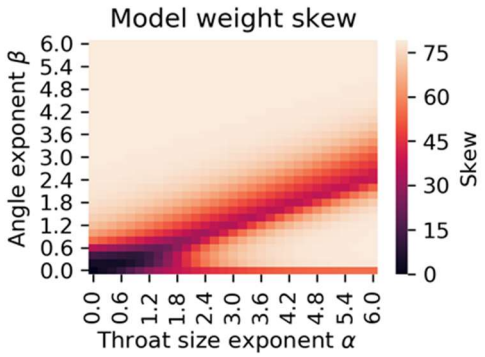

Figure 5-20: Edge weight distribution skew for all model weights.

Appendix 5-D: Full model experimental match for the best model for Experiment 1: $(\boldsymbol{\alpha}, \boldsymbol{\beta}) = (\mathbf{2.2}, \mathbf{0.6})$ with a high intensity threshold on the pore activity classification. Flow intensity is shown in greyscale within the porous network. The color code is given in Figure 5-7. Flow is from top to bottom.

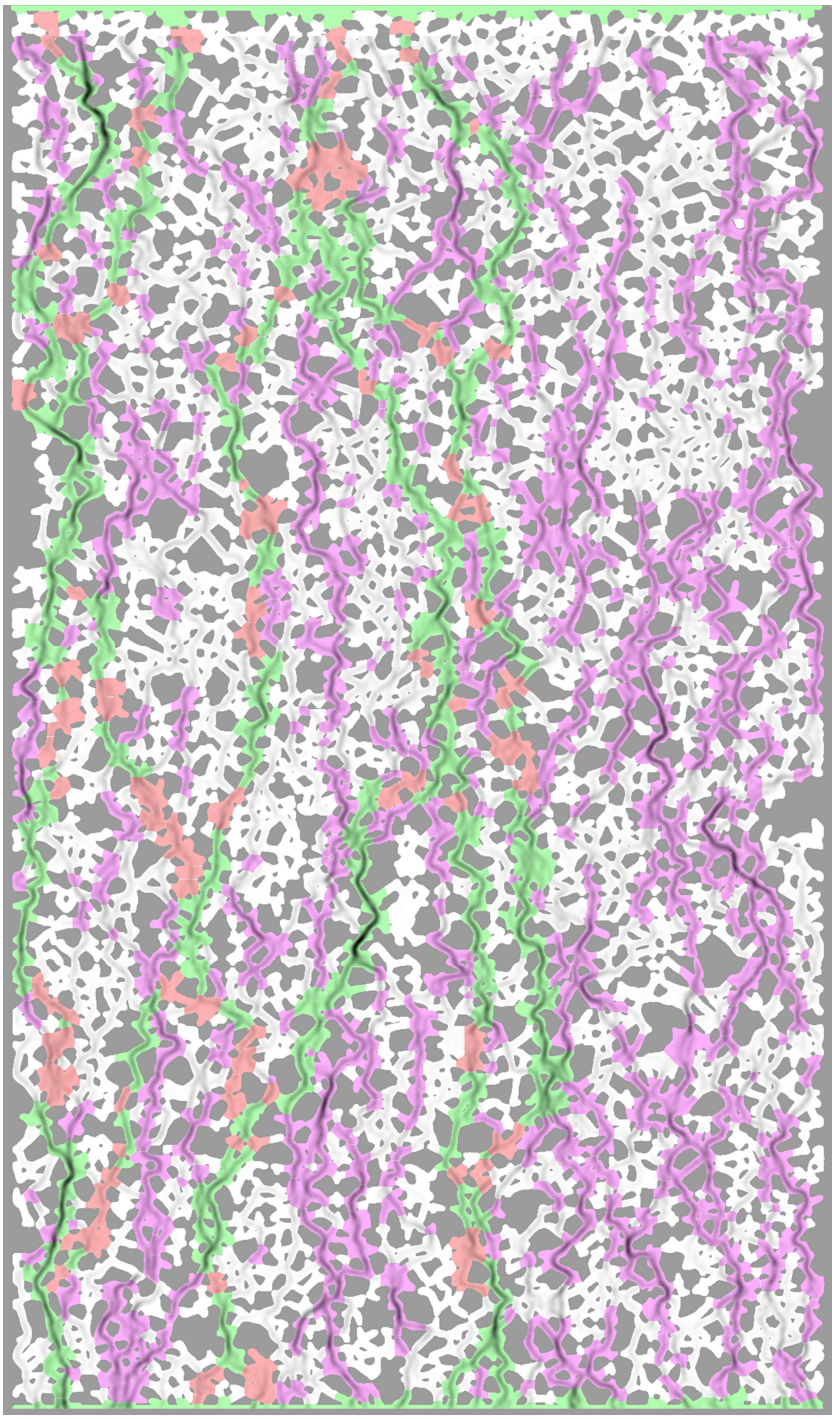

Appendix 5-E: Full model experimental match for the best model for Experiment 2: $(\boldsymbol{\alpha}, \boldsymbol{\beta}) = (\mathbf{1.2}, \mathbf{0})$ with a high intensity threshold on the pore activity classification. The color code is given in Figure 5-7. Flow is from top to bottom.

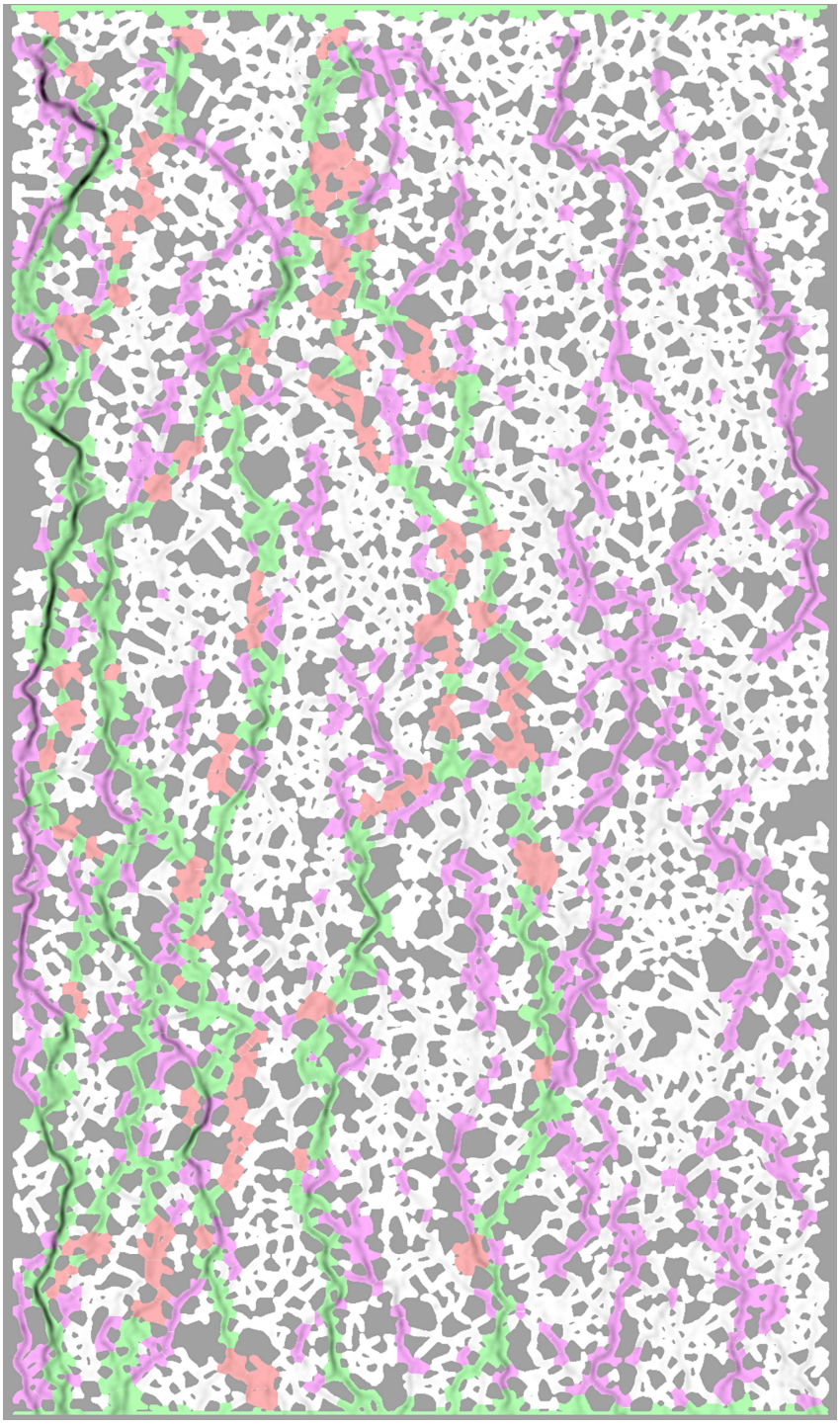

Appendix 5-F: First 5 proposed paths for comparison models used in Figure 5-12.

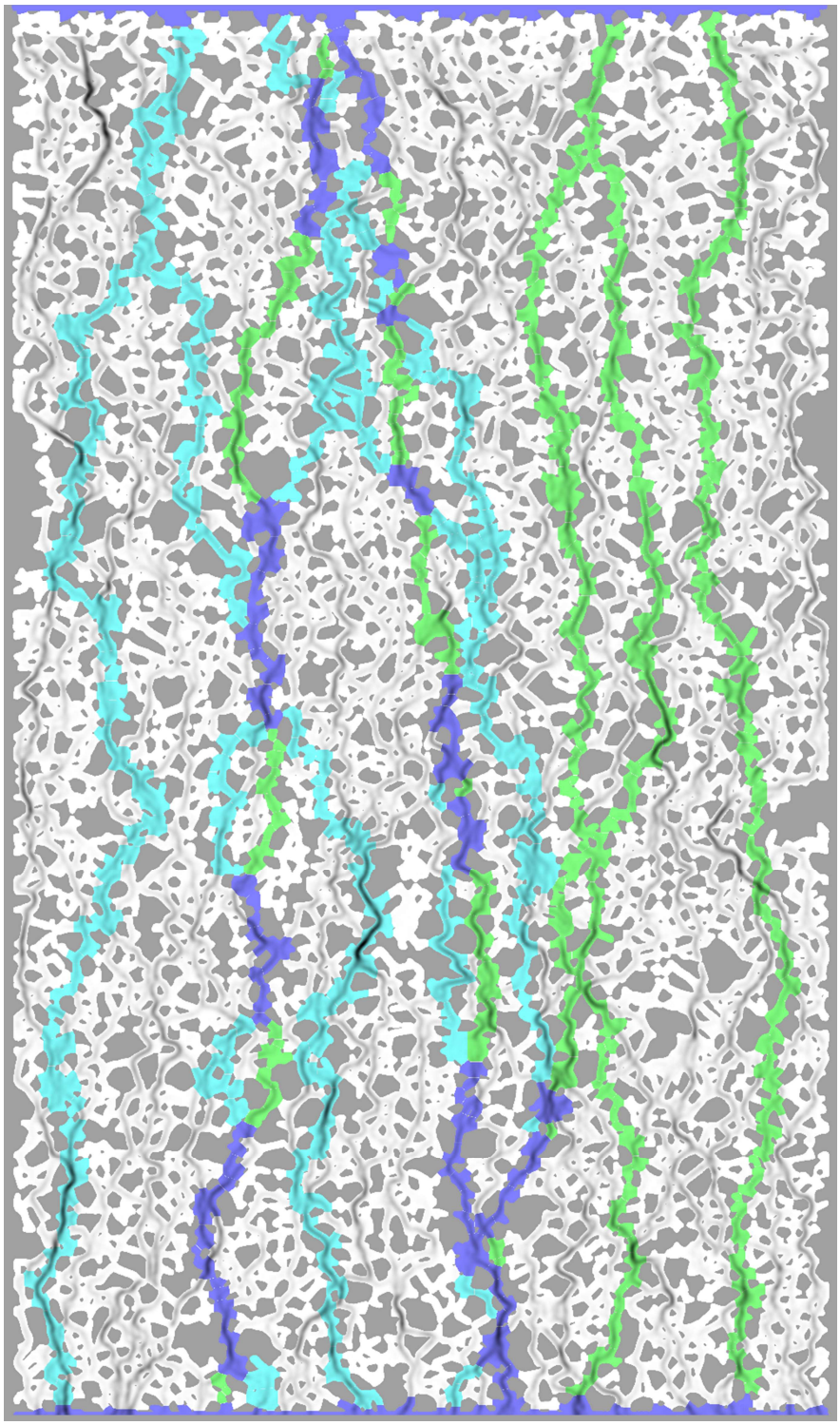

The paths in light green are proposed by the model minimizing physical distance, whereas the paths in light blue are proposed by the model minimizing the number of pores. The areas in dark

blue are common to both sets of paths. The velocity intensity of Exp. 1 with flow from top to bottom is shown in grayscale within the porous area for comparison. We note that for the shortest distance paths (green), the mean path distance is 19826 μm, composed of a mean 91.8 pores per path. The paths minimizing the number of pores have a path distance of 21582 μm and are composed of 79.2 pores per path.

Submitted article ends here

5.6 Model Generalization

In the previous section we showed how a simple graph-based model could characterize to some degree high-flow preferential paths of largest bubbles in a complex micromodel. We showed that the paths proposed by integrating throat properties into a representative graph of the model sufficed to determine at least some of the high-flow paths and zones inside the model for 2 different experiments. In this section we apply the previously described path-proposing framework and model optimization to a series of different cases in order to generalize both the validity and explore the potential variation in optimal model parameter we can observe.

5.6.1 Application to a reversed orientation experiment

The 1-dimensional graph model is fully isotropic, in the sense that proposed paths linking top to bottom of the model will resemble paths linking left to the right, as they are purely based on minimal combinations of throat size. The 2-dimensional model integrates the notion of alignment to pressure gradient, therefore models with non-zero β parameters are only isotropic with respect to the direction of pressure gradient. Furthermore, the graph model is undirected, in the sense that source and target nodes can be substituted, and the proposed paths will be the same. The foam flow inside the medium however, is obviously directed from one end of the model to another, with implications that the high intensity areas may be dependent on the injection direction, due to local shear-thinning of foam occurring when setting up preferential paths. The results of the undirected model should therefore be tested on an experiment in the opposite direction.

With reference to the experiments visible in Figure 3-1, we shall make a comparison between two experiments of relatively similar injection conditions. We choose here to use flow data from the

experiment C1, situated close to the experiment A1 (known as experiment 1 in the article above). In supplement, the injection bubble size distribution parameters are quite similar in between the A1 and C1 experiments Table 3-1. Indeed, they both show intermediate to large average bubble sizes and standard size deviations. We can expect a significant degree of bubble size adaptation in both.

We show the model parameter optimization as well as the best proposed paths overlaid on velocity maps of the experiment. The bubble sizes used for the construction of the preferential path flowmap corresponded to the top 20% of bubbles in terms of frequency, which are shown in Figure 5-21 within the weighted histogram expressing spatial probability.

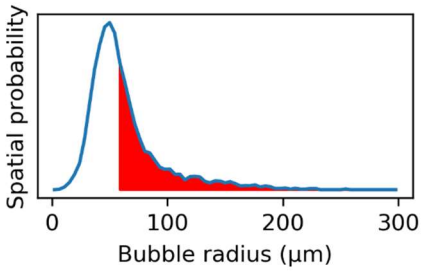

Figure 5-21: Spatial probability of bubbles from experiment C1 with the bubble sizes used for the creation of the preferential paths flowmap highlighted in red.

The bubble size cut off value was similar to the ones used in the previous two examples. We show the parameter optimization, using the same paths as output by the model in the previous section, only applied to a new flowmap.

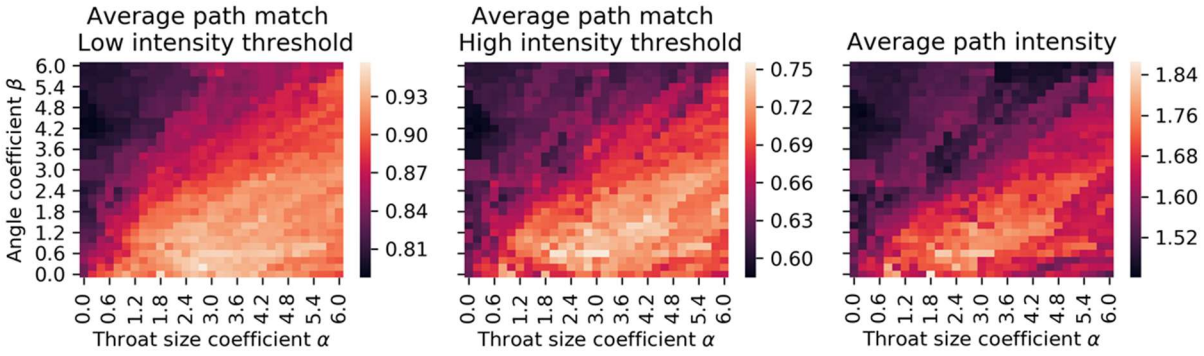

Figure 5-22: Model parameter optimization for the reversed flow experiment C1.

We observe that the best models are situated in a zone with $1.8 < \alpha < 3.2$ and $0.2 < \beta < 0.8$. This region bears a strong resemblance to the region of best fit for experiment A1. The model showing the highest number of highly active pores (Figure 5-22, center) is the same as for experiment A1, i.e. $(\alpha, \beta) = (2.2, 0.6)$. This indicates that the high flow zones can be characterized in the same way with respect to model orientation, which renders our use of an undirected graph model wholly appropriate. We display the best model paths and high active pore matches in Figure 5-23.

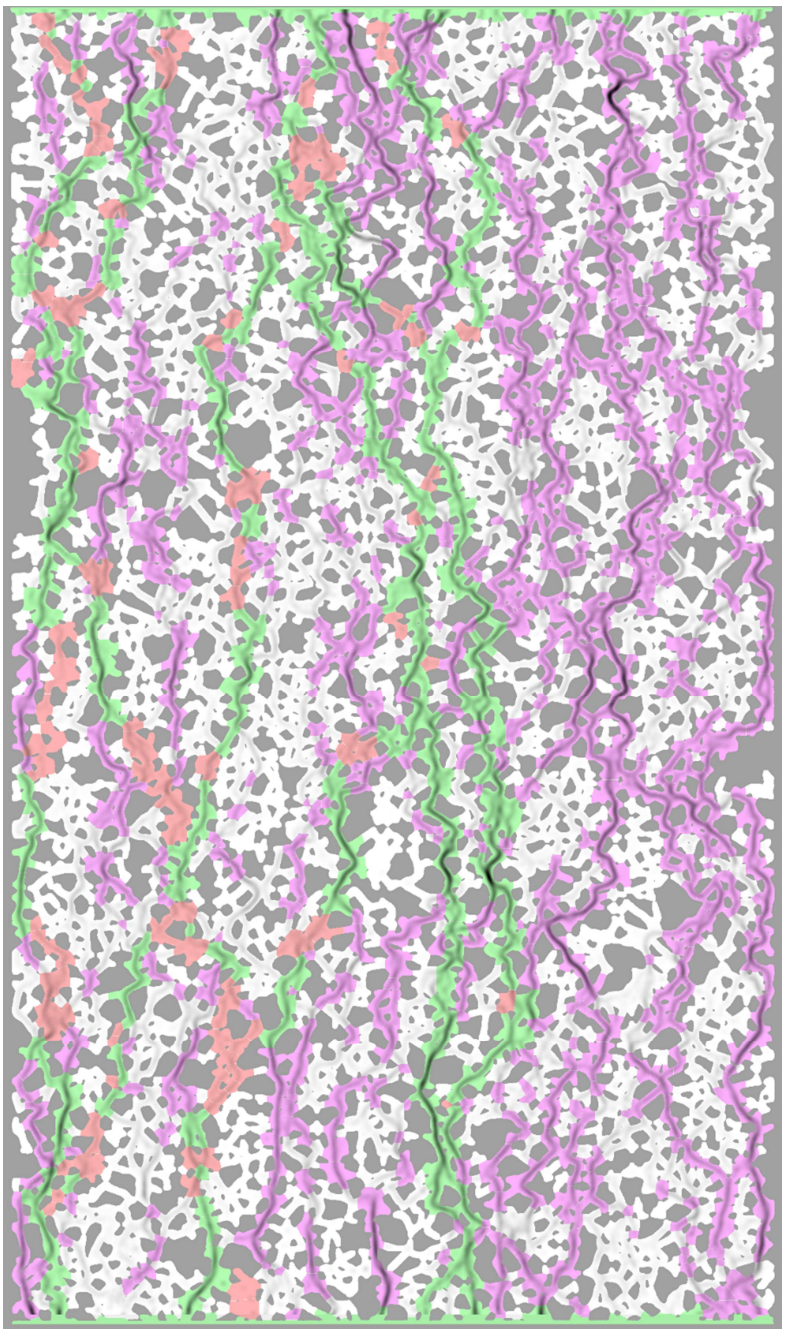

Figure 5-23: Full model experimental match for the largest bubble flowmap, experiment C1: $(\alpha, \beta) = (2.2, 0.6)$, high intensity threshold on the pore activity classification. The color code is given in Figure 5-7. In this case flow is from bottom to top.

5.7 Generalization to a different 2D porous medium

Within this subsection we shall apply the path-proposing framework to another example of pore-scale foam flow from the literature. We shall use flowmaps shown in Géraud et al. (2016), from which data has been extracted simply using the color intensity from the digital version of the publications. The data shown in this subsection differs in two notable ways to the data presented above. First, the experiments were performed on a larger scale. The authors use a porous medium composed of cylindrical obstacles inside a 17.8 cm long and 9.6 cm wide Hele Shaw cell. The cell depth was of 2mm, and the average throat radius of 1.75 mm. Secondly, the networks used were of lower complexity, displaying a lower number of obstacles (approximately 200 versus 2600) and showing a constant obstacle geometry. The authors give two examples of flowmaps, which are achieved similarly as here: via image binarization and using an unspecified individual bubble tracking algorithm. The steps leading from the bubble tracking data to the flowmap were also unspecified, and it is not clear if any smoothing or longitudinal image intensity uniformization were performed, to account for bubble size evolution and consequential tracking density evolution. While the general setup was the same between the two experiments from Géraud et al. (2016) explored, the exact position of the obstacles in the medium was changed between experiments, providing two distinct networks to analyze. The specific experiments shown in both flowmaps (coherent with the original publication numbering) are Experiment 7 and Experiment 43. The experiments are performed under different injection conditions. Compared to Experiment 43, Experiment 7 shows a lower gas fraction (0.72 versus 0.99), a smaller injected bubble radius with little size evolution through the model (0.65 times the average injection bubble size of Experiment 43), a lower total flow rate (less than half of Experiment 43) and a different surfactant formulation. However, we show here the applicability of the graph-based algorithm in both cases.

While the authors do provide an example (Exp. 7 only) of decomposition of the porous space into throats pores using an elegant method described in their Appendix, based on filtering the segments obtained from Delaunay triangulation of pore centers, we shall make use of the adjustable watershed algorithm described in the previous section to obtain a decomposition we deem appropriate.

We now display each experiment's data and porous network before showing a brief series of results including a small model optimization section in both cases.

5.7.1 Experiment 7, Géraud et al. (2016)

In Figure 5-24 we display the image extracted from the publication of the flowmap for Experiment 7 and show in greyscale the extracted velocity intensity we used for the analysis.

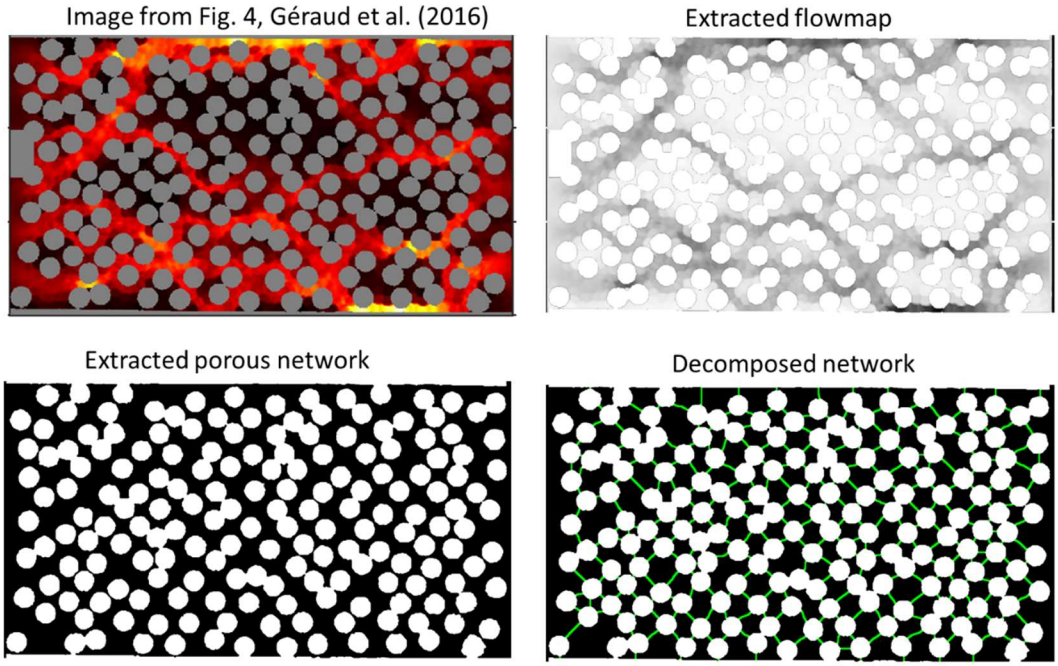

Figure 5-24: Image processing steps to extract the flow map from the publication and network characteristics. A decomposition of the porous space was also performed shown in the bottom right corner, in which the throats are shown in light green decomposing the black porous space

The image was obtained from a screenshot the publication at maximal resolution and saved as an RGB image. The porous network was first extracted from the captured image by splitting the image into different RGB (Red – Green – Blue) and HSB (Hue – Saturation – Brightness) stacks and performing intensity thresholds on the greyscale value in the grains for different images, multiple thresholds on different images were necessary as the grayscale value of the color flow color scheme sometimes intersected the grayscale of the grains in different stack decompositions. The network mask was then subtracted out of the flow map and the flow intensity was obtained by summing the slices of the RGB stack created from the image. For visibility, the flow map is shown with high values in black (i.e. inverted intensity scale) in Figure 5-24.

From the extracted network image, we use the adjustable watershed algorithm (with a tunable parameter set to 3) to decompose the network into throats and pores. A source node and target node were created, by removing throats adjacent to either left- or right-hand side of the network. The network created has 167 pores and 283 throats. A graph was then extracted using a 2D network extraction code in ImageJ. For simplicity, paths were only evaluated on the basis on the average path pixel intensity, i.e. the average grayscale flowmap value in all the pores contained in the path. Due to the lower number of available paths, and the high degree of overlapping paths visible in Figure 5-24, top left, we only choose the first 5 paths and allow an overlap of 30% between the paths.

A brief parameter optimization is performed, with the same exponent α and β with values and definition as described in the previous section. The average path intensity is then shown in Figure 5-25.

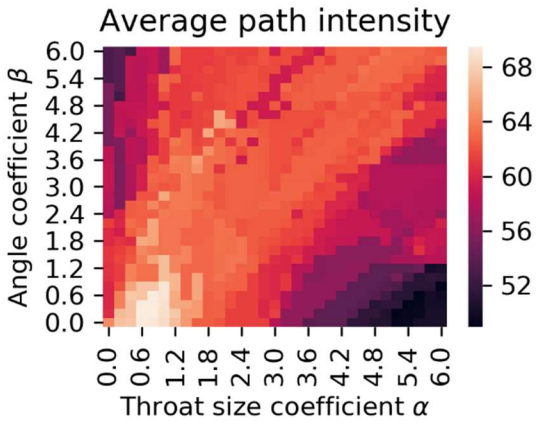

Figure 5-25: Average predicted path intensity for paths proposed for Experiment 7 of Géraud et al. (2016).

We note here that a zone of good fit is situated in the low left corner for low values of α and β. The best value of the grid is obtained for values of $(\alpha, \beta) = (0.6, 0.4)$ at an average path grayscale intensity of 69.51 but $(\alpha, \beta) = (0.6, 0)$ is ranked second with 69.46. In fact, the entire light patch in Figure 5-25 has similarly valued average path image intensities. Due to the shortness of the model most of these series of paths only vary by one or two pores, therefore displaying most of these model's output paths would be largely equivalent. We show the paths of the simplest model $(\alpha, \beta) = (0.6, 0)$ in Figure 5-26.

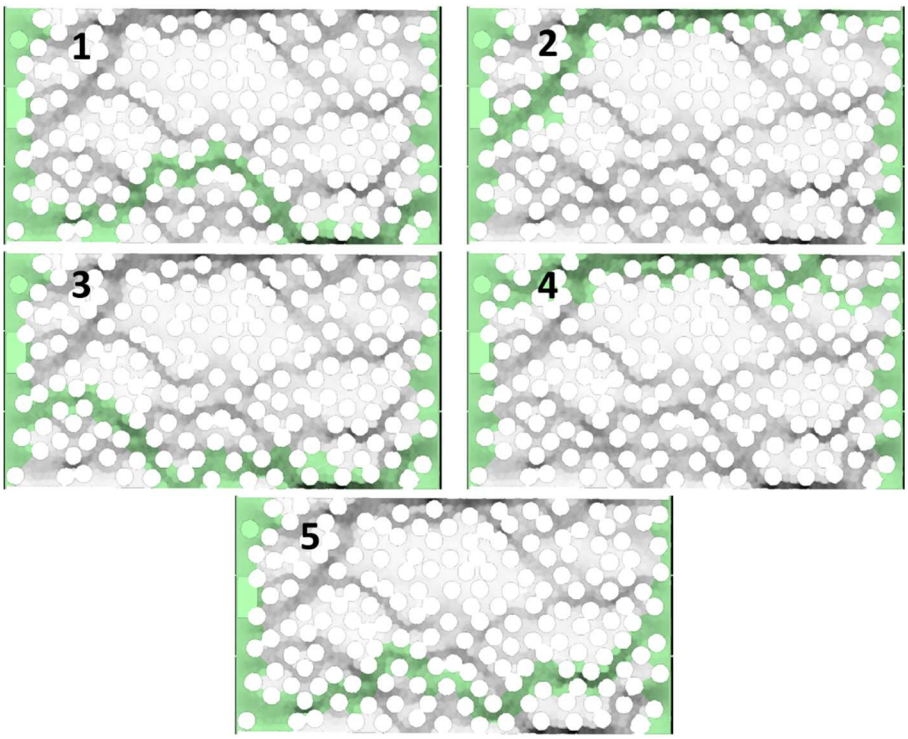

Figure 5-26: Top 5 paths described the model (α,β)=(0.6,0). Note: highlighting in green is simply to highlight the paths and not describe active pores as previously used.

The paths proposed by the algorithm agree very well the high velocity areas inside the model. Most of the high velocity areas are in fact captured by the paths. However, the central dark streaks seen in the model flowmap are not accessed by the top 5 paths. Interestingly, these paths correspond to areas described by the authors in which a large degree of intermittency, i.e. stopping and starting of flow, is observed. We offer an explanation here. In fact, this central path is of inferior rank as it doesn't appear in the top 5 paths proposed by the model. We investigate further paths of this setting to find the first appearance of the central paths. The first time they are observed are in paths 8 and 9 shown in Figure 5-27; with the intermittent zones shown in blue circles.

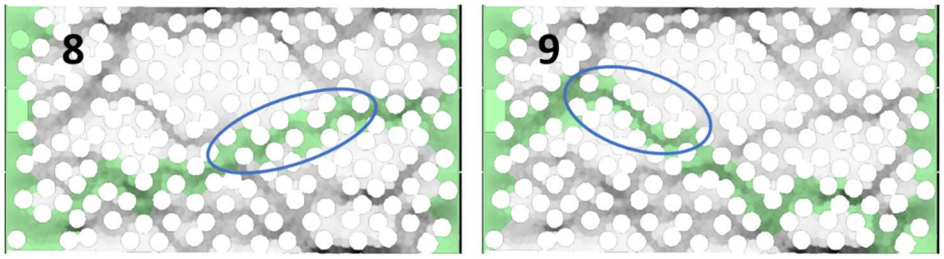

Figure 5-27: First appearance of the intermittent paths as described in Géraud et al. (2016), as output by the path proposing model. The intermittent paths appeared at a lower rank of 8 and 9, compared to the paths showing consistent flow shown in Figure 5-26.

Therefore, as well as capturing high flow zones, description of flow areas according to their path rank leads to building a hierarchy in flow activity: the best paths contain flow consistently whereas lower ranking paths may contain flow only intermittently if the local fluctuations in pressure or local differences in foam density permit.

5.7.2 Experiment 43, Géraud et al. (2016)

Once again, we extract the relevant flow map and network structure from the Figure 12 of Géraud et al. (2016) and present the decomposed network in which the throats are shown at the bottom left of Figure 5-28. The network analysis algorithm was then applied to the decomposed network to extract the neighborhood graph.

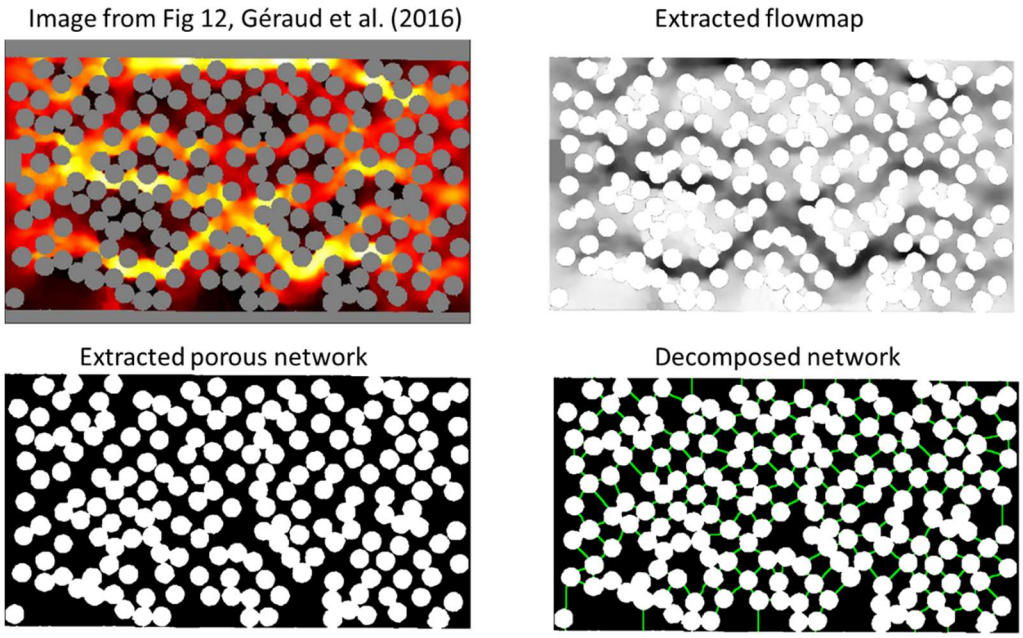

Figure 5-28: Image processing steps to extract the flow map for Experiment 43 of Géraud et al (2016). A decomposition of the porous space was also performed shown in the bottom right corner, in which the throats are shown in light green amidst the black porous space.

From these images, throat properties and neighborhood graph, we can perform a similar parameter optimization for this new flow map. We show the results for this experiment in Figure 5-29. As above, 5 paths were output using a 30% overlap tolerance value. However, for faster calculation we only take values of α and β up to 4 in a grid of 21 values.

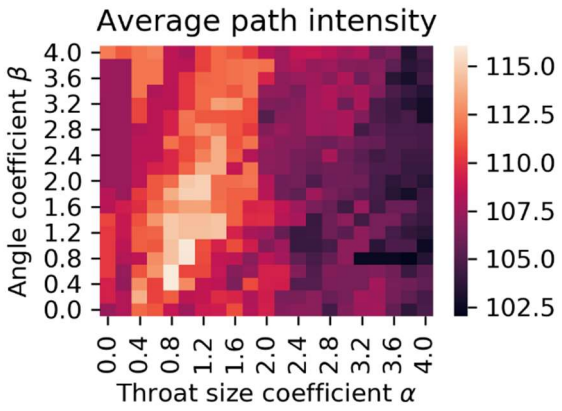

Figure 5-29: Average predicted path pixel intensity for paths proposed for Experiment 43 of Géraud et al. (2016).

We observe that the location of the best models is not as well localized as for Experiment 7. The best 2 ranked models are found in $(\alpha, \beta) = (0.8, 0.4)$ and in $(\alpha, \beta) = (0.8, 0.6)$. We observe a

good fit area along a zone diagonal of both increasing α and β. We show the 5 paths of the best model fit at $(\alpha, \beta) = (0.8, 0.4)$ superimposed on the flow map in Figure 5-30:

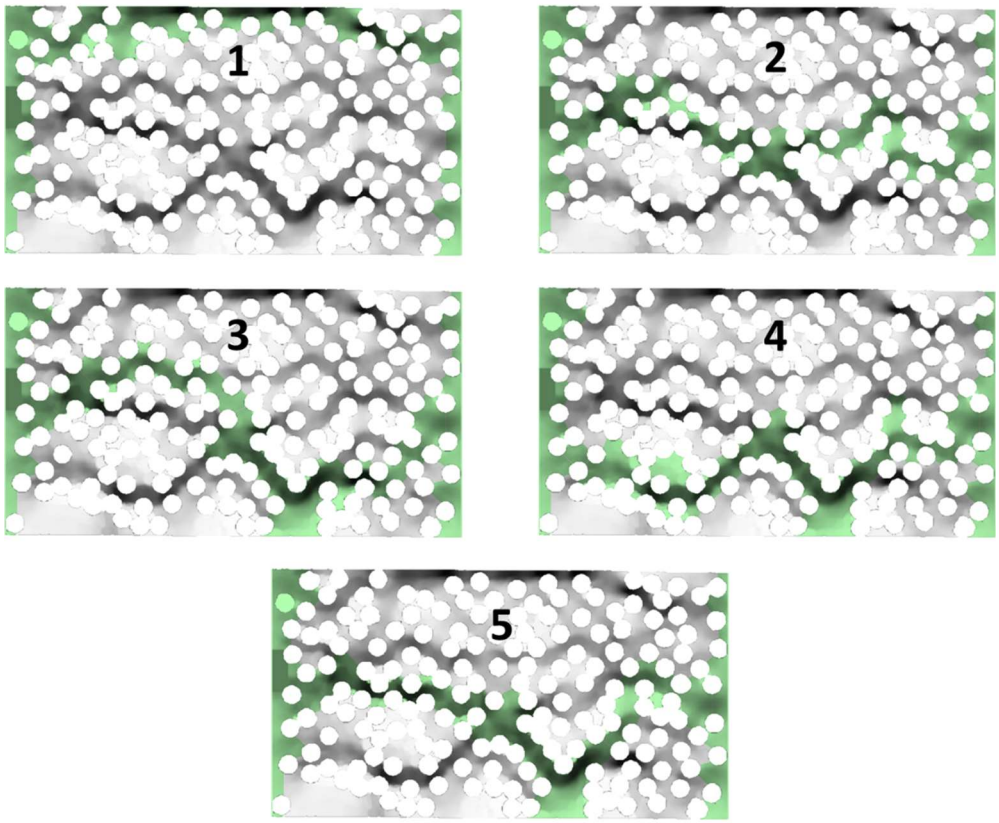

Figure 5-30: First 5 paths for the best model fit of $(\alpha, \beta) = (0.8, 0.4)$ for Experiment 43 of Géraud et al (2016). Note: the highlighting in green is simply to highlight the paths and not describe active pores as previously used.

We see that the model best fit captures most of the high flowing paths shown in the flowmap. The network used was decomposed into a smaller number of pores and throats than for Experiment 7, as many grains are touching and less throats were created. This network has 134 pores for 217 throats. In fact, the model output paths were very similar in most parameter combinations for this network. The path-proposing optimization process seems to reach a lower applicability limit in this case, in which most model settings seem to output equivalent paths which all contain flow and it becomes hard to distinguish which setting is the best.

This is to be contrasted with the results from the micromodel used in this study. Within our previously shown results, we used a network of 3968 pores and 6284 throats. While we were able to find a fitted weight function that resulted in paths that captured many of the high-flow areas in

the model, in some cases the paths made jumps in and out of high-flow paths, and only predicted correctly large sections of high intensity flow rather than full, model-spanning paths. It may well be worth considering that in our micromodel, the network complexity is superior to the modeling framework upper limit, within which a full, model-spanning path, while insightful, is maybe not fully appropriate. One possibility to consider may be to establish intermediate-sized portions (rather than full paths) than are consistently proposed when allowing a large degree of overlap in the output paths.

5.7.3 Discussion on optimal exponents

Using data from Géraud et al (2016), we obtain lower dependences on throat size coefficients that for the best fits for our micromodel. The best fits show α values inferior or equal to 0.8. When looking more closely at the aspect ratio H/W of these experiments, we observe that the throats are always larger than the model depth. We display the aspect ratio counts in Figure 5-31, left. The hydraulic resistance dependence on throat width should therefore be lower than for our data. This is demonstrated in Figure 5-31, right, in which the log values of R_h, calculated using equation (32), clearly scatter along a W^{-1} dependence.

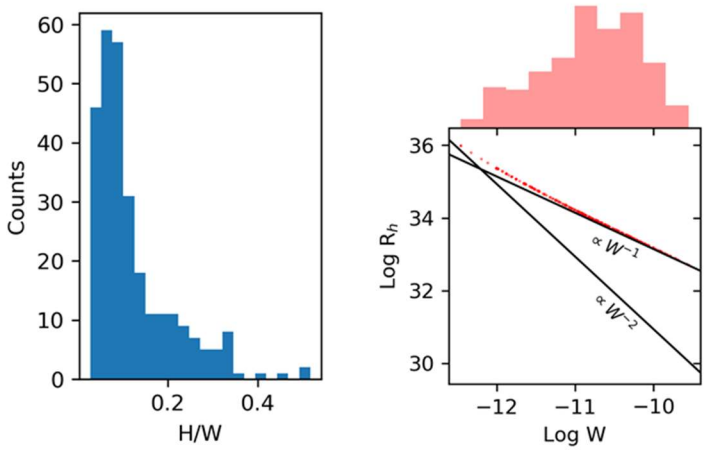

Figure 5-31: Aspect ratio and calculated hydraulic resistance for the network shown in Géraud et al (2016).

While the observed best fit exponents are coherent with the lower hydraulic resistances observed in the networks used by Géraud et al (2016), they are still consistently lower than the predicted resistance for a monophasic fluid in a rectangular channel. This lower dependence on throat width

is not fully understood and requires more investigation. One aspect that may explain the lower than expected throat size exponent may be a system demonstration of system hysteresis. Indeed, during a foam injection, the first paths to break through the porous medium and set up connected flow paths between both ends will see an increase in velocity at the moment of breakthrough as the pressure buildup over the model is released. Path resistance within that path will then decrease due to local shear-thinning of the foam and such a path will maintain a high level of flow. The first paths to breakthrough, however, will in fact be the shortest, and not those with the largest throats, assuming constant bubble flow rate. This could explain some of the lower dependence to throat size observed for the experiments here.

5.8 Returning to local structural features from graph-based characteristics

We have shown that it is possible to capture high-flow zones from a structural origin. These zones are not predicted locally but rather as components of preferential paths within the medium. Through our model framework we choose a limited number of paths, characterized by a given value of overlap within one another. Such choice is motivated partly by the observation that foam preferential paths seem to overlap only for a certain distance, but also due to the realization that the K-shortest paths for a complex network are essentially small variants of the same path. The K-shortest paths are the first K paths when ranked from decreasing path edge weight sum. While they are all distinct, some have equal path edge weight sum (in the case of equal edge weights, multiple shortest paths may share the same number of nodes).

The high degree of overlap of these K-shortest paths is true even for large values of K. The K-shortest paths have no condition of maximal overlap. They must simply be different from each other by at least one element. As an example, we show the first 1000 paths the K-shortest path algorithm between the inlet and outlet node, Figure 5-32, setting all edge weights equal (i.e. the simplest model). We add 1 to each count measurement to use a logarithmic color scale consistently.

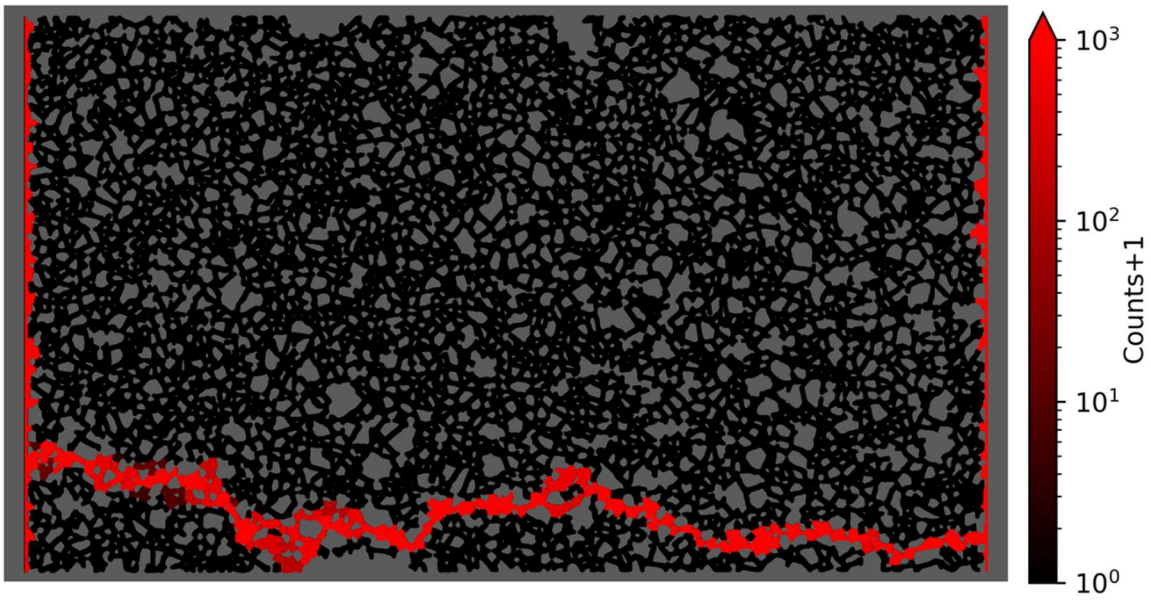

Figure 5-32: 1000 shortest paths using with no overlap constraint, using constant weights, from inlet to outlet node. The paths must be distinct in at least one element.

Visibly, all the paths are focusing around a single path but vary to a small degree in each new instance. This is not very useful for predicting high-flow zones in the entire network. Instead of choosing a fixed source and target nodes as the inlet and outlet nodes, we can choose instead two random nodes within the graph and construct the optimal path between them. If we repeat this process a series of times, we can get an estimate of the nodes that are important in connecting the various point of the graph. For comparison, in Figure 5-33 we show the first 1000 paths having random source and target nodes. Inlet and outlet nodes are excluded from this analysis, as their increased connectivity would create unphysical paths passing through the inlet or outlet node to reach target nodes more efficiently.

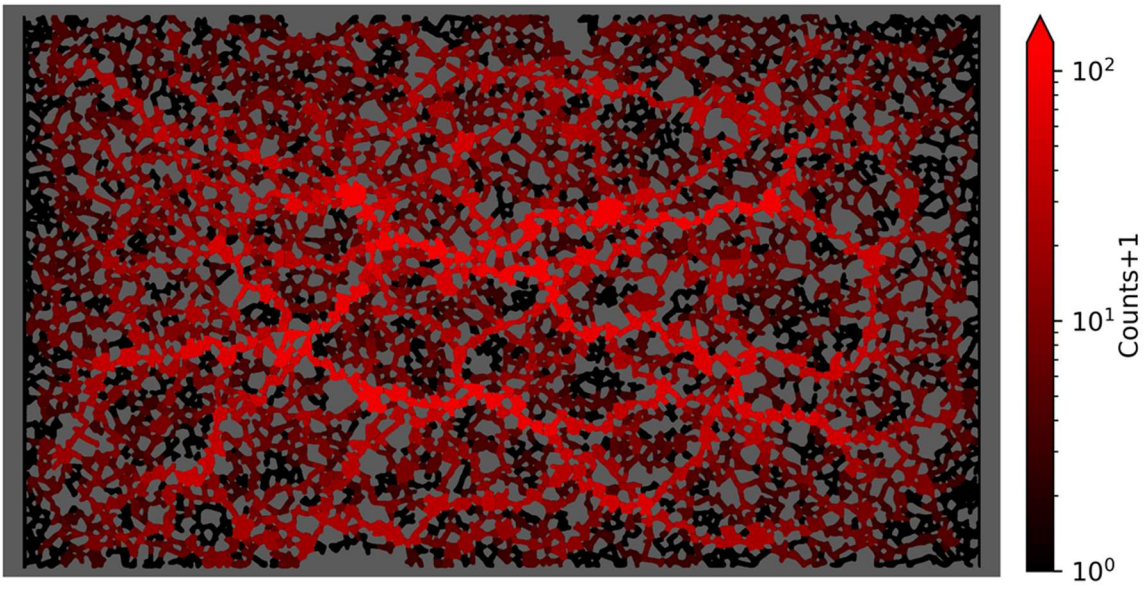

Figure 5-33: 1000 optimal paths using random source and origin nodes, using constant weights.

We can already see that certain central nodes and path segments are favored in the network. We can further build on this method by using the weights derived from the best model: $(\alpha, \beta) = (2.2, 0.6)$, taking 1000 random source and target nodes, therefore calculating the optimal paths based on the weights integrating both the notion of throat size and throat orientation. We show these paths in Figure 5-34. A, example of a foam flowmap is given for comparison. We show the data from experiment A1, all bubble sizes in the bottom image of Figure 5-34. We can see some of the distinctive trapped zones observed in the foam map appear darker in this map, dashed by light green ovals. Similarly, some of the high flow zones are captured in the brighter path segments and nodes, shown by full light green ovals in both images.

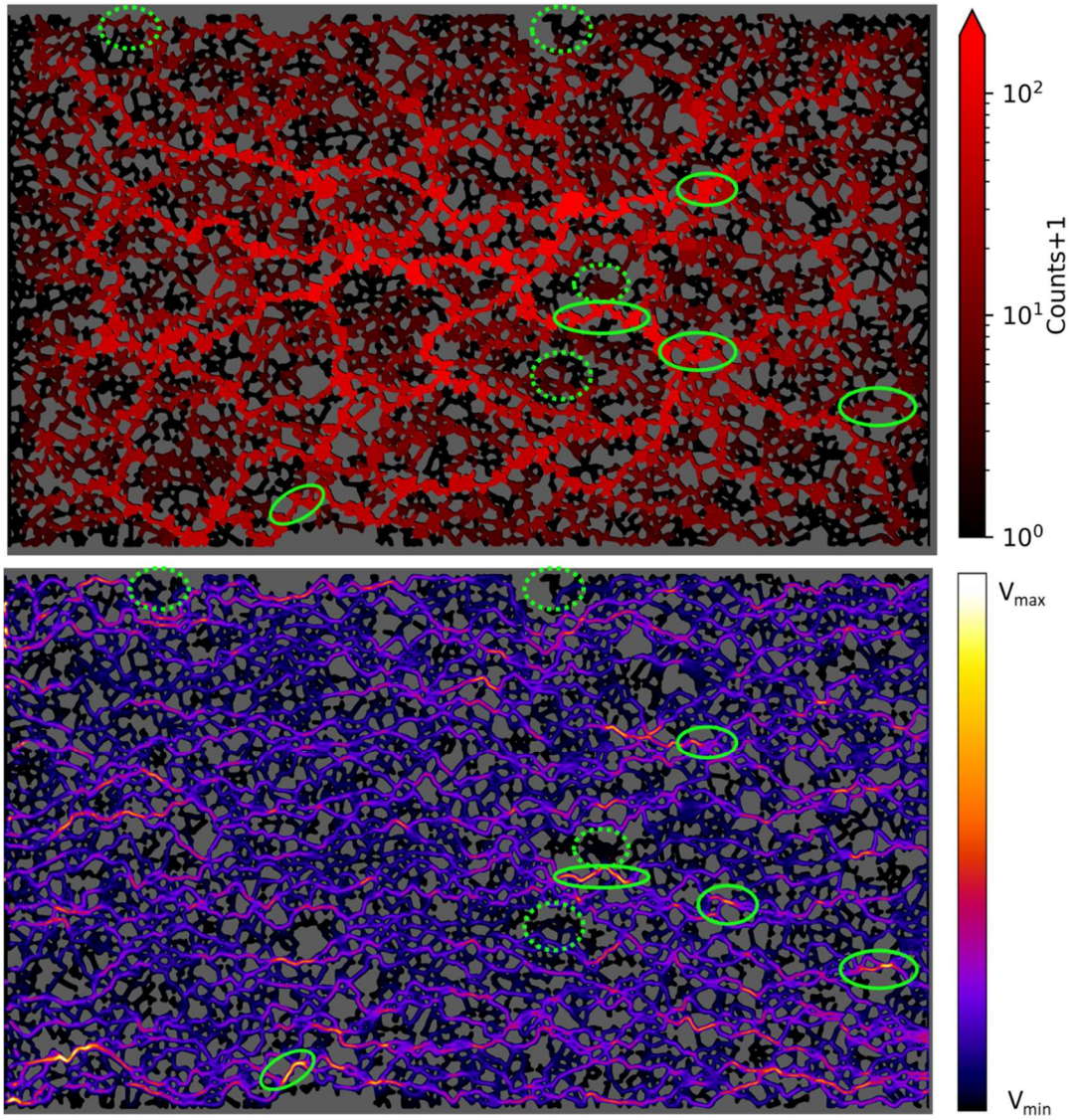

Figure 5-34: 1000 shortest paths using random source and origin nodes, using weights corresponding to best fit model described above $(\alpha, \beta) = (2.2, 0.6)$*. The bottom flow map corresponds to the total flow map of experiment A1, all bubble sizes.*

In fact, a well-known local property of graphs generalizes this type of procedure. Graph betweenness centrality is essentially the number of times each node is traversed by all the shortest paths between all other nodes in the graph, rather than a limited number of random sources and targets. Graph betweenness centrality was first introduced by Bavelas (1948) but was first formally defined by Freeman (1977). Here we give a general definition for the betweenness centrality BC of a node v. The number of shortest paths between all source and targets nodes traversing v is $N_{p(s\to v\to t)}$ are then divided by the number of shortest paths $N_{p(s\to t)}$ between s and t (i.e. number

of paths with the smallest edge weight sum). Indeed, for some graphs multiple paths can have equal edge weight sum values despite being distinct.

$$BC(v) = \sum_{s,t \epsilon V} \frac{N_{p(s \to v \to t)}}{N_{p(s \to t)}} \tag{33}$$

where V is the set of nodes of the graph. If $s = t$, $N_{p(s \to t)} = 1$, and if $v \epsilon \{s, t\}$, $N_{p(s \to t)} = 0$ (Brandes and Pich 2007).

Such a value can be calculated for various choices of weights. Visualizations of the graph centrality are in fact almost indistinguishable from the figures shown above. Graph centrality can rapidly be calculated using the Python library NetworkX (Varoquaux et al. 2008) from an input graph.

While high betweenness centrality does seem to locally describe to some degree areas susceptible to contain higher flow, and in some cases low centrality can correlate with low flow, one drawback is the concentration of high values in the center of the graph, with measured centrality values decreasing radially outwards from the center of the model. Indeed, as most diagonal paths will cross the center of the network, centrality value will naturally increase. However other centrality measurements exist that may better capture local contrasts in centrality (Piraveenan et al. 2013; Gregory 2003) and call for further investigation.

Nonetheless, we integrate the local betweenness centrality values for different weight functions as new pore structural features into the machine learning framework. Starting from the previously established 4 top features for predicting pore flow intensity in Chapter 4, we can test the usefulness of each betweenness centrality calculation by training and testing the models with each added individually. We then only use 5 features for each model: 1-Throat size average, 1-Throat cos(ν) average, Coordination, 2-Coordination, and finally the specific betweenness centrality used. We therefore test for no use of betweenness centrality for comparison, betweenness centrality with equal weights, i.e. $(\alpha, \beta) = (0, 0)$, betweenness centrality with a 1-parameter model, i.e. $(\alpha, \beta) = (1, 0)$, betweenness Figure 5-35 centrality with the best fitted 2-parameter model, i.e. $(\alpha, \beta) = (2.2, 0.6)$.

We display the model accuracies predicting flow intensity in all the flowmaps and classifications explored in Chapter 4, comparing the supplementary effect of adding different calculations of betweenness centrality.

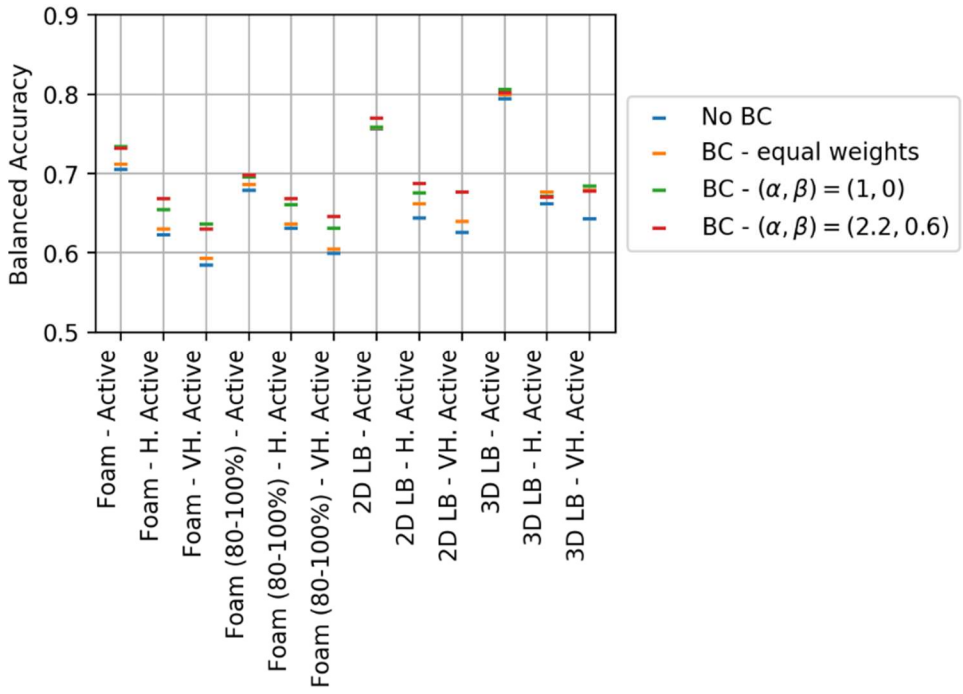

Figure 5-35: Comparison of betweenness centrality feature usefulness.

Evidently, the inclusion betweenness centrality with weights given by the best model fits $(\alpha, \beta) = (2.2, 0.6)$ and $(\alpha, \beta) = (1, 0)$ providing useful information, with the Random Forest algorithm achieving higher accuracy scores for most flow maps with its inclusion. The inclusion of the betweenness centrality using edge weights $(\alpha, \beta) = (2.2, 0.6)$ increases the accuracy in some cases of more than 5% versus using only the original four top features established in Chapter 4. As we hypothesized, including local characteristics derived from network-level considerations is more effective for the higher activity classifications, which see the larger increases in accuracy. The lower activity classifications see little added benefit from the betweenness centrality.

5.9 Conclusion

Through this chapter we presented a graph-based framework that proposes preferential paths in the aim of capturing pores containing high velocity in various foam flow situations. We first optimized a 1-parameter (throat size only) and 2-parameter model (throat size and neighboring pore alignment to pressure gradient) on two different experiments at varying injection rates.

While achieving good results in a large series of parameter combinations, the best models were slightly different for each experiment, with the lower velocity model not integrating the neighbor

alignment parameter in the best fit. The best fit dependence to the throat size was coherent with a known expression of hydraulic resistance for rectangular channels.

The framework was then generalized as it was applied first to an experiment in which the injection direction was reversed, showing the same best fit as for the original experiment.

Generalization to a porous medium of a different scale and structure was then performed. Another two flow maps obtained from a larger, simpler network obtained from the literature were analyzed and a best fit model was found for them both. The best fit models showed notably lower dependence to the throat size than expected from knowledge of the throat sizes and aspect ratios.

Finally, we tested the integration of betweenness centrality in the machine learning framework of Chapter 3, as a local pore parameter that is derived from network-level calculations of best paths for all the nodes in the network. This led to an increase in predictive power to the algorithms used of more than 5% in some cases, with the largest increases being seen predicting the highest velocity pores.

General Conclusion

This thesis presents several experiments performed on a micromodel with a fixed structure. The aim of the thesis is to gain insights into foam flow behavior through a combination of data types and a complex model with, when applicable, systematic reference to an origin in terms of the porous medium structure. We have approached this task using multiple scales and modeling frameworks.

Initially, through only observations on one experiment, we established the existence of a large degree of local flow heterogeneity in our model with flow behaviors varying from trapped zones to high velocity preferential paths, showing global similarities to Newtonian flow, but in many cases accentuating the contrasts of flow distributions found in the Newtonian simulations. Furthermore, we observe differences in flow paths used by different bubble sizes, with larger bubbles using exclusively the straighter preferential paths, travelling at higher velocity, whereas smaller bubbles were also present in transversal paths perpendicular to the pressure gradient direction at generally lower flow intensity.

Next, we sought to understand the dependence of these behaviors on injection parameters by varying injection rates, foam qualities and inlet bubble size distributions. With regards to the link between local and macroscopic flow parameters, we observe that the main contributor to foam apparent viscosity variation within our experiments is the trapped foam fraction, which we found to vary greatly with respect to flow rates and inlet bubble properties. To a smaller degree, we refined our viscosity model to include the total perimeter of bubbles within the model, a more specific version of bubble density, applicable to heterogeneous bubble flow. This result may be specific to our porous medium and experimental conditions, as our foam bubble density is roughly on the same order of magnitude throughout. Nonetheless, it became evident that characterization of the trapped areas was paramount in describing flow on a macroscopic level. With regards to the structural parameter dependence, we can cite certain observations that don’t show a structural origin and therefore escape any detailed characterization in terms of pore scale or model scale structural parameters. Indeed, the large-scale flow distribution of foam inside the model, showing sometimes a preference to flow on one side or the other, was sensitive to the inlet local foam quality and size distributions. Large fluctuations in flow intensity and distribution can be inherited

from the irregularities in inlet foam injections. While this is not necessarily a weakness of the experimental set up, and could be a characteristic of foam transport in real 3D media, it shows that to a certain degree, particularly in low injection rate and high foam quality injections, local structural descriptions of both high-flow areas or trapped zones are in fact irrelevant due to the overwhelming influence of upstream flow and bubble size characteristics. However, in other cases, a repeated observation of certain local trapped and high-velocity zones throughout experiments that were not dominated by inlet irregularities indicated that a structural origin does in fact exist.

Subsequently, through an extensive local structural parameter search using a Random Forest algorithm we uncovered that the most influential parameters in predicting trapped zones were the neighboring throat sizes and orientation, along with the pore coordination. While the trapped zones were relatively well characterized and predicted using only these parameters, high-flow zones were unable to be correctly predicted within this local framework and required a different type of model.

Therefore, we introduced a network-spanning model that built on the observation of preferential paths to characterize high flow zones of the model. The models make use of a recently published algorithm that proposes full-model length paths respecting a maximal value of overlap, a shared characteristic with the observed preferential foam paths. Through the previously understood importance of throat size and throat orientation, we proposed models that integrate successively only the throat size, and then throat size with the neighboring pore alignment of the throats. We successfully fit models that capture many of the high-velocity local elements, with exponent dependencies that are coherent with well-established expressions of hydraulic resistance of the throats. The models are additionally generalized to experiments with opposite injection direction and then to data obtained in the literature of other porous 2D models. In a final section, we make use of betweenness centrality, a well-known graph property, in conjunction with the fitted preferential path model parameters to return to predict more successfully local pore velocity, showing definitively the multi-scale nature of foam flow characteristics.

Publication bibliography

A. Gauglitz, P.; Friedmann, F.; I. Kam, S.; R. Rossen, W. (2002): Foam generation in homogeneous porous media. In *Chemical Engineering Science* 57 (19), pp. 4037–4052. DOI: 10.1016/S0009-2509(02)00340-8.

Aarra, Morten Gunnar; Skauge, Arne; Solbakken, Jonas; Ormehaug, Per Arne (2014): Properties of N2- and CO2-foams as a function of pressure. In *Journal of Petroleum Science and Engineering* 116, pp. 72–80. DOI: 10.1016/j.petrol.2014.02.017.

Almajid, Muhammad M.; Kovscek, Anthony R. (2015): Pore-level mechanics of foam generation and coalescence in the presence of oil. In *Advances in colloid and interface science. DOI:* 10.1016/j.cis.2015.10.008.

AlQuaimi, B. I.; Rossen, W. R. (2019): Study of foam generation and propagation in fully characterized physical-model fracture. In *Journal of Petroleum Science and Engineering* 175, pp. 1169–1181. DOI: 10.1016/j.petrol.2018.06.025.

Altman, N. S. (1992): An Introduction to Kernel and Nearest-Neighbor Nonparametric Regression. In *The American Statistician* 46 (3), pp. 175–185. DOI: 10.1080/00031305.1992.10475879.

Alvarez, J. M.; Rivas, H. J.; Rossen, W. R. (2001): Unified Model for Steady-State Foam Behavior at High and Low Foam Qualities. In *SPE Journal* 6 (03), pp. 325–333. DOI: 10.2118/74141-PA.

Aronson, A. S.; Bergeron, V.; Fagan, M. E.; Radke, C. J. (1994): The influence of disjoining pressure on foam stability and flow in porous media. In *Colloids and Surfaces A: Physicochemical and Engineering Aspects* 83 (2), pp. 109–120. DOI: 10.1016/0927-7757(94)80094-4.

Basheva, Elka S.; Ganchev, Dragomir; Denkov, Nikolai D.; Kasuga, Kenichi; Satoh, Naoki; Tsujii, Kaoru (2000): Role of Betaine as Foam Booster in the Presence of Silicone Oil Drops. In *Langmuir* 16 (3), pp. 1000–1013. DOI: 10.1021/la990777.

Bavelas, Alex (1948): A mathematical model for group structures. In *Human organization* 7.

Bear, Jacob (1988): Dynamics of fluids in porous media.

Bergeron, V.; Fagan, M. E.; Radke, C. J. (1993): Generalized entering coefficients. A criterion for foam stability against oil in porous media. In *Langmuir* 9 (7), pp. 1704–1713. DOI: 10.1021/la00031a017.

Bernard, George G.; Holm, L. W. (1964): Effect of Foam on Permeability of Porous Media to Gas. In *Society of Petroleum Engineers Journal* 4 (03), pp. 267–274. DOI: 10.2118/983-PA.

Bernard, George G.; Jacobs, W. L. (1965): Effect of Foam on Trapped Gas Saturation and on Permeability of Porous Media to Water. In *Society of Petroleum Engineers Journal* 5 (04), pp. 295–300. DOI: 10.2118/1204-PA.

BP Energy Outlook (2019): BP Energy Outlook. 2019 Edition.

Brandes, Ulrik; Pich, Christian (2007): Centrality Estimation In Large Networks. In *Int. J. Bifurcation Chaos* 17 (07), pp. 2303–2318. DOI: 10.1142/S0218127407018403.

Breiman, Leo (2001). In *Machine Learning* 45 (1), pp. 5–32. DOI: 10.1023/A:1010933404324.

Breiman, Leo; Friedman, Jerome H.; Olshen, Richard A.; Stone, Charles J. (1984): Classification And Regression Trees: Routledge.

Bretherton, F. P. (1961): The motion of long bubbles in tubes. In *J. Fluid Mech.* 10 (02), p. 166. DOI: 10.1017/S0022112061000160.

Brodersen, Kay Henning; Ong, Cheng Soon; Stephan, Klaas Enno; Buhmann, Joachim M. (2010): The Balanced Accuracy and Its Posterior Distribution. In : Proceedings of the 2010 20th International Conference on Pattern Recognition. Washington, DC, USA: IEEE Computer Society (ICPR '10), pp. 3121–3124. Available online at https://doi.org/10.1109/ICPR.2010.764.

Chambers, K. T.; Radke, C. J. (1990): Micromodel foam flow study.

Chen, Qing; Gerritsen, Margot; Kovscek, Anthony R. (2010): Modeling Foam Displacement With the Local-Equilibrium Approximation. Theory and Experimental Verification. In *SPE Journal* 15 (01), pp. 171–183. DOI: 10.2118/116735-PA.

Chondrogiannis, Theodoros; Bouros, Panagiotis; Gamper, Johann; Leser, Ulf (2017): Exact and Approximate Algorithms for Finding k-Shortest Paths with Limited Overlap.

Conn, Charles A.; Ma, Kun; Hirasaki, George J.; Biswal, Sibani Lisa (2014): Visualizing oil displacement with foam in a microfluidic device with permeability contrast. In *Lab on a chip* 14 (20), pp. 3968–3977. DOI: 10.1039/c4lc00620h.

Couto, Hudson J. B.; Massarani, Guilio; Biscaia, Evaristo C.; Sant'Anna, Geraldo L. (2009): Remediation of sandy soils using surfactant solutions and foams. In *Journal of hazardous materials* 164 (2-3), pp. 1325–1334. DOI: 10.1016/j.jhazmat.2008.09.129.

Dijkstra, E. W. (1959): A note on two problems in connexion with graphs. In *Numer. Math.* 1 (1), pp. 269–271. DOI: 10.1007/BF01386390.

Dollet, Benjamin; Jones, Siân A.; Méheust, Yves; Cantat, Isabelle (2014): Influence of the elastic deformation of a foam on its mobility in channels of linearly varying width. In *Physical review. E, Statistical, nonlinear, and soft matter physics* 90 (2), p. 23006. DOI: 10.1103/PhysRevE.90.023006.

Dollet, Benjamin; Raufaste, Christophe (2014): Rheology of aqueous foams. In *Liquid and solid foams / Mousses liquides et solides* 15 (8–9), pp. 731–747. DOI: 10.1016/j.crhy.2014.09.008.

Dullien, F.A.L. (1992): Pore Structure. In F. A. L. Dullien (Ed.): Porous media. Fluid transport and pore structure. 2nd ed.: Elsevier, pp. 5–115.

Ettinger, R. A.; Radke, C. J. (1992): Influence of Texture on Steady Foam Flow in Berea Sandstone. In *SPE Reservoir Engineering* 7 (01), pp. 83–90. DOI: 10.2118/19688-PA.

Falls, A. H.; Hirasaki, G. J.; Patzek, T. W.; Gauglitz, D. A.; Miller, D. D.; Ratulowski, T. (1988): Development of a Mechanistic Foam Simulator. The Population Balance and Generation by Snap-Off. In *SPE Reservoir Engineering* 3 (03), pp. 884–892. DOI: 10.2118/14961-PA.

Falls, A. H.; Musters, J. J.; Ratulowski, J. (1989): The Apparent Viscosity of Foams in Homogeneous Bead Packs. In *SPE Reservoir Engineering* 4 (02), pp. 155–164. DOI: 10.2118/16048-PA.

Fernø, Martin A.; Gauteplass, Jarand; Pancharoen, Monrawee; Haugen, Åsmund; Graue, Arne; Kovscek, Anthony R.; Hirasaki, George (2016): Experimental Study of Foam Generation, Sweep Efficiency, and Flow in a Fracture Network. In *SPE Journal* 21 (04), pp. 1140–1150. DOI: 10.2118/170840-PA.

Freeman, Linton C. (1977): A Set of Measures of Centrality Based on Betweenness. In *Sociometry* 40 (1), p. 35. DOI: 10.2307/3033543.

Freeze, R. Allan; Cherry, John A. (1979): Groundwater. Englewood Cliffs, London: Prentice-Hall.

Friedmann, Francois; Chen, W. H.; Gauglitz, P. A. (1991): Experimental and Simulation Study of High-Temperature Foam Displacement in Porous Media. In *SPE Reservoir Engineering* 6 (01), pp. 37–45. DOI: 10.2118/17357-PA.

Gassara, O.; Douarche, F.; Braconnier, B.; Bourbiaux, B. (2017): Equivalence Between Semi-empirical and Population-Balance Foam Models. In *Transp Porous Med* 120 (3), pp. 473–493. DOI: 10.1007/s11242-017-0935-8.

Gauteplass, Jarand; Chaudhary, Kuldeep; Kovscek, Anthony R.; Fernø, Martin A. (2015): Pore-level foam generation and flow for mobility control in fractured systems. In *Colloids and Surfaces A: Physicochemical and Engineering Aspects* 468, pp. 184–192. DOI: 10.1016/j.colsurfa.2014.12.043.

Géraud, Baudouin; Jones, Siân A.; Cantat, Isabelle; Dollet, Benjamin; Méheust, Yves (2016): The flow of a foam in a two-dimensional porous medium. In *Water Resour. Res.* 52 (2), pp. 773–790. DOI: 10.1002/2015WR017936.

Géraud, Baudouin; Méheust, Yves; Cantat, Isabelle; Dollet, Benjamin (2017): Lamella Division in a Foam Flowing through a Two-Dimensional Porous Medium. A Model Fragmentation Process. In *Physical review letters* 118 (9), p. 98003. DOI: 10.1103/PhysRevLett.118.098003.

Gido, Samuel P.; Hirt, Douglas E.; Montgomery, Susan M.; Prud'homme, Robert K.; Rebenfeld, Ludwig (1989): Foam Bubble Size Measured using Image Analysis Before and After Passage through a Porous Medium. In *Journal of Dispersion Science and Technology* 10 (6), pp. 785–793. DOI: 10.1080/01932698908943199.

Gregory, Steve (2003): Local Betweenness for Finding Communities in Networks.

Hatziavramidis, D. T.; Alameddine, B. R.; Weinstein, H. G.; Djabbarah, N. F.; Revay, J. M. (1995): A Mechanistic Foam Model for Simulation of Steamfoam Field Applications. In : SPE Annual Technical Conference and Exhibition. Dallas, Texas, 1995-10-22.

Hirasaki, G. J.; Lawson, J. B. (1985): Mechanisms of Foam Flow in Porous Media. Apparent Viscosity in Smooth Capillaries. In *Society of Petroleum Engineers Journal* 25 (02), pp. 176–190. DOI: 10.2118/12129-PA.

Höhler, R.; Cohen-Addad, S. (2005): Rheology of liquid foam. In *Journal of Physics: Condensed Matter* 17 (41), pp. R1041. Available online at http://stacks.iop.org/0953-8984/17/i=41/a=R01.

Höhler, Reinhard; Sang, Yann Yip Cheung; Lorenceau, Elise; Cohen-Addad, Sylvie (2008): Osmotic pressure and structures of monodisperse ordered foam. In *Langmuir : the ACS journal of surfaces and colloids* 24 (2), pp. 418–425. DOI: 10.1021/la702309h.

Huh, D. G.; Cochrane, T. D.; Kovarik, F. S. (1989): The Effect of Microscopic Heterogeneity on CO2-Foam Mobility. Part 1--Mechanistic Study. In *Journal of Petroleum Technology* 41 (08), pp. 872–879. DOI: 10.2118/17359-PA.

Jiménez, A. I.; Radke, C. J. (1989): Dynamic Stability of Foam Lamellae Flowing Through a Periodically Constricted Pore. In John K. Borchardt, Teh Fu Yen (Eds.): Oil-field chemistry. Enhanced recovery and production stimulation / John K. Borchardt, editor, Teh Fu Yen, editor, vol. 396. Washington, D.C.: American Chemical Society (ACS Symposium Series, 396), pp. 460–479.

Jones, Eric; Oliphant, Travis; Peterson, Pearu; others (2001-): SciPy. Open source scientific tools for Python. Available online at http://www.scipy.org/.

Jones, S. A.; Getrouw, N.; Vincent-Bonnieu, S. (2018a): Foam flow in a model porous medium. I. The effect of foam coarsening. In *Soft Matter* 14 (18), pp. 3490–3496. DOI: 10.1039/c7sm01903c.

Jones, S. A.; Getrouw, N.; Vincent-Bonnieu, S. (2018b): Foam flow in a model porous medium. II. The effect of trapped gas. In *Soft Matter* 14 (18), pp. 3497–3503. DOI: 10.1039/c7sm02458d.

Kam, S. I.; Rossen, W. R. (2003): A Model for Foam Generation in Homogeneous Media. In *SPE Journal* 8 (04), pp. 417–425. DOI: 10.2118/87334-PA.

Khatib, Z. I.; Hirasaki, G. J.; Falls, A. H. (1988): Effects of Capillary Pressure on Coalescence and Phase Mobilities in Foams Flowing Through Porous Media. In *SPE Reservoir Engineering* 3 (03), pp. 919–926. DOI: 10.2118/15442-PA.

Khristov, Khr; Krugljakov, P.; Exerowa, D. (1979): Influence of the pressure in the Plateau-Gibbs borders on the drainage and the foam stability. In *Colloid & Polymer Sci* 257 (5), pp. 506–511. DOI: 10.1007/BF01626229.

Kilbane, John; Chowdiah, P.; Kayser, Kevin; Misra, B.; Jackowski, K. A.; Srivastava, Vipul et al. (1997): Remediation of contaminated soils using foams. In *Land Contamination & Reclamation* 5, pp. 41–54.

Kovscek, A. R.; Bertin, H. J. (2003): Foam mobility in heterogeneous porous media - (I: Scaling concepts). In *Transport in Porous Media* 52 (1), pp. 17–35. DOI: 10.1023/A:1022312225868.

Kovscek, A. R.; Patzek, T. W.; Radke, C. J. (1995): A mechanistic population balance model for transient and steady-state foam flow in Boise sandstone. In *Chemical Engineering Science* 50 (23), pp. 3783–3799. DOI: 10.1016/0009-2509(95)00199-F.

Kovscek, A. R.; Radke, C. J. (1996): Gas bubble snap-off under pressure-driven flow in constricted noncircular capillaries. In *Colloids and Surfaces A: Physicochemical and Engineering Aspects* 117 (1-2), pp. 55–76. DOI: 10.1016/0927-7757(96)03637-0.

Legland, David; Arganda-Carreras, Ignacio; Andrey, Philippe (2016): MorphoLibJ. Integrated library and plugins for mathematical morphology with ImageJ. In *Bioinformatics (Oxford, England)* 32 (22), pp. 3532–3534. DOI: 10.1093/bioinformatics/btw413.

Li, Robert Feng; Yan, Wei; Liu, Shunhua; Hirasaki, George; Miller, Clarence A. (2013): Foam Mobility Control for Surfactant Enhanced Oil Recovery. In *SPE Journal* 15 (04), pp. 928–942. DOI: 10.2118/113910-PA.

Liontas, Rachel; Ma, Kun; Hirasaki, George J.; Biswal, Sibani Lisa (2013): Neighbor-induced bubble pinch-off. Novel mechanisms of in situ foam generation in microfluidic channels. In *Soft Matter* 9 (46), p. 10971. DOI: 10.1039/c3sm51605a.

Lundberg, Scott M.; Lee, Su-In (2017): A Unified Approach to Interpreting Model Predictions. In I. Guyon, U. V. Luxburg, S. Bengio, H. Wallach, R. Fergus, S. Vishwanathan, R. Garnett (Eds.): Advances in Neural Information Processing Systems 30: Curran Associates, Inc, pp. 4765–4774. Available online at http://papers.nips.cc/paper/7062-a-unified-approach-to-interpreting-model-predictions.pdf.

Ma, Kun; Ren, Guangwei; Mateen, Khalid; Morel, Danielle; Cordelier, Philippe (2015): Modeling Techniques for Foam Flow in Porous Media. In *SPE Journal* 20 (03), pp. 453–470. DOI: 10.2118/169104-PA.

Manchuk, J. G.; Leuangthong, O.; Deutsch, C. V. (2009): The Proportional Effect. In *Math Geosci* 41 (7), pp. 799–816. DOI: 10.1007/s11004-008-9195-z.

Mast, R. F. (1972): Microscopic Behavior of Foam in Porous Media. In : Fall Meeting of the Society of Petroleum Engineers of AIME. San Antonio, Texas, 1972-10-08.

Moré, Jorge J.; Garbow, Burton S.; Hillstrom, Kenneth E. (1980): User Guide for MINPACK-1. pub-ANL. pub-ANL:adr (ANL-80-74).

Muggeridge, Ann; Cockin, Andrew; Webb, Kevin; Frampton, Harry; Collins, Ian; Moulds, Tim; Salino, Peter (2014): Recovery rates, enhanced oil recovery and technological limits. In *Philosophical transactions. Series A, Mathematical, physical, and engineering sciences* 372 (2006), p. 20120320. DOI: 10.1098/rsta.2012.0320.

Mulligan, Catherine N.; Eftekhari, Farzad (2003): Remediation with surfactant foam of PCP-contaminated soil. In *Engineering Geology* 70 (3-4), pp. 269–279. DOI: 10.1016/S0013-7952(03)00095-4.

Nguyen, Quoc P.; Currie, Peter K.; Buijse, Marten; Zitha, Pacelli L.J. (2007): Mapping of foam mobility in porous media. In *Journal of Petroleum Science and Engineering* 58 (1-2), pp. 119–132. DOI: 10.1016/j.petrol.2006.12.007.

Nguyen, Quoc P.; Rossen, William R.; Zitha, Pacelli L.J.; Currie, Peter K. (2009): Determination of Gas Trapping With Foam Using X-Ray Computed Tomography and Effluent Analysis. In *SPE Journal* 14 (02), pp. 222–236. DOI: 10.2118/94764-PA.

Nguyen, Quoc P.; Thissen, Michiel H.G.; Zitha, Pacelli L.J. (2002): Effect of Trapped Foam on Gas Tracer Diffusion in a Visual Microflow Model. In : SPE/DOE Improved Oil Recovery Symposium. Tulsa, Oklahoma, 2002-04-13.

Nussbaum-Krammer, Carmen I.; Neto, Mário F.; Brielmann, Renée M.; Pedersen, Jesper S.; Morimoto, Richard I. (2015): Investigating the spreading and toxicity of prion-like proteins using the metazoan model organism C. elegans. In *Journal of visualized experiments : JoVE* (95), p. 52321. DOI: 10.3791/52321.

Osei-Bonsu, Kofi; Shokri, Nima; Grassia, Paul (2016): Fundamental investigation of foam flow in a liquid-filled Hele-Shaw cell. In *Journal of Colloid and Interface Science* 462, pp. 288–296. DOI: 10.1016/j.jcis.2015.10.017.

Osterloh, W. T.; Jante, M. J. (1992): Effects of Gas and Liquid Velocity on Steady-State Foam Flow at High Temperature. In : SPE/DOE Enhanced Oil Recovery Symposium. Tulsa, Oklahoma, 1992-04-22.

Ouali, Chakib (2019): Caractérisation multi-échelle des mousses en milieux poreux en contexte EOR. Doctoral Thesis. Sorbonne Université, Paris.

Pang, Zhan-Xi (2010): The Blocking Ability and Flowing Characteristics of Steady Foams in Porous Media. In *Transp Porous Med* 85 (1), pp. 299–316. DOI: 10.1007/s11242-010-9563-2.

Patzek, T. W. (1989): Description of Foam Flow in Porous Media by the Population Balance Method. In John K. Borchardt, Teh Fu Yen (Eds.): Oil-field chemistry. Enhanced recovery and production stimulation / John K. Borchardt, editor, Teh Fu Yen, editor, vol. 373. Washington, D.C.: American Chemical Society (ACS Symposium Series, 396), pp. 326–341.

Pedregosa et al (2011): Scikit-learn: Machine Learning in Python. In *Journal of Machine Learning Research* 12, pp. 2825–2830.

Pedroni, Lucas (2017): Experimental study of mobility control by foams. Potential of a FAWAG process in pre-salt reservoir conditions.

Piraveenan, Mahendra; Prokopenko, Mikhail; Hossain, Liaquat (2013): Percolation centrality. Quantifying graph-theoretic impact of nodes during percolation in networks. In *PloS one* 8 (1), e53095. DOI: 10.1371/journal.pone.0053095.

Plateau, J.A.F. (1873): Statique expérimentale et théorique des liquides soumis aux seules forces moléculaires. Chap. 5: Gauthier-Villiard, Paris. Available online at https://archive.org/details/statiqueexprime00platgoog.

Prieditis, John. (1988): A pore level investigation of foam flow behavior in porous media. University of Houston, Houston.

Quennouz, N.; Ryba, M.; Argillier, J.-F.; Herzhaft, B.; Peysson, Y.; Pannacci, N. (2014): Microfluidic Study of Foams Flow for Enhanced Oil Recovery (EOR). In *Oil Gas Sci. Technol. – Rev. IFP Energies nouvelles* 69 (3), pp. 457–466. DOI: 10.2516/ogst/2014017.

Radke, C. J.; Gillis, J. V. (1990): A Dual Gas Tracer Technique for Determining Trapped Gas Saturation During Steady Foam Flow in Porous Media. In *SPE Annual Technical Conference and Exhibition. DOI:* 10.2118/20519-MS.

Ransohoff, T. C.; Radke, C. J. (1988): Mechanisms of Foam Generation in Glass-Bead Packs. In *SPE Reservoir Engineering* 3 (02), pp. 573–585. DOI: 10.2118/15441-PA.

Ribeiro, Marco Tulio; Singh, Sameer; Guestrin, Carlos (2016): "Why Should I Trust You?". Explaining the Predictions of Any Classifier. Available online at https://arxiv.org/pdf/1602.04938.

Rizzo, Calogero B.; Barros, Felipe P. J. de (2017): Minimum Hydraulic Resistance and Least Resistance Path in Heterogeneous Porous Media. In *Water Resour. Res.* 53 (10), pp. 8596–8613. DOI: 10.1002/2017WR020418.

Rossen, W. R.; Wang, M. W. (1996): Modeling Foams for Acid Diversion. In *SPE Journal* 4 (02), pp. 92–100. DOI: 10.2118/56396-PA.

Rossen, William R. (1990a): Minimum pressure gradient for foam flow in porous media. Effect of interactions with stationary lamellae. In *Journal of Colloid and Interface Science* 139 (2), pp. 457–468. DOI: 10.1016/0021-9797(90)90118-8.

Rossen, William R. (1990b): Theory of mobilization pressure gradient of flowing foams in porous media: I. Incompressible foam. In *Journal of Colloid and Interface Science* 136 (1), pp. 1–16. DOI: 10.1016/0021-9797(90)90074-X.

Rossen, William R. (1990c): Theory of mobilization pressure gradient of flowing foams in porous media: II. Effect of compressibility. In *Journal of Colloid and Interface Science* 136 (1), pp. 17–37. DOI: 10.1016/0021-9797(90)90075-Y.

Rossen, William R. (1990d): Theory of mobilization pressure gradient of flowing foams in porous media: III. Asymmetric lamella shapes. In *Journal of Colloid and Interface Science* 136 (1), pp. 38–53. DOI: 10.1016/0021-9797(90)90076-Z.

Rossen, William R. (2003): A critical review of Roof snap-off as a mechanism of steady-state foam generation in homogeneous porous media. In *Colloids and Surfaces A: Physicochemical and Engineering Aspects* 225 (1-3), pp. 1–24. DOI: 10.1016/S0927-7757(03)00309-1.

Rossen, William R. (2008): Comment on "Verification of Roof snap-off as a foam-generation mechanism in porous media at steady state". In *Colloids and Surfaces A: Physicochemical and Engineering Aspects* 322 (1-3), pp. 261–269. DOI: 10.1016/j.colsurfa.2008.02.034.

Schramm, Laurier L. (1994): Foams: Fundamentals and Applications in the Petroleum Industry. Washington, DC: American Chemical Society (242).

Schramm, Laurier L.; Wassmuth, Fred (1994): Foams: Basic Principles. In Laurier Lincoln Schramm (Ed.): Foams. Fundamentals and applications in the petroleum industry / Laurier L. Schramm, editor, vol. 242. Washington, D.C.: American Chemical Society (Advances in chemistry series, 0065-2393, 242), pp. 3–45.

Schramm, Laurier Lincoln (2005): Emulsions, foams, and suspensions. Fundamentals and applications / Laurier L. Schramm. Weinheim, Great Britain: Wiley-VCH.

Sheng, James J. (2013): Foams and Their Applications in Enhancing Oil Recovery. In James Sheng (Ed.): Enhanced oil recovery field case studies. Amsterdam: Gulf Professional Publishing, pp. 251–280.

Soille, Pierre; Vincent, Luc M. (1990): <title>Determining watersheds in digital pictures via flooding simulations</title>. In Murat Kunt (Ed.). Lausanne - DL tentative. Lausanne, Switzerland, Monday 1 October 1990: SPIE (SPIE Proceedings), pp. 240–250.

Spearman Rank Correlation Coefficient (2008). In Yadolah Dodge (Ed.): The concise encyclopedia of statistics. Germany?, London: Springer, pp. 502–505.

Talon, L.; Bauer, D.; Gland, N.; Youssef, S.; Auradou, H.; Ginzburg, I. (2012): Assessment of the two relaxation time Lattice-Boltzmann scheme to simulate Stokes flow in porous media. In *Water Resour. Res.* 48 (4), p. 691. DOI: 10.1029/2011WR011385.

Tang, G.-Q.; Kovscek, A. R. (2006): Trapped Gas Fraction During Steady-State Foam Flow. In *Transp Porous Med* 65 (2), pp. 287–307. DOI: 10.1007/s11242-005-6093-4.

Tanyeri, Melikhan; Ranka, Mikhil; Sittipolkul, Natawan; Schroeder, Charles M. (2011): A microfluidic-based hydrodynamic trap. Design and implementation. In *Lab on a chip* 11 (10), pp. 1786–1794. DOI: 10.1039/c0lc00709a.

Tiago Ferreira (2016): Hipnat. Hipnat 1.0.1: Zenodo.

Tsau, Jyun-Syung; Grigg, Reid B. (2013): Assessment of Foam Properties and Effectiveness in Mobility Reduction for CO2-Foam Floods. In : International Symposium on Oilfield Chemistry. International Symposium on Oilfield Chemistry. Houston, Texas, 1997-02-18: Society of Petroleum Engineers.

U.S. Department of Energy (2017): Enhanced Oil Recovery. Available online at https://energy.gov/fe/science-innovation/oil-gas-research/enhanced-oil-recovery.

Varoquaux, Gaël; Vaught, Travis; Millman, Jarrod (Eds.) (2008): Proceedings of the 7th Python in Science Conference. Pasadena, CA USA.

Venturoli, Maddalena; Boek, Edo S. (2006): Two-dimensional lattice-Boltzmann simulations of single phase flow in a pseudo two-dimensional micromodel. In *Physica A: Statistical Mechanics and its Applications* 362 (1), pp. 23–29. DOI: 10.1016/j.physa.2005.09.006.

Viswanathan, H. S.; Hyman, J. D.; Karra, S.; O'Malley, D.; Srinivasan, S.; Hagberg, A.; Srinivasan, G. (2018): Advancing Graph-Based Algorithms for Predicting Flow and Transport in Fractured Rock. In *Water Resour. Res.* 54 (9), pp. 6085–6099. DOI: 10.1029/2017WR022368.

Wagner, T and Lipinski, H (2013): IJBlob. An ImageJ Library for Connected Component Analysis and Shape Analysis. In *Journal of Open Research Software* 1 (1), e6. DOI: 10.5334/jors.ae.

Walker, Strother H.; Duncan, David B. (1967): Estimation of the Probability of an Event as a Function of Several Independent Variables. In *Biometrika* 54 (1/2), p. 167. DOI: 10.2307/2333860.

Weaire, Denis L.; Hutzler, Stefan (2001): The physics of foams. Chap. 1: Oxford University Press.

Yeates, Christopher; Youssef, Souhail; Lorenceau, Elise (2019): New insights of foam flow dynamics in high-complexity 2D micromodels. In *Colloids and Surfaces A: Physicochemical and Engineering Aspects. DOI:* 10.1016/j.colsurfa.2019.04.092.

Yen, Jin Y. (1970): An algorithm for finding shortest routes from all source nodes to a given destination in general networks. In *Quart. Appl. Math.* 27 (4), pp. 526–530. DOI: 10.1090/qam/253822.

Youssef, S.; Rosenberg, E.; Gland, N.; Bekri, S.; Vizika, O. (2007): Quantitative 3D characterization of the pore space of real rocks. Improved μ-CT resolution and pore extraction methodology. In *Soc. Core Anal.*

Zuiderveld, Karel (1994): Contrast limited adaptive histogram equalization. In : Graphics gems IV. Academic Press Professional, Inc, pp. 474–485.